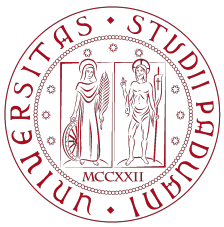

UNIVERSITÀ
DEGLI STUDI
DI PADOVA

University of Padova

Department of Chemical Sciences

PhD course: **Molecular Sciences**

Curriculum: **Chemical Sciences**

Cycle: **XXXVI**

Shaping molecular excited-state properties by means of localized surface plasmon resonances

Supervisor: **Prof. Stefano Corni**

Ph.D. Student: **Marco Romanelli**

Academic Year: **2022/2023**

Contents

List of Publications

Publications related to this thesis:

(† = authors that equally contributed to the work)

1. Romanelli, M.; Dall'Osto, G.; Corni S. Role of metal-nanostructure features on tip-enhanced photoluminescence of single molecules. *The Journal of Chemical Physics*, **2021**, 155, 214304.

2. Coane, C.; Romanelli, M.; Dall'Osto, G.; Di Felice, R.; Corni, S. Unraveling the Mechanism of Tip-Enhanced Molecular Energy Transfer. *preprint arXiv:2305.17265*, **2023**.

3. Kuttruff†, J.; Romanelli†, M.; Pedrueza-Villalmanzo†, E.; Allerbeck, J.; Fregoni, J.; Saavedra-Becerril, V.; Andréasson, J.; Brida, D.; Dmitriev, A.; Corni,S.; Maccaferri, N. Sub-picosecond collapse of molecular polaritons to pure molecular transition in plasmonic photoswitch-nanoantennas. *Nature Communications*, **2023**, 14, 3875.

4. Romanelli†, M.; Riso†, R. R.; Haugland, T. S.; Ronca, E.; Corni, S.; Koch, H. Effective Single-Mode Methodology for Strongly Coupled Multimode Molecular-Plasmon Nanosystems. *Nano Letters*, **2023**, 23, 4938-4946.

5. Romanelli, M.; Dall'Osto, G.; Corni, S. Identifying differences between Semi-Classical and Full-Quantum descriptions of plexcitons. *in preparation*, **2023**.

Other publications:

6. Kabaciński†, P.; Romanelli†, M.; Ponkkonen, E.; Jaiswal, V. K.; Carell, T.; Garavelli, M.; Cerullo, G.; Conti, I. Unified description of ultrafast excited state decay processes in epigenetic deoxycytidine derivatives. *The Journal of Physical Chemistry Letters*, **2021**, 12, 11070-11077.

7. Carone, A.; Mariani, P.; Desert, A.; Romanelli, M.; Marcheselli, J.; Garavelli, M.; Corni, S.; Rivalta, I.; Parola, S. Insight on chirality encoding from small thiolated molecule to plasmonic Au@ Ag and Au@ Au nanoparticles. *ACS nano*, **2022**, 16, 1089-1101.

8. Koya†, A. N.; Romanelli†, M.; Kuttruff†, J.; Henriksson†, N.; Stefancu†, A.; Grinblat†, G.; De Andres†, A.; Schnur†, F.; Vanzan†, M.; Marsili†, M.; Rahaman†, M., et al. Advances in ultrafast plasmonics. *Applied Physics Reviews*, **2023**, 10, 021318 .

Introduction

While not always rigorously understood, light-matter interactions have been fascinating mankind since the dawn of time. As chemists of modern age we nowadays tend to give for granted that colour is nothing but the result of a subtle interplay between absorption and scattering processes due to light visible photons interacting with atoms and molecules all around us. Nevertheless, way before Maxwell's electromagnetism and 20th century quantum mechanics took hold, colors and pigments had been influencing ancient cultures, languages and artists for long time. For instance, in 1969 the anthropologists Brent Berlin and Paul Kay advanced the idea that basic color terms[1–3], such as black and white, sequentially appear in the development of each language, thus suggesting that there could be some sort of significant connection between language, colors and cultural development of populations throughout history.
On the other hand, with regard to art, Van Gogh himself witnessed the importance of colors as a source of inspiration for his work, writing to his brother Theo[4]:

"I have got new ideas and I have new means of expressing what I want, because better brushes will help me, and I am crazy about those two colours, carmine and cobalt. Cobalt is a divine colour, and there is nothing so beautiful for putting atmosphere around things. Carmine is the red of wine, and it is warm and lively like wine. The same with emerald-green. It is bad economy not to use these colours, the same with cadmium".

Undoubtedly, the list of examples and evidences of this long-standing human attraction towards light driven phenomena could be endlessly expanded, and in recent times, by cleverly harnessing scientific knowledge built up over the years, we have also been trying to turn this curious attraction into something practically useful for our society. It is indeed well-established that sunlight is one of the most promising "green" energy renewable resource that Earth has access to, and it is certainly one of the most valuable that we must focus on if we want to successfully deal with next decades humanity greatest challenges, such as climate change, energy shortage and greenhouse gas emissions[5–8]. In this respect, controlling light-matter interactions at the nanoscale, where one can selectively manipulate single small objects instead of dealing with the full complexity of a macroscopic system, surely paves the way for grasping the underlying physico-chemical first principles behind light-driven energy phenomena and thus increasing our chances to build up functional devices able to successfully cope with those arduous tasks[9–12].

To this end, over recent years there has been growing attention towards combining metallic nanostructures with molecular materials, as light-induced molecular excitations usually fall into the same spectral region of collective electronic transitions of widely adopted metals, such as silver, gold, aluminum and so forth, thus setting the stage for interesting phenomena. More

precisely, metallic nanoparticles (NPs) of different size and shape feature a coherent and collective oscillation of the metal conduction electrons arising upon light excitation, which is usually known as Localized Surface Plasmon Resonance (LSPR). This phenomenon leads to the confinement of the external far-field radiation down to the nanoscale, thus leading to the formation of spatial points ("hot-spots"), placed nearby the plasmonic surface, that feature a large electromagnetic field (Fig.1). In other words, the plasmonic system acts as a sort of nanoantenna confining light down to molecular scale, thus paving the way for precise light-matter coupling control[11, 13–19]. This purely electromagnetic effect, called "local field enhancement", is one of the key features of Molecular Plasmonics[20–22], the latter being a wide and currently-active area of research where my PhD thesis exactly lies in. The core idea of this research field is to couple molecules with

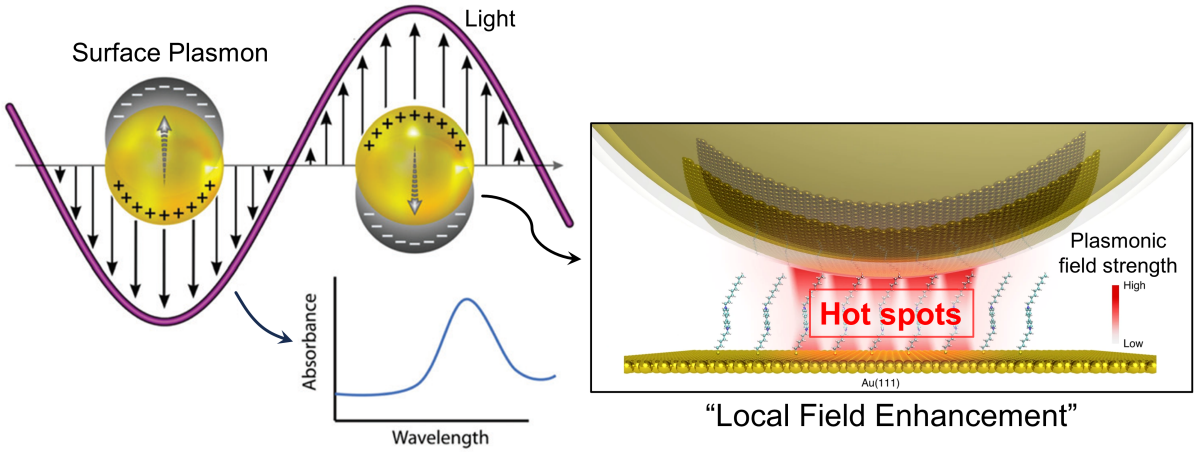

Figure 1: Pictorial representation of LSPR charge oscillation and resulting local field enhancement effect. Adapted from refs.[23, 24]. Copyright 2020 Springer Nature, Copyright 2020 Royal Society of Chemistry.

confined light to ultimately tailor molecular properties by means of plasmon-induced effects, thus achieving accurate control over light-matter coupling at the nanoscale.

Over last decades many scientific works have shown that by cleverly harnessing such kind of interactions, molecular photophysics, for instance, can be sizably affected. Molecular light absorption[25–28], Raman scattering[29, 30] and photoluminescence[31, 32] can all be boosted to such an extent that even single-molecule imaging with sub-molecular resolution has been reported recently[33, 34]. This astonishing control over single molecules that have been possible in recent times, is typically achieved by resorting to atomistically-sharp metallic tip of scanning probe microscopes (like STM) which are able to confine the incoming electromagnetic field down to a spatial scale that is compatible with molecules dimensions, thanks to LSPR-induced local field enhancement. These state of the art techniques are paving the way for quantitatively investigating molecular phenomena, such as energy transfer, chemical reactions, light absorption and emission, at single molecule level, laying the ground for accurate understanding and control of energy flow in the nano world.

At the same time, even when photochemistry is of interest surface plasmons may be of help. Indeed, when the plasmon-mediated light-matter interaction is so strong that hybrid eigenstates

of the coupled system are formed because of the strong coupling, electronic energy levels and so molecular potential energy surfaces can be reshaped. This regime, referred to as "strong coupling", has been drawing more and more attention over last few years as it proved to be a viable and non-invasive way of affecting chemical/photochemical reaction rates[35–38]. It all started ten years ago upon the seminal work of Hutchison et al.[39] where it was shown that the photochemical conversion rate of a spyropiran derivative to the corresponding merocyanine form can be slowed down by placing the molecules inside an optical cavity, the latter being a simpler alternative device to plasmonic systems to reach the strong-coupling regime. Since then, many other works involving also plasmonic platforms came out, eventually leading to the flourishing of an entire area of research called "Polaritonic Chemistry", whose name originate from the newly formed eigenstates upon strong light-matter interaction, i.e. "Polaritons" (or more precisely "Plexcitons" , plasmon + exciton, when dealing with plasmons instead of optical cavities).
In this context the use of plasmonic systems has some clear advantages, such as the possibility of achieving larger coupling values and thus leading to even single-molecule strong-coupling, where the complexity of the full system is to some extent reduced as few molecules are responsible for the investigated processes. Nevertheless, plasmonic systems are well-known to be rather lossy, that is the LSPR excitation gets quickly dissipated within the metal with a well-known list of consecutive events that start with plasmon dephasing, which takes place on a femtosecond (fs) timescale[15], thus posing serious challenges in view of controlling molecular processes by strong plasmon-molecule coupling.

All these examples unambiguously illustrate that the use of plasmonic systems to control molecular photophysics and photochemistry is definitely promising but clearly far from being trivial, therefore a combined synergistic effort between theory and experiments is of utmost importance. Experiments are obviously fundamental to validate models, explanations, but Theory not only can have access to quantities that are difficult to tackle experimentally, but it also has the capability of anticipating phenomena that later on can be experimentally explored and thus, whether disproved or confirmed, pushing our understanding of light-driven molecular phenomena at the nanoscale.

In this regard, this thesis aims at shedding light on the complex interplay between plasmon-molecule interactions that are typically hidden behind experimentally measured quantities. This is done by employing state of the art theoretical and computational modelling techniques to target modern highly-sophisticated experiments or test case systems of great scientific interest. Both new methods development and applications are presented along the following chapters.

In the context of Molecular Plasmonics, due to the size difference between commonly used molecules (Å-nm) and plasmonic nanostructures (tens-hundreds of nm), as well as the wide spatial and temporal scales of the investigated phenomena, accurate modelling is an arduous task. Clearly, a complete *ab initio* description of the full system is out of reach considering the currently available computational resources and expensive scaling of fully quantum-mechanical atomistic theories. On these grounds, multiscale modelling is therefore instrumental as it allows one to focus on system component of most interest (i.e. molecules) with high accuracy, while treating the surroundings, namely nanostructures and/or solvent molecules, with more approx-

imate methods. Remarkably, this strategy has often proved to be good enough to accurately describe the modified molecular response, which is often the target, due to mutual plasmon-molecules interactions. On top of this, which is already tricky to be dealt with properly, external driving , i.e. light excitation, should be also taken into consideration. For most spectroscopic experiments of interest that deals with such hybrid molecular-plasmonic nanosystems, visible light is used and the light intensity is usually high enough to correspond to a very large number of photons, therefore, according to the correspondence principle, a classical description of the driving field usually suffices[40].

In this thesis, I have focused on theoretically investigating different plasmon-molecules interaction regimes, starting with simpler semiclassical perturbative descriptions and moving then to strong-coupling situations, where a quantized description of the plasmonic response needs to be recovered. Effects and applications arising from such light-matter interactions are reported and discussed throughout the thesis. This has been done by combining a quantum chemistry description of target molecules, mainly relying on Density Functional Theory (DFT) or Coupled-Cluster (CC), with a continuum description of the plasmonic system, which is modelled as a classical (or quantum) polarizable homogeneous object based on the Polarizable Continuum Model - NanoParticle[41, 42] (PCM-NP), the latter being essentially rooted in a Boundary Element Method (BEM) approach to solve the electromagnetic problem.
The underlying basics of such theories are described in the next chapter, entitled *Methods*, whereas new method developments and applications to state of the art systems directly related to my PhD activity are reported in the following ones.

Outline

The next chapter, entitled *Methods*, aims at succinctly summarizing the theoretical and computational methods which the following work developed during this thesis relies on. It begins with a brief description of DFT and CC, then a section on BEM follows, where the PCM-NP model is finally introduced. This initial chapter contains theories and methods that had been developed long before this PhD thesis started and do not involve my direct participation. The subsequent chapters are instead strictly related to my PhD activity, and are presented in the form of published articles or manuscript drafts, either in preparation or already submitted and currently under review.
The various chapters follows the line of increasing complexity in the modelling and phenomena being investigated.

Chapter 1, which is based on the article by Romanelli, M.; Dall'Osto, G.; Corni S. *The Journal of Chemical Physics*, 2021, 155, 214304, it presents an application of the PCM-NP model to a molecular-plasmonic system composed of one molecule and a classically-described nanostructure. In this work, state of the art Tip-Enhanced Photoluminescence experiments (TEPL) that target single-molecule imaging with sub-molecular resolution by employing sophisticated STM plasmonic tips are analyzed. The theoretical simulations, validated against recent experimental data, focus on inspecting the role of plasmonic features, such as tip geometrical details and metal

dielectric function in determining the detectable response. The most relevant finding discussed is that experimentally-missing information of the plasmonic tip, such as morpholophy and size of atomistic protrusions located at the tip apex, can drastically impact on the plasmon-induced local field, both in terms of maximum intensity and frequency dependence, thus pointing out that such geometrical features can be considered as an actual control knob to be exploited in order to precisely manipulate plasmon-molecules interactions in such STM junctions.

In Chapter 2, that is presented as preprint (currently under review) by Coane, C.; Romanelli, M.; Dall'Osto, G.; Di Felice, R.; Corni, S. *preprint arXiv:2305.17265*, 2023, similar STM junctions as discussed in Chapter 1 are analyzed, but now the molecular complexity is increased, as two molecules are simultaneously taken into consideration. The presence of an additional nearby molecule opens up additional photophysical processes, such as the possibility of having excitation energy transfer (EET) between a donor (D) species to an acceptor one (A). The motivation underlying this work is exactly to understand how the plasmonic system can quantitatively influence the EET process, thus shedding light on how to steer the energy flow at the nanoscale by means of tip surface plasmons. Following the previous work about TEPL, where the theoretical methodology to model photoluminescence in STM environments is presented, modelling of plasmon-mediated EET is here additionally described. Remarkably, by comparing simulated results with state of the art experimental evidence, it is revealed that the standard criterion to distinguish between Dexter-like or Forster-like mechanisms of energy transfer, i.e. exponential vs d^{-6} decay, is no longer valid because of nanoscale plasmonic effects taking place in such D-A pairs in STM junctions.

So far the complexity of the system being modelled has been progressively increased by acting only on the molecular side, as a classical description of NPs have sufficed to capture the modified molecular photophysics due to interactions with plasmons. Nevertheless, as mentioned in the *Introduction*, there are cases where one needs to go beyond such semiclassical perturbative regime, for instance when dealing with strongly-coupled molecular-plasmonic nanosystems that feature plexciton formation, and so fundamental changes with respect to the unperturbed wavefunctions and energy levels due to strong light-matter coupling. In those situations, a quantized description of the plasmonic system needs to be developed to formally describe a proper exciton-plasmon hybridization.

In this regard, Chapter 3, which is based on the article by Romanelli, M.; Riso, R. R.; Haugland, T. S.; Ronca, E.; Corni, S.; Koch, H. *Nano Letters*, 2023, 23, 4938-4946, tackles cases where the plasmon-molecule coupling leads to profound changes in the molecular structure and molecular properties, such as transition dipoles/densities, due to strong hybridization with the plasmonic modes. In this specific case, *ab initio* quantum electrodynamics (QED) theories including the effect of quantized plasmons/fields already at the level of the full system Hamiltonian are necessary. Nevertheless, despite their accuracy in describing strongly-coupled systems, the computational cost of such methods is significantly higher because of the additional complexity coming from the field degrees of freedom that is added on top of standard *ab initio* quantum chemistry methods. In this chapter, building on a previously developed extension of CC suitable to describe molecules in the presence of single quantized plasmon modes (quantum electrodynamics Coupled Cluster, QED-CC), an inexpensive-yet-accurate extension to multimode plasmonic

systems is presented, thus paving the way for going beyond oversimplified single mode pictures. It is indeed known that assemblies of plasmonic nanostructures of different shape and size may exhibit modes degeneracy and so multiple modes, going beyond simple dipolar resonances of the nanostructures, could be simultaneously relevant to describe phenomena of much scientific interest, e.g. plasmon-mediated chirality[43–46], accurately. In this chapter an effective mode approach able to capture multimode effects while retaining the same computational cost of single mode QED *ab initio* calculations is discussed.

In Chapter 4 the complexity and reality of the system being investigated is even pushed further, combining a quantized description of the plasmonic system with an ensemble of molecules, thus focusing on plexcitonic collective effects. In this chapter, which is reported as published article by Kuttruff, J.; Romanelli, M.; Pedrueza-Villalmanzo, E.; Allerbeck, J.; Fregoni, J.; Saavedra-Becerril, V.; Andréasson, J.; Brida, D.; Dmitriev, A.; Corni,S.; Maccaferri, N. *Nature Communications*, 2023, 14, 3875, the ultrafast sub-picosecond response of an ensemble of merocyanine molecules strongly-coupled to aluminum plasmonic nanoellipses is investigated by combining theory and ultrafast pump-probe experiments. The motivation that prompted us to investigate the ultrafast dynamics of plexcitonic states stems from the well-know observation that plasmon dynamics is extremely fast, that is the initial LSPR excitation gets quickly dephased within the metal few tens of femtoseconds after driving. Therefore, the feasibility of using plasmonic platforms to control light-induced chemical reactions thanks to plexciton formation is still elusive and under debate, since most photochemical processes proceed on longer times scales, from hundreds of fs onwards[47]. Here, based on a synergistic effort between theory and experiments it is revealed that the ultrafast plasmon dephasing leads to a fast ($\approx 10fs$) collapse of an initial plexcitonic collective state to a single molecule transition and the detected transient dynamics can be ascribed to intramolecular excited state dynamics of an excited molecule whose excited state decay is accelerated due to the interaction with the plasmonic local field.

Given the main finding discussed in Chapter 4, it is evident that proper modelling of plexciton formation and dynamics cannot disregard a quantitative inclusion of plasmon losses, especially in view of comparing theoretical predictions with experimental data to ultimately understand how to potentially steer photochemical reactions in the strong-coupling limit. This brings us to Chapter 5, which is also the final part of this thesis, where an effective full-quantum theory aiming at formally describing in real-time plexciton electron dynamics while subjected to plasmon-induced dissipative losses is presented. This chapter, which is reported as a manuscript draft currently in preparation by Romanelli, M.; Dall'Osto, G.; Corni, S. *in preparation*, focuses on directly comparing full-quantum and semi-classical descriptions of molecular electron dynamics of hybrid molecular-plasmonic nanosystems upon external driving i.e. light pulse excitation, while taking plasmonic dissipation into account. In doing so, discrepancies between the two approaches under different excitation and coupling regimes are pinpointed, thus laying the groundwork for real-time investigations of molecules weakly and strongly coupled to arbitrarily-shaped plasmonic NPs under different driving conditions.

All results and methods development achieved during my PhD activity and related to this thesis are reported below in the respective chapters above-mentioned, either in the form of

published articles or manuscript drafts, along with the corresponding supporting information. Each chapter is prefaced by a short introduction where the most relevant details, results and advancements of the presented work are summarized together with my direct contribution to it, which is made explicit. With respect to the initial state of scientific knowledge in the molecular plasmonics field when my PhD activity begun, the results and methods that are collected in this thesis have provided novel and significant contributions towards controlling light-molecules interactions at the nanoscale by means of plasmonic devices.

References

(1) Hardin, C. L.; Maffi, L. E., *Color categories in thought and language.* Cambridge University Press: 1997.

(2) Backhaus, W. G.; Kliegl, R.; Werner, J. S., *Color vision: Perspectives from different disciplines*; Walter de Gruyter: 2011.

(3) Ball, P., *Bright earth: art and the invention of color*; University of Chicago Press: 2003.

(4) Van Gogh, V., *The Letters of Vincent Van Gogh*; Roskill, M., Ed.; Simon & Schuster: 1997.

(5) Gong, J.; Li, C.; Wasielewski, M. R. *Chemical Society Reviews* **2019**, *48*, 1862–1864.

(6) Obaideen, K.; AlMallahi, M. N.; Alami, A. H.; Ramadan, M.; Abdelkareem, M. A.; Shehata, N.; Olabi, A. *International Journal of Thermofluids* **2021**, *12*, 100123.

(7) Jaiswal, K. K.; Chowdhury, C. R.; Yadav, D.; Verma, R.; Dutta, S.; Jaiswal, K. S.; Karuppasamy, K. S. K., et al. *Energy Nexus* **2022**, *7*, 100118.

(8) Kabir, E.; Kumar, P.; Kumar, S.; Adelodun, A. A.; Kim, K.-H. *Renewable and Sustainable Energy Reviews* **2018**, *82*, 894–900.

(9) Yu, H.; Peng, Y.; Yang, Y.; Li, Z.-Y. *npj Computational Materials* **2019**, *5*, 45.

(10) Weiner, J.; Ho, P.-T.; Dee, K. C., *Light-matter interaction: fundamentals and applications*; Wiley Online Library: 2003; Vol. 1.

(11) Giannini, V.; Fernández-Domínguez, A. I.; Heck, S. C.; Maier, S. A. *Chemical reviews* **2011**, *111*, 3888–3912.

(12) Gutzler, R.; Garg, M.; Ast, C. R.; Kuhnke, K.; Kern, K. *Nature Reviews Physics* **2021**, *3*, 441–453.

(13) Ye, W.; Long, R.; Huang, H.; Xiong, Y. *Journal of Materials Chemistry C* **2017**, *5*, 1008–1021.

(14) De Aberasturi, D. J.; Serrano-Montes, A. B.; Liz-Marzán, L. M. *Advanced Optical Materials* **2015**, *3*, 602–617.

(15) Koya[†], A. N.; Romanelli[†], M.; Kuttruff[†], J.; Henriksson[†], N.; Stefancu[†], A.; Grinblat[†], G.; De Andres[†], A.; Schnur[†], F.; Vanzan[†], M.; Marsili[†], M.; Rahaman[†], M., et al. *Applied Physics Reviews* **2023**, *10*, 021318.

(16) Barbillon, G. *Materials* **2019**, *12*, 1502.

(17) Shahbazyan, T. V.; Stockman, M. I., *Plasmonics: theory and applications*; Springer: 2013; Vol. 15.

(18) Jiang, N.; Zhuo, X.; Wang, J. *Chemical reviews* **2017**, *118*, 3054–3099.

(19) Maier, S. A. et al., *Plasmonics: fundamentals and applications*; Springer: 2007; Vol. 1.

(20) Van Duyne, R. P. *Science* **2004**, *306*, 985–986.

(21) Lauchner, A.; Schlather, A. E.; Manjavacas, A.; Cui, Y.; McClain, M. J.; Stec, G. J.; García de Abajo, F. J.; Nordlander, P.; Halas, N. J. *Nano letters* **2015**, *15*, 6208–6214.

(22) Della Sala, F.; D'Agostino, S., *Handbook of molecular plasmonics*; CRC Press: 2013.

(23) Li, C.-Y.; Duan, S.; Wen, B.-Y.; Li, S.-B.; Kathiresan, M.; Xie, L.-Q.; Chen, S.; Anema, J. R.; Mao, B.-W.; Luo, Y., et al. *Nature Nanotechnology* **2020**, *15*, 922–926.

(24) Masson, J.-F. *Analyst* **2020**, *145*, 3776–3800.

(25) Kim, S.-S.; Na, S.-I.; Jo, J.; Kim, D.-Y.; Nah, Y.-C. *Applied Physics Letters* **2008**, *93*.

(26) Itoh, T.; Yamamoto, Y. S.; Ozaki, Y. *Chemical Society Reviews* **2017**, *46*, 3904–3921.

(27) Li, M.; Cushing, S. K.; Wu, N. *Analyst* **2015**, *140*, 386–406.

(28) Lieberman, I.; Shemer, G.; Fried, T.; Kosower, E. M.; Markovich, G. *Angewandte Chemie International Edition* **2008**, *47*, 4855–4857.

(29) Campion, A.; Kambhampati, P. *Chemical society reviews* **1998**, *27*, 241–250.

(30) Langer, J.; Jimenez de Aberasturi, D.; Aizpurua, J.; Alvarez-Puebla, R. A.; Auguié, B.; Baumberg, J. J.; Bazan, G. C.; Bell, S. E.; Boisen, A.; Brolo, A. G., et al. *ACS nano* **2019**, *14*, 28–117.

(31) Li, J.-F.; Li, C.-Y.; Aroca, R. F. *Chemical Society Reviews* **2017**, *46*, 3962–3979.

(32) Dong, J.; Zhang, Z.; Zheng, H.; Sun, M. *Nanophotonics* **2015**, *4*, 472–490.

(33) Yang, B.; Chen, G.; Ghafoor, A.; Zhang, Y.; Zhang, Y.; Zhang, Y.; Luo, Y.; Yang, J.; Sandoghdar, V.; Aizpurua, J., et al. *Nature Photonics* **2020**, *14*, 693–699.

(34) Lee, J.; Crampton, K. T.; Tallarida, N.; Apkarian, V. A. *Nature* **2019**, *568*, 78–82.

(35) Feist, J.; Galego, J.; Garcia-Vidal, F. J. *ACS Photonics* **2018**, *5*, 205–216.

(36) Fregoni, J.; Garcia-Vidal, F. J.; Feist, J. *ACS photonics* **2022**, *9*, 1096–1107.

(37) Herrera, F.; Owrutsky, J. *The Journal of chemical physics* **2020**, *152*.

(38) Bhuyan, R.; Mony, J.; Kotov, O.; Castellanos, G. W.; Gómez Rivas, J.; Shegai, T. O.; Börjesson, K. *Chemical Reviews* **2023**.

(39) Hutchison, J. A.; Schwartz, T.; Genet, C.; Devaux, E.; Ebbesen, T. W. *Angewandte Chemie International Edition* **2012**, *51*, 1592–1596.

(40) McHale, J. L., *Molecular spectroscopy*; CRC Press: 2017.

(41) Corni, S.; Tomasi, J. *The Journal of Chemical Physics* **2001**, *114*, 3739–3751.

(42) Mennucci, B.; Corni, S. *Nature Reviews Chemistry* **2019**, *3*, 315–330.

(43) Carone, A.; Mariani, P.; Desert, A.; Romanelli, M.; Marcheselli, J.; Garavelli, M.; Corni, S.; Rivalta, I.; Parola, S. *ACS nano* **2022**, *16*, 1089–1101.

(44) Mun, J.; Rho, J. *Optics Letters* **2018**, *43*, 2856–2859.

(45) Mun, J.; Rho, J. *Nanophotonics* **2019**, *8*, 941–948.

(46) Wu, T.; Zhang, W.; Wang, R.; Zhang, X. *Nanoscale* **2017**, *9*, 5110–5118.

(47) Turro, N. J., *Modern molecular photochemistry*; University science books: 1991.

Methods

Quantum Chemistry

Standard molecular electronic structure theory focuses on solving the non-relativistic time-independent Schrödinger Equation describing the interaction of nuclei and electrons that constitute molecules,

$$\hat{H}\,|\Psi\rangle = E\,|\Psi\rangle \tag{1}$$

where the molecular Hamiltonian $\hat{H}$ expressed in second-quantization reads[1],

$$\hat{H} = \sum_{pq}\sum_{\sigma} h_{pq}\hat{a}^{\dagger}_{p\sigma}\hat{a}_{q\sigma} + \sum_{pqrs}\sum_{\sigma\tau} g_{pqrs}\hat{a}^{\dagger}_{p\sigma}\hat{a}^{\dagger}_{r\tau}\hat{a}_{s\tau}\hat{a}_{q\sigma} + h_{nuc} \tag{2}$$

with $\hat{a}^{\dagger}_{p\sigma}/\hat{a}_{p\sigma}$ being the corresponding creation/annihilation operator for an electron with spin σ in the p orbital. In eq. 2 the zero-, one- and two- electron integrals have been introduced, which can be computed from the corresponding operators as

$$\begin{aligned} h_{nuc} &= \frac{1}{2}\sum_{A\neq B}\frac{Z_A Z_B}{|R_A - R_B|} \\ h_{pq} &= \int \phi^*_p(r_i)\left(-\frac{1}{2}\hat{\nabla}^2_i + \sum_A \frac{Z_A}{|\hat{r}_i - R_A|}\right)\phi_q(r_i)dr_i \\ g_{pqrs} &= \int\int \frac{\phi^*_p(r_i)\phi^*_r(r_j)\phi_q(r_i)\phi_s(r_j)}{|\hat{r}_i - \hat{r}_j|}dr_i dr_j \end{aligned} \tag{3}$$

where $\hat{r}_i$ is the position operator of the ith electron and $Z_A\,, R_A$ are the Ath nuclear charge and position, respectively. In eq. 2 the common Born-Oppenheimer approximations has been adopted and so nuclei kinetic energy operator does not enter into $\hat{H}$.

Analytical solution of eq. 2 is only possible for mono-electronic systems, like hydrogen atom, while multi-electronic atoms and molecules can in principle be solved "exactly" within a finite but complete basis-set using Full-Configuration Interaction (FCI)[1, 2]; however, it is actually feasible for very small systems only.

Historically, the progenitor of modern quantum chemistry methods is Hartree-Fock (HF), which essentially relies on determining the ground state energy and wavefunction of a multi-electronic system by applying the variational principle to the Hamiltonian of eq. 2 with a mono-configurational reference wavefunction, which for a closed-shell system of N_e electrons reads

$$|R\rangle = \prod_{i}^{1/2N_e} \hat{a}^{\dagger}_{i\alpha}\hat{a}^{\dagger}_{i\beta}\,|vac\rangle \tag{4}$$

where i labels occupied orbitals and α, β are the corresponding possible spin states. Variational minimization of the energy with respect to the orbital basis leads to the well-know Fock matrix problem from which molecular orbitals determining the ground state Hartree-Fock wavefunction can be self-consistently determined[1, 2]. Unfortunately, the so-optimized ground state Hartree-Fock wavefunction $|HF\rangle$ leads to an energy difference with respect to the exact one that is sizeable compared to most chemical phenomena of interest, thus making the HF theory not accurate enough for treating problems of realistic practical significance. This energy difference is known as "correlation energy" and all post-HF methods basically try to recover this fundamental missing contribution which has to do with two-electron interactions.

Among all methods available today, Density Functional Theory (DFT) and Coupled-Cluster (CC) are surely widely known, the first being amply widespread due to its good compromise between accuracy and computational cost, while the second being known as one of the most accurate *ab initio* methods currently available, albeit costly.

In the following, an introduction to the basic concepts behind these methods that are used in this thesis is given.

Density Functional Theory

Density Functional Theory (DFT) relies on shifting the paradigm from the many-electron wavefunction to the electron density, thus moving from a rather complex object of 3N electronic degrees of freedom to a much simpler one featuring only 3, with N being the number of electrons of the system. DFT is rooted in two fundamental theorems by Hohenberg and Kohn[3] which essentially laid the groundwork for the following developments. According to the first theorem, in any finite system made of N interacting electrons, there exists a one-to-one correspondence between the external potential $v(r)$, for instance due to the nuclei, and the ground state electron density $\rho(r)$, up to a constant additive factor. Consequently, since the Hamiltonian of a specific multi-electron system is uniquely determined by the external potential, as electron kinetic energy and electron-electron interaction operators always have the same shape, the full system properties, such as energies and wavefunctions, can all be expressed as functionals of the density, uniquely determined by the given external potential. Furthermore, according to the second theorem, the proper ground state density can be variationally obtained by minimizing the following energy functional

$$E[\rho] = F[\rho] + \int d^3r \rho(r) v(r) \tag{5}$$

where

$$F[\rho] = \langle \psi[\rho] | \, \hat{T} + \hat{W} \, | \psi[\rho] \rangle = T[\rho] + W[\rho] \tag{6}$$

with $\hat{T}, \hat{W}$ being respectively the kinetic and electron-electron interaction operators

$$\begin{aligned} \hat{T} &= \sum_{i}^{N} -\frac{1}{2} \hat{\nabla}_i^2 \\ \hat{W} &= \frac{1}{2} \sum_{i \neq j}^{N} \frac{1}{|\hat{r}_i - \hat{r}_j|} \ . \end{aligned} \tag{7}$$

According to Hohenberg and Kohn theorems, functional minimization of eq. 5 would lead to the exact ground state, but the difficulty lies in the form of $F[\rho]$, which is not known despite being universal[4]. The mostly-used DFT practical implementation in quantum chemistry is based on Kohn-Shamn theory, which basically stems from realizing that the kinetic energy functional entering into eq. 6 can at least be obtained exactly for a reference system of non-interacting electrons whose density can be made to match the exact density of the interacting system upon choosing a proper effective potential. The latter assumption of Kohn and Shamn, which has no formal proof, is followed by introducing Kohn-Shamn orbitals that can be used to express the exact ground-state wavefunction of the non-interacting system as

$$\psi(r_1, \cdots, r_n) = \frac{1}{\sqrt{N!}} \begin{vmatrix} \phi_1(r_1) & \cdots & \phi_1(r_1) \\ \vdots & \vdots & \vdots \\ \phi_1(r_N) & \cdots & \phi_1(r_N) \end{vmatrix} \tag{8}$$

which is nothing but a single Slater determinant written in terms of orbitals ϕ_i.
In this convenient picture, the exact kinetic energy functional $T_{ni}[\rho]$ of the non interacting system can be conveniently calculated and the Kohn-Shamn ground state density can be expressed as a sum over occupied orbitals

$$\rho(r) = \sum_{i}^{N} |\phi_i(r)|^2 \,. \tag{9}$$

Starting from this bright idea, the total energy functional of the true interacting system can be rearranged in the following form

$$E[\rho] = T_{ni}[\rho] + \int d^3r \rho(r) v(r) + \frac{1}{2} \int\int d^3r d^3r' \frac{\rho(r)\rho(r')}{|r - r'|} + E_{xc}[\rho] \tag{10}$$

where the exchange-correlation functional has been introduced

$$E_{xc}[\rho] = T[\rho] - T_{ni}[\rho] + W[\rho] - \frac{1}{2} \int\int d^3r d^3r' \frac{\rho(r)\rho(r')}{|r - r'|} \tag{11}$$

collecting all terms that are not explicitly known. Notably, starting by minimizing the functional of eq. 10 one arrives at the so-called Kohn-Shamn single-particle equations

$$\left(-\frac{1}{2}\nabla^2 + v_{eff}[\rho](r) \right) \phi_i(r) = \epsilon_i \phi_i(r) \tag{12}$$

where the effective potential has been introduced

$$v_{eff}[\rho](r) = v(r) + \int d^3r' \frac{\rho(r')}{|r - r'|} + \frac{\delta E_{xc}[\rho]}{\delta \rho(r)} \,. \tag{13}$$

eq. 12 needs to be solved self-consistently as the KS density that is obtained through the orbitals upon resolution enters into the form of $v_{eff}[\rho](r)$, thus leading to a non-linear eigenvalue problem.

In principle, the DFT theory so far presented is exact but the precise form of $E_{xc}[\rho]$ functional is unknown. Different strategies have tried to tackle this complex object, starting from the simplest local density approximation (LDA) which solely accounts for the local density of the system to express the XC functional, derived from an homogeneous electron gas model. Further refinements have been introduced adding a dependence on the gradient of the density, thus resulting in generalized gradient approximation (GGA) functionals. Nowadays, thanks to its good accuracy that have been proved in different cases, the mostly-used functional in chemistry is B3LYP, which mixes the exact exchange energy contribution of HF with other DFT-based exchange-correlation functionals. In this thesis, this is the functional that has been mostly adopted for DFT calculations.

Furthermore, even if Hohenberg-Kohn theorem implicitly proves that also excited states properties can be inferred from the exact ground-state density, as there is a direct mapping with the external potential and so the full system Hamiltonian, nobody knows how to do that. Extension to excited states has been made possible within the framework of Time-Dependent Density Functional Theory (TDDFT) which originates from the Runge-Gross theorem that can be seen as the time-dependent version of the first Hohenberg-Kohn theorem. Without getting into further details, among the TDDFT approaches available today one that is worth mentioning

because of its wide use in chemistry is linear-response TDDFT (LR-TDDFT), which is essentially rooted in linear response theory applied to a Kohn-Sham picture. In doing so, excitation energies and transition properties can be derived inspecting the system density linear response upon external driving[4]. This is the approach that has been used in TDDFT simulations contained in this thesis.

Coupled Cluster Theory

The Coupled Cluster (CC) method focuses on improving over Hartree-Fock by recovering electron-electron correlation with the following wavefunction ansatz

$$|CC\rangle = e^{\hat{T}} |HF\rangle \tag{14}$$

where the Cluster excitation operator is defined as

$$\hat{T} = \sum_{\mu} t_{\mu} \hat{\tau}_{\mu} \tag{15}$$

with $\hat{\tau}_{\mu}$ being excitation operators that upon acting on $|HF\rangle$ leads to the orthonormal excited configurations $|\mu\rangle$[1]. The t_{μ} coefficients are commonly known as cluster amplitudes and need to be determined to properly define the $|CC\rangle$ wavefunction.
Usually, $\hat{T}$ can be sorted according to different excitation orders up to the total number of electrons N

$$\hat{T} = \hat{T}_1 + \hat{T}_2 + \cdots + \hat{T}_N \,. \tag{16}$$

For instance, for singlet excitations, $\hat{T}_1$ and $\hat{T}_2$, which are respectively single and double excitation operators, read

$$\begin{aligned} \hat{T}_1 &= \sum_{ai} \sum_{\sigma} t_{ai} \hat{a}^{\dagger}_{a\sigma} \hat{a}_{i\sigma} \\ \hat{T}_2 &= \sum_{\sigma\tau} \sum_{aibj} t_{aibj} \hat{a}^{\dagger}_{a\sigma} \hat{a}_{i\sigma} \hat{a}^{\dagger}_{b\tau} \hat{a}_{j\tau} \end{aligned} \tag{17}$$

where a,b label unoccupied orbitals while i,j label occupied ones.
Given eq. 14 the CC ground state energy is found by

$$E_{CC} = \langle HF| \, e^{-\hat{T}} \hat{H} e^{\hat{T}} \, |HF\rangle = \langle HF| \, \hat{\bar{H}} \, |HF\rangle \tag{18}$$

where the similarity transformed Hamiltonian $\hat{\bar{H}} = e^{-\hat{T}} \hat{H} e^{\hat{T}}$ has been introduced. In the limit of including all excitations in eq. 16 CC matches exact FCI results. In practice, this is often computationally unfeasible for most molecular systems of interests, and truncation up to $\hat{T}_2$ already suffices to sizeably improve over HF, recovering much correlation energy. This is known as Coupled Cluster Singles and Doubles (CCSD).
Once a given truncation is chosen, the ground state energy is obtained by eq. 18 while the ground state wavefunction is determined by means of the following projection equations

$$\Omega_{\mu} = \langle \mu| \, \hat{\bar{H}} \, |HF\rangle = 0 \tag{19}$$

which are satisfied for the exact CC ground state.
So far it has been shown how to get ground state CC energy and wavefunction, but no information

about excited states has been given. In CC theory there are two main approaches to electronic excited states. One is CC response theory[5] (CCRT) based on a time-dependent formalism and the other one is equation-of-motion CC[1] (EOMCC). The latter, which is based on a simpler time-independent formalism, is what we focus on in the following due to its broader use, even though system properties are not guaranteed to scale correctly with system size[6].
In EOMCC, the similarity transformed Hamiltonian in the $\{|HF\rangle, |\mu\rangle\}$ basis reads

$$\bar{\boldsymbol{H}} = \begin{pmatrix} \langle HF| \hat{\bar{H}} |HF\rangle & \langle HF| \hat{\bar{H}} |\nu\rangle \\ \langle \mu| \hat{\bar{H}} |HF\rangle & \langle \mu| \hat{\bar{H}} |\nu\rangle \end{pmatrix} = \begin{pmatrix} E_{CC} & \eta_\nu \\ 0 & A_{\mu\nu} + \delta_{\mu\nu} E_{CC} \end{pmatrix} \tag{20}$$

where the following Jacobian matrix has been introduced

$$A_{\mu\nu} = \langle \mu| [\hat{\bar{H}}, \hat{\tau}_\nu] |HF\rangle . \tag{21}$$

Basically, EOMCC relies on diagonalization of eq. 20 to get excited state energies and wavefunctions, although different left and right eigenvectors (i.e. excited states wavefunctions) can be obtained since the similarity transformed Hamiltonian is not hermitian.

Boundary Element Method and PCM-NP model

Modelling the plasmonic response of metallic nanostructures embedded in a surrounding medium upon external driving calls for solving the corresponding Maxwell's equations, i.e. knowing fields and potentials throughout space. Unfortunately, analytical solutions to Maxwell's equations are available only for simple objects, such as spheres and ellipsoids, which have been originally disclosed by Mie[7] and Gans[8], respectively. Despite their undoubted usefulness, they cannot be applied to plasmonic systems of more realistic and complex shape that we can nowadays meticulously synthesize thanks to well-established colloidal-chemistry techniques. In this regard, a numerical solution to Maxwell equations in case of arbitrarily-shaped objects is unavoidable. Over the years different methodologies have been devised, tackling the problem either in frequency or time domain and with different levels of approximation. Among them, the most known and widely used are the Discrete Dipole Approximation (DDA)[9, 10], which focuses on solving the electromagnetic problem by discretizing the whole volume of interest and assigning polarizable point dipoles to each element, Boundary Element Method (BEM)[11–13], which resorts to a discretization of the boundary surface between the metallic body and the environment, and Finite-Difference Time-Domain (FDTD)[14, 15], that aims at solving Maxwell'equations in time domain by direct discretization of the partial differential equations.
Among the methods mentioned, BEM is less computationally demanding, as it requires only a surface discretization of the metallic surface of interest and does not need a large parametrization volume extending over the target particle, as it is commonly required in FDTD[13], thus making it an efficient and versatile electromagnetic solver to model plasmonic nanoparticles of arbitrary shape and couple them with *ab initio* molecular descriptions.

BEM intimately relies on the rigorous proof that fields and potentials inside each region delimited by the metal-environment boundary surface are unambiguously determined by fields and corresponding surface derivatives at the boundary region, and this can be conveniently expressed in terms of charges and currents lying on the boundary surface. This is the mathematical foundation of BEM that can be rigorously proved starting from Maxwell's equations and then recasting the electromagnetic problem into boundary integral equations by making use of Green's theorems and imposing the proper boundary conditions for the tangential and normal component of the fields, as well as the continuity of the potentials, across the boundary[12, 16, 17]. Upon solving these integral equations surface charges and currents are obtained, from which fields and potentials throughout space can be computed. Usually, these integral equations do not feature an easy analytical solution and so they require a numerical treatment that can be conveniently recast as a linear algebra problem upon surface discretization (Fig.2).

The full electrodynamics picture can be simplified if the wavelength of the exciting light is so bigger than NPs dimensions such that the electromagnetic fields do not appreciably vary over the system space. In this limit the BEM problem reduces to solving the following quasi-static Poisson's equation for the scalar potential[12, 17, 18] ϕ,

$$-\nabla \cdot \epsilon(\omega) \nabla \phi = 0 \tag{22}$$

where the local frequency-dependent metal dielectric function $\epsilon(\omega)$ has been introduced. Under

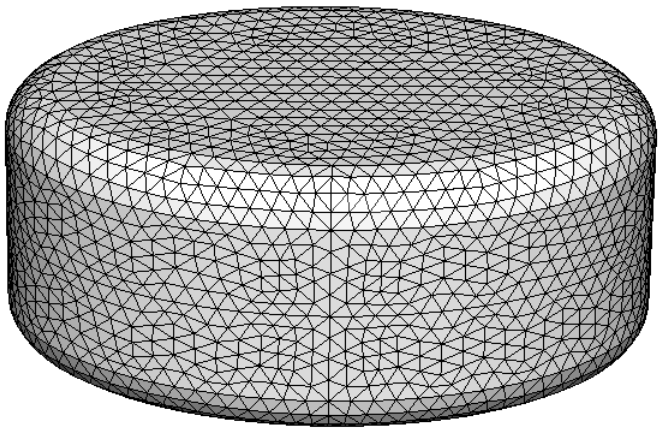

Figure 2: Model of a plasmonic nanodisk whose surface is discretized to numerically solve the BEM equations.

this approximation, the exact solution of eq. 22 can be expressed as an integral over the metal-environment boundary surface S[12]

$$\phi(r) = \phi_{ext}(r) + \oint_S G(r,s)\sigma(s)ds \tag{23}$$

where $\sigma(s)$ is the surface charge density sitting on the infinitesimal surface element s of area ds, ϕ_{ext} is the external potential acting on the system and G is the electrostatic Green's function that is solution of the simpler Poisson's problem related to a point-like source immersed in an homogeneous unbounded medium[16–18], i.e. $G(r,r') = \frac{1}{|r-r'|}$. Starting from eq. 23 and applying the fields boundary conditions across the boundary region the following integral equation for the surface charges is obtained

$$2\pi\frac{\epsilon(\omega)+\epsilon_{out}}{\epsilon(\omega)-\epsilon_{out}}\sigma(s) + \oint_S \frac{\partial G(s,s')}{\partial n}\sigma(s)ds' = -\frac{\partial\phi_{ext}(s)}{\partial n} \tag{24}$$

where ϵ_{out} is the dielectric constant of the embedding medium and the surface derivative of the electrostatic Green's function is taken along the direction of the outward surface normal n. So far no other assumption than applying the quasi-static approximation has been made, which makes eqs. 23-24 exact in this limit. The BEM approach comes into play to numerically solve eq. 24 upon surface discretization, thus leading to the following matrix equation

$$2\pi\frac{\epsilon(\omega)+\epsilon_{out}}{\epsilon(\omega)-\epsilon_{out}}\boldsymbol{\sigma} + \boldsymbol{F\sigma} = \boldsymbol{E_{n,ext}} \tag{25}$$

where $\boldsymbol{\sigma}$ is a column vector storing the surface charges densities sitting on the corresponding discretized surface elements, $\boldsymbol{F}$ is the matrix representation of the Green's function surface derivative connecting different discrete elements on the boundary surface and $\boldsymbol{E_{n,ext}}$ is the vector collecting the normal component of the electric field acting on each surface element.

Matrix inversion of eq. 25 gives access to surface charges from which scattered field throughout space can be computed.

In most investigated systems in the Molecular Plasmonics field, the metallic object is often much larger than target molecules, thus making a full *ab initio* description of the plasmonic systems practically intractable. Therefore, coupling a BEM-based continuum modelling of the plasmonic object with an atomistic *ab initio* molecular description is often convenient and desirable, especially considering that the focus is often on the molecular side. This is the strong point of the Polarizable Continuum Model-Nanoparticle (PCM-NP)[19, 20], which combines a quasistatic BEM-based description of the plasmonic system with a quantum chemistry modelling of real molecular species, thus leading to a multiscale state of the art method suitable to describe plasmon-molecules interactions in the field of Molecular Plasmonics.

In the PCM-NP approach, which stems from the well-known Polarizable Continuum Model originally applied in Chemistry to model solute molecules immersed in an homogeneous solvent[21], the NP optical response upon external driving is expressed in terms of BEM surface charges spread over the metal surface (eqs. 23-25). These charges, which express the NP electromagnetic linear response due to direct light excitation or nearby molecular electron densities, can be used to compute the scattered field of the plasmonic system at the molecules location, thus modelling plasmonic local field effects and so resulting plasmon-mediated molecular properties.

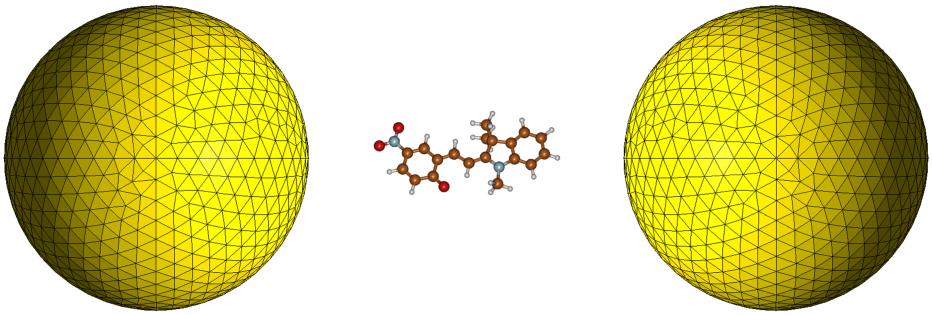

Figure 3: PCM-NP modelling setup illustrating a molecular species described at atomistic *ab initio* level and plasmonic nanospheres whose surfaces are discretized to solve the PCM-NP quasi-static equations.

The PCM-NP response charges can be formally expressed in frequency domain as[22]

$$\mathbf{q}(\omega) = \mathbf{Q}(\omega)\mathbf{V}(\omega) \ , \tag{26}$$

where

$$\mathbf{Q}(\omega) = -\mathbf{S}^{-1}\left(2\pi\frac{\epsilon(\omega)+1}{\epsilon(\omega)-1}\mathbf{I}+\mathbf{DA}\right)^{-1}(2\pi\mathbf{I}+\mathbf{DA}) \ . \tag{27}$$

$\mathbf{q}(\omega)$ is the vector collecting the response charges sitting on the NP discrete surface elements (also known as "tesserae"), while the BEM matrices $\mathbf{S}$ and $\mathbf{D}$ are representative of the Calderon's projectors[21] (i.e. electrostatic Green's function and its surface derivative, respectively) with elements $D_{ij} = \frac{(\vec{r}_i-\vec{r}_j)\cdot\vec{n}_j}{|\vec{r}_i-\vec{r}_j|^3}$, $S_{ij} = \frac{1}{|\vec{r}_i-\vec{r}_j|}$, where $\vec{r}_i$ is the position vector pointing to the centre of the *ith* tessera and $\vec{n}_j$ is the outward normal to the *jth* tessera, while $\mathbf{A}$ is a diagonal matrix with elements equal to the tesserae areas. The external potential that drives the plasmonic system $\mathbf{V}(\omega)$ is generated either by an exciting external electric field or by nearby molecular electron densities. In the latter case, the quantum chemistry molecular description is coupled to the plasmonic response via the molecular electrostatic potential operator evaluated at the NP surface, which is the key quantity where *ab initio* molecular description comes in and let the two systems interact (Fig. 3). Eqs. 26-27 do consitute a specific case of the quasi-static BEM equation (eq. 25).

Although most of the following chapters involve the frequency-domain formulation of the PCM-NP matrix equation (eq. 26), the same expression can also be reformulated in time domain upon Fourier transform and introducing equations of motion[22], which is the starting point to describe in real-time plasmon-molecules interactions within the PCM-NP theory.

Practical numerical tests have shown that the quasi-static approximation works well for particles size roughly smaller than one tenth of the light wavelength used to drive the system, and progressively break down as the particles get bigger and bigger [23], eventually approaching a regime where field retardation effects and non-dipolar higher-order modes significantly contribute to the plasmonic scattered field[24, 25]. In such cases, full Maxwell equations need to be solved and both scalar and vector potentials have to fulfill a Helmholtz wave equation. Even in this case both potentials can be expressed in an ad-hoc form[12] similar to eq. 23, where even surface currents now additionally appear. After imposing the proper boundary conditions, equations to determine surface charges and currents are obtained, which can be practically implemented as matrix equations after numerical surface discretization. Once surface charges and currents are obtained, electromagnetic fields throughout space can be obtained.

Full-electrodynamics calculations are always much more computationally demanding than solving the quasi-static problem (instead of only a surface charge density, also the surface current density should be solved for) and usually makes the coupling with a molecular quantum chemistry description practically difficult to derive and implement.

For most applications discussed in this thesis, the quasi-static approximation suffices to capture most plasmonic features of the systems being investigated.

Quantum PCM-NP model (Q-PCM-NP)

The PCM-NP model (eqs.26-27) is a classical theory, but as it is shown in Chapters 3-5 a quantized description of the plasmonic object is needed to properly describe strongly-coupled molecular-plasmonic systems. Such quantized model, named Q-PCM-NP[26], can be conveniently derived from the diagonal form of the PCM-NP response kernel of eq.27, that is

$$\mathbf{Q}(\omega) = -\mathbf{S}^{-1/2}\mathbf{T}\mathbf{K}(\omega)\mathbf{T}^{\dagger}\mathbf{S}^{-1/2} \tag{28}$$

with $\mathbf{K}(\omega)$ being a diagonal matrix whose elements read

$$K_p(\omega) = \frac{2\pi + \lambda_p}{2\pi\frac{\epsilon(\omega)+1}{\epsilon(\omega)-1} + \lambda_p} \tag{29}$$

where $\mathbf{T}$ and $\mathbf{\Lambda}$ are the eigenvectors and eigenvalues matrices of $\mathbf{S}^{-1/2}\mathbf{D}\mathbf{A}\mathbf{S}^{1/2} = \mathbf{T}\mathbf{\Lambda}\mathbf{T}^{\dagger}$. Quantization is straightforward to achieve in the case of a Drude-Lorentz dielectric function, namely

$$\epsilon(\omega) = 1 + \frac{\Omega_p^2}{\omega_0^2 - \omega^2 - i\Gamma\omega} \tag{30}$$

where Γ is the damping rate and Ω_p^2 is the squared plasma frequency of the metal. Indeed, upon substituting eq.30 into eq.29 and neglecting second-order terms in Γ the following expression of the response matrix comes up

$$Q_{kj}(\omega) = -\sum_p (\mathbf{S}^{-1/2}\mathbf{T})_{kp}\sqrt{\frac{\omega_p^2-\omega_0^2}{2\omega_p}}\left(\frac{1}{\omega_p - \omega - i\Gamma/2} + \frac{1}{\omega_p + \omega + i\Gamma/2}\right)\sqrt{\frac{\omega_p^2-\omega_0^2}{2\omega_p}}(\mathbf{T}^{\dagger}\mathbf{S}^{-1/2})_{pj} \tag{31}$$

with $\omega_p = \omega_0 + \left(1 + \frac{\lambda_p}{2\pi}\right)\frac{\Omega_p^2}{2}$.
Upon inspecting eq.31 and introducing the corresponding quantized surface charge operators[26], the following quantity can be defined $\langle 0|\,\hat{q}_k\,|p\rangle = (\mathbf{S}^{-1/2}\mathbf{T})_{kp}\sqrt{\frac{\omega_p^2-\omega_0^2}{2\omega_p}}$ and the usual shape of a quantum linear response function can be obtained,

$$Q_{kj}(\omega) = -\sum_p \left(\frac{\langle p|\,\hat{q}_k\,|0\rangle\,\langle 0|\,\hat{q}_j\,|p\rangle}{\omega_p - \omega - i\Gamma/2} + \frac{\langle 0|\,\hat{q}_k\,|p\rangle\,\langle p|\,\hat{q}_j\,|0\rangle}{\omega_p + \omega + i\Gamma/2}\right) \tag{32}$$

from which plasmon modes transition frequencies can be identified with ω_p and $\langle 0|\,\hat{q}_k\,|p\rangle$ correspond to the *kth* surface transition charge associated with the quantum plasmon mode $|p\rangle$ of the nanostructure. Quantization within PCM-NP is thus achieved and strongly-coupled systems can be formally studied considering the quantum modes of a given nanostructure (see Chapters 3-5).

References

(1) Helgaker, T.; Jorgensen, P.; Olsen, J., *Molecular electronic-structure theory*; John Wiley & Sons: 2013.

(2) Szabo, A.; Ostlund, N. S., *Modern quantum chemistry: introduction to advanced electronic structure theory*; Courier Corporation: 2012.

(3) Hohenberg, P.; Kohn, W. *Physical review* **1964**, *136*, B864.

(4) Ullrich, C. A., *Time-dependent density-functional theory: concepts and applications*; OUP Oxford: 2011.

(5) Koch, H.; Jørgensen, P. *The Journal of chemical physics* **1990**, *93*, 3333.

(6) Koch, H.; Kobayashi, R.; Sanchez de Merás, A.; Jo/rgensen, P. *The Journal of chemical physics* **1994**, *100*, 4393–4400.

(7) Mie, G. *Annalen der Physik*, *330*, 377–445.

(8) Gans, R. *Ann. Phys* **1912**, *37*, 422.

(9) Yang, W.-H.; Schatz, G. C.; Van Duyne, R. P. *The Journal of chemical physics* **1995**, *103*, 869–875.

(10) Yurkin, M. A.; Hoekstra, A. G. *Journal of Quantitative Spectroscopy and Radiative Transfer* **2007**, *106*, 558–589.

(11) Ida, N., *Numerical modeling for electromagnetic non-destructive evaluation*; Springer Science & Business Media: 1994; Vol. 1.

(12) De Abajo, F. G.; Howie, A. *Physical Review B* **2002**, *65*, 115418.

(13) Myroshnychenko, V.; Rodríguez-Fernández, J.; Pastoriza-Santos, I.; Funston, A. M.; Novo, C.; Mulvaney, P.; Liz-Marzán, L. M.; De Abajo, F. J. G. *Chemical Society Reviews* **2008**, *37*, 1792–1805.

(14) Kunz, K. S.; Luebbers, R. J., *The finite difference time domain method for electromagnetics*; CRC press: 1993.

(15) Taflove, A.; Hagness, S. C.; Piket-May, M. *The Electrical Engineering Handbook* **2005**, *3*, 15.

(16) Jackson, J. D., *Classical electrodynamics*; John Wiley & Sons: 2021.

(17) Hohenester, U.; Trügler, A. *Computer Physics Communications* **2012**, *183*, 370–381.

(18) Hohenester, U.; Trugler, A. *IEEE Journal of Selected Topics in Quantum Electronics* **2008**, *14*, 1430–1440.

(19) Corni, S.; Tomasi, J. *The Journal of Chemical Physics* **2001**, *114*, 3739–3751.

(20) Mennucci, B.; Corni, S. *Nature Reviews Chemistry* **2019**, *3*, 315–330.

(21) Tomasi, J.; Mennucci, B.; Cammi, R. *Chemical reviews* **2005**, *105*, 2999–3094.

(22) Pipolo, S.; Corni, S. *J. Phys. Chem. C* **2016**, *120*, 28774–28781.

(23) Della Sala, F.; D'Agostino, S., *Handbook of molecular plasmonics*; CRC Press: 2013.

(24) Yu, R.; Liz-Marzán, L. M.; de Abajo, F. J. G. *Chemical Society Reviews* **2017**, *46*, 6710–6724.

(25) Carone, A.; Mariani, P.; Desert, A.; Romanelli, M.; Marcheselli, J.; Garavelli, M.; Corni, S.; Rivalta, I.; Parola, S. *ACS nano* **2022**, *16*, 1089–1101.

(26) Fregoni, J.; Haugland, T. S.; Pipolo, S.; Giovannini, T.; Koch, H.; Corni, S. *Nano Letters* **2021**, *21*, 6664–6670.

Chapter 1.

Role of metal-nanostructure features on tip-enhanced photoluminescence of single molecules

This initial chapter represents the beginning of my PhD pathway in the molecular plasmonics field and features an application of the PCM-NP theory to a molecular-plasmonic system of the simplest complexity, that is, one single molecule is coupled with a classically-described plasmonic body. More precisely, the focus of this work is to understand how molecular photoluminescence can be modified by highly spatially-confined plasmonic fields, such as those originating from plasmonic tips of scanning tunneling microscopes (STMs). This phenomenon has nowadays given rise to proper experimental techniques, such as tip-enhanced photoluminescence[1] (TEPL), where single molecule imaging is possible by cleverly harnessing the extremely-enhanced and spatially-confined plasmonic field originating from tip surface plasmon excitation. This kind of experiments have even reached the capability of pushing optical resolution down to sub-molecular level when plasmonic fields are confined on a spatial scale that is compatible with molecules dimensions[1–4], thus revealing sub-molecular features in the output images. This is often achieved thanks to atomistic geometrical protrusions located at the STM tip apex which are able to promote such plasmonic lightning rod effects. Despite their proven effectiveness in TEPL experiments, the way such plasmonic details affect the overall detectable response is far from being trivial and fully understood, especially because they are often experimentally inaccessible.

In this chapter, which is reproduced as a published article in *The Journal of Chemical Physics* with permission (Copyright 2021 AIP Publishing), a thorough theoretical analysis on TEPL imaging of a zinc phthalocyanine molecule placed underneath a silver STM tip is reported. Simulations, which are benchmarked against state of the art TEPL experiment on the same system, discloses that metallic features, such as protrusion geometrical shape, metal dielectric function and tip-molecule distance drastically impact on the spatial distribution and frequency dependence of the local field acting on the molecule, thus pinpointing the physical reasons why TEPL measurements are much affected by plasmonic tip features.

In this work, which has been carried out in collaboration with Giulia dall'Osto (UniPd), I performed all simulations and data analysis whose outcome is reported in the manuscript, while Giulia Dall'Osto took care of some code implementation needed to solve the PCM-NP problem

in the case of complex-shaped plasmonic structures and to obtain physical quantities necessary to evaluate the photoluminescence intensity. Writing of the first version of the manuscript was equally divided among me and Giulia Dall'Osto, whereas figures were prepared by me. A first reply letter draft to referees' comments was drafted by me.

References

(1) Yang, B.; Chen, G.; Ghafoor, A.; Zhang, Y.; Zhang, Y.; Zhang, Y.; Luo, Y.; Yang, J.; Sandoghdar, V.; Aizpurua, J., et al. *Nature Photonics* **2020**, *14*, 693–699.

(2) Lee, J.; Crampton, K. T.; Tallarida, N.; Apkarian, V. A. *Nature* **2019**, *568*, 78–82.

(3) Lee, H.; Lee, D. Y.; Kang, M. G.; Koo, Y.; Kim, T.; Park, K.-D. *Nanophotonics* **2020**, *9*, 3089–3110.

(4) Lee, D. Y.; Park, C.; Choi, J.; Koo, Y.; Kang, M.; Jeong, M. S.; Raschke, M. B.; Park, K.-D. *Nature Communications* **2021**, *12*, 3465.

The Journal of Chemical Physics ARTICLE scitation.org/journal/jcp

Role of metal-nanostructure features on tip-enhanced photoluminescence of single molecules

Cite as: J. Chem. Phys. 155, 214304 (2021); doi: 10.1063/5.0066758
Submitted: 12 August 2021 • Accepted: 5 November 2021 •
Published Online: 3 December 2021

Marco Romanelli,[1] Giulia Dall'Osto,[1] and Stefano Corni[1,2,a)]

AFFILIATIONS

[1] Department of Chemical Sciences, University of Padova, via Marzolo 1, Padova, Italy
[2] CNR Institute of Nanoscience, via Campi 213/A, Modena, Italy

Note: This paper is part of the JCP Special Topic on Chemical Imaging.
[a)] **Author to whom correspondence should be addressed:** stefano.corni@unipd.it

ABSTRACT

Tip-enhanced photoluminescence (TEPL) experiments have recently reached the ability to investigate single molecules exploiting resolution at the submolecular level. Localized surface plasmon resonances of metallic nanostructures have the capability of enhancing an impinging electromagnetic radiation in the proximity of their surface, with evident consequences both on absorption and emission of molecules placed in the same region. We propose a theoretical analysis of these phenomena in order to interpret TEPL experiments on single molecules, including a quantum mechanical description of the target molecule equilibrated with the presence of two nanostructures representative of the nanocavity usually employed in STMs. The approach has been applied to the zinc phthalocyanine molecule, previously considered in recent TEPL experiments [Yang *et al.*, Nat. Photonics **14**, 693–699 (2020)]. This work has the aim of providing a comprehensive theoretical understanding of the experimental results, particularly focusing on the investigation of the tip features that majorly influence the excitation and fluorescence processes of the molecule, such as the geometry, the dielectric function, and the tip–molecule distance.

I. INTRODUCTION

Localized surface plasmon resonances (LSPRs) of metallic nanostructures can lead to strong field enhancements where the impinging electromagnetic radiation is focused at the nanoscale, thus allowing one to get around Abbe's diffraction limit of classical optics.[1–3] Among many different peculiar consequences, focusing light at the nanoscale has proved to be extremely useful for single-molecule imaging,[4–6] where by cleverly harnessing subtle plasmon–molecule interactions, it was possible to detect and visualize single molecules in real life experiments,[7–10] even achieving submolecular resolution.[11,12] Various kinds of "tip-enhanced" spectroscopies take advantage of the local field enhancement related to the excitation of plasmons associated with the metallic tip of scanning probe microscopes, giving rise to highly resolved, both in space and time, experimental techniques, such as tip-enhanced Raman spectroscopy (TERS).[13–21] Recently, it has been shown that sub-nanometer single-molecule resolution is also attainable in photoluminescence imaging, where the metallic atomistic tip of a STM has been used to confine the electromagnetic field down to the nanoscale,[22,23] eventually leading to an enhanced fluorescence emission of a single molecular compound that has been used to record photoluminescence images with submolecular spatial resolution [tip-enhanced photoluminescence (TEPL)].[24–27]

The interpretation of the outcomes of such experiments is not trivial, and thus, a theoretical approach is helpful in elucidating the complex dynamics that is taking place. Hereafter, we theoretically investigate the influence of a metallic STM-like nanostructure on the photoluminescence properties of a single zinc phthalocyanine molecule that has been used for single-molecule TEPL imaging in recent experiments,[24] eventually pointing out some features of the system[28] that affect the PL images significantly.

Different approaches[29] have been explored so far to study plasmonic nanostructures as the classical dielectric description through Mie theory,[30,31] the discrete dipole approximation,[32] the boundary element method (BEM),[33–37] and the finite difference time domain

method.[38] These latter two approaches have also been coupled to an atomistic quantum mechanical description of nearby molecules to model their plasmon-affected optical properties without giving up molecular chemical details.[35,39–44]

Other proposed models are based on a classical but atomistic description of the metallic nano-object, while the molecule is still described through quantum-mechanics.[45,46] The coupling between molecular emitters and plasmonic cavities has been recently investigated by Neuman *et al.*[42] adopting the canonical quantization of plasmons and density functional theory (DFT) treatment of the molecule, and very recently, the coupling between quantized plasmons and molecules has been considered at the coupled cluster level.[47] Moreover, the full quantum mechanical description of the overall system has been reported,[48] allowing one to directly study the whole hybrid system on the same footing. This approach allows us to take into account challenging effects, such as "strong-coupling," with the limit of considering rather small nanostructures (i.e., composed of few hundred atoms), but it becomes unfeasible when larger nanostructures are considered as those employed in STMs.

Here, we employ a semiclassical description of the overall system through the Polarizable Continuum Model–NanoParticle, PCM-NP (an extension of the PCM implicit solvation model),[49] where the metallic nanostructure is described as an homogeneous body of complex shape characterized by its own frequency-dependent dielectric function, whereas the molecule is treated at an atomistic quantum mechanical level.[35,50,51] This approach allows us to have submolecular information, overcoming the limitation of using point-dipole models for the molecule, while keeping a description of the nanostructures that takes into account the main plasmonic effects. In our model, the electromagnetic problem is solved at an affordable computational cost through the BEM, which requires discretizing in small portions only the nanostructure surface (as opposed to its volume). A similar approach has been satisfactorily used to interpret the experimental data in Ref. 24. Here, this approach has been employed to analyze the role of some critical features of both the tip and the substrate, which affect the photoluminescence process of a molecule in their proximity. In particular, we focus our investigation on the geometry of the metal nano-tip, the empirical dielectric function employed to describe the metal response and the tip–molecule distance. Moreover, we specifically analyze an issue that was not investigated before: The presence of the tip can polarize the ground and excited electronic states of the molecule and thus can indirectly change excited state properties as well. To clearly identify the origin of the dependence of the results on the investigated parameters, we do not only calculate photoluminescence intensity maps as a function of tip position, but we also analyze absorption spectra, the local enhancement of the incident fields, and the non-radiative decay rates induced by the presence of the metallic tip and substrate.

This work is organized as follows: Sec. II summarizes the theoretical approach employed to describe the system and to calculate the photoluminescence intensity of the molecule (the original theory can be found in Refs. 35, 50, 52, and 53, and an overall account is given in Ref. 54), followed by Sec. III that reports the computational details of our calculations; all the analysis and results are reported in Sec. IV, and the conclusions are drawn in Sec. V.

II. METHODS

A. The PCM NP model

The NP is considered as a continuum body in the quasi-static limit, i.e., retardation effects are not included, described within the PCM framework in the integral equation formalism. The PCM problem is numerically solved with the BEM approach: The NP surface is discretized in small portions called tesserae, each of which is associated with a polarization charge located in its geometrical center. The polarization charges describe the interaction between the NP and the external potential that could be generated by the presence of an incident electric field or by the transition potential of a molecule close to its surface.[35] The polarization charges are expressed as a function of potential $\mathbf{V}(\omega)$, a vector containing the transition potential numerically evaluated at each tessera position, and the response matrix $\mathbf{Q}(\omega)$,

$$\mathbf{q}(\omega) = \mathbf{Q}(\omega)\mathbf{V}(\omega), \tag{1}$$

where

$$\mathbf{Q}(\omega) = -\mathbf{S}^{-1}\left(2\pi\frac{\epsilon(\omega)+1}{\epsilon(\omega)-1}\mathbf{I} + \mathbf{DA}\right)^{-1}(2\pi\mathbf{I} + \mathbf{DA}). \tag{2}$$

The BEM matrices $\mathbf{S}$ and $\mathbf{D}$ are representative of Calderon's projectors,[49] and $\mathbf{A}$ is a diagonal matrix with elements equal to the tessera areas. In the present work, the external potential $\mathbf{V}(\omega)$ is generated either by an incident electric field when the field enhancement is calculated nearby the NP or by the transition potential of a molecule when molecular photoluminescence calculations are performed in the presence of the NP.

Previously,[55] the inversion in Eq. (2) has been solved through the transformation of $\mathbf{DA}$, exploiting the integral relation $\mathbf{DAS} = \mathbf{SAD}^{\dagger}$,

$$\mathbf{Q}(\omega) = -\mathbf{S}^{-1/2}\left(2\pi\frac{\epsilon(\omega)+1}{\epsilon(\omega)-1}\mathbf{I} + \mathbf{S}^{-1/2}\mathbf{DAS}^{1/2}\right)^{-1} \cdot \left(2\pi\mathbf{I} + \mathbf{S}^{-1/2}\mathbf{DAS}^{1/2}\right)\mathbf{S}^{-1/2}. \tag{3}$$

In this procedure, the matrix $\mathbf{S}$ is diagonalized in order to calculate $\mathbf{S}^{1/2}$ and $\mathbf{S}^{-1/2}$, but occasionally, we have experienced numerical problems (non-positive eigenvalues) for complex meshes. A different approach is here explored to obtain a diagonal version of Eq. (2). This is done through the diagonalization of the term $\mathbf{DA} = \mathbf{U\Lambda U}^{-1}$ leading to

$$\mathbf{Q}(\omega) = -\mathbf{S}^{-1}\mathbf{U}\left(2\pi\frac{\epsilon(\omega)+1}{\epsilon(\omega)-1}\mathbf{I} + \mathbf{\Lambda}\right)^{-1}(2\pi\mathbf{I} + \mathbf{\Lambda})\mathbf{U}^{-1}, \tag{4}$$

$$\mathbf{Q}(\omega) = -\mathbf{S}^{-1}\mathbf{U}\mathbf{K}(\omega)\mathbf{U}^{-1}, \tag{5}$$

where $\mathbf{K}(\omega)$ encloses the diagonal elements. The matrix $\mathbf{DA}$ is a real non-symmetric matrix; therefore, it is not Hermitian and its diagonalization does not lead to a unitary eigenvector matrix $\mathbf{U}$ as assured with Eq. (3). This alternative diagonalization procedure should be more robust than the previous one [through Eq. (3)] in all those situations (e.g., complex meshes) where some eigenvalues of $\mathbf{S}$ might be negative, thus hindering the calculation of $\mathbf{S}^{1/2}$. Real

eigenvalues and eigenvectors are expected as a result of the equivalence of Eq. (2) with Eq. (3); however, we observe that it is not always fulfilled due to numerical reason. If complex eigenvectors (and thus also eigenvalues) are obtained, they are always complex conjugated pairs.

The nanoparticle is a neutral body, and thus, the total charge on its surface should be equal to zero. From a numerical point of view, this is not trivial and some corrections have to be applied in order to assure this condition. Two possible strategies have been exploited to do so. In first place, the elements of matrices $\mathbf{U}^{-1}$ and $\mathbf{S}^{-1}\mathbf{U}$ have been scaled in order to assure that the sum over each eigenvector coefficient is equal to zero,

$$\left(U^{-1}\right)'_{ij} = \left(U^{-1}\right)_{ij} - \frac{\sum_k \left(U^{-1}\right)_{ik}}{N_{tess}} \tag{6}$$

and

$$\left(S^{-1}U\right)'_{ij} = \left(S^{-1}U\right)_{ij} - \frac{\sum_k \left(S^{-1}U\right)_{kj}}{N_{tess}}, \tag{7}$$

where the sum runs over the tesserae on the NP surface and N_{tess} is the number of tesserae. This step has the aim to ensure *a priori* that the sum over the polarization charges is zero. The second strategy is *a posteriori* normalization: After the calculation of the polarization charges, they are averaged in order to obtain a null total charge on the NP surface, as

$$\mathbf{q}'(\omega) = \mathbf{q}(\omega) - \frac{\sum_i \mathrm{q}_i(\omega)}{N_{tess}}, \tag{8}$$

where the sum runs over the tesserae on the NP surface. When disjointed nanostructures are considered in the same calculation, as in the present case, the sum of the surface charges has to be zero for each part of the system (in this case separately for the tip and the substrate) in order to avoid fictitious charge transfer effects that would affect the results of calculation. For the shapes considered here, we have numerically verified that the second approach, with the *a posteriori* normalization, is more effective than the first one (see Figs. S1 and S2 of the supplementary material): With the first approach, eigenvector coefficients related to different NPs are separately normalized, but they mix in the subsequent step when using Eq. (5) and the null sum over polarization charges on separate NPs is no more assured.

B. Photoluminescence calculations

The photoinduced molecular fluorescence is influenced by the presence of the metal nanostructure in different ways.[56–64] First, the absorption of the incident radiation is increased by means of a strong field enhancement due to the presence of the nearby metallic nano-object[65] that we describe in terms of induced dipole on the nanostructure by the molecular transition potentials [see Eqs. (10) and (11)]. Then, after vibrational relaxation upon light excitation, the molecule decay to the ground state through radiative and non-radiative processes is in both cases affected by the presence of nanostructures. Specifically, in this work, the molecule under study, zinc phthalocyanine, has two degenerate emitting states; therefore, both of them can be excited by the incident radiation and then decay, leading to fluorescence emission.

The tip-enhanced photoluminescence intensity has been computed by using the following equation, making the use of the Einstein coefficients (in a.u.) to calculate the modified absorption and emission rates:[54]

$$\frac{I}{I_0} = \frac{\eta_1^{enh} \cdot A_1^{enh} + \eta_2^{enh} \cdot A_2^{enh}}{\eta_1^0 \cdot A_1^0 + \eta_2^0 \cdot A_2^0}, \tag{9}$$

where η is the quantum efficiency discussed later, A is the absorption coefficient, the indices 1 and 2 indicate the two lowest isoenergetic excited states S_1 and S_2, respectively, of the molecule responsible for the emission, and I_0 is the intensity of photoluminescence *in vacuo*. Moreover, the enhanced absorption A_1^{enh} (the same for state 2) in the presence of the NP is expressed as[53]

$$A_1^{enh} = \frac{2\pi |\vec{\mu}_{abs,1}^{met} + \vec{\mu}_{abs,1}^{\mathrm{ind}}|^2}{3c}, \tag{10}$$

where $\vec{\mu}_{abs,1}^{met}$ is the molecular transition dipole in the presence of nanostructure, which is computed from the QM transition density of the ground to S1 transition, which is in turn evaluated from the TDDFT equation. The latter includes the interacting terms with the metallic object (more details can be found in Fig. S7 of the supplementary material and Refs. 50 and 66). $\vec{\mu}_{abs,1}^{ind}$ is instead the dipole induced in the metallic nano-object by the molecular transition density, which is evaluated as

$$\vec{\mu}_{abs,1}^{ind} = \sum_i q_{i,abs,1}^{ind} \vec{s}_i, \tag{11}$$

where $q_{i,abs,1}^{ind}$ is the polarization charge induced by the molecular transition density located in the i-th tessera and $\vec{s}_i$ is the center of such tessera. The quantum efficiency η_1^{enh} is instead given by[50,54]

$$\eta_1^{enh} = \frac{\Gamma_1^{rad}}{\Gamma_1^{rad} + \Gamma_1^{nr,met} + \Gamma^{nr,0}}, \tag{12}$$

where Γ_1^{rad} is the radiative decay rate evaluated as[50,54]

$$\Gamma_1^{rad} = \frac{4\omega_1^3 |\vec{\mu}_{emi,1}^{met} + \vec{\mu}_{emi,1}^{\mathrm{ind}}|^2}{3c^3}, \tag{13}$$

while $\Gamma^{nr,0}$ is the intrinsic non-radiative decay rate of the molecule and $\Gamma_1^{nr,met}$ is the non-radiative decay rate due to the presence of the metal (which does not include non-local contributions from the metal response[67]). The latter has been evaluated through the imaginary component of the self-interaction between the surface charges and the molecular transition potentials, i.e.,[52]

$$\Gamma_1^{nr,met} = -2 \cdot \mathrm{Im}\left\{\sum_i q_i V_i\right\}, \tag{14}$$

where V_i is the molecular transition potential evaluated at the position of the i-th tessera.

It is worth pointing out that even though Eqs. (10) and (13) involve analogous quantities ($\vec{\mu}_{abs,1}^{\mathrm{ind}}$, $\vec{\mu}_{abs,1}^{met}$, $\vec{\mu}_{emi,1}^{\mathrm{ind}}$, and $\vec{\mu}_{emi,1}^{met}$), they are calculated at different frequencies (that of the absorption and that of the emission, respectively) and for different transition densities [that at the ground state geometry for Eq. (10) and that at the excited state geometry for Eq. (13)].

The real component of the self-interaction is instead associated with the medium-induced Lamb shift $\Delta\omega$, that is, the transition energy of the excited states is affected by the interaction with the polarization charges induced by the molecular transition potentials,[66]

$$\Delta\omega = \mathrm{Re}\left\{\sum_i q_i V_i\right\}. \tag{15}$$

The gas-phase radiative quantum efficiency η^0 for the two states in Eq. (9) is related to the intrinsic non-radiative decay of the molecule through

$$\eta_1^0 = \frac{\Gamma_1^{rad,0}}{\Gamma_1^{rad,0} + \Gamma^{nr,0}}, \tag{16}$$

where $\Gamma_1^{rad,0}$ is the vacuum radiative decay rate for the excited state 1 that can be evaluated through Eq. (13) using the gas-phase molecular transition dipole and removing the term due to the metal response. Starting from Eq. (16), $\Gamma^{nr,0}$ can be computed if experimental values of η_1^0 are available. Since experimental data are only available in solution, η_1^0 has been set to 0.2, as reported by previous measurements in DMSO.[68] This assumption, even if approximated because we are using solvent-based molecular quantum efficiency for gas-phase calculations, is a reasonable choice, as shown in Sec. IV. Indeed, the photoluminescence emission in the presence of the metal is strongly enhanced compared to the vacuum values, even assuming unitary gas-phase quantum efficiency [that would result by neglecting $\Gamma^{nr,0}$ in Eq. (16)]; thus, the choice of this parameter (setting it either to 1 or to 0.2) does not strongly affect the order of magnitude of the TEPL ratio (see Figs. 9 and S3 for a comparison between two different values of η^0). Therefore, the contribution of the intrinsic non-radiative decay rate in Eq. (12) has been neglected, which is a sensible approximation keeping in mind that the main contribution to the overall non-radiative decay rate in the presence of the nanostructure is due to the metal–molecule interaction $\Gamma_1^{nr,met}$.

III. COMPUTATIONAL DETAILS

The NP structure (Fig. 1) is similar to that reported in a recent study.[24] The tip was modeled as a truncated cone with a height of 200 nm and a radius of 50 nm, featuring an additional atomistic protrusion (Fig. 1, red inset) that we defined as a smaller truncated cone at the tip apex with a base radius of 0.6 nm and a radius of the spherical cap of 0.5 nm. The cylindrical substrate has an height of 100 nm and a radius of 100 nm, where we left out the NaCl dielectric spacer used in the experiments[24] [we also tested the explicit inclusion of part of the NaCl layer (see Fig. S9 of the supplementary material)]. The structures of the tip and substrate are close to each other in order to generate a picocavity, shown in the inset, where to place the molecule. All results were obtained by setting the tip–molecule distance to 0.4 nm and the molecule–substrate separation to 1.4 nm unless specified differently. The molecule, if present, is placed in the point with coordinates (0,0,0), lying on the xy plane (parallel to the substrate surface), and the tip-axis direction is oriented along the z axis. More in detail, the substrate and tip meshes have been computed separately by using the Gmsh code[69] and then has been joined. The overall structure is characterized by 3818 tesserae more refined close to the atomistic protrusion and has been described using the

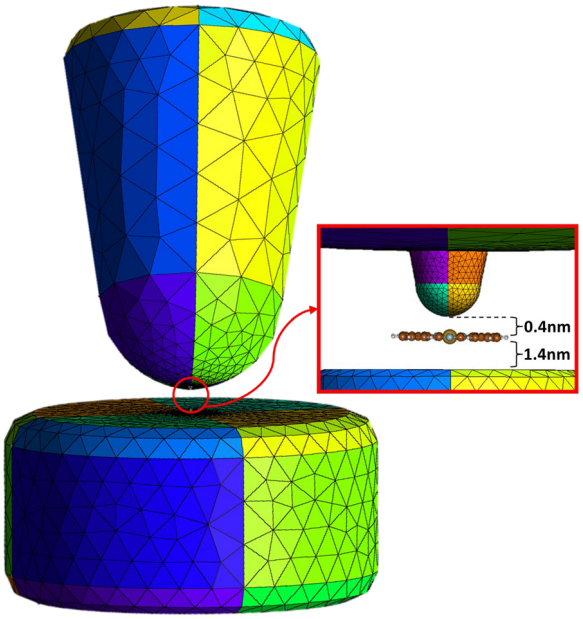

FIG. 1. Reference mesh structure used for the simulations computed by the Gmsh code.[69] In the red inset, a close-up of the atomistic protrusion at the tip apex responsible for the strong field enhancement predicted by the simulations is shown. The tip–molecule distance is always set to 0.4 nm, and the protrusion base radius is 0.6 nm unless specified differently.

Brendel–Bormann[70] fitting model of the silver dielectric function[71] unless otherwise stated.

The molecule, zinc phthalocyanine, has been considered at the atomistic level, and DFT calculations with the software Gaussian[72] have been performed for the gas-phase. No explicit Ag atoms were considered in the QM part, so charge transfer states are not included. More in detail, the ground state geometry of the molecule has been optimized at the B3LYP/6-31G(d) level of theory and excited state transition dipole moments in the gas-phase have been computed through time-dependent DFT calculations. The optimization of the first excited state has been done at the B3LYP/6-31G(d) level of theory; the comparison of ground and excited state optimized geometries is reported in the supplementary material (Fig. S5). After the calculation of the vibrational normal modes in the ground and first excited state, the vibrationally resolved emission spectrum has been computed through the code FCclasses.[73] The spectrum has been reported in the supplementary material (Fig. S6) comparing it with the experimental one[24] obtained in a vacuum for a molecule close to the nanostructures and in DMSO.[74] The spectrum shows signatures of the vibrational structure, represented by the Q(0,1) band (transition between the lowest level of the first excited state to excited vibrational states of the ground state). In the calculation of the PL intensity, we focused on the Q(0,0) band only; the ground state optimized geometry was considered for evaluating the absorption rates, whereas emission-related quantities were computed from the excited state optimized structure. We also note that throughout this work, photoluminescence data are calculated by exciting the lowest excited states from which emission occurs. Starting from the

ground state geometry optimized in a vacuum, we performed DFT calculations of the molecule in the presence of the nanostructures (both the tip and substrate together) at the B3LYP/6-31G(d,p) level of theory with a locally modified version of GAMESS[75,76] in order to compute the excited state energies, transition dipole moments, and molecular potential on NP tesserae. The potential on the nanostructure surface computed with GAMESS is equilibrated with the molecule charge distribution, i.e., a self-consistent procedure assures that the molecule ground state is in equilibrium with the surrounding nanostructures, and this effect is exploited in Sec. IV E. The basis set of the molecule wave function employed in the calculation of photoluminescence intensity includes, in addition to the ground state, ten excited states computed as frozen states that is they are influenced by the nanostructure polarization equilibrated with the ground state of the molecule. Another set of input data (energies, transition dipole moments, and potential) has been computed to also include the equilibration of the excited states with the surrounding nanostructures. To this point, the CIS calculation of the molecule close to the nanostructures has also been performed in order to compute the transition dipole moments between electronic excited states, needed to perform SCF equilibration of excited states with the nanostructures and go beyond the approximation of frozen excited states. Considering the first five excited states, we performed the self-consistent equilibration of the molecular ground and excited states in the presence of the nanostructures to compute energies, transition dipole moments, and the transition potentials on the tesserae. These results have been employed in Sec. IV E where the effect of the presence or absence of excited state equilibration with the nanostructures is investigated. In order to obtain the results reported in Sec. IV, we performed GAMESS calculations moving the molecule with respect to the tip and substrate center along the x and y axis through a grid with step 2.5 Å to finally obtain results on 36 different molecule positions. The z coordinate of the molecule has not been varied.

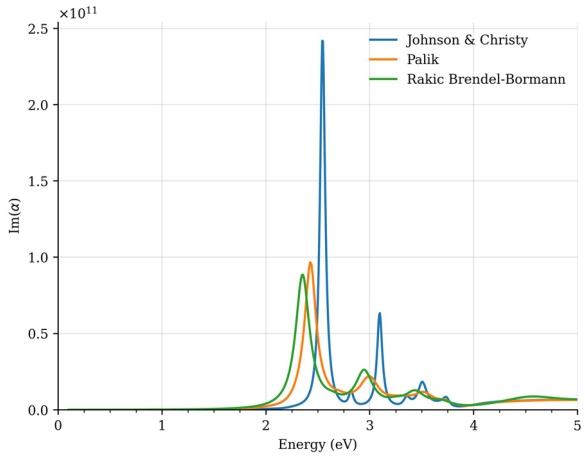

FIG. 2. Different absorption spectra of the same structure (Fig. 1 is the reference structure) calculated using three distinct dielectric functions: Johnson and Christy[77] (blue), Palik[71] (yellow), and Rakić-BB[70] (green).

The polarization charges located on each tessera have been computed with the homemade code TDPlas[55] in both cases with or without the presence of the molecule. In the first case, an incident radiation along the z axis has been considered to compute the potential on the polarization charges, while in photoluminescence calculations (e.g., in the presence of the molecule), the transition potential from the GAMESS TDDFT calculations due to the first two degenerate excited states has been employed in order to calculate the photoluminescence intensity due to the excitation of these degenerate low-lying states.

In photoluminescence calculation, the absorption frequency has been set to 532 nm (as in the experiment[24]), which is close to the maximum absorption of the silver nanostructures, as shown in Sec. IV by Fig. 2, while the emission frequency is set to 653 nm that corresponds to the experimental one.[24]

IV. RESULTS AND DISCUSSION

In this section, we report the results obtained with the methods explained in Sec. II. First, the results concerning the isolated nanostructure are reported as a benchmark test regarding the choice of the dielectric function, where we consider some choices between those that are mostly employed in the literature for modeling silver: Palik,[71] Johnson and Christy,[77] and the Brendel–Bormann fitting of Palik data.[70] In Sec. IV B, we report a study related to the effect of the nanostructure geometry, in particular the protrusion of the tip, on the local field enhancement. In Sec. IV C, the effect of the absorption frequency of the incident radiation is investigated, considering the calculation of the local field performed with the same nanostructure. Then, a study related to the effect of the distance between the tip and substrate on the intensity of the field enhancement is reported. Finally, in Sec. IV E, our results on the tip-enhanced photoluminescence of a single zinc phthalocyanine molecule are displayed. They include the calculation of the enhanced absorption rate, the enhanced radiative decay, the spectral shift, and the non-radiative decay rate induced by the molecule–metal interaction, as well as a comparison of the photoluminescence intensity computed when the self-consistent equilibration of the molecular states with the nanostructures is or is not considered.

A. Comparison of different dielectric functions

We computed the imaginary part of the polarizability, proportional to the absorption cross section, of the silver nanostructure reported in Fig. 1 for different dielectric functions documented in the literature, by plotting the imaginary component of the polarizability associated with the induced dipole originated by an incoming electric field polarized along the tip-axis direction. As it is shown in Fig. 2, the energy of the brighter plasmonic resonance of interest (≈2.3–2.4 eV) is quite sensitive to the dielectric function that is considered to model the metallic response. In the tests performed, two experimental dielectric functions have been considered (Palik[71] and Johnson and Christy[77]), while the Rakić[70] dielectric function is the result of the fitting of Palik data through the Brendel–Bormann model; indeed, as expected, the two profiles are very close to each other. Comparing the two experimental sets of data (Palik[71] and Johnson and Christy[77]), the results show some differences not only in the intensity of the absorption but also on the energies of the

peaks. Moreover, the damping of the excitation related with the broadening of the bands is different in the two cases; it is larger when the Palik or Rakic dielectric functions are employed than in the case of Johnson and Christy. In the following calculations, the Rakic dielectric function is employed, which is the less efficient due to a larger damping, as shown by Fig. 2.

B. Dependence of the local field on the tip geometrical parameters

The response of a NP interacting with an incident electric field directed along the z axis has been computed by solving the frequency-dependent BEM equations [Eq. (2)] for different

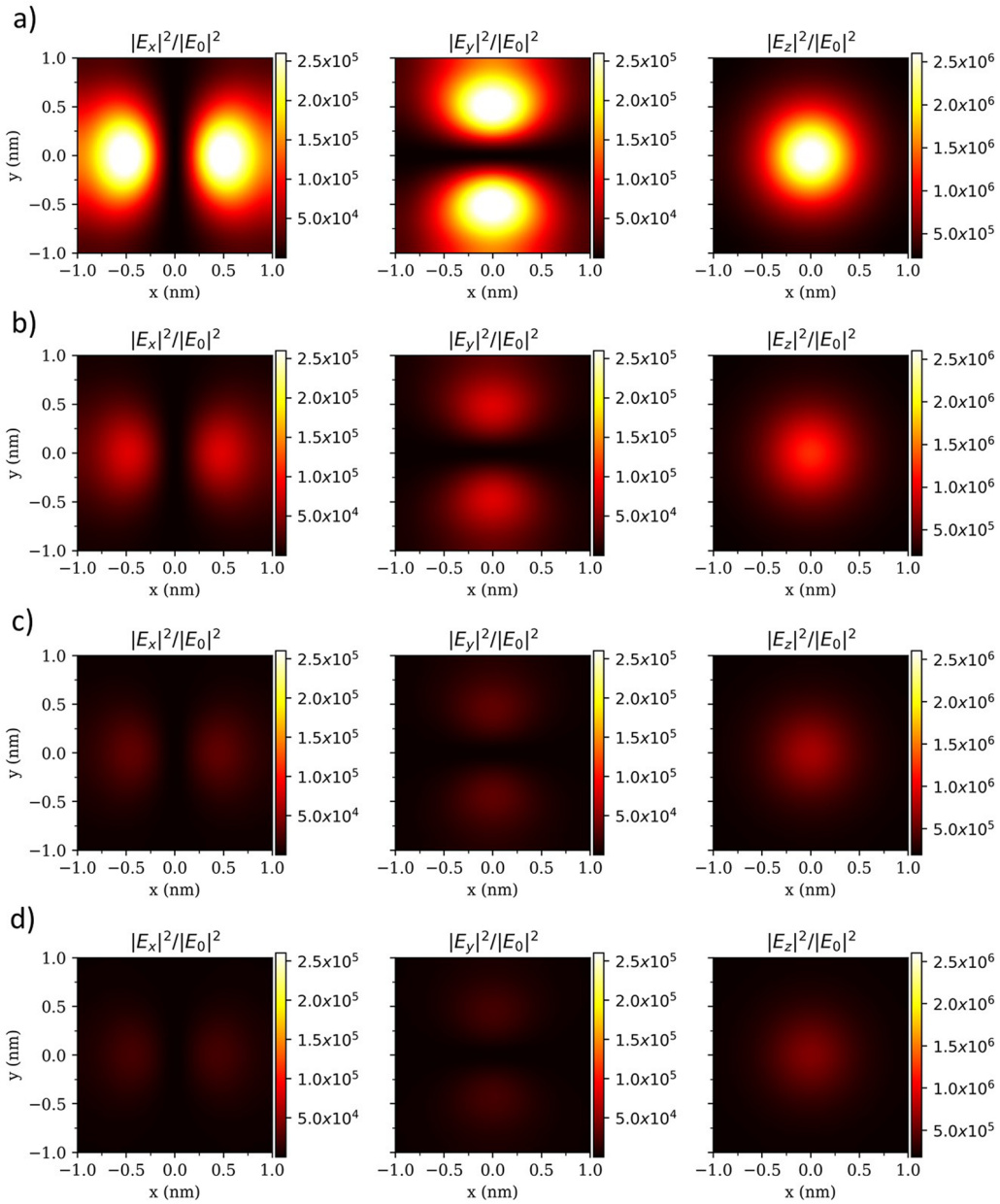

FIG. 3. Local field enhancement on a 1.0 × 1.0 nm^2 grid centered at z = 0.0 nm for different structures. From (a) to (d), the protrusion base radius (Fig. 1, red inset) increases [the radius is respectively: 0.5, 0.6, 0.8, 1.0 nm, as in Fig. 4(b)]. The local field enhancement is computed as the ratio $|E_i|^2/|E_0|^2$, where E_0 is the incoming electric field polarized along the tip-axis direction (z axis), whereas E_i assumes the values of E_x, E_y, E_z that are the components of the total local field obtained as the sum of the incident field $\vec{E}_0$ and the field generated by the charges on the nanostructure surface. The grid plane coincides with the molecular plane in the subsequent simulations (see Fig. 9).

structures obtained by changing the protrusion base radius (Fig. 1, red inset) in order to study the effect of structural modifications of the sharpest part of the tip. We found out that the local field on a 1.0 × 1.0 nm^2 grid oriented along the xy plane (z-coordinate = 0) has the maximum intensity in the same spatial points varying the NP structure: The field along the z axis has a spherical symmetry, while the x component of the field has the maximum intensity along the x axis and analogously the y component of the field has the maximum intensity along the y axis. On the other hand, the intensity of the field is strongly affected by the geometrical feature of the NP, as shown in Fig. 3. Indeed, the enhancement of the total local field upon excitation at 2.33 eV decreases as the protrusion base radius becomes larger, as can be inferred by Fig. 4 that shows the local field enhancement as a function of frequency for five different tip radii. This result is due to two main effects: an overall reduction of the intensity of the local field, particularly when structures with radius 0.6 and 0.7 nm are employed, and a gradual blue-shifting of the "local" resonance when the base radius increases. As Fig. 4 shows, if we considered the electric field at its maximum value for each structure, we would obtain color maps representing the field on a grid very close to each other, but the intermediate cases with radius protrusion equal to 0.6 and 0.7 nm would show a lower intensity of the enhanced field in correspondence with the maximum value.

C. Frequency dependence of the local field enhancement

As already suggested by Fig. 4, the intensity of the field enhancement strongly depends on the frequency. This is of particular interest when molecules close to the NP are considered: The closer the maximum frequency of the molecular absorption and the local field enhancement are, the more relevant the plasmonic effect on the molecule response will be. To better analyze this point, the local field enhancement has been computed on a 1.0 × 1.0 nm^2 grid oriented along the xy plane at different frequencies. In Fig. 5, we report the x and y components of the total field over the incoming electric field for different x [Fig. 5(a), top] and y [Fig. 5(a), bottom] displacements. As illustrated by the colored curves that correspond to different frequencies at which we evaluated the metallic response upon excitation, the maximum of the local field is reached at energies slightly higher than the "global" plasmonic resonance, which is at 2.33 eV (see Fig. 2, green curve).

Moreover, due to the symmetry of the structures involved in the calculation, the field intensity along the x direction (top panel) should be identical but for numerical accuracy to the field intensity along the y direction (bottom panel) for each frequency considered. Similar results can be observed in Fig. 6(a) that shows the field intensity along the x direction as a function of frequency, where the maximum of the total field for different grid points along the x direction is always achieved at energies above the "global" resonance. In addition, the frequency at which the x component of the total field reaches a maximum does not change moving on the grid along the x axis.

D. Field enhancement as a function of tip–molecule distance

Previous experiments and simulations[24] illustrated that TEPL measured for this kind of STM-like setup is distinctly affected by the tip–molecule distance. To investigate this point, we considered different distances between the tip and substrate moving the tip also along the x axis. Our results are reported in Fig. 7 where the x component of the local field intensity has been reported as a function of

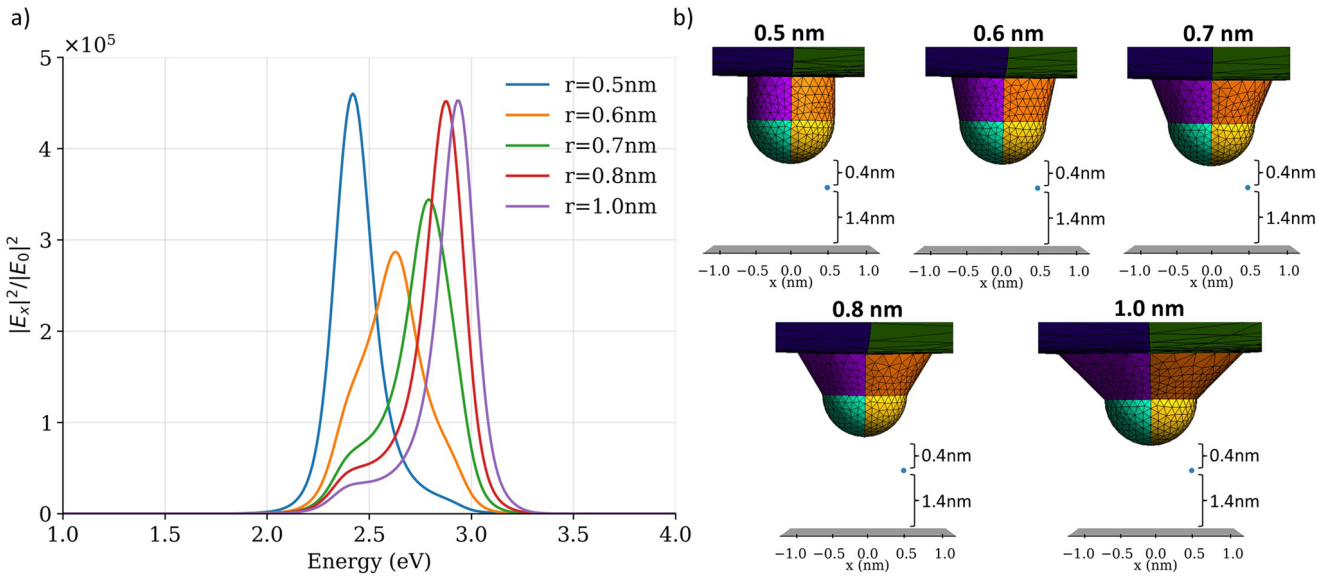

FIG. 4. (a) Local field enhancement as a function of frequency calculated on the grid point (x = 0.5 nm, y = 0.0 nm) for the five different structures reported in panel (b) (only the x component of the total field is shown). (b) Five different protrusion radii considered for the simulations in Fig. 3 and (a). The pale blue dot is the grid point where the field is computed, whereas the gray plane represents the substrate surface.

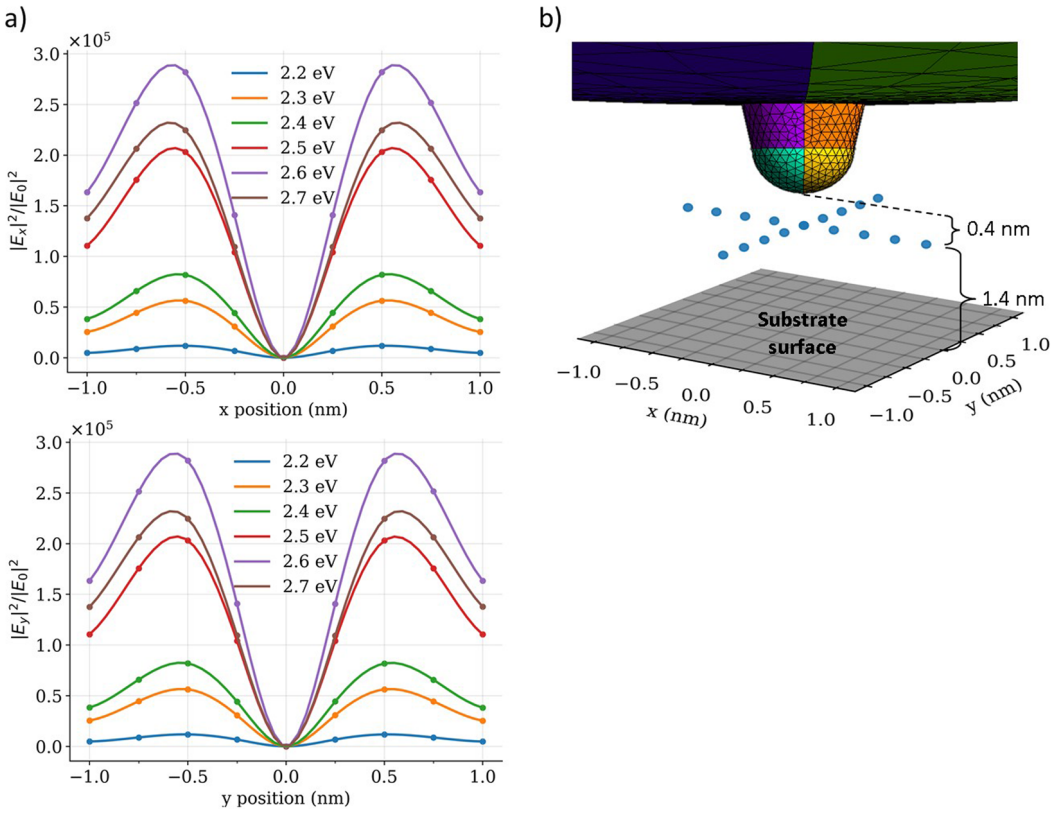

FIG. 5. (a) Square modulus of the x and y components of the total field over the incoming electric field along x (top) and y (bottom) displacements (the dots represent the calculated values, while the corresponding curves were obtained through cubic interpolation). The different colored lines correspond to the total field at different frequencies. The "global" plasmonic resonance of interest is predicted to be at 2.33 eV in the absorption spectrum (Fig. 2, highest green peak). (b) Schematic representation of the simulation setup used to obtain the results shown in panel (a), where the blue dots are representative of points where the electric field has been computed.

x position (with both y and z coordinates equal to 0 nm). The distances reported on the top of the figure are those between the tip and the center of the grid where the electric field is computed [with coordinates (0,0,0) nm] that would correspond to the molecule center. When the tip–molecule distance increases from 0.4 to 0.9 nm [blue to red line, Fig. 7(a)], the x component of the total field, which is along with the y component, responsible for the coupling with the molecular transition dipoles, decreases in amplitude as expected. Moreover, the corresponding peak broadens, which means that the local field becomes less confined in the cavity.

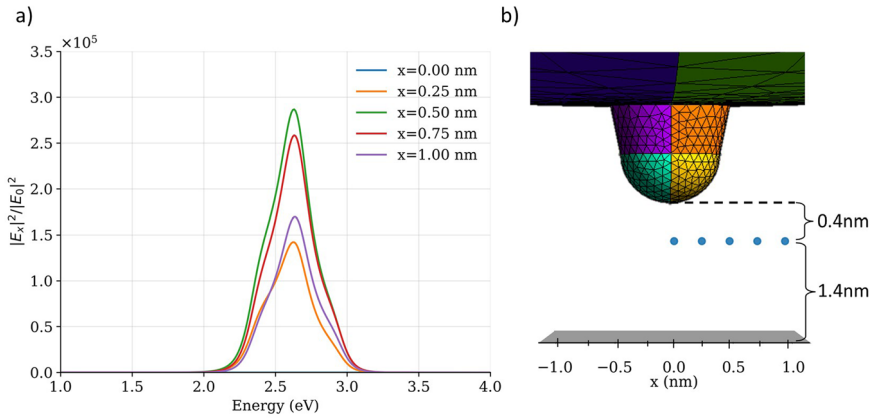

FIG. 6. (a) Local field enhancement as a function of frequency for different grid points along the x axis as shown in panel (b). The symmetrical results were obtained for the y component. The blue line has very low intensity, and it lies on the x axis. (b) Schematic representation of the simulation setup used to obtain the results shown in panel (a); the y coordinate is always set to 0.0 nm as in the top plot of Fig. 5(a).

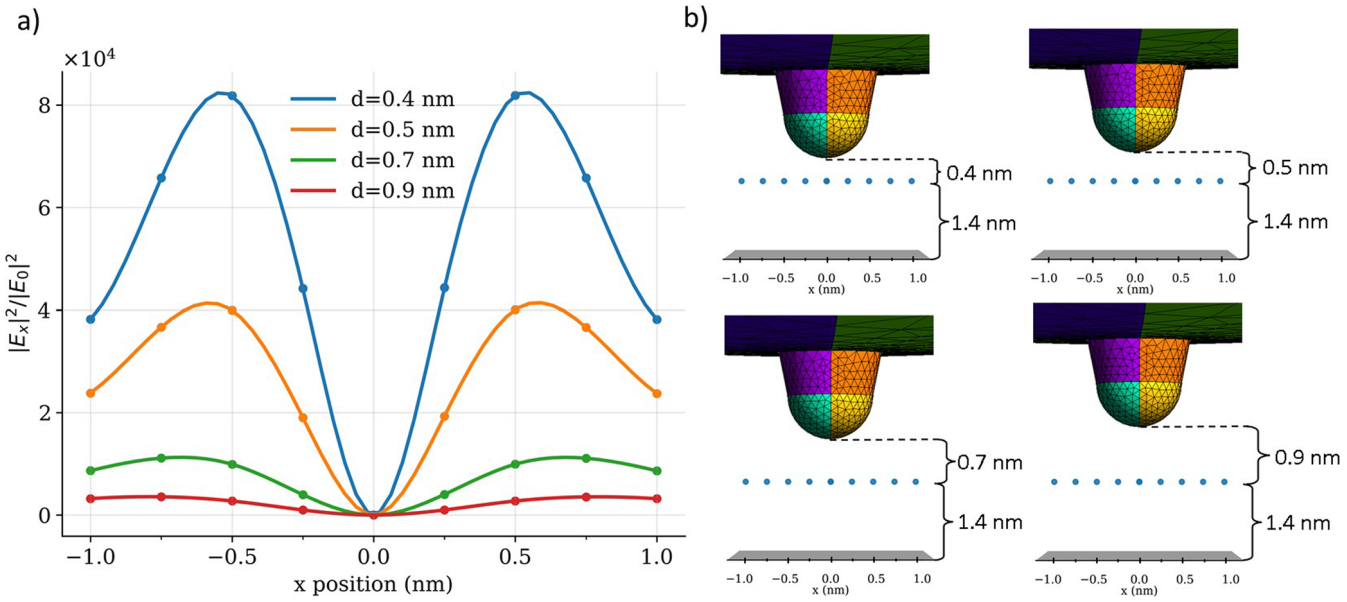

FIG. 7. (a) Square modulus of the x component of the total field over the incoming electric field along x for different tip–molecule distances (colored lines). The symmetrical results were obtained for the y component along the y-displacement (the dots represent the calculated values, while the corresponding curves were obtained through cubic interpolation). (b) Schematic representation of the simulation setup used to obtain the results shown in panel (a).

E. Coupling with the zinc phthalocyanine molecule

So far, we have focused our attention on the electromagnetic problem of the bare nanostructures without considering any molecular species. In order to simulate the electromagnetic effects due to the presence of the nanostructure on the photophysical properties of the zinc phthalocyanine molecule, we solved the frequency-dependent BEM equation [see Eq. (1)] where the perturbation term $\mathbf{V}(\omega)$ represents the transition potential associated with the molecular excited state of interest. The potential has been computed at the quantum mechanical level assuming the ground state electron density of the molecule polarized by the mutual interaction with the metallic nanoparticle. In particular, for this molecule, the first and second excited states are degenerate, so the contribution to photoluminescence (and also radiative and non-radiative decay rates) due to both excited states has been considered. We first present the simulated "photoluminescence quantities" that are necessary to compute the TEPL map, and then, we directly compare the results obtained with/without the self-consistent equilibration of the molecular states with the nanostructures.

1. Photoluminescence quantities

Using Eqs. (9)–(14), the corresponding radiative and non-radiative decay rates have been evaluated, allowing us to observe the effects of the metallic nanostructure on the excited state properties of the molecule, as shown in Fig. 8. It turned out that when the tip–molecule distance is set to 0.4 nm and the tip is above one of the molecular lobes (x = 0.5 nm and y = 0.5 nm), both stronger absorption [Fig. 8(a)] and a net reduction of the quantum yield [Fig. 8(b)] with respect to the vacuum value (0.2, as stated in Sec. II B) are observed. The enhancement in absorption means more molecules in excited states, which more than compensate for the decreased quantum yield, overall resulting in a strong photoluminescence enhancement of the single molecule when the plasmon oscillation is efficiently able to couple with the molecular transition dipoles (see Fig. 9). It is worth noting that the images reported in Figs. 8 and 9 resemble the molecular structure, displaying stronger interactions at the position of the lobes. The possibility of retaining such "resolution" is made possible by the use of the transition potentials as the source of the perturbation instead of a point dipole, which encode the information related to the molecular shape. Moreover, we also noticed that the non-radiative decay rate due to the molecule–metal interaction [see Eq. (14)] is faster without the presence of the tip when the molecule is alone above the substrate, and taking this into account, the TEPL ratio (with respect to the tip-free setup) is predicted to be $\approx 10^8$, in agreement with the experimental estimate of Yang *et al.*[24] The computed linewidths in Fig. 8(d) provide an interval of variation that is essentially the same as in the experiment[24] (around 2.5–3 meV). However, the experiment features an additional, apparently spatially independent, contribution of around 8 meV. This additional value is much in line with the vibronic broadening we estimate for the emission process, as shown in Fig. S6 (supplementary material), which is ≈9 meV (FWHM) and that we did not included in Fig. 8(d).

2. Molecule SCF equilibration with nanostructures

Additionally, we investigated the possible effects of the molecular electron density relaxation due to the presence of the nanostructure on the TEPL values. In order to do so, we computed self-consistently the equilibrated molecular electron density for both the ground state (which may affect the absorption rate) and the excited state (which may affect the emission rate), obtaining the results

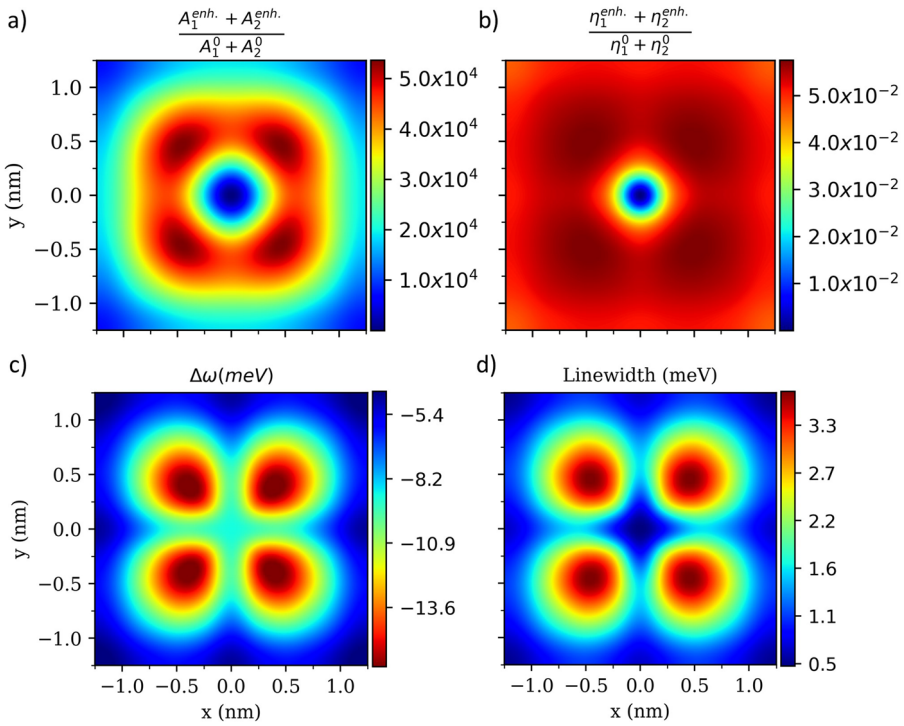

FIG. 8. 2D-maps on a 1.25 × 1.25 nm^2 grid of (a) the enhanced absorption rate, (b) quantum efficiency, (c) spectral shift, and (d) non-radiative decay rate due to the molecule–metal interaction [see Eqs. (10)–(15)]. The position of the molecular center is x = y = 0.0 nm. Panels (c) and (d) were obtained considering the contribution coming from each state weighted by the corresponding PL intensity on the same grid point.

shown in Fig. 9(b). By comparing the TEPL images in Figs. 9(a) and 9(b), it can be seen that at the position of the molecular lobes, where the tip–molecule interaction is stronger, only a negligible difference of ≈0.1 × 10^3 (over a value of ≈6 × 10^3) in the TEPL ratios is observed, and there is no significant change in the energy of the two isoenergetic excited states with respect to the center of the grid, where the tip–molecule interaction is much weaker. The outcomes clearly point out that the molecular electron density

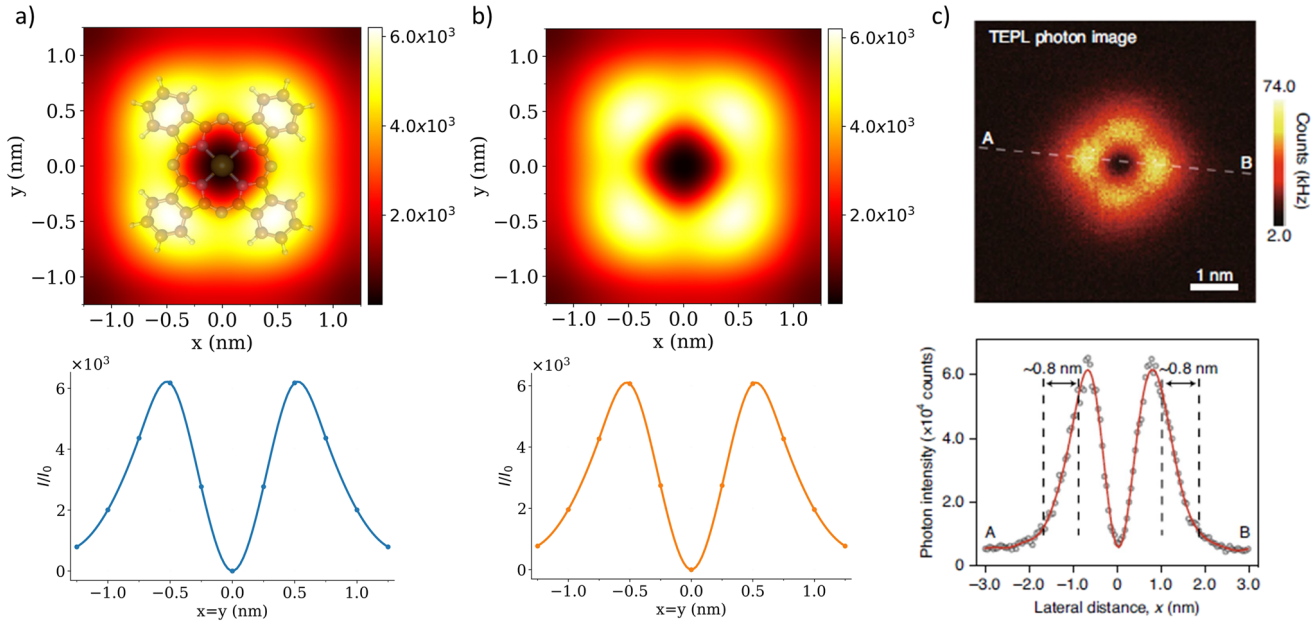

FIG. 9. (a) Tip-enhanced photoluminescence (TEPL) ratio simulated using Eq. (9) (Sec. II) on a 1.25 × 1.25 nm^2 grid (top) and along the main diagonal of the grid (bottom), without considering any electron density relaxation due to the nanostructure. I_0 is the computed vacuum emission obtained setting η^0 to the experimental value of 0.2 (see Sec. II B). (b) The same simulations obtained considering the self-consistent electron density relaxation for both ground and excited states. (c) Previously reported experimental results on the same system.[24]

equilibration with the nano-object does not strongly influence the computed photoluminescence intensity and thus, at least for this molecule in the applied conditions, can be disregarded. In light of these results, the approximation of ignoring the molecular electron density equilibration with the nanostructures[24] is justified.

V. CONCLUSIONS

Inspired by recent experimental work,[24] we investigated the photophysical properties of a single zinc phthalocyanine molecule underneath the atomistic protrusion of an STM-like silver nanostructure by means of a suitable PCM-NP description of the nanoparticle and full quantum mechanical treatment of the molecule. We found out that the geometrical features of the atomistic protrusion at the tip apex strongly influence the PL measurements, in particular varying the frequency of the plasmon enhanced local field maximum. This result suggests that the geometrical features of the nano-tip strongly influence the features of the picocavity and thus also the molecule–plasmon interaction strength. Therefore, in order to optimize the photoluminescence intensity, one needs to cleverly design the geometrical features of the nano-tip.

Moreover, concerning the theoretical side, we pointed out that the photoluminescence results are sensitive to the measurement uncertainty of the dielectric function, and for this reason, different experimental dielectric functions for the metal of interest have to be considered. Therefore, discrepancies between theoretical and experimental results on photoluminescence intensity can also depend on the choice of the dielectric function model. In addition, we illustrated that additional attention has to be paid to the adopted theoretical model because fictitious charge transfer excitation between different metallic nanoparticles within the same system might come up, as a result of numerical issues in the calculations. Additionally, we remark that the electronic polarization interaction with the tip is negligible. To conclude, taking into account each detail previously mentioned, theoretical simulations might be able to predict and support the state-of-the-art experiments, thus paving the way for studying plasmon–molecule interactions at the submolecular level, as well as to design new experiments.

SUPPLEMENTARY MATERIAL

See the supplementary material for additional details and numerical tests concerning charge conservation analysis, influence of the gas-phase radiative quantum efficiency η^0 on the TEPL results, basis set numerical test, ground and excited state optimized structures of zinc phthalocyanine, simulated vibrationally resolved emission spectrum of zinc phthalocyanine, detailed contribution of $\vec{\mu}^{met}$ and $\vec{\mu}^{ind}$ to Fig. 8(a), comparison between enhanced absorption rates and enhanced radiative decay rates, and influence of a single NaCl monolayer on the TEPL results.

ACKNOWLEDGMENTS

We acknowledge financial support from the European Research Council (ERC) under the European Union's Horizon 2020 research and innovation program through the project TAME-Plasmons (Grant Agreement No. 681285). Computational work has been carried out on the C3P (Computational Chemistry Community in Padua) HPC facility of the Department of Chemical Sciences of the University of Padua. G.D. and M.R. acknowledge MIUR "Dipartimenti di Eccellenza" under the project Nanochemistry for energy and Health (NExuS) for funding the Ph.D. grant.

AUTHOR DECLARATIONS

Conflict of Interest

The authors have no conflicts to disclose.

DATA AVAILABILITY

The data that support the findings of this study are available within the article and its supplementary material.

REFERENCES

[1] V. Giannini, A. I. Fernández-Domínguez, S. C. Heck, and S. A. Maier, Chem. Rev. **111**, 3888 (2011).
[2] D. K. Gramotnev and S. I. Bozhevolnyi, Nat. Photonics **4**, 83 (2010).
[3] L. Xu, F. Li, Y. Liu, F. Yao, and S. Liu, Appl. Sci. **9**, 861 (2019).
[4] A. B. Taylor and P. Zijlstra, ACS Sens. **2**, 1103 (2017).
[5] A. B. Zrimsek, N. Chiang, M. Mattei, S. Zaleski, M. O. McAnally, C. T. Chapman, A.-I. Henry, G. C. Schatz, and R. P. Van Duyne, Chem. Rev. **117**, 7583 (2017).
[6] Z. Liu, S.-Y. Ding, Z.-B. Chen, X. Wang, J.-H. Tian, J. R. Anema, X.-S. Zhou, D.-Y. Wu, B.-W. Mao, X. Xu *et al.*, Nat. Commun. **2**, 305 (2011).
[7] J. Lee, K. T. Crampton, N. Tallarida, and V. A. Apkarian, Nature **568**, 78 (2019).
[8] F. Benz, M. K. Schmidt, A. Dreismann, R. Chikkaraddy, Y. Zhang, A. Demetriadou, C. Carnegie, H. Ohadi, B. De Nijs, R. Esteban *et al.*, Science **354**, 726 (2016).
[9] H. Imada, K. Miwa, M. Imai-Imada, S. Kawahara, K. Kimura, and Y. Kim, Phys. Rev. Lett. **119**, 013901 (2017).
[10] K. Kimura, K. Miwa, H. Imada, M. Imai-Imada, S. Kawahara, J. Takeya, M. Kawai, M. Galperin, and Y. Kim, Nature **570**, 210 (2019).
[11] F. Mohn, L. Gross, N. Moll, and G. Meyer, Nat. Nanotechnol. **7**, 227 (2012).
[12] C. Chen, P. Chu, C. A. Bobisch, D. L. Mills, and W. Ho, Phys. Rev. Lett. **105**, 217402 (2010).
[13] N. Jiang, D. Kurouski, E. A. Pozzi, N. Chiang, M. C. Hersam, and R. P. Van Duyne, Chem. Phys. Lett. **659**, 16 (2016).
[14] J. Langer, D. Jimenez de Aberasturi, J. Aizpurua, R. A. Alvarez-Puebla, B. Auguié, J. J. Baumberg, G. C. Bazan, S. E. J. Bell, A. Boisen, A. G. Brolo *et al.*, ACS Nano **14**, 28 (2019).
[15] N. Chiang, N. Jiang, D. V. Chulhai, E. A. Pozzi, M. C. Hersam, L. Jensen, T. Seideman, and R. P. Van Duyne, Nano Lett. **15**, 4114 (2015).
[16] P. Liu, X. Chen, H. Ye, and L. Jensen, ACS Nano **13**, 9342 (2019).
[17] M. D. Sonntag, J. M. Klingsporn, A. B. Zrimsek, B. Sharma, L. K. Ruvuna, and R. P. Van Duyne, Chem. Soc. Rev. **43**, 1230 (2014).
[18] P. Liu, D. V. Chulhai, and L. Jensen, ACS Nano **11**, 5094 (2017).
[19] M. D. Sonntag, J. M. Klingsporn, L. K. Garibay, J. M. Roberts, J. A. Dieringer, T. Seideman, K. A. Scheidt, L. Jensen, G. C. Schatz, and R. P. Van Duyne, J. Phys. Chem. C **116**, 478 (2012).
[20] K. Fiederling, M. Abasifard, M. Richter, V. Deckert, S. Gräfe, and S. Kupfer, Nanoscale **12**, 6346 (2020).
[21] F. Latorre, S. Kupfer, T. Bocklitz, D. Kinzel, S. Trautmann, S. Gräfe, and V. Deckert, Nanoscale **8**, 10229 (2016).
[22] W. Zhu, R. Esteban, A. G. Borisov, J. J. Baumberg, P. Nordlander, H. J. Lezec, J. Aizpurua, and K. B. Crozier, Nat. Commun. **7**, 11495 (2016).
[23] M. Schnell, A. García-Etxarri, A. J. Huber, K. Crozier, J. Aizpurua, and R. Hillenbrand, Nat. Photonics **3**, 287 (2009).

[24]B. Yang, G. Chen, A. Ghafoor, Y. Zhang, Y. Zhang, Y. Zhang, Y. Luo, J. Yang, V. Sandoghdar, J. Aizpurua, Z. Dong, and J. G. Hou, Nat. Photonics **14**, 693–699 (2020).
[25]W. Su, N. Kumar, S. Mignuzzi, J. Crain, and D. Roy, Nanoscale **8**, 10564 (2016).
[26]T. Kumagai, Nat. Photonics **14**, 653 (2020).
[27]K.-Q. Lin, J. Yi, J.-H. Zhong, S. Hu, B.-J. Liu, J.-Y. Liu, C. Zong, Z.-C. Lei, X. Wang, J. Aizpurua *et al.*, Nat. Commun. **8**, 14891 (2017).
[28]K. L. Kelly, E. Coronado, L. L. Zhao, and G. C. Schatz, J. Phys. Chem. B **107**, 668–677 (2003).
[29]N. A. Mortensen, S. Raza, M. Wubs, T. Søndergaard, and S. I. Bozhevolnyi, Nat. Commun. **5**, 3809 (2014).
[30]G. Mie, Ann. Phys. **330**, 377 (1908).
[31]P. Gonçalves, T. Christensen, N. Rivera, A.-P. Jauho, N. A. Mortensen, and M. Soljačić, Nat. Commun. **11**, 366 (2020).
[32]W. H. Yang, G. C. Schatz, and R. P. Van Duyne, J. Chem. Phys. **103**, 869 (1995).
[33]R. Fuchs, Phys. Rev. B **11**, 1732 (1975).
[34]F. J. García de Abajo and J. Aizpurua, Phys. Rev. B **56**, 15873 (1997).
[35]S. Corni and J. Tomasi, J. Chem. Phys. **114**, 3739 (2001).
[36]F. J. García de Abajo and A. Howie, Phys. Rev. B **65**, 115418 (2002).
[37]U. Hohenester and A. Trügler, Comput. Phys. Commun. **183**, 370 (2012); arXiv:1109.5783.
[38]F. Hao and P. Nordlander, Chem. Phys. Lett. **446**, 115 (2007).
[39]K. Lopata and D. Neuhauser, J. Chem. Phys. **130**, 104707 (2009).
[40]H. Chen, J. M. McMahon, M. A. Ratner, and G. C. Schatz, J. Phys. Chem. C **114**, 14384 (2010).
[41]A. Sakko, T. P. Rossi, and R. M. Nieminen, J. Phys.: Condens. Matter **26**, 315013 (2014).
[42]T. Neuman, R. Esteban, D. Casanova, F. J. García-Vidal, and J. Aizpurua, Nano Lett. **18**, 2358 (2018).
[43]F. Aguilar-Galindo, S. Díaz-Tendero, and A. G. Borisov, J. Phys. Chem. C **123**, 4446 (2019).
[44]Y. Zhang, Z.-C. Dong, and J. Aizpurua, J. Phys. Chem. C **124**, 4674 (2020).
[45]S. M. Morton and L. Jensen, J. Chem. Phys. **133**, 074103 (2010).
[46]V. Arcisauskaite, J. Kongsted, T. Hansen, and K. V. Mikkelsen, Chem. Phys. Lett. **470**, 285 (2009).
[47]J. Fregoni, T. S. Haugland, S. Pipolo, T. Giovannini, H. Koch, and S. Corni, Nano Lett. **21**, 6664 (2021).
[48]T. P. Rossi, T. Shegai, P. Erhart, and T. J. Antosiewicz, Nat. Commun. **10**, 3336 (2019).
[49]J. Tomasi, B. Mennucci, and R. Cammi, Chem. Rev. **105**, 2999 (2005).
[50]O. Andreussi, S. Corni, B. Mennucci, and J. Tomasi, J. Chem. Phys. **121**, 10190 (2004).
[51]B. Mennucci and S. Corni, Nat. Rev. Chem. **3**, 315 (2019).
[52]S. Corni and J. Tomasi, J. Chem. Phys. **118**, 6481 (2003).
[53]M. Caricato, O. Andreussi, and S. Corni, J. Phys. Chem. B **110**, 16652 (2006).
[54]S. Vukovic, S. Corni, and B. Mennucci, J. Phys. Chem. C **113**, 121 (2009).
[55]S. Pipolo and S. Corni, J. Phys. Chem. C **120**, 28774 (2016).
[56]J. R. Lakowicz, C. D. Geddes, I. Gryczynski, J. Malicka, Z. Gryczynski, K. Aslan, J. Lukomska, E. Matveeva, J. Zhang, R. Badugu, and J. Huang, J. Fluoresc. **14**, 425 (2004).
[57]J. R. Lakowicz, Anal. Biochem. **337**, 171 (2005).
[58]J. R. Lakowicz, K. Ray, M. Chowdhury, H. Szmacinski, Y. Fu, J. Zhang, and K. Nowaczyk, Analyst **133**, 1308 (2008).
[59]T. V. Shubina, A. A. Toropov, V. N. Jmerik, D. I. Kuritsyn, L. V. Gavrilenko, Z. F. Krasil'nik, T. Araki, Y. Nanishi, B. Gil, A. O. Govorov, and S. V. Ivanov, Phys. Rev. B **82**, 073304 (2010).
[60]S. M. Morton, D. W. Silverstein, and L. Jensen, Chem. Rev. **111**, 3962 (2011).
[61]A. J. Haes, C. L. Haynes, A. D. McFarland, G. C. Schatz, R. P. Van Duyne, and S. Zou, MRS Bull. **30**, 368 (2005).
[62]P. Anger, P. Bharadwaj, and L. Novotny, Phys. Rev. Lett. **96**, 113002 (2006).
[63]B. L. Darby, B. Auguié, M. Meyer, A. E. Pantoja, and E. C. Le Ru, Nat. Photonics **10**, 40 (2016).
[64]M. Pelton, Nat. Photonics **9**, 427 (2015).
[65]F. Della Sala and S. D'Agostino, *Handbook of Molecular Plasmonics* (CRC Press, 2013).
[66]S. Corni and J. Tomasi, J. Chem. Phys. **117**, 7266 (2002).
[67]P. Johansson, H. Xu, and M. Käll, Phys. Rev. B **72**, 035427 (2005).
[68]A. Ogunsipe, D. Maree, and T. Nyokong, J. Mol. Struct. **650**, 131 (2003).
[69]C. Geuzaine and J.-F. Remacle, Int. J. Numer. Methods Eng. **79**, 1309 (2009).
[70]A. D. Rakić, A. B. Djurišić, J. M. Elazar, and M. L. Majewski, Appl. Opt. **37**, 5271 (1998).
[71]E. Palik, *Handbook of Optical Constants of Solids* (Academic Press, Cambridge, MA, 1998).
[72]M. J. Frisch, G. W. Trucks, H. B. Schlegel, G. E. Scuseria, M. A. Robb, J. R. Cheeseman, G. Scalmani, V. Barone, G. A. Petersson, H. Nakatsuji, X. Li, M. Caricato, A. V. Marenich, J. Bloino, B. G. Janesko, R. Gomperts, B. Mennucci, H. P. Hratchian, J. V. Ortiz, A. F. Izmaylov, J. L. Sonnenberg, D. Williams Young, F. Ding, F. Lipparini, F. Egidi, J. Goings, B. Peng, A. Petrone, T. Henderson, D. Ranasinghe, V. G. Zakrzewski, J. Gao, N. Rega, G. Zheng, W. Liang, M. Hada, M. Ehara, K. Toyota, R. Fukuda, J. Hasegawa, M. Ishida, T. Nakajima, Y. Honda, O. Kitao, H. Nakai, T. Vreven, K. Throssell, J. A. Montgomery, Jr., J. E. Peralta, F. Ogliaro, M. J. Bearpark, J. J. Heyd, E. N. Brothers, K. N. Kudin, V. N. Staroverov, T. A. Keith, R. Kobayashi, J. Normand, K. Raghavachari, A. P. Rendell, J. C. Burant, S. S. Iyengar, J. Tomasi, M. Cossi, J. M. Millam, M. Klene, C. Adamo, R. Cammi, J. W. Ochterski, R. L. Martin, K. Morokuma, O. Farkas, J. B. Foresman, and D. J. Fox, Gaussian 16, Revision B.01, Gaussian, Inc., Wallingford, CT, 2016.
[73]F. Santoro, R. Improta, A. Lami, J. Bloino, and V. Barone, J. Chem. Phys. **126**, 084509 (2007).
[74]J. Savolainen, D. van der Linden, N. Dijkhuizen, and J. L. Herek, J. Photochem. Photobiol., A **196**, 99 (2008).
[75]C. Dykstra, G. Frenking, K. Kim, and G. Scuseria, *Theory and Applications of Computational Chemistry: The First Forty Years* (Elsevier, 2011).
[76]M. W. Schmidt, K. K. Baldridge, J. A. Boatz, S. T. Elbert, M. S. Gordon, J. H. Jensen, S. Koseki, N. Matsunaga, K. A. Nguyen, S. Su *et al.*, J. Comput. Chem. **14**, 1347 (1993).
[77]P. B. Johnson and R. W. Christy, Phys. Rev. B **6**, 4370 (1972).

Role of metal-nanoparticle features on tip-enhanced photoluminescence of single molecules

Marco Romanelli[a], Giulia Dall'Osto[a] and Stefano Corni[ab‡]

[a] *Department of Chemical Sciences, University of Padova, via Marzolo 1, Padova, Italy*
[b] *CNR Institute of Nanoscience, via Campi 213/A, Modena, Italy*

Contents

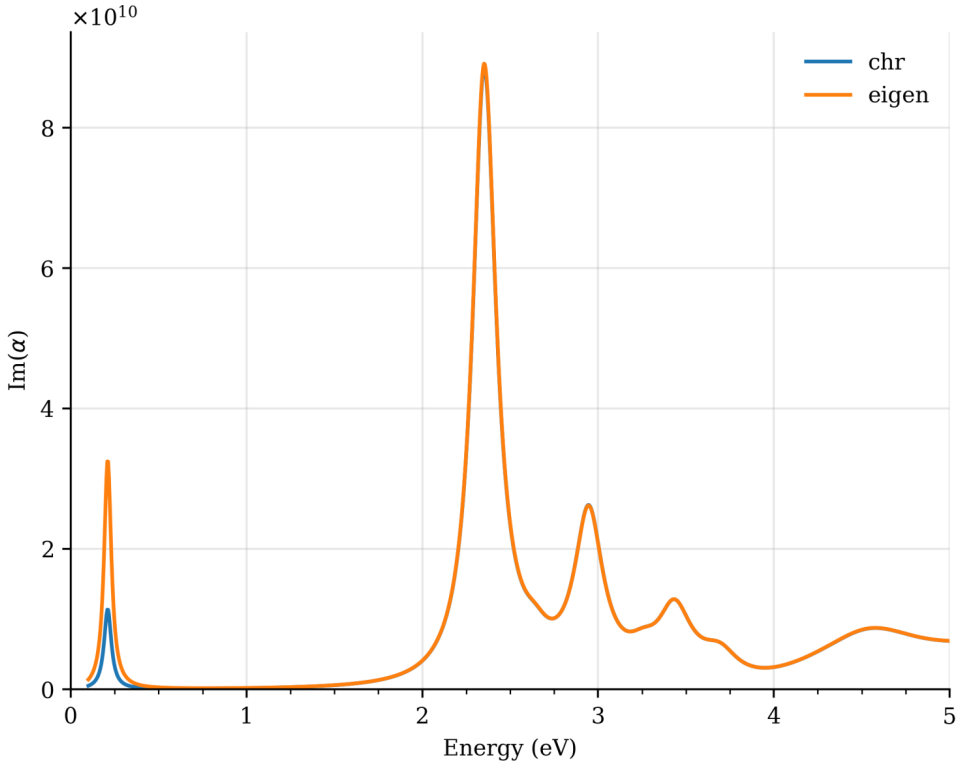

Figure S1: Absorption spectra of the nanostructure reported in Fig.1 (main text) computed by using the two different approaches mentioned in section II-A (main text) for ensuring 'charge conservation'. The a-posteriori normalization is the blue curve, whereas the normalization through the eigenvectors' coefficients is the orange one. The main difference between the two methods can be observed only at low energies (less than 1 eV), where the fictitious charge-transfer peak appears.

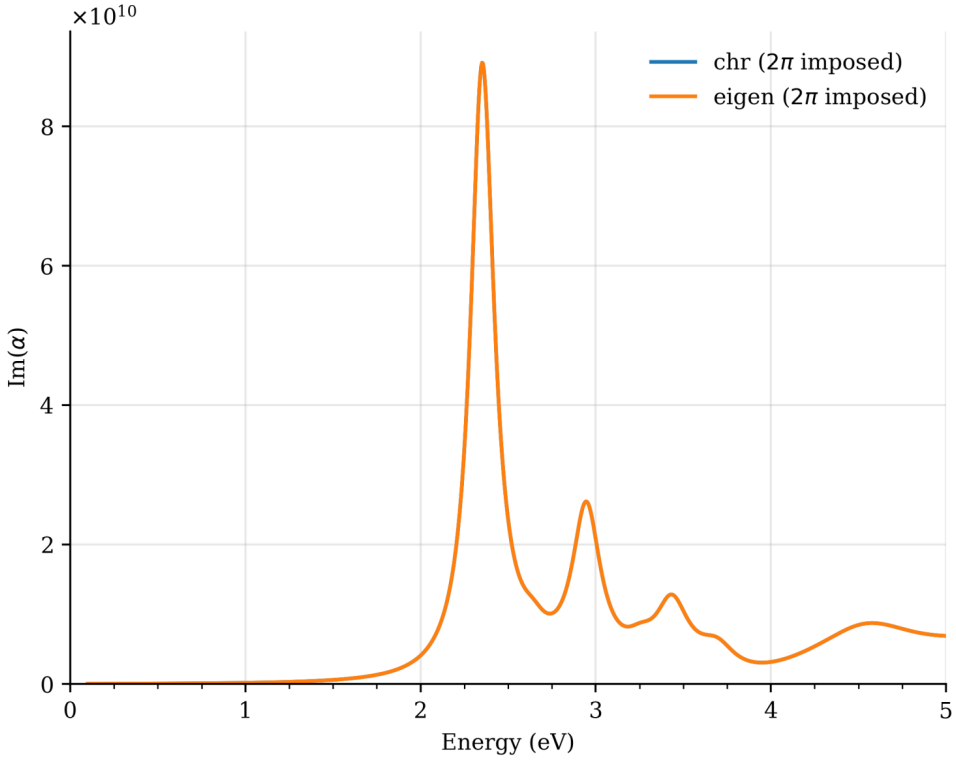

Figure S2: Absorption spectra of the nanostructure reported in FIG.1 (main text) computed by using the two different approaches mentioned in section II-A for ensuring 'charge conservation' and simultaneously forcing the two lowest eigenvalues of DA exactly to -2π (see equation 3, main text). The plasmon eigenmodes associated with these two eigenvalues are responsible for the charge-transfer peak that appears at low energies (FIG. S1). Indeed, if these two eigenvalues are exactly set to -2π their contribution to the induced charges should vanish (eq.3, main text). Although, in this figure, the fictitious peak is no longer evident in both methods,the total sum of the surface charges for the separate structures ,tip and substrate respectively, is closer to zero in the 'a posteriori' approach, which yields a more realistic scenario.

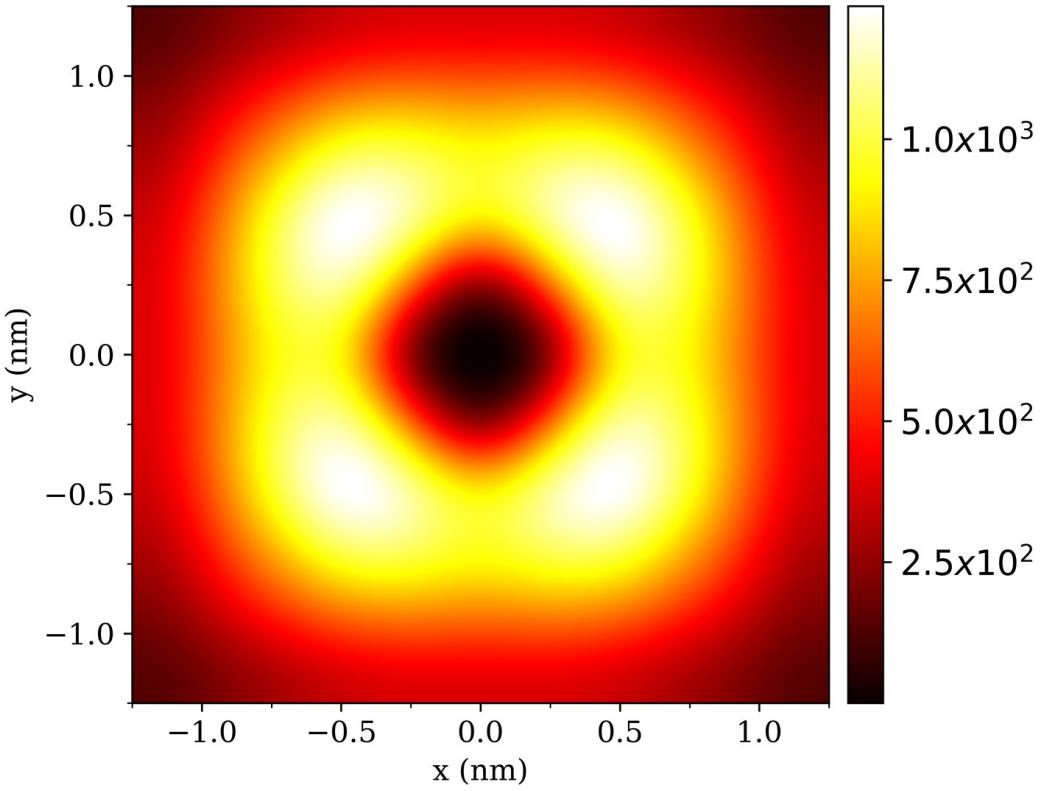

Figure S3: Tip-Enhanced Photo-luminescence (TEPL) ratio simulated using equation 5 (Section II-B, main text) on a 1.25 nm × 1.25 nm grid considering η^0 equals to 1 (i.e. unitary radiative quantum efficiency in vacuum).

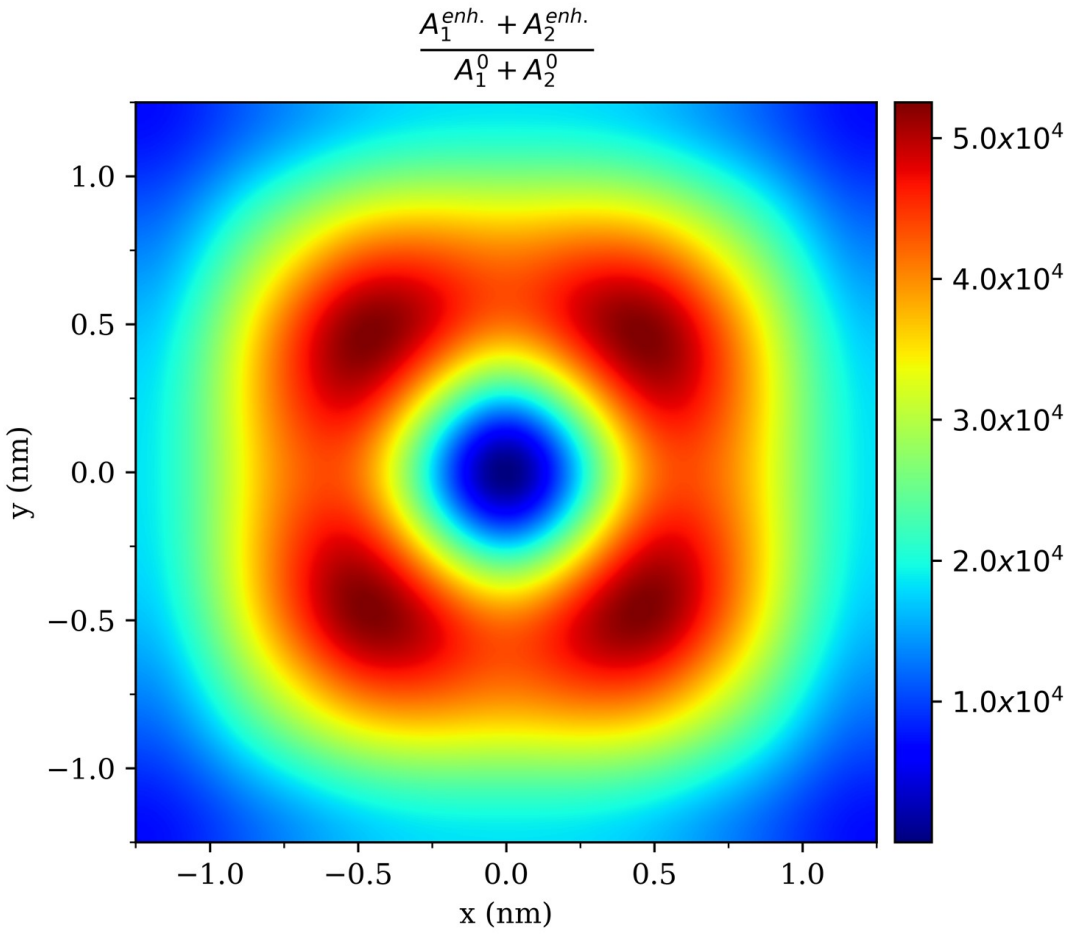

Figure S4: Enhanced absorption rate simulated using equation 10 (Section II-B, main text) on a 1.25 nm × 1.25 nm grid considering the TZP basis-set as implemented in GAMESS [1,2]. By comparing these data with Figure 8a) main text, it can be seen that the improvement of the basis set does not change the results.

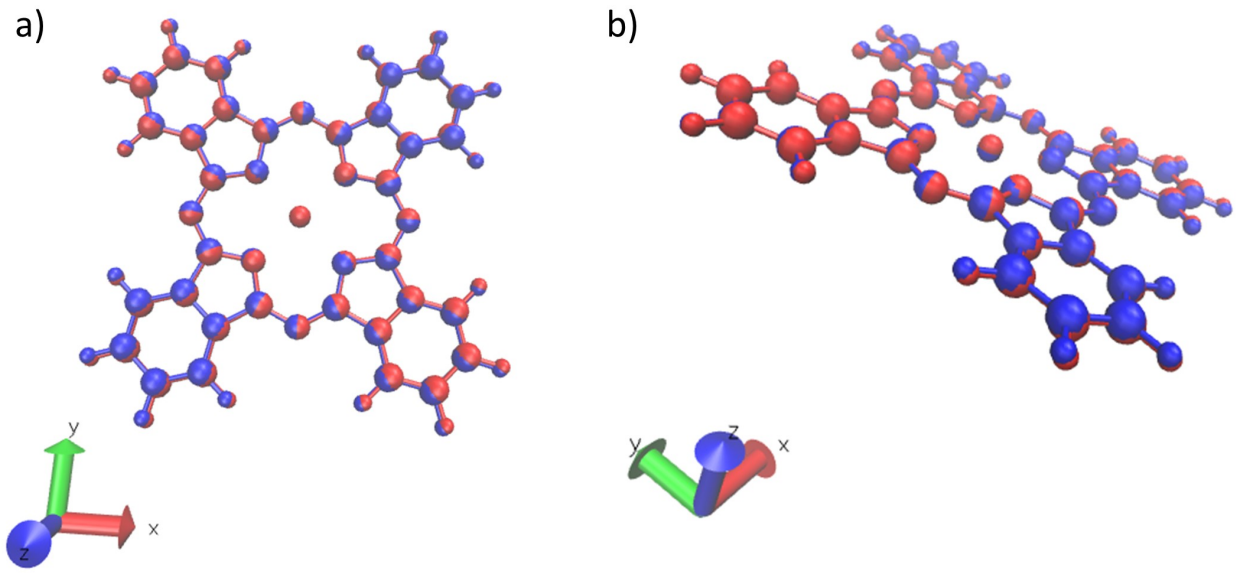

Figure S5: Superposition of ground and first excited state optimized geometries of Zinc-phthalocyanine, a) top view, b) side view.

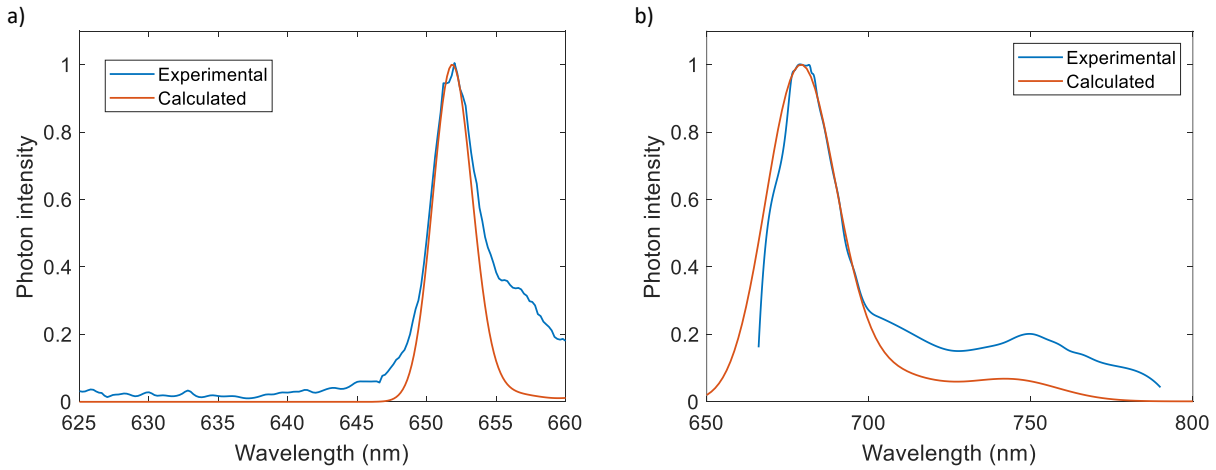

Figure S6: Comparison between computed vibrational resolved emission spectrum and experimental emission spectrum in vacuum when the molecule is close to the silver nanostructures where the computed one is red-shifted by 20.8 nm (panel a)[3] and in DMSO where the computed one is red-shifted by 49.6 nm (panel b).[4] It has to be noticed that the wavelength scale considered is shorter in panel (a) than in panel (b) and to compare the spectra, two different broadening have been considered to obtain the convoluted spectrum from emission transition calculations. In panel (a) the computed spectrum does not reproduce the shoulder detected experimentally at ≈ 657 nm, therefore it could be a result of the interaction between the molecule and the substrate rather than the effect of the presence of a vibronic structure, as mentioned in the experimental work.[3] On the other hand, the calculated spectrum is in good agreement with experimental spectrum in DMSO (panel b), although the shoulder at 700 nm is underestimated.

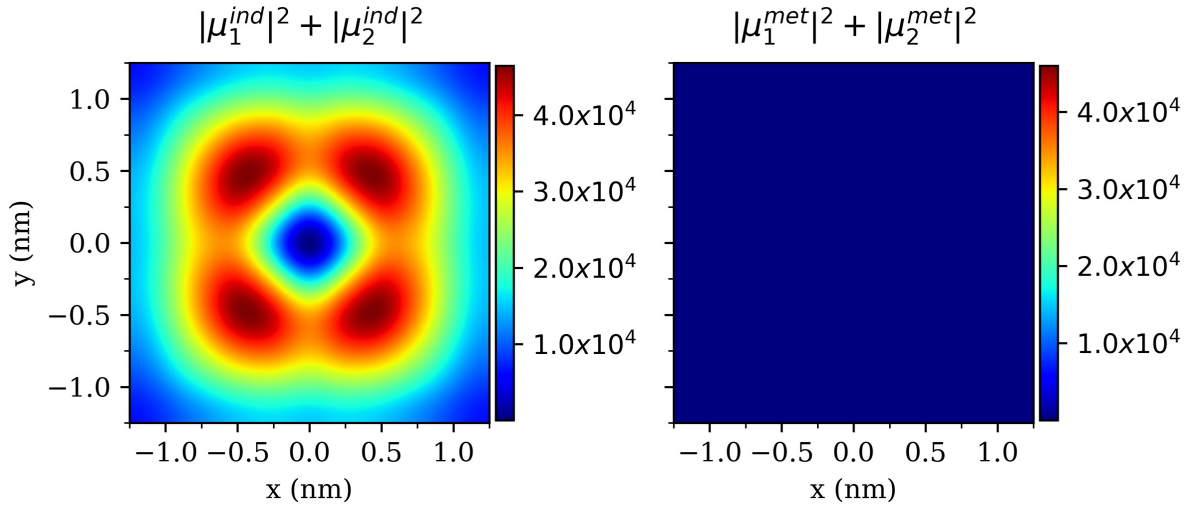

Figure S7: Detailed contribution of $\vec{\mu}^{ind}$ (left) and $\vec{\mu}^{met}$ (right) to the panel a) of Figure 8, main text. The contribution coming from the metallic response ($|\vec{\mu}^{ind}|^2$) is predominant, the molecular part($|\vec{\mu}^{met}|^2$) is ≈ 3 orders of magnitude lower. We also note that $\vec{\mu}^{met}$, which is the molecular transition dipole in the presence of the nanostructure, has been calculated by including in the typical TDDFT equations the following polarization term $K^{pol}_{st,uv}(\omega) = \sum_i q_\omega(s_i, [\psi^*_s \psi_t]) \cdot V(s_i, [\psi^*_u \psi_v])$, where $V(s_i, [\psi^*_u \psi_v])$ is the electrostatic potential evaluated at the i-th tessera due to the charge distribution $\psi^*_u \psi_v$ with ψ_u and ψ_v being molecular orbitals (more details can be found in[5,6]). The corresponding Casida response equations, that now account for the mutual molecule-metal polarization, have to be solved self-consistently as the matrix elements depend themselves on the eigenvalues that have to be found.

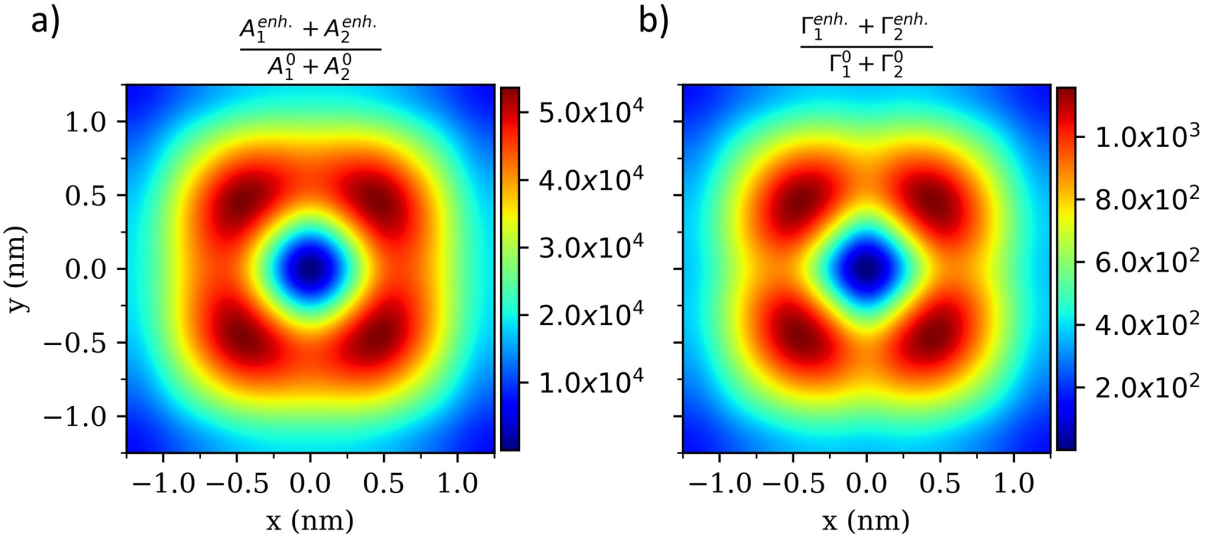

Figure S8: Comparison between enhanced absorption rate a) computed according to eq.10 (main text) and enhanced radiative decay rate b) computed according to eq.13 (main text). As stated in the main manuscript on page 7, even if the two quantities are analogous, they are calculated at different frequencies (that of the absorption and that of the emission, respectively) and for different transition densities (that at the ground state geometry a) and that at the excited state geometry b).

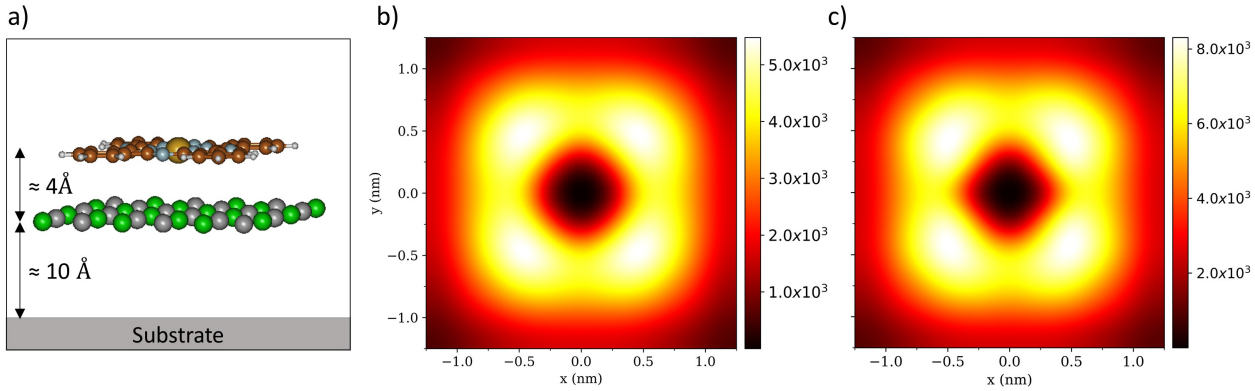

Figure S9: a) Scheme of the computational setup used to assess the influence of the NaCl layer on the simulated TEPL results. The single monolayer was directly included in the QM region fully treated at B3LYP/6-31g. The STM-like tip is not shown for simplicity, but it is always there, 0.4 nm above the molecular plane. The ground-state optimized geometry was considered both for the absorption and emission properties to save computational time, but as the excited-state minimum is very similar to the GS geometry (Figure S5), similar results are expected even considering the S_1 relaxed structure for the luminescence quantities. b) Simulated TEPL map with the presence of the NaCl single monolayer. c) Simulated TEPL map without the presence of the NaCl single monolayer. There is a fairly small quantitative difference in the TEPL intensity maxima between panels b) and c), but the overall result is qualitatively the same. In panel b) the intensity maximum is $\approx 5.5 \times 10^3$, whereas in panel c) it is $\approx 8.0 \times 10^3$.

References

[1] C. Dykstra, G. Frenking, K. Kim and G. Scuseria, *Theory and applications of computational chemistry: the first forty years*, Elsevier, 2011.

[2] M. W. Schmidt, K. K. Baldridge, J. A. Boatz, S. T. Elbert, M. S. Gordon, J. H. Jensen, S. Koseki, N. Matsunaga, K. A. Nguyen, S. Su *et al.*, *Journal of computational chemistry*, 1993, **14**, 1347–1363.

[3] B. Yang, G. Chen, A. Ghafoor, Y. Zhang, Y. Zhang, Y. Zhang, Y. Luo, J. Yang, V. Sandoghdar, J. Aizpurua, Z. Dong and J. G. Hou, *Nature Photonics*, 2020, **14**, 693–699.

[4] J. Savolainen, D. van der Linden, N. Dijkhuizena and J. L. Herek, *Journal of Photochemistry and Photobiology A: Chemistry*, 2008, **196**, 99–105.

[5] S. Corni and J. Tomasi, *The J. Chem. Phys.*, 2002, **117**, 7266.

[6] O. Andreussi, S. Corni, B. Mennucci and J. Tomasi, *J. Chem. Phys.*, 2004, **121**, 10190–10202.

Additional notes after thesis review

The non-hermitian matrix diagonalization and the charge normalization procedures that are discussed have been coded on an ad hoc basis for the specific system that is targeted. Coding has been performed in a development branch of the homemade code TDPlas, which will be merged with the master branch soon (freely available at `https://github.com/stefano-corni/WaveT_TDPlas`). The subroutine for photoluminescence calculations is instead already included in the master branch, therefore it is ready to be used by anyone.
Concerning the charge numerical issues that have been discussed, it has been found out that such numerical instabilities show up appreciably only when two or more nanostructures are simultaneously considered, and so in the case of a single nanoparticle no similar precautions have to be taken since the numerical solution of the PCM-NP problem turned out to be numerically robust and total charge neutralization is always ensured. This numerical artifact is not strictly related to the phenomenon that is investigated, photoluminescence in this case, but rather to the presence of more than a single nanostructure in the PCM-NP calculation.

Chapter 2.

Unraveling the Mechanism of Tip-Enhanced Molecular Energy Transfer

This chapter extends what has been reported in chapter 1 to an additional level of complexity. Indeed, the phenomenon that is here investigated still involves an STM plasmonic structure, but now two molecules are simultaneously considered. The presence of two nearby molecules in a STM junction opens up additional excited state relaxation processes, such as excitation energy transfer (EET) between an excited donor molecule and a nearby acceptor. This process can be described as a non-radiative phenomenon where an excited donor molecule can relax back to its ground state by transferring its energy to a nearby acceptor species, the latter being excited upon EET. In order for this process to take place energy conservation must be fulfilled and two alternative mechanisms, respectively named Förster and Dexter[1], are usually invoked to understand the physics behind the phenomenon. According to the Förster theory, the non-radiative transfer of energy is mediated via Coulombic interactions between the donor-acceptor pair and in its mostly-known form an analytical point-dipole model for the two molecules is considered. In other words, the Coulombic interaction is limited to dipole-dipole interactions and this leads to the well-known d^{-6} Förster distance dependence of efficiency of energy transfer with d being the dipole-dipole distance. On the other hand, according to the Dexter mechanism the transfer of energy takes places via an exchange of electrons between the two species and so it requires overlap of the two molecules wavefunctions. For this reason, the Dexter mechanism results in an exponential decay of energy transfer efficiency as a function of molecule-molecule distance and it usually becomes irrelevant for molecular separation above 1 nm[1, 2]. Above such distance EET can still take place only via Coulombic interactions, thus making the Förster mechanism the only plausible one.

The core idea underlying this chapter work is to assess the effect of the plasmonic system on the direct energy transfer process between chromophores placed close to atomistically sharp tips of STM junctions, such as those used for TEPL or STM-induced luminescence (STM-L) experiments. The latter involve tunneling electrons as excitation source instead of light photons. The accurate control over molecules spatial positions and orientations that is possible with these experimental setups paves the way for understanding how the energy flow can be steered through nanoscale plasmonic effects.

In this chapter, which is reported as a preprint article currently under review, the theoret-

ical modelling of plasmonic effects on EET is presented. This has been done by building on the previous work about TEPL (chapter 1), where plasmonic effects on single molecule excited state processes were already computationally addressed. The proposed theoretical framework is applied to investigate the energy transfer process between a palladium-phthalocyanine molecule (PdPc, donor) and a bare phthalocyanine molecule (H_2Pc, acceptor), upon excitation of the former by tunneling electrons. The same system has been experimentally probed recently[3], showing that the efficiency of energy transfer (RET_{eff}) between the two chromophores decreases very fast by enlarging the molecule-molecule separation, featuring an exponential decay. In that experimental work the Dexter mechanism of energy transfer was speculated to be responsible for such steep decrease of RET_{eff}. In this chapter, by quantitatively accounting for the role of the plasmonic system in mediating each excited state process, including EET, it is revealed that the usual criterion to distinguish between the widely-known mechanisms of energy transfer (, i.e. d^{-6} vs exponential decay) is no longer appropriate due to the relevance of nanoscale plasmonic effects taking place in such STM junctions, thus leading to very fast exponential-like decay of RET_{eff} even if only plasmon-mediated classical electromagnetic effects are considered.

Most of the simulations carried out in this work have been performed by Colin Coane, who has visited our group during his bachelor degree from the University of Southern California (USC). During Colin's stay I was in charge of supervising his work. I taught him how to perform quantum chemistry calculations in the presence of the plasmonic system and I also showed him how to elaborate the output of such calculations to evaluate the effect of the plasmonic system in mediating molecular decay processes, including EET. In this regard, we together started creating a python post-processing tool that he further developed on his own to finally produce the data that is reported in the manuscript. We equally contributed to the writing of the initial article draft, whereas Colin prepared most of the figures. I personally drafted the first version of the reply letter to reviewers, while he performed additional simulations necessary to revise the manuscript.

This work has been recently published in *Communications Chemistry*[4] (note added after thesis review).

References

(1) Olaya-Castro, A.; Scholes, G. D. *International Reviews in Physical Chemistry* **2011**, *30*, 49–77.

(2) May, V.; Kühn, O., *Charge and energy transfer dynamics in molecular systems*; John Wiley & Sons: 2023.

(3) Cao, S.; Rosławska, A.; Doppagne, B.; Romeo, M.; Féron, M.; Chérioux, F.; Bulou, H.; Scheurer, F.; Schull, G. *Nature Chemistry* **2021**, *13*, 766–770.

(4) Coane, C. V.; Romanelli, M.; Dall'Osto, G.; Di Felice, R.; Corni, S. *Communications Chemistry* **2024**, *7*, 32.

Unraveling the Mechanism of Tip-Enhanced Molecular Energy Transfer

Colin V. Coane[1,2], Marco Romanelli[1], Giulia Dall'Osto[1], Rosa Di Felice[2,*], and Stefano Corni[1,3,*]

[1]Department of Chemical Sciences, University of Padova, via Marzolo 1, Padova, Italy
[2]Department of Physics and Astronomy, University of Southern California, Los Angeles, CA, 90089, USA
[3]CNR Institute of Nanoscience, via Campi 213/A, Modena, Italy
[*]Corresponding authors: difelice@usc.edu; stefano.corni@unipd.it

ABSTRACT

Electronic Energy Transfer (EET) between chromophores is fundamental in many natural light-harvesting complexes, serving as a critical step for solar energy funneling in photosynthetic plants and bacteria. The complicated role of the environment in mediating this process in natural architectures has been addressed by recent scanning tunneling microscope experiments involving EET between two molecules supported on a solid substrate. These measurements demonstrated that EET in such conditions has peculiar features, such as a steep dependence on the donor-acceptor distance, reminiscent of a short-range mechanism more than of a Förster-like process. By using state of the art hybrid ab initio/electromagnetic modeling, here we provide a comprehensive theoretical analysis of tip-enhanced EET. In particular, we show that this process can be understood as a complex interplay of electromagnetic-based molecular plasmonic processes, whose result may effectively mimic short range effects. Therefore, the established identification of an exponential decay with Dexter-like effects does not hold for tip-enhanced EET, and accurate electromagnetic modeling is needed to identify the EET mechanism.

Introduction

Probing and controlling Electronic Energy Transfer (EET) between chromophores in complex environments has drawn increased scientific attention over the last few decades. The EET process is crucial in many natural light-harvesting complexes[1–3] and is a critical step in photosynthesis[4–7], thus making it extremely interesting and potentially useful for developing devices for human use[8–11]. Because photosynthetic complexes operate surrounded by a natural or artificial environment, understanding the role of this environment in their activity is essential, including its influence on EET. This is an arduous task, and in the case of natural architectures, the systems under investigation are so complex that disentangling the various contributions affecting the overall EET efficiency is far from trivial[12–15]. Nonetheless, the process itself primarily relies on the interactions between distinct molecular species, thus making single-molecule experiments vital for dissecting the EET process and eventually shedding light on how it can be controlled. Experiments on self-standing single molecules are limited by their ability to detect optical signals due to diffraction limits and weak molecular luminescence responses.[16,17] Therefore, a promising strategy developed for investigating energy transfer processes is based on utilizing metal-molecule-metal junctions to confine optical signals in a small region, enhancing molecular responses.[18–22]

Recent works[23–29] disclose how scanning tunneling microscopy (STM) may be used to effectively probe single-molecule fluorescence by cleverly harnessing tip surface plasmons. This approach leads to strong photoluminescence (tip-enhanced photoluminescence, TEPL) and electroluminescence (STM-induced luminescence, STML) signals of individual molecules placed underneath an atomistic, metallic STM tip, even reaching sub-molecular resolution in certain cases[29]. Experiments of this kind pave the way for real-space tracking of energy transfer between nearby molecules[30,31]. For instance, Cao et al.[30] utilized tip-molecule-substrate junctions to detect the energy flow between different chromophores while accurately controlling their spatial position. Experiments were carried out in ultra-high vacuum at low temperature (4.5 K) and molecules were deposited on a NaCl trilayer placed on top of a silver metallic substrate. By measuring light intensity emitted by donor (D) and acceptor (A) molecules upon selective excitation of the former via tunneling electrons, they could quantitatively probe the energy transfer process. They showed that the efficiency of EET (denoted RET_{eff} in their work[30], for resonance energy transfer) between a palladium-phthalocyanine (PdPc) donor molecule and a free-base phthalocyanine (H_2Pc) acceptor molecule exhibits a fast, exponential-like decay trend as a function of the donor-acceptor (D-A) distance. This measured exponential trend cannot be explained in terms of simple dipole-dipole interactions (Förster theory)[32–34], indicating a more thorough theoretical description of the system is needed to decipher experimental data. In addition to the features of the system that are usually employed to explain EET processes such as the spectral overlap, D-A distance, and the orientation between D-A dipole

moments,[35–37] environmental effects cannot be ignored, and in particular the effect of the metallic nanostructure used to scan the system studied must be accounted for to explain the measured decay trend. The scanning tip can induce new decay pathways and modify existing ones, including the energy transfer process itself.[38–40] Careful attention to the nanostructure's physical features and geometry is required, since tuning its plasmonic frequency may either augment or hinder the EET process.[41–48]

In the following, we present a comprehensive theoretical framework for a nanostructure-donor-acceptor system, which is able to describe the tip-mediated EET rate along with radiative and non-radiative relaxation processes. This framework allows us to shed light on the experimental results described above. This study builds on the previously developed Polarizable Continuum Model-NanoParticle (PCM-NP) approach and related works[2,49–56], which rely on an ab initio quantum mechanical description of molecules interacting with classically-described metallic nanostructures. The theoretical model introduced here allows us to go beyond the dipole-dipole interaction model by including a thorough description of the molecular electronic structure, utilizing full electron densities and including effects on molecular decay pathways induced by the metallic STM tip. Similar approaches that have been used in this context have shown that a proper ab initio description of target molecules in such sophisticated plasmonic structures is necessary to fully capture subtle plasmon-molecule interactions that can be revealed by experiments targeting sub-molecular resolution[57–61]. With regard to EET in STM junctions, Kong et al.[31] have recently shown that for D-A distances > 1.7 nm, the use of full transition densities instead of the dipole-dipole approximation to evaluate the direct (metal free) D-A EET rate still leads to an R^{-6} Förster-like dependence of the acceptor emission intensity upon donor tunneling excitation, which only approximately matches the experimental trend that is observed. In their modelling, the effect of the plasmonic system in mediating molecular decay pathways (including EET) is not included. Notably, we find here that the effect of the metal on the molecular decay rates in systems coupled to a metallic nanostructure is not negligible over a wide range of intermolecular distances[49,51,62–64]. Quite surprisingly, our calculations show how the proper accounting of all the relevant molecule-metal and molecule-molecule electromagnetic interaction pathways results in a trend that deceptively mimics an exponential decay. In other words, we disclose a situation where the popular criterion to distinguish between Förster-like and Dexter-like energy transfer mechanisms is no longer appropriate due to the relevance of plasmonic nanoscale effects occurring in tip-molecule-substrate STM junctions.

Results

Metal mediated RET efficiency

In the experimental work of Cao et al.[30], the definition of "RET efficiency", $\mathrm{RET_{eff}}$, is based on emission intensities of the acceptor (I_A) and donor molecules (I_D) upon excitation of the donor,

$$\mathrm{RET_{eff}} = \frac{I_\mathrm{A}}{I_\mathrm{A} + I_\mathrm{D}}. \tag{1}$$

However, we highlight that the above quantity $\mathrm{RET_{eff}}$ does not depend only on the theoretical efficiency of the EET step unless special restrictive conditions are met, such as the donor and acceptor molecules being identical, ideal emitters.

More generally, such empirical energy transfer efficiency depends on multiple radiative and nonradiative decay processes within the system, and the presence of the metallic tip may influence and modify these processes, as schematically illustrated in Figure 1.

Given the fluorescence quantum yield of the donor Φ_D, its emission intensity reads

$$I_\mathrm{D} = \Gamma_\mathrm{ex} \cdot \Phi_\mathrm{D} = \Gamma_\mathrm{ex} \cdot \frac{\Gamma_\mathrm{rad,D}}{\Gamma_\mathrm{EET} + \Gamma_\mathrm{rad,D} + \Gamma_\mathrm{nr,met,D} + \Gamma_\mathrm{nr,0,D}} \tag{2}$$

where Γ_ex is the excitation rate (in this case promoted by tunneling electrons), $\Gamma_\mathrm{rad,D}$ is the radiative decay rate of the donor in presence of the metal tip, $\Gamma_\mathrm{nr,met,D}$ is the nonradiative decay rate induced by the metal tip, $\Gamma_\mathrm{nr,0,D}$ is the intrinsic, purely-molecular nonradiative decay rate, and Γ_EET is the EET rate from the donor to the acceptor, which is also modified by the presence of the metal tip.

On the other hand, the emission intensity of the acceptor, assuming that the donor undergoes EET to the acceptor upon excitation, is:

$$I_\mathrm{A} = \Gamma_\mathrm{ex} \cdot \eta_\mathrm{EET} \cdot \Phi_\mathrm{A} = \Gamma_\mathrm{ex} \cdot \frac{\Gamma_\mathrm{EET}}{\Gamma_\mathrm{EET} + \Gamma_\mathrm{rad,D} + \Gamma_\mathrm{nr,met,D} + \Gamma_\mathrm{nr,0,D}} \cdot \frac{\Gamma_\mathrm{rad,A}}{\Gamma_\mathrm{rad,A} + \Gamma_\mathrm{nr,met,A} + \Gamma_\mathrm{nr,0,A}}, \tag{3}$$

where $\Gamma_\mathrm{rad,A}$, $\Gamma_\mathrm{nr,0,A}$ and $\Gamma_\mathrm{nr,met,A}$ are the radiative decay rate, intrinsic nonradiative decay rate, and metal-induced nonradiative decay rate of the acceptor, respectively. We note that the quantity η_EET is the general theoretical definition of the efficiency of EET from the donor to the acceptor.

Equations 2 and 3 assume only one donor state and one acceptor state, which is a good approximation in the absence of degenerate excited states. However, for the donor molecule (palladium-phthalocyanine, PdPc) the first two excited states

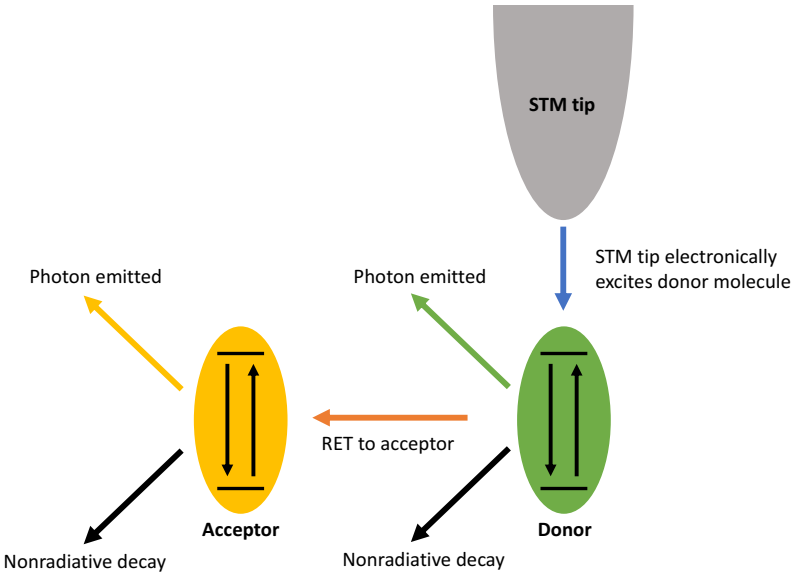

Figure 1. Schematic diagram of energy transfer processes in the STM-donor-acceptor system. The STM tip excites the donor molecule through a tunneling current, and the donor may decay to its ground state radiatively, nonradiatively, or through EET to the acceptor. If the acceptor is excited through EET, it subsequently may decay to its ground state radiatively or nonradiatively. The excitation energy of the donor's first excited state is larger than that of the acceptor's, which typically prevents energy flow back to the donor. All possible decay processes in both donor and acceptor are affected by the presence of the metallic tip. Indeed, the tip may not only modify the radiative emission of each emitter, but also provides an additional source of nonradiative decay for the molecular excited states.

are degenerate, so they both may be excited by the tip and participate in the EET process. Moreover, the acceptor molecule (free-base phthalocyanine, H_2Pc) has two excited states that are close in energy and may both be excited by EET from the donor. To account for these degeneracies, we consider the emission intensity of the donor from state i, namely

$$I_{\mathrm{D}}^{\mathrm{i}} = \Gamma_{\mathrm{ex}}^{\mathrm{i}} \cdot \Phi_{\mathrm{D}}^{\mathrm{i}} = \Gamma_{\mathrm{ex}}^{\mathrm{i}} \cdot \frac{\Gamma_{\mathrm{rad,D}}^{\mathrm{i}}}{\sum_{\mathrm{j}} \Gamma_{\mathrm{EET}}^{\mathrm{i}\to\mathrm{j}} + \Gamma_{\mathrm{rad,D}}^{\mathrm{i}} + \Gamma_{\mathrm{nr,met,D}}^{\mathrm{i}} + \Gamma_{\mathrm{nr,0,D}}}, \tag{4}$$

where the index i indicates the i-th excited state of the donor, and the index j indicates the j-th excited state of the acceptor.

Likewise, the total acceptor emission intensity after tip-induced excitation of donor state i ($I_{\mathrm{A}}^{\mathrm{i}}$) is the sum over emission intensities from possible acceptor states j, after EET between donor state i and acceptor state j,

$$I_{\mathrm{A}}^{\mathrm{i}} = \Gamma_{\mathrm{ex}}^{\mathrm{i}} \cdot \sum_{j} \eta_{\mathrm{EET}}^{\mathrm{i}\to\mathrm{j}} \cdot \Phi_{\mathrm{A}}^{\mathrm{j}}, \tag{5}$$

where $\Phi_{\mathrm{A}}^{\mathrm{j}}$ is the j-th state emission quantum yield of the acceptor, as defined by the third term in Eq. 3. Thus, the net RET efficiency, as defined in Eq. 1, for a given donor state i becomes

$$(\mathrm{RET_{eff}})^{\mathrm{i}} = \frac{\sum_{\mathrm{j}} \eta_{\mathrm{EET}}^{\mathrm{i}\to\mathrm{j}} \cdot \Phi_{\mathrm{A}}^{\mathrm{j}}}{\sum_{\mathrm{j}} \eta_{\mathrm{EET}}^{\mathrm{i}\to\mathrm{j}} \cdot \Phi_{\mathrm{A}}^{\mathrm{j}} + \Phi_{\mathrm{D}}^{\mathrm{i}}} \tag{6}$$

as excitation rates $\Gamma_{\mathrm{ex}}^{\mathrm{i}}$ cancel out.

This quantity in Eq. 6 can be evaluated experimentally from the emission intensities considered above. It can also be theoretically obtained from the decay properties of the donor and acceptor molecules alone. Substituting the expressions of $\eta_{\mathrm{EET}}^{\mathrm{i}\to\mathrm{j}}, \Phi_{\mathrm{D}}^{\mathrm{i}}, \Phi_{\mathrm{A}}^{\mathrm{j}}$ into Eq. 6, it is possible to formulate the RET efficiency directly in terms of decay rates,

$$(\mathrm{RET_{eff}})^{\mathrm{i}} = \left(1 + \Gamma_{\mathrm{rad,D}}^{\mathrm{i}} \cdot \left[\sum_{\mathrm{j}} \frac{\Gamma_{\mathrm{EET}}^{\mathrm{i}\to\mathrm{j}} \cdot \Gamma_{\mathrm{rad,A}}^{\mathrm{j}}}{\Gamma_{\mathrm{rad,A}}^{\mathrm{j}} + \Gamma_{\mathrm{nr,met,A}}^{\mathrm{j}} + \Gamma_{\mathrm{nr,0,A}}}\right]^{-1}\right)^{-1}. \tag{7}$$

Eq. 7 reveals that the RET efficiency upon exciting the i-th donor state is independent of all nonradiative decay properties of the donor, and has the functional form

$$\frac{1}{1+f} \tag{8}$$

where f is a complicated function that depends on the EET rate from donor to acceptor, radiative decay rate of the donor and all decay rates of the acceptor.

Within the PCM-NP framework (see Methods), each of the quantities described in this section can be analytically or numerically determined, retaining a realistic electronic structure description of both donor and acceptor molecules at the ab initio level. The EET rate between molecules in the presence of a metallic nanostructure is given by[46]

$$\Gamma_{\mathrm{EET}} = \frac{2\pi}{\hbar} |V_0 + V_{\mathrm{met}}|^2 J, \tag{9}$$

where J is the spectral overlap factor, V_0 is the electronic coupling between donor and acceptor in vacuum, and V_{met} is the coupling mediated by the metal nanostructure. V_0 is calculated as the volume integral over the molecular transition densities of the donor and acceptor ($\rho_{\mathrm{X}}^{\mathrm{T}}$)[65], thus

$$V_0 = \int \rho_{\mathrm{A}}^{\mathrm{T}}(\vec{\mathbf{r}})\rho_{\mathrm{D}}^{\mathrm{T}}(\vec{\mathbf{r}}')\frac{1}{|\vec{\mathbf{r}}-\vec{\mathbf{r}}'|}\mathrm{d}\vec{\mathbf{r}}\mathrm{d}\vec{\mathbf{r}}' + \int \rho_{\mathrm{A}}^{\mathrm{T}}(\vec{\mathbf{r}})\rho_{\mathrm{D}}^{\mathrm{T}}(\vec{\mathbf{r}}')g_{\mathrm{xc}}(\vec{\mathbf{r}},\vec{\mathbf{r}}')\mathrm{d}\vec{\mathbf{r}}\mathrm{d}\vec{\mathbf{r}}' - \omega_0 \int \rho_{\mathrm{A}}^{\mathrm{T}}(\vec{\mathbf{r}})\rho_{\mathrm{D}}^{\mathrm{T}}(\vec{\mathbf{r}})\mathrm{d}\vec{\mathbf{r}}, \tag{10}$$

where g_{xc} is the exchange-correlation kernel and the third term in the right-hand side is the overlap between molecular transition densities weighted by the transition energy. Transition densities for donor emission and acceptor absorption are used instead of dipolar or multipolar approximations to take into account the charge distribution within each molecule during electronic excitations.

V_{met} is expressed in terms of response charges q_{k} located at the centroid of each k-th tessera on the metal's surface induced by the donor transition potential.[46] Response charges are multiplied by the acceptor transition potential evaluated at the same spatial coordinates,

$$V_{\mathrm{met}} = \sum_{\mathrm{k}\in\mathrm{met}} \left(\int \rho_{\mathrm{A}}^{\mathrm{T}}(\vec{\mathbf{r}}) \frac{1}{|\vec{\mathbf{r}}-\vec{\mathbf{s}}_{\mathrm{k}}|}\mathrm{d}\vec{\mathbf{r}} \right) q_{\mathrm{k}}\left(\vec{\mathbf{s}}_{\mathrm{k}}, \varepsilon_{\mathrm{met}}(\omega), \rho_{\mathrm{D}}^{\mathrm{T}}\right) \tag{11}$$

with $\varepsilon_{\mathrm{met}}(\omega)$ being the nanostructure's frequency-dependent dielectric function that enters Eq. 17.

As reported in previous work, the radiative decay rate of the donor and acceptor in a generic state b, $\Gamma_{\mathrm{rad,X}}^{\mathrm{b}}$ (with X=A,D), in the presence of the metal nanostructure can be evaluated in terms of the sum of the molecular transition dipole in the presence of the metal $\vec{\boldsymbol{\mu}}_{\mathrm{met,X}}^{\mathrm{b}}$ and the dipole induced in the nanostructure by the molecular transition density $\vec{\boldsymbol{\mu}}_{\mathrm{ind,X}}^{\mathrm{b}}$[53]

$$\Gamma_{\mathrm{rad,X}}^{\mathrm{b}} = \frac{4\omega_{\mathrm{b,X}}^3}{3\hbar c^3} \left| \vec{\boldsymbol{\mu}}_{\mathrm{met,X}}^{\mathrm{b}} + \vec{\boldsymbol{\mu}}_{\mathrm{ind,X}}^{\mathrm{b}} \right|^2. \tag{12}$$

Additionally, the nonradiative decay rate in the presence of the metal is determined by the imaginary part of the self-interaction between surface response charges and transition potentials evaluated at the same k-th tessera[52] on the metal's surface, that is

$$\Gamma_{\mathrm{nr,met,X}}^{\mathrm{b}} = -2 \cdot \mathrm{Im}\left\{ \sum_{\mathrm{k}} q_{\mathrm{k}} V_{\mathrm{k}} \right\}. \tag{13}$$

On a final note, the intrinsic nonradiative decay rate of the acceptor that enters Eq. 7 ($\Gamma_{\mathrm{nr,0,A}}$) is not readily available, but it can be roughly estimated from the vacuum radiative quantum efficiency $\eta_{0,\mathrm{A}}$[49]

$$\eta_{0,\mathrm{A}} = \frac{\Gamma_{\mathrm{rad,0,A}}}{\Gamma_{\mathrm{rad,0,A}} + \Gamma_{\mathrm{nr,0,A}}}. \tag{14}$$

Since $\Gamma_{\mathrm{rad,0,A}}$ can be evaluated considering only the vacuum molecular dipole, $\Gamma_{\mathrm{nr,0,A}}$ may be computed if $\eta_{0,\mathrm{A}}$ is accessible[49]. Experimental data of radiative quantum efficiency are only available in solution, so for this work we use the solution value $\eta_{0,\mathrm{A}} = 0.6$ for H_2Pc as reported in ref. 66. While H_2Pc is studied here in dry conditions, the same assumption was adopted in a previous work[49] where it was also shown for a similar molecule (ZnPc) that the intrinsic nonradiative decay rate is significantly smaller than other metal-mediated decay rates involved in the process, thus not affecting results whether or not it is included.

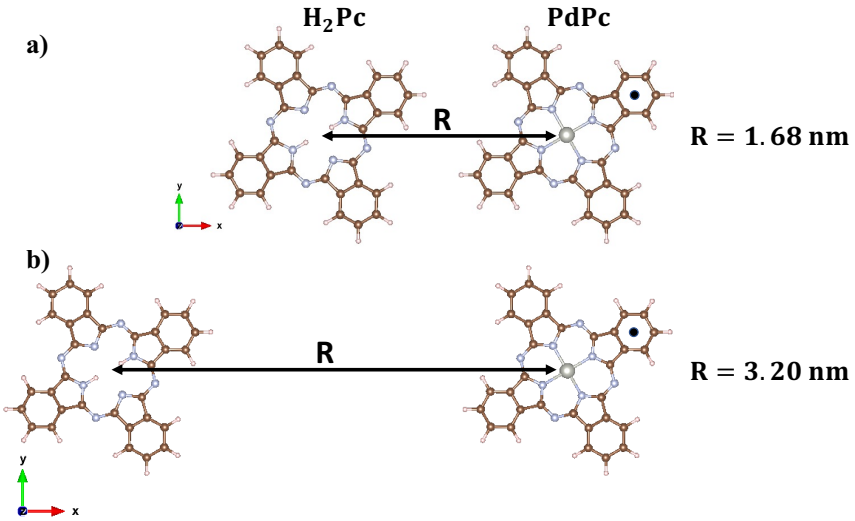

Figure 2. Geometrical configuration of PdPc and H_2Pc molecular structures. PdPc (donor) and H_2Pc (acceptor) molecules shown at center-center distances of 1.68 nm (a) and 3.20 nm (b). Aromatic lobes of both molecules are oriented 30 degrees from the x and y axes, as shown. The relative orientation between donor and acceptor is kept rigid throughout the samples separation range.

Investigated systems

The chromophores studied here in the presence of an STM tip are a palladium-pthalocyanine (PdPc) donor and a free-base pthalocyanine (H_2Pc) acceptor. The two molecules were situated with their aromatic lobes co-planar, lying on the plane that we hereby denote as the xy plane, and treated at the quantum level using Density Functional Theory (DFT) and Time-Dependent Density Functional Theory (TDDFT) when excited state properties are needed. Within the xy plane, the aromatic lobes of each molecule are rotated by 30 degrees from the x and y axes, roughly mimicking the orientation shown by previous experimental STM images[30]. Different D-A distances in the range 1.59-3.20 nm have been investigated to characterize the effect of molecular separation on RET (Figure 2). Further information related to ab initio calculations and EET modelling based on Eqs.1-13 can be found in Computational Details.

Regarding the plasmonic system, two different STM setups were considered to model the tip-molecule-substrate nanojunctions, illustrated in Figure 3. One setup was based on a previous STML experimental study[28]: a silver tip was modeled as a truncated cone with rounded edges, with the molecular species adsorbed on a silver cylindrical substrate (Figure 3a). In the referenced experiment, a three-layer NaCl spacer was placed as a buffer between the metal substrate and the molecules. This insulating buffer was omitted in our calculations, as previous studies revealed it contributes minimally to the observed molecular response[29,49]. For this geometry, the tip was located 2.0 nm above the substrate to generate a nanocavity hosting the donor molecule, which itself sat 0.5 nm below the tip and 1.5 nm above the substrate. The second setup considered was used in previous single-molecule TEPL calculations[49] and consists of a much larger STM tip with an atomistic protrusion at its apex (Figure 3b). For this case, the tip-molecule vertical separation was set to 0.4 nm and molecule-substrate separation to 1.4 nm.

Following previous works[28,67] and exploiting the knowledge that the experimentally applied bias voltage is negative[30], we assume that tunneling excitation is achieved by initial electron withdrawal from the donor HOMO orbital by the STM tip. Subsequent electron injection into the LUMO or LUMO+1 takes place via the substrate with equal probability, because the LUMO and LUMO+1 are degenerate and there is no justifiable reason why the substrate should prefer one over the other (both orbitals are equally diffused over the substrate surface). As a result of this, both S_1 (HOMO $\rightarrow$ LUMO) and S_2 (HOMO $\rightarrow$ LUMO+1) degenerate excited states of PdPc can become equally populated upon tunneling, and each state can couple to either one of the first two excited states of the acceptor. This translates to summing over the index i in Eq. 6 to obtain the full $\mathrm{RET_{eff}}$ reported below,

$$\mathrm{RET_{eff}} = \frac{\sum_i I_A^i}{\sum_i \left(I_A^i + I_D^i\right)} \tag{15}$$

Two different tip positions were tested, as shown in Figure 4a (labeled black dots 1,2), where the tip apex is either placed above the middle of one peripheral aromatic ring or above the center of a nearby molecular orbital lobe, respectively. In Supplementary Figure 1 we show that the main results discussed hereafter are not sensitive to this change in the tip position.

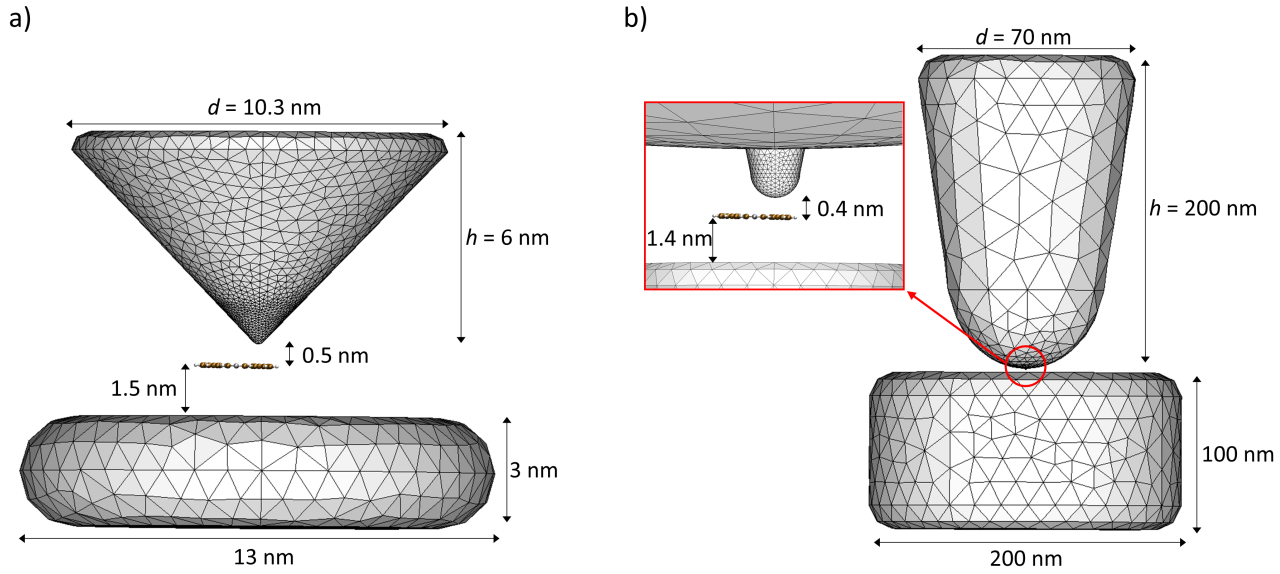

Figure 3. Computational models of the STM structures. a) Nanojunction model employed in EET calculations, based on a previous experimental STML study[28]. Both tip and substrate are made of silver. The tip has a terminal spherical curvature of radius 0.2 nm. b) Alternative nanojunction model employed in EET calculations, taken from a previous computational TEPL work[49]. Both tip and substrate are made of silver. The tip features an atomistic protrusion (close-up, red box) with a base radius of 0.6 nm and a radius of 0.5 nm for the terminal spherical cap. In both panels (a-b) only the PdPc (donor) molecule is shown and it is placed such that the corresponding tip edge is directly above one hexagonal lobe (see also Figure 2, black dots).

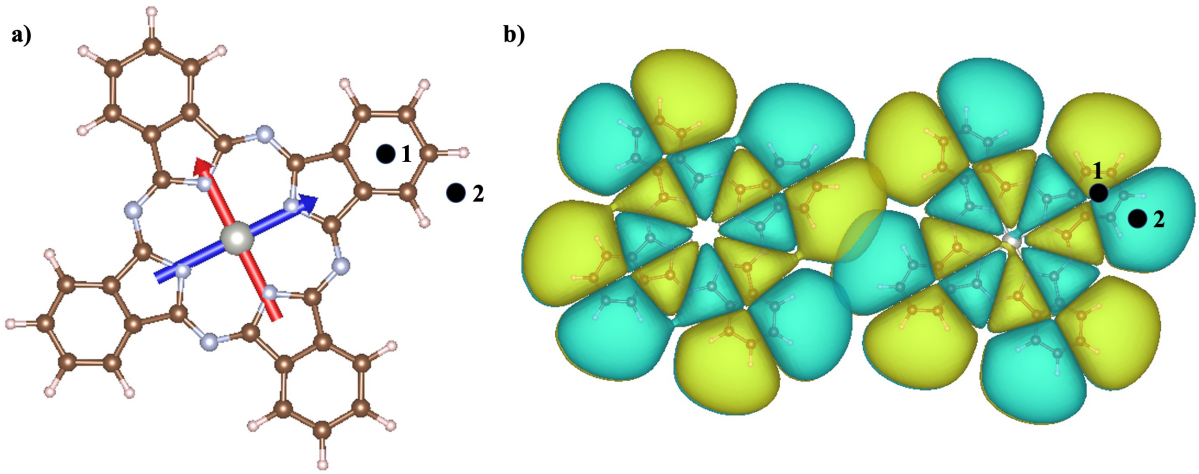

Figure 4. Molecular structures and properties. a) Transition dipoles of the first two excited states of the donor molecule PdPc, overlaid on its atomic structure. The black dots correspond to two different locations of the STM tip apex above the molecule, which have been sampled in this work. b) Computed HOMO density of both donor and acceptor molecules, displaying overlap between the two.

Since the plasmonic absorption peak of the two metallic tips was not on-resonance with the excitation frequencies of the donor and acceptor (see Figure 5), additional calculations were performed to study the effect of the nanostructure plasmonic resonance peak's location on RET. In doing so, the response of the metal, i.e. the response charges and related quantities of Eqs. 11,12,13, were evaluated at different frequencies to model cases in which the donor and acceptor energies were detuned with respect to the plasmonic peak frequency. To do so, donor and acceptor excitation frequencies were shifted by a constant value, keeping the difference between the two the same, $\omega_{\mathrm{DA}} = \omega_{\mathrm{D}} - \omega_{\mathrm{A}} \approx 2.11 - 2.02 = 0.09$ eV. This forced frequency shift is illustrated in Figure 5 (see vertical colored lines), and was done for various frequencies such that: I. the donor frequency

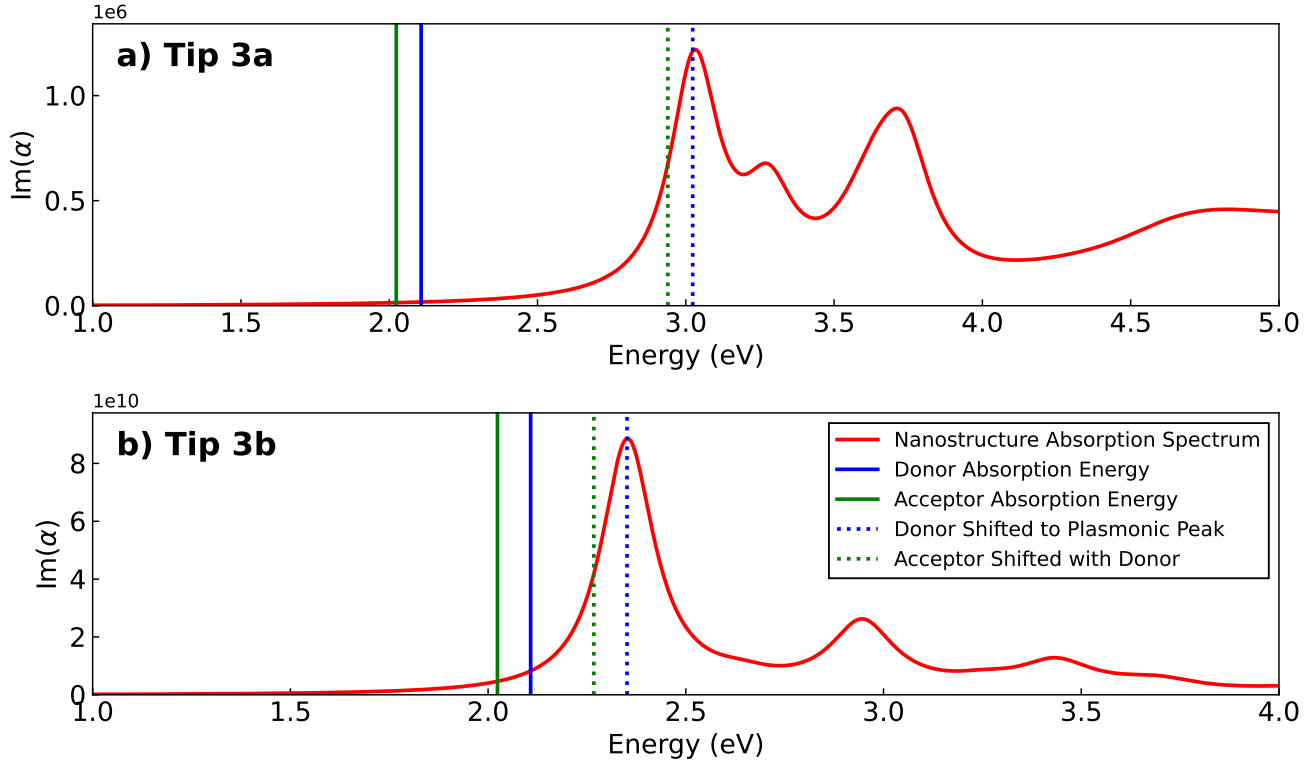

Figure 5. Optical response of the STM structures. (a-b) Optical absorption spectra of the STM-like silver tips of Figures 3(a-b), computed with the Brendel-Bormann fitting model of the silver dielectric function[68]. The plotted quantity is the imaginary part of the frequency-dependent polarizability $\alpha(\omega)$, which is proportional to the absorption cross-section. $\mathrm{Im}[\alpha(\omega)]$ was obtained from the electric dipole induced in the corresponding nanostructure upon excitation by an electric field polarized along the tip's z axis (corresponding to the tip central axis). The green (blue) solid line represents the absorption energy of the first excited state of the acceptor (donor). As mentioned previously, the donor's first and second excited states are degenerate, while the acceptor's are close in energy, both of which were considered in EET calculations. Here, only the lowest excited state of the acceptor is plotted for clarity. The green and blue dashed lines represent the excitation energies rigidly shifted so that the donor transition is on resonance with the nanostructure plasmonic peak at 3.02 eV for tip 3a and 2.35 eV for tip 3b. Source data for panels a-b can be found in Supplementary Data 1.

matched the tip's plasmonic peak ($\omega_{\mathrm{D}} = 3.02$ eV for tip 3a and 2.35 eV for tip 3b), II. the acceptor frequency matched the plasmonic peak ($\omega_{\mathrm{A}} = 3.02$ eV for tip 3a and 2.35 eV for tip 3b), and III. (IV.) the donor and acceptor frequencies were both below (above) the tip's plasmonic response to fully characterize its effect on EET (see Figure 6). We remark that in doing so, the donor or acceptor frequency entering Eq. 12 is always the proper molecular one obtained by TDDFT calculations. This means the shifting procedure just mimics results which would have been obtained using the same molecules (same absorption frequencies) but with a different, shifted metallic response, therefore serving as a proxy for modifying the tip's characteristics.

Numerical evaluation of $\mathrm{RET}_{\mathrm{eff}}$ and comparison with experiments

In the quasistatic limit, the absorption cross section of a given metallic nanostructure is related to the imaginary part of its frequency-dependent polarizability, $\mathrm{Im}[\alpha(\omega)]$, which can be computed from the dipole induced in the nanostructure upon excitation by an external electric field. In Figure 5 we plot the frequency-dependent polarizability for the STM tips of Figure 3 excited by an electric field polarized along the corresponding tip longitudinal axis (z axis). Absorption energies of the PdPc and H_2Pc molecules are overlaid on Figure 5, and we remark that both donor and acceptor excitation energies (solid green and blue lines) computed with TDDFT are off-resonance with respect to the first bright plasmonic peaks of the nanostructures. However, it was previously shown for similar structures that the plasmonic peak energies are quite sensitive to the choice of the dielectric function model and to detailed geometrical features of the tip which are experimentally unknown[49]. Thus, it is important to assess the impact of the frequency-dependent response of the metal tip on the EET process.

To address this, we performed calculations of relevant frequency-dependent quantities and evaluated the RET efficiency at

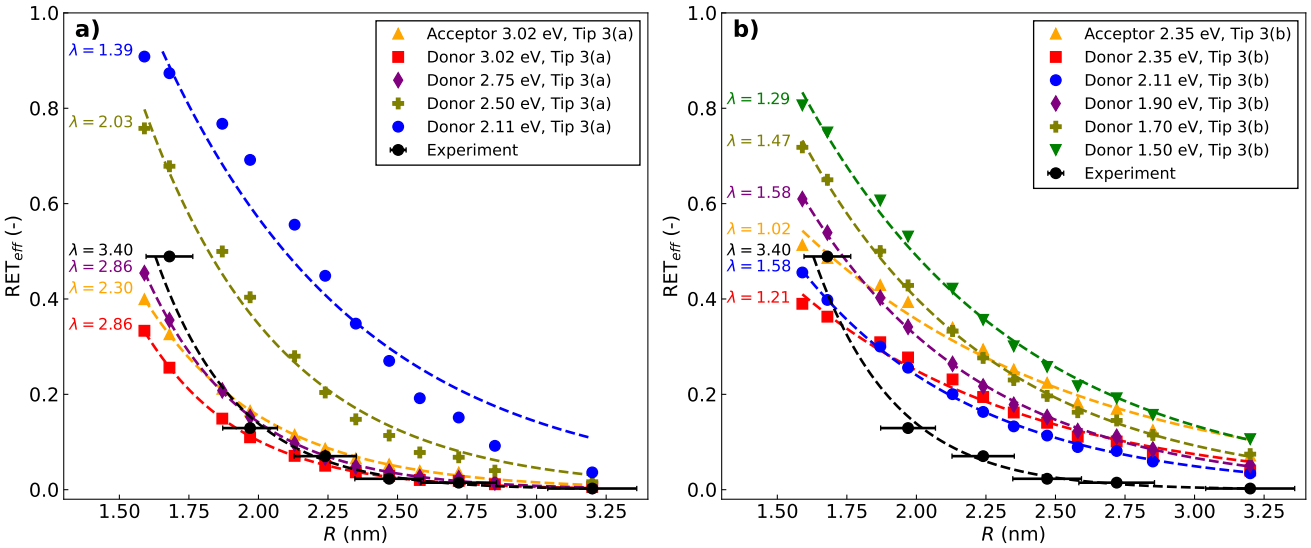

Figure 6. Efficiency of energy transfer. (a) RET efficiency as a function of the distance between the centers of donor (PdPc) and acceptor (H_2Pc) molecules computed with Eq. 1 (see also Eqs. 2-7,15) in the presence of the nanostructure of Figure 3a. Results are compared with experimental data obtained from ref. 30 (black dots with error bar). The RET_{eff} was evaluated with the donor excitation energy set to: 2.11 eV (unmodified case, dashed blue line), 2.50 eV (dashed olive-green line), 2.75 eV (dashed purple line), and 3.02 eV (i.e., on resonance with the brightest plasmonic peak, dashed red line). Additionally, the RET_{eff} was evaluated with the acceptor excitation energy on-resonance with the brightest plasmonic transition (dashed yellow line). More details on how this frequency-shift procedure was implemented are given in the Investigated Systems section. Each RET curve has been fitted with an exponential decay function, $RET_{eff}(R) = A_0 e^{-\lambda R}$. For each data set, including experimental data[30], the exponential fitting curve is plotted and the spatial exponential decay constant λ is indicated to the left of the corresponding curve. (b) Similar analysis and RET_{eff} curves obtained in the presence of the tip of Figure 3b. In this case the plasmonic peak resonance is located at 2.35 eV. See also Figure 5 for a direct comparison of the two tips absorption spectra. Source data for panels a-b can be found in Supplementary Data 1.

different excitation frequencies of the donor and acceptor. Such quantities include the frequency-dependent response charges of the tip (Eqs. 16) and the related metal-affected properties given in Eqs. 11-13, which appear in the theoretical expression of the RET efficiency (Eqs. 6-7,15). Computational results are presented in Figure 6 for the two tip structures of Figure 3, along with experimental data from ref. 30. We find that in all theoretical calculations, $\mathrm{RET_{eff}}$ decreases monotonically with the distance between molecules, similar to observed trends in the experimental data.

Upon observation, it was found that each curve of computed $\mathrm{RET_{eff}}$ as a function of distance can be accurately fitted with a simple exponential decay function, $\mathrm{RET_{eff}}(R) = A_0 \mathrm{e}^{-\lambda R}$, as shown in Figure 6. This effective exponential decay trend is not obvious in the theoretical expression for RET efficiency, but correctly matches trends observed in experiments which could not be explained previously[30]. Indeed, in these experiments it was noted that the observed fast decay of RET with D-A distance could not be understood in terms of simple dipole-dipole interactions (Förster mechanism), and it was speculated that both multipolar RET and Dexter-like energy transfer may be possible explanations for the observed behavior. The finding that a combination of purely electromagnetic effects may mimic an exponential decay with distance is the main result of this present work. The shape of the decay curve is universally used to classify Förster versus Dexter EET mechanisms, and we show here that in case of tip-mediated EET, such a simple indicator cannot be reliably used.

Although the simulated decay of $\mathrm{RET_{eff}}$ has a somewhat smaller spatial decay parameter λ than in experiments, we are able to reproduce the same qualitative exponential trend in terms of bare electrostatic interactions that are combined in a complex manner according to Eq. 6. In fact, the computed exponential trend matches the experimental data when the tip structure of Figure 3a is used and the donor is close to the resonance condition (purple curve of Figure 6a). This tip structure was effectively used before to model STML experiments on single $\mathrm{H_2Pc}$ molecules[28] .
We note that all the relevant quantities reported in Eqs. 9-13 are essentially functions of electromagnetic effects, as the transition density overlap (the last term of Eq. 10), is completely negligible even at the shortest distance of ≈ 1.6 nm. Based on this observation, we disclose that a Dexter-like energy transfer mechanism is of minor relevance here. More precisely, both the exchange and direct density overlap terms of Eq. 10 ,which are usually related to a Dexter-like process, are 4-5 orders of magnitude smaller than the total coupling value $V_0 + V_{\mathrm{met}}$ of Eq. 9 , thus pointing out that a Dexter mechanism plays a minor role in the present case. The quantity of interest, $\mathrm{RET_{eff}}$, is the result of a rather complex combination of different terms (see Eq. 6,15), each having its own frequency and spatial dependence with respect to the metal nanostructure and donor-acceptor distance. Each term is the result of purely classical electromagnetic interactions and should spatially decay as a polynomial function of the donor-acceptor or donor/acceptor-tip distance (see Figure 7). However, the particular combination of these terms yielding $\mathrm{RET_{eff}}$ according to Eqs. 6-7,15 can be reasonably well fitted by an exponential curve even if the quantum overlap of the donor and acceptor wavefunctions is negligible. Based on these findings a similar trend of $\mathrm{RET_{eff}}$ could be observed for other different D-A pairs in similar STM junctions when such range of intermolecular distances is investigated. Shorter D-A separation far below 1.5 nm may feature a non-negligible contribution stemming from the Dexter mechanism.

Looking closely at Figure 6a, we find a remarkable dependence of the spatial decay rate of the $\mathrm{RET_{eff}}$ on the resonance condition between the molecules and the tip. Specifically, moving from a condition in which either the acceptor or donor absorption frequency is exactly on-resonance with the tip's plasmonic peak (yellow and red curve, respectively), to progressively more off-resonance conditions (purple to blue curves), leads to a shallower decay of $\mathrm{RET_{eff}}$ as a function of distance. This shallower decay is accompanied, on the other hand, by larger absolute values of $\mathrm{RET_{eff}}$ at the shortest distances, with magnitudes larger than experimental observations (black dots in Figure 6a).

The emergent monotonically decreasing behavior of the $\mathrm{RET_{eff}}$ and the dependence of its magnitude on the resonance conditions of absorption frequencies can be further investigated by studying how the contributing decay rates vary with intermolecular distance. As shown in Eq. 7, $\mathrm{RET_{eff}}$ depends on the metal-affected radiative decay of the donor and the radiative and nonradiative decay rates of the acceptor. In Figure 7(a,b), we plot the various contributing rates computed at the respective donor and acceptor original frequencies ($\omega_{\mathrm{D}} = 2.11$ eV/$\omega_{\mathrm{A}} = 2.02$ eV), corresponding to the blue $\mathrm{RET_{eff}}$ curve in Figure 6a. In Figure 7(c,d) the same decay rates computed with the donor absorption frequency shifted to the plasmonic peak of tip 3a ($\omega_{\mathrm{D}} = 3.02$ eV/$\omega_{\mathrm{A}} = 2.93$ eV) are reported. We remark that most quantities associated with the donor are independent of intermolecular distance, since in the computational scheme the donor is fixed in space beneath the metallic tip while only the acceptor is translated to vary D-A distance R. These plots illustrate that only the metal-mediated rates significantly affect the magnitude of the $\mathrm{RET_{eff}}$. Notably, by moving the donor closer to resonance (panels c and d of Figure 7), we observe a large increase in both the donor's and the acceptor's plasmon-mediated radiative and nonradiative decay rates, ($\Gamma_{\mathrm{rad,D/A}}$, $\Gamma_{\mathrm{nr,met,D/A}}$), the latter always dominating. Basically, moving closer to resonance leads to an increase of the magnitude of the denominator of Eqs. 6-7 resulting in smaller overall $\mathrm{RET_{eff}}$ values than at off-resonance conditions. Overall, results indicate that the magnitude of $\mathrm{RET_{eff}}$ decreases as the molecular transition energies approach the nanostructure plasmonic transitions. The theoretical treatment developed in this work allows us to attribute these changes to the fast, metal-enhanced decay channels in the donor and acceptor species. Moreover, we highlight that the quantities in Figure 7 are plotted on a logarithmic scale but do not display a linear dependence on distance, as one may expect from exponentially decaying terms. Decay rates appear either constant

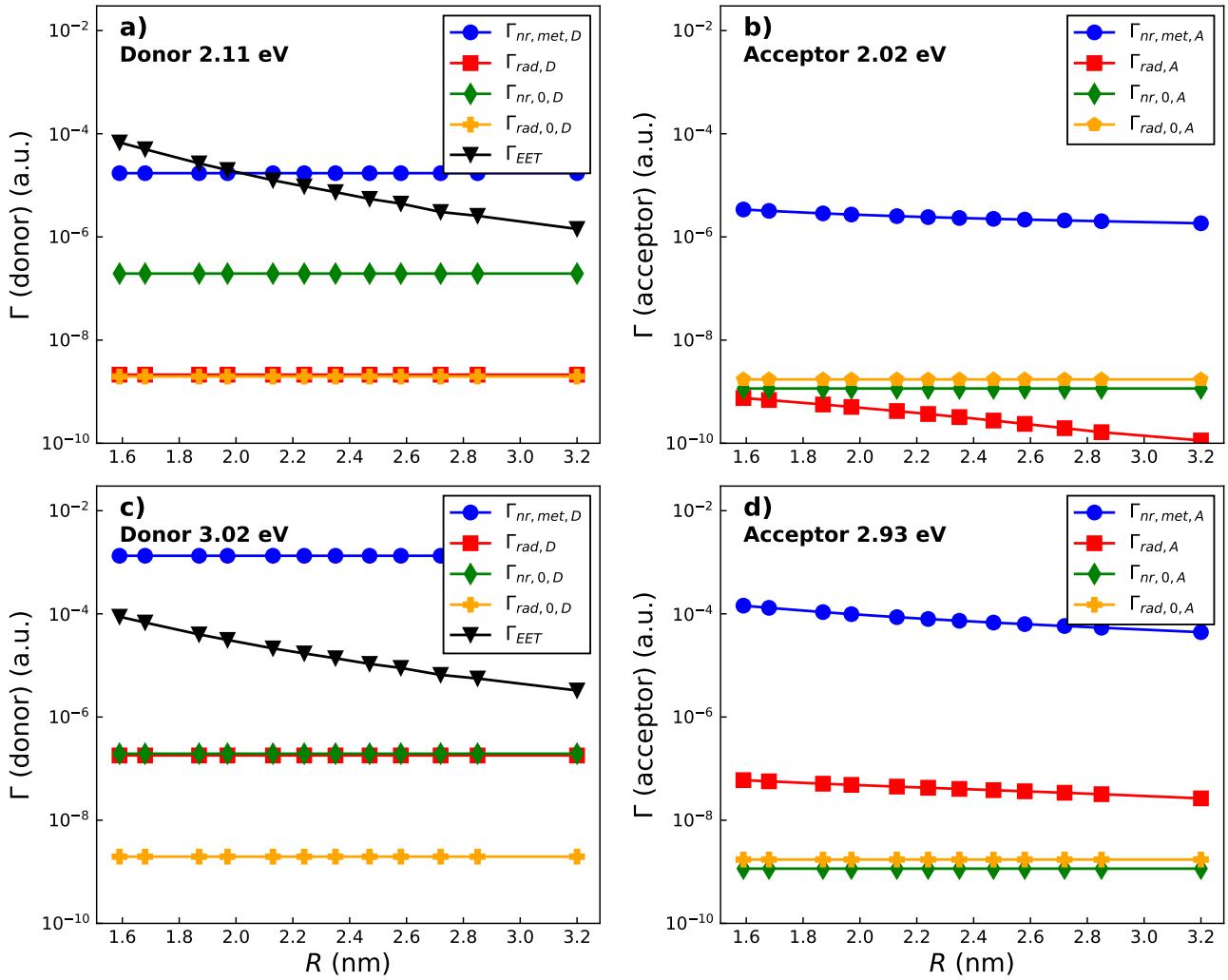

Figure 7. Dependence of individual decay rates on donor-acceptor distance. Comparison of donor and acceptor S_1 states decay rates that contribute to the EET efficiency as a function of donor-acceptor distance in a logarithmic scale in the presence of the tip structure of Figure 3a. The metallic response affecting the different rates has been evaluated at the respective donor and acceptor excitation frequencies ($\omega_D \approx 2.11$ eV and $\omega_A \approx 2.02$ eV, panels a and b, respectively) and with the donor frequency shifted to the tip's resonance peak energy ($\omega_D = 3.02$ eV) while keeping the same difference between donor and acceptor $\omega_{DA} \approx 0.09$ eV (panels c and d, respectively). Panels a and c show the nonradiative decay rate of the donor induced by the metal ($\Gamma_{nr,met,D}$, blue line, see Eq. 13), the radiative decay rate of the donor in the presence of the metal ($\Gamma_{rad,D}$, red line, see Eq. 12), the intrinsic nonradiative decay rate of the donor ($\Gamma_{nr,0,D}$, green line, computed according to Eq. 14 but for the donor molecule, with $\eta_{0,D} = 5 \times 10^{-4}$, taken from ref.[66]), the intrinsic (vacuum) radiative decay rate of the donor ($\Gamma_{rad,0,D}$, yellow line, see Eq. 14) and the metal-mediated electronic energy transfer rate (Γ_{EET},black line, see Eq. 9). Panels b and d show the corresponding quantities for the acceptor molecule (excluding the EET rate), evaluated at the acceptor frequency. A similar analysis in the case of the tip structure of Figure 3b is reported in Supplementary Figure 2. Source data for panels a-d can be found in Supplementary Data 1.

with R or curvilinear, thus corroborating the proper role of bare electromagnetic interactions, which scale polynomially with distance. A similar analysis on decay rates when the tip of Figure 3b is used is reported in Supplementary Figure 2, whereas the effect of the tip-molecule distance on RET_{eff} for the same structure is shown in Supplementary Figure 3.

It is important to note the range of magnitude and decay steepness of the theoretical RET_{eff} in calculations on- and off-resonance at different absorption frequencies. As mentioned in the section Investigated systems, shifting the donor and acceptor absorption frequencies ω_D and ω_A, while maintaining a consistent STM plasmonic response, is analogous to tuning the STM tip's response, i.e. to modifying its geometry. Indeed, calculations performed for the STM-like nanostructure of Figure 3b yield qualitatively similar but quantitatively different results (see Figure 6b) with respect to those performed for the smaller STM-like nanostructure of Figure 3a. For both setups, the RET_{eff} decays exponentially with the donor-acceptor distance. However, the decay rate depends on the setup, being significantly larger and in agreement with experimental data for the setup of Figure 3a under resonance conditions. We remark that the setup of Figure 3a was previously used to model STML experiments on single H_2Pc molecules[28], while the setup of Figure 3b was previously used to model TEPL experiments[29,49]. The absorption spectra of the two STM geometries (Figure 5) are quite different from each other, not only in terms of plasmonic peak frequencies, but also in terms of absorption magnitude, as there is a difference of $\approx$ 4-5 orders of magnitude in the maximum value of the imaginary part of the polarizability. These differences between STM geometries, both in absorption spectra and computed decay quantities, highlight the impact of the STM tip geometry on numerical results and in particular on the exact values of the RET_{eff}. Consequently, the detailed features of the tip, which are experimentally unavailable, are a plausible source of the remaining small discrepancy between the outcome of our theoretical calculations and the outcome of experiments[30], thus suggesting that a more detailed experimental characterization of these features would be instrumental. We stress the evidence, emerging from our computational work, that the tip geometry plays a fundamental role in the EET process. In fact, we have shown that theoretical results depend on the shape of the modeled tip and that the results obtained for the setup of Figure 3a quantitatively agree almost perfectly with experiments. This suggests the possibility to further tune the STM tip geometry and absorption spectrum to either maximize or minimize EET efficiency between donor and acceptor molecules and to control how steeply EET drops off as the molecules are brought farther apart.

Conclusion

In this work, we build on the previously developed PCM-NP theory[46,50,52,62,69] aimed to describe the interaction between classical nanoparticles and ab initio molecules, extending the procedure to account for energy transfer processes in multichromphoric systems in the presence of a plasmonic nanoparticle. The proposed modelling strategy was applied to an intriguing case study that was recently explored experimentally[30], where a plasmonic STM tip was used to monitor the energy transfer process in a donor (PdPc, palladium-phthalocyanine)-acceptor (H_2Pc, bare phthalocyanine) pair as a function of the donor-acceptor distance. This theoretical approach helped clarify and explain the exponential-like decay trend of $RET_{eff} = \frac{I_A}{I_A+I_D}$, which was previously observed[30]. In fact, the main result of this work is that for tip-mediated EET, an almost exponential decay is obtained as a consequence of the complex interplay of purely electromagnetic effects. Thus, the established identification of an exponential decay with a Dexter-like mechanism does not hold for tip-mediated EET. Remarkably, we also observed that the frequency-dependent response of the plasmonic nanostructure, which is strongly dictated by the nanostructure's geometric shape and metallic composition, can drastically impact the efficiency of energy transfer in such systems, thus paving the way for engineering these systems to control energy flow at the nanoscale. We believe the theoretical model proposed here may be a valuable starting point for exploring the role of plasmonic nanostructures in tailoring energy flow across molecules in more sophisticated multichromophoric architectures, such as artificial and natural light-harvesting complexes.

Methods

PCM NP Model

Following previous work[49] on a similar STM-like setup, the coupling between molecular species and the nanostructured metallic tip is described by the PCM-NP model[50,69] (Polarizable Continuum Model-NanoParticle). In this approach, molecular electronic structure is computed using ab initio methods. The resulting molecular charge densities perturb the metal nanostructure, and the nanostructure's response to the molecule-induced external perturbation is treated classically with the Polarizable Continuum Model (PCM), making use of the frequency-dependent dielectric function of the nanostructure. The PCM electromagnetic problem is numerically solved using the Boundary Element Method (BEM), where the surface of the metallic nanostructure is discretized into elementary areas, called tesserae. Each tessera is associated with a polarization charge $q_i(\omega)$ located in its geometrical center $\vec{s}_i$ that describes the interaction between the nanostructure and the potential of a nearby molecule, $V_i(\omega)$. Polarization charges are computed on the nanostructure surface as

$$\mathbf{q}(\omega) = \mathbf{Q}(\omega)\mathbf{V}(\omega), \tag{16}$$

where $\mathbf{Q}(\omega)$ is the PCM response matrix in the frequency domain,

$$\mathbf{Q}(\omega) = -\mathbf{S}^{-1}\left(2\pi\frac{\varepsilon(\omega)+1}{\varepsilon(\omega)-1}\mathbf{I}+\mathbf{DA}\right)^{-1}(2\pi\mathbf{I}+\mathbf{DA})\,. \tag{17}$$

Here, $\mathbf{A}$ is a diagonal matrix whose elements are the tesserae areas, while the matrices $\mathbf{S}$ and $\mathbf{D}$ are representative of Calderons' projectors[50],

$$S_{ij} = \frac{1}{\left|\vec{\mathbf{s}}_i - \vec{\mathbf{s}}_j\right|} \qquad D_{ij} = \frac{\left(\vec{\mathbf{s}}_i - \vec{\mathbf{s}}_j\right)\cdot\vec{\mathbf{n}}_j}{\left|\vec{\mathbf{s}}_i - \vec{\mathbf{s}}_j\right|^3}, \tag{18}$$

where the vector $\vec{\mathbf{s}}_j$ is representative of the j-th tessera's position on the nanoparticle surface, and $\vec{\mathbf{n}}_j$ is the unit vector normal to the j-th tessera, pointing outward from the nanoparticle.

Computational Details

Geometry optimization of molecular structures was performed for gas-phase PdPc and H_2Pc with DFT calculations using the software Gaussian16.[70] More specifically, ground state optimization DFT calculations were performed using the B3LYP functional with the LanL2DZ basis set for palladium (Pd) and the 6-31G(d)**++ basis set for non-metal atoms (C, H, N). The Gmsh code[71] was used for meshing the surface of the tip and substrate and for generating the discretized tesserae. For both tips, meshes were more refined in the proximity of the tip's apex and of the center of the substrate. The setup in Figure 3a(b) required the use of 6690 (3818) tesserae. In both setups, the Brendel-Bormann fitting model of the dielectric function of silver[68] was used for characterizing the metal's optical response and non-local metal effects are neglected[72].

Utilizing the optimized ground state geometries of the two molecules, electronic energy transfer (EET) between donor and acceptor was calculated in vacuum at a set distance R, using TDDFT at the B3LYP/6-31G(d)**++ level of theory for nonmetals and the B3LYP/LanL2DZ level for palladium, consistent with the level of theory used in structural optimizations. Calculations were again performed in Gaussian16[70] to obtain transition dipoles of the first two excited states of each molecule and the vacuum electronic couplings between each of these excited states. In this regard we note that increasing the basis set size to aug-cc-pVDZ or def2-TZVP as well as using a range-separated functional such as CAM-B3LYP did not lead to significant differences in the value of V_0 (Eq. 10) whose exchange and density overlap contributions always remain 4-5 orders of magnitude smaller that the purely classical electrostatic term.

The first two bright excited states of each molecule that fall in the spectral region probed experimentally[30] are degenerate or close in energy, so both were considered in simulations.

In addition to the TDDFT calculations of donor-acceptor complexes in vacuum, TDFFT calculations were also carried out for each self-standing molecule in the nanojunction setup. To this end, we computed the molecular electrostatic potential at the center of each nanostructure tessera (see section PCM NP Model), using the same level of theory as above and a modified version of the GAMESS code[73] which accounts for the presence of the metallic structure (see also Supplementary Note 1). We note that the presence of the plasmonic system polarizes the ground state molecular electron densities and so leads to small shift in the molecular excitation energies. Nevertheless this shift is negligible for the investigated setup, in agreement with previous studies[49]. Moreover, at each D-A distance, R, considered, the donor remained in the same position and orientation relative to the nanostructure while the acceptor was translated, so calculations were performed for only one donor configuration, but were repeated at each R for the acceptor (atomic coordinates can be found in Supplementary Data 2). The results of the GAMESS calculations were then used to evaluate the polarization charges on the nanostructure surface (Eq. 16) in the presence of each molecule with the homemade code TDPlas[74]. Additionally, TDPlas calculations yielded radiative decay rates of each molecule, with and without the metal present, as well as nonradiative decay rates mediated by the metal (Eqs. 12-13). Moreover, by taking the real part of the plasmon-molecule self-interaction[49] (Eq. 13) the plasmon-induced Lamb shift of excitation energies can be assessed. In the present case the largest computed shift value is ≈ 8 meV for the donor molecule, making it practically negligible. All these quantities are frequency dependent, and the corresponding metal-mediated rates included in Eq. 7 were evaluated at the TDDFT vertical excitation frequencies of the ground state optimized structures of the donor ($S_1/S_2 = 2.11/2.11$ eV) and acceptor molecules ($S_1/S_2 = 2.02/2.05$ eV), respectively. We note that there is a mismatch of ≈ 0.2 eV between experimental and simulated excitation energies. This systematic small discrepancy does not affect the overall interpretation of the theoretical results discussed in the present work. The spectral overlap value J entering into Γ_{EET} of Eq. 9 is set to its experimental value of 1.4 eV^{-1}[30]. However, we note that in ref.[30] this value is the estimated spectral overlap between PdPc and the S_1 state of H_2Pc (Q_x band). An experimental estimation of the spectral overlap between PdPc and the S_2 state of H_2Pc (Q_y band) is absent. However, all results reported in Figures 6-7 are obtained assuming the same J value for both acceptor states, since the $\mathrm{RET}_{\mathrm{eff}}$ decay profiles are not qualitatively different if the spectral overlap value for the acceptor S_2 state is substantially changed, as shown in Supplementary Figure 4.

We also note that previous works have shown that H_2Pc can undergo tautomerization under tunneling conditions (current-induced tautomerization[75]), even when the tunneling current is not directly passing through the molecule, thus proving that it is

an excited-state reaction process[28]. In the work of Cao et al.[30] which we compare our results with, there is no explicit evidence of tautomerization. It could be possible that due to the intense tunneling currents and long spectra acquisition times an average presence of the two tautomers remains buried in the measured signal[26], and so it becomes undetectable. Regardless, the results presented here would effectively take into account such an issue, since upon tautomerization the S_2 state accounted for here would convert to S_1 of the tautomer, conserving similar electronic properties.

Furthermore, in ref.[31] Kong et al. observed exciton formation, namely an excitation delocalized over more than one molecule, for a similar D-A pair in an STM junction. In our case, at the shortest D-A distance the largest metal-mediated coupling calculated as $V_0 + V_{\text{met}}$ under the resonance condition is rather small, ≈ 5 meV, thus making exciton formation irrelevant in the present case. Indeed, coherence and exciton formation are not reported in the experimental work of Cao et al.[30].

Data availability

Source data of Figures 5-7 can be found in Supplementary Data 1. Atomic coordinates of molecular structures used for calculations can be found in Supplementary Data 2. The authors declare that the data supporting the findings of this study are available within the paper, its Supplementary Information file, and as Supplementary Data files.

Code availability

The TDPlas code used to model the plasmonic systems and couple them with molecules is freely available at https://github.com/stefano-corni/WaveT_TDPlas. The post-processing python code used to evaluate RET_{eff} and to make the corresponding figures is available from the authors upon reasonable request.

Supplementary Information

Additional material can be found in the Supplementary Information.

Acknowledgements

The authors acknowledge financial support from the European Union's Horizon 2020 research and innovation program through the project PROID (Grant Agreement No. 964363). Computational work has been carried out on the C3P (Computational Chemistry Community in Padua) HPC facility of the Department of Chemical Sciences of the University of Padua. G.D. and M.R. acknowledge MIUR "Dipartimenti di Eccellenza" under the project Nanochemistry for energy and Health (NExuS) for funding the Ph.D. grant. R.D.F. and C.V.C. acknowledge the USA Department of Energy Office of Science, Basic Energy Sciences, award DE-SC0019432.

Author contribution

C.V.C. performed all the calculations and prepared the images, supported by M.R. and G.D. C.V.C., M.R. and G.D. equally contributed to the first draft of the manuscript. S.C. and R.D.F. supervised the research, and contributed to the paper revision.

Competing interests

The authors declare no competing interests.

References

1. Balzani, V., Credi, A. & Venturi, M. Photochemical conversion of solar energy. *ChemSusChem: Chem. & Sustain. Energy & Mater.* **1**, 26–58 (2008).
2. Mennucci, B. & Corni, S. Multiscale modelling of photoinduced processes in composite systems. *Nat. Rev. Chem.* **3**, 315–330 (2019).
3. Mirkovic, T., Ostroumov, E. E., Anna, J. M., Van Grondelle, R. & Scholes, G. D. Light absorption and energy transfer in the antenna complexes of photosynthetic organisms. *Chem. reviews* **117**, 249–293 (2017).
4. Collini, E., Curutchet, C., Mirkovic, T. & Scholes, G. D. Electronic energy transfer in photosynthetic antenna systems. In *Energy Transfer Dynamics in Biomaterial Systems*, 3–34 (Springer, 2009).
5. Collini, E. & Scholes, G. D. Coherent intrachain energy migration in a conjugated polymer at room temperature. *science* **323**, 369–373 (2009).

6. Scholes, G. D., Fleming, G. R., Olaya-Castro, A. & Van Grondelle, R. Lessons from nature about solar light harvesting. *Nat. chemistry* **3**, 763–774 (2011).

7. Fleming, G. R., Schlau-Cohen, G. S., Amarnath, K. & Zaks, J. Design principles of photosynthetic light-harvesting. *Faraday discussions* **155**, 27–41 (2012).

8. Jares-Erijman, E. A. & Jovin, T. M. Fret imaging. *Nat. biotechnology* **21**, 1387–1395 (2003).

9. Zhou, Q. & Swager, T. M. Fluorescent chemosensors based on energy migration in conjugated polymers: The molecular wire approach to increased sensitivity. *J. Am. Chem. Soc.* **117**, 12593–12602 (1995).

10. Halls, J. *et al.* Efficient photodiodes from interpenetrating polymer networks. *Nature* **376**, 498–500 (1995).

11. Yu, G., Gao, J., Hummelen, J. C., Wudl, F. & Heeger, A. J. Polymer photovoltaic cells: enhanced efficiencies via a network of internal donor-acceptor heterojunctions. *Science* **270**, 1789–1791 (1995).

12. Arsenault, E. A., Yoneda, Y., Iwai, M., Niyogi, K. K. & Fleming, G. R. Vibronic mixing enables ultrafast energy flow in light-harvesting complex ii. *Nat. communications* **11**, 1–8 (2020).

13. Ma, F., Romero, E., Jones, M. R., Novoderezhkin, V. I. & van Grondelle, R. Both electronic and vibrational coherences are involved in primary electron transfer in bacterial reaction center. *Nat. communications* **10**, 1–9 (2019).

14. Giannini, V., Fernández-Domínguez, A. I., Heck, S. C. & Maier, S. A. Plasmonic nanoantennas: fundamentals and their use in controlling the radiative properties of nanoemitters. *Chem. reviews* **111**, 3888–3912 (2011).

15. Ming, T., Chen, H., Jiang, R., Li, Q. & Wang, J. Plasmon-controlled fluorescence: beyond the intensity enhancement. *The J. Phys. Chem. Lett.* **3**, 191–202 (2012).

16. Kastrup, L. & Hell, S. W. Absolute optical cross section of individual fluorescent molecules. *Angewandte Chemie Int. Ed.* **43**, 6646–6649 (2004).

17. Born, M. & Wolf, E. *Principles of optics: electromagnetic theory of propagation, interference and diffraction of light* (Elsevier, 2013).

18. Xu, W. *et al.* Investigation of electronic excited states in single-molecule junctions. *Nano Res.* 1–20 (2022).

19. Dong, J., Zhang, Z., Zheng, H. & Sun, M. Recent progress on plasmon-enhanced fluorescence. *Nanophotonics* **4**, 472–490 (2015).

20. Zhu, W. *et al.* Quantum mechanical effects in plasmonic structures with subnanometre gaps. *Nat. communications* **7**, 1–14 (2016).

21. Wang, Y. & Ding, T. Optical tuning of plasmon-enhanced photoluminescence. *Nanoscale* **11**, 10589–10594 (2019).

22. Song, B. *et al.* Probing the mechanisms of strong fluorescence enhancement in plasmonic nanogaps with sub-nanometer precision. *ACS nano* **14**, 14769–14778 (2020).

23. Qiu, X., Nazin, G. & Ho, W. Vibrationally resolved fluorescence excited with submolecular precision. *Science* **299**, 542–546 (2003).

24. Merino, P., Große, C., Rosławska, A., Kuhnke, K. & Kern, K. Exciton dynamics of c60-based single-photon emitters explored by hanbury brown–twiss scanning tunnelling microscopy. *Nat. communications* **6**, 1–6 (2015).

25. Zhang, Y. *et al.* Visualizing coherent intermolecular dipole–dipole coupling in real space. *Nature* **531**, 623–627 (2016).

26. Imada, H. *et al.* Real-space investigation of energy transfer in heterogeneous molecular dimers. *Nature* **538**, 364–367 (2016).

27. Imada, H. *et al.* Single-molecule investigation of energy dynamics in a coupled plasmon-exciton system. *Phys. review letters* **119**, 013901 (2017).

28. Doppagne, B. *et al.* Single-molecule tautomerization tracking through space-and time-resolved fluorescence spectroscopy. *Nat. nanotechnology* **15**, 207–211 (2020).

29. Yang, B. *et al.* Sub-nanometre resolution in single-molecule photoluminescence imaging. *Nat. Photonics* **14**, 693–699 (2020).

30. Cao, S. *et al.* Energy funnelling within multichromophore architectures monitored with subnanometre resolution. *Nat. Chem.* **13**, 766–770 (2021).

31. Kong, F.-F. *et al.* Wavelike electronic energy transfer in donor–acceptor molecular systems through quantum coherence. *Nat. Nanotechnol.* **17**, 729–736 (2022).

32. Wong, K. F., Bagchi, B. & Rossky, P. J. Distance and orientation dependence of excitation transfer rates in conjugated systems: beyond the förster theory. *The J. Phys. Chem. A* **108**, 5752–5763 (2004).

33. Beljonne, D., Curutchet, C., Scholes, G. D. & Silbey, R. J. Beyond forster resonance energy transfer in biological and nanoscale systems. *The journal physical chemistry B* **113**, 6583–6599 (2009).

34. Nelson, T., Fernandez-Alberti, S., Roitberg, A. E. & Tretiak, S. Conformational disorder in energy transfer: beyond förster theory. *Phys. Chem. Chem. Phys.* **15**, 9245–9256 (2013).

35. Haas, E., Katchalski-Katzir, E. & Steinberg, I. Z. Effect of the orientation of donor and acceptor on the probability of energy transfer involving electronic transitions of mixed polarization. *Biochemistry* **17**, 5064–5070 (1978).

36. Giribabu, L., Ashok Kumar, A., Neeraja, V. & Maiya, B. G. Orientation dependence of energy transfer in an anthracene–porphyrin donor–acceptor system. *Angewandte Chemie Int. Ed.* **40**, 3621–3624 (2001).

37. Saini, S., Srinivas, G. & Bagchi, B. Distance and orientation dependence of excitation energy transfer: from molecular systems to metal nanoparticles. *The J. Phys. Chem. B* **113**, 1817–1832 (2009).

38. Muskens, O., Giannini, V., Sánchez-Gil, J. A. & Gómez Rivas, J. Strong enhancement of the radiative decay rate of emitters by single plasmonic nanoantennas. *Nano letters* **7**, 2871–2875 (2007).

39. Belacel, C. *et al.* Controlling spontaneous emission with plasmonic optical patch antennas. *Nano letters* **13**, 1516–1521 (2013).

40. Faggiani, R., Yang, J. & Lalanne, P. Quenching, plasmonic, and radiative decays in nanogap emitting devices. *ACS photonics* **2**, 1739–1744 (2015).

41. Zhao, L., Ming, T., Shao, L., Chen, H. & Wang, J. Plasmon-controlled forster resonance energy transfer. *The J. Phys. Chem. C* **116**, 8287–8296 (2012).

42. Li, J. *et al.* Plasmon-induced photonic and energy-transfer enhancement of solar water splitting by a hematite nanorod array. *Nat. communications* **4**, 1–8 (2013).

43. Li, J. *et al.* Plasmon-induced resonance energy transfer for solar energy conversion. *Nat. Photonics* **9**, 601–607 (2015).

44. Hsu, L.-Y., Ding, W. & Schatz, G. C. Plasmon-coupled resonance energy transfer. *The journal physical chemistry letters* **8**, 2357–2367 (2017).

45. Ghenuche, P. *et al.* Matching nanoantenna field confinement to fret distances enhances forster energy transfer rates. *Nano letters* **15**, 6193–6201 (2015).

46. Angioni, A., Corni, S. & Mennucci, B. Can we control the electronic energy transfer in molecular dyads through metal nanoparticles? a qm/continuum investigation. *Phys. Chem. Chem. Phys.* **15**, 3294–3303 (2013).

47. Andrew, P. & Barnes, W. Energy transfer across a metal film mediated by surface plasmon polaritons. *science* **306**, 1002–1005 (2004).

48. Qian, H. *et al.* Exciton energy transfer in pairs of single-walled carbon nanotubes. *Nano letters* **8**, 1363–1367 (2008).

49. Romanelli, M., Dall'Osto, G. & Corni, S. Role of metal-nanostructure features on tip-enhanced photoluminescence of single molecules. *The J. Chem. Phys.* **155**, 214304 (2021).

50. Tomasi, J., Mennucci, B. & Cammi, R. Quantum mechanical continuum solvation models. *Chem. reviews* **105**, 2999–3094 (2005).

51. Vukovic, S., Corni, S. & Mennucci, B. Fluorescence enhancement of chromophores close to metal nanoparticles. optimal setup revealed by the polarizable continuum model. *The J. Phys. Chem. C* **113**, 121–133 (2009).

52. Corni, S. & Tomasi, J. Lifetimes of electronic excited states of a molecule close to a metal surface. *The J. chemical physics* **118**, 6481–6494 (2003).

53. Andreussi, O., Corni, S., Mennucci, B. & Tomasi, J. Radiative and nonradiative decay rates of a molecule close to a metal particle of complex shape. *The J. chemical physics* **121**, 10190–10202 (2004).

54. Caricato, M., Andreussi, O. & Corni, S. Semiempirical (zindo-pcm) approach to predict the radiative and nonradiative decay rates of a molecule close to metal particles. *The J. Phys. Chem. B* **110**, 16652–16659 (2006).

55. Coccia, E. *et al.* Hybrid theoretical models for molecular nanoplasmonics. *The J. Chem. Phys.* **153**, 200901 (2020).

56. Marsili, M. & Corni, S. Electronic dynamics of a molecular system coupled to a plasmonic nanoparticle combining the polarizable continuum model and many-body perturbation theory. *The J. Phys. Chem. C* (2022).

57. Neuman, T., Esteban, R., Casanova, D., García-Vidal, F. J. & Aizpurua, J. Coupling of molecular emitters and plasmonic cavities beyond the point-dipole approximation. *Nano Lett.* **18**, 2358–2364 (2018).

58. Zhang, Y. *et al.* Sub-nanometre control of the coherent interaction between a single molecule and a plasmonic nanocavity. *Nat. Commun.* **8**, 15225 (2017).

59. Rosławska, A. *et al.* Mapping lamb, stark, and purcell effects at a chromophore-picocavity junction with hyper-resolved fluorescence microscopy. *Phys. Rev. X* **12**, 011012 (2022).

60. Rossi, T. P., Shegai, T., Erhart, P. & Antosiewicz, T. J. Strong plasmon-molecule coupling at the nanoscale revealed by first-principles modeling. *Nat. communications* **10**, 3336 (2019).

61. Zhang, Y., Dong, Z.-C. & Aizpurua, J. Influence of the chemical structure on molecular light emission in strongly localized plasmonic fields. *The J. Phys. Chem. C* **124**, 4674–4683 (2020).

62. Corni, S. & Tomasi, J. Enhanced response properties of a chromophore physisorbed on a metal particle. *The J. Chem. Phys.* **114**, 3739–3751 (2001).

63. Andreussi, O. *et al.* Plasmon enhanced light harvesting: Multiscale modeling of the fmo protein coupled with gold nanoparticles. *The J. Phys. Chem. A* **119**, 5197–5206 (2015).

64. Gil, G., Corni, S., Delgado, A., Bertoni, A. & Goldoni, G. Excitation energy-transfer in functionalized nanoparticles: Going beyond the förster approach. *The J. Chem. Phys.* **144**, 074101 (2016).

65. Iozzi, M. F., Mennucci, B., Tomasi, J. & Cammi, R. Excitation energy transfer (eet) between molecules in condensed matter: A novel application of the polarizable continuum model (pcm). *The J. chemical physics* **120**, 7029–7040 (2004).

66. Vincett, P., Voigt, E. & Rieckhoff, K. Phosphorescence and fluorescence of phthalocyanines. *The J. Chem. Phys.* **55**, 4131–4140 (1971).

67. Miwa, K. *et al.* Many-body state description of single-molecule electroluminescence driven by a scanning tunneling microscope. *Nano letters* **19**, 2803–2811 (2019).

68. Rakić, A. D., Djurišić, A. B., Elazar, J. M. & Majewski, M. L. Optical properties of metallic films for vertical-cavity optoelectronic devices. *Appl. Opt.* **37**, 5271–5283 (1998).

69. Mennucci, B., Cances, E. & Tomasi, J. Evaluation of solvent effects in isotropic and anisotropic dielectrics and in ionic solutions with a unified integral equation method: theoretical bases, computational implementation, and numerical applications. *The J. Phys. Chem. B* **101**, 10506–10517 (1997).

70. Frisch, M. J. *et al.* Gaussian~16 Revision B.01 (2016). Gaussian Inc. Wallingford CT.

71. Geuzaine, C. & Remacle, J.-F. Gmsh: A 3-d finite element mesh generator with built-in pre- and post-processing facilities. *Int. J. Numer. Methods Eng.* **79**, 1309–1331 (2009).

72. Johansson, P., Xu, H. & Käll, M. Surface-enhanced raman scattering and fluorescence near metal nanoparticles. *Phys. Rev. B* **72**, 035427 (2005).

73. Pipolo, S. & Corni, S. Real-time description of the electronic dynamics for a molecule close to a plasmonic nanoparticle. *The J. Phys. Chem. C* **120**, 28774–28781 (2016).

74. https://github.com/stefano-corni/WaveT_TDPlas.

75. Liljeroth, P., Repp, J. & Meyer, G. Current-induced hydrogen tautomerization and conductance switching of naphthalocyanine molecules. *Science* **317**, 1203–1206 (2007).

Supplementary Information for Unraveling the Mechanism of Tip-Enhanced Molecular Energy Transfer

Colin V. Coane,[†,‡] Marco Romanelli,[†] Giulia Dall'Osto,[†] Rosa Di Felice,[*,‡,¶] and Stefano Corni[*,†,¶]

†*Department of Chemical Sciences, University of Padova, via Marzolo 1, Padova, Italy*

‡*Department of Physics and Astronomy, University of Southern California, Los Angeles, CA, 90089, USA*

¶*CNR Institute of Nanoscience, via Campi 213/A, Modena, Italy*

* E-mail: difelice@usc.edu; stefano.corni@unipd.it

Supplementary Note 1. Technical issues in evaluating $\Gamma_{\mathbf{EET}}$

Given calculations were performed using multiple different softwares, for instance Gaussian16 and GAMESS were used for evaluating V_0 and V_{met}, respectively, so care had to be taken to prevent inconsistencies. One important consideration was that transition dipoles calculated with Gaussian16 and GAMESS for the same molecule at the same donor-acceptor distance had to match in both direction and phase, so that the sum of Eq. 9 (main text) could be evaluated without any fictitious inconsistency regarding the two terms in the sum. For instance, as the first two excited states of the donor are degenerate, state ordering may swap between calculations, and so transition dipoles had to be correctly matched between softwares when combining quantities, e.g. when taking the sum V_{met} and V_0 in order not to mix up

quantities belonging to different excited states. Additionally, each dipole phase may differ up to a factor of ± 1 between calculations, so a convention based on the GAMESS results was adopted and used to ensure the phases of V_0 and V_{met} matched this convention across calculations and could be added with their corresponding proper sign. This a posteriori correction was done by reversing the sign of the computed quantities when the transition dipole included an arbitrary phase swap. This correction was done for calculations at each individual distance R as phase discrepancies existed across the same calculations done at different values of R.

Supplementary Note 2. Dependence of the EET results on the tip position

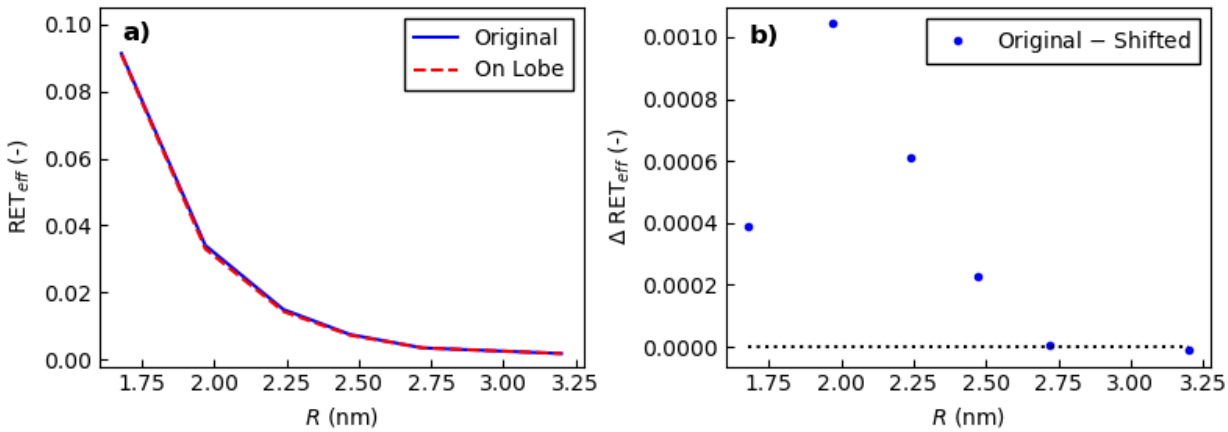

Supplementary Figure 1: a) RET_{eff} as a function of distance between the molecule centres obtained with the tip's protrusion centre placed on the middle of the PdPc aromatic ring (solid blue line) and on the middle of the nearby lobe (red dashed line), as depicted in Figure 4a (main text) via black spots 1-2. b) Corresponding numerical difference of the simulated data of panel a).

As shown in Figure 4a (main text) two different tip positions have been considered for evaluating RET_{eff}. In one case, the tip apex is placed exactly on the middle of one of the PdPc aromatic ring, whereas in the other it is located on the centre of the nearby orbital lobe. In Supplementary Figure 1 we show the computed RET_{eff} as a function of distance

between PdPc and H_2Pc for the two tip positions (decay rates evaluated at the original unmodified donor and acceptor frequencies), clearly showing that this spatial shift of the tip protrusion does not affect the outcome of the simulations.

Supplementary Note 3. Dependence of the donor and acceptor decay rates on the tip structure

Similar to Figure 7 (main text), plasmon-mediated decay rates are analyzed here in the case of the larger tip structure of Figure 3b (main text), as illustrated in Supplementary Figure 2. In this case, moving closer to resonance leads to a sizeable increase of both donor and acceptor radiative and nonradiative decay rates which results in a decrease of the absolute RET_{eff} value (see Figure 6 main text), in agreement with results reported in Figure 7 (main text). Nevertheless, with this tip structure radiative emission is much more enhanced than metal-induced non radiative decay, compared to results of Figure 7 (main text) where the other tip structure is used. This is mostly due to the tip's larger size, which translates into a larger NP-induced dipole moment that sizably contribute to the radiative rate expression of Eq. 12 (main text). Indeed, this tip structure was previously shown to considerably boost photoluminescence emission of single molecules, making TEPL experiments able to disclose sub-molecular features.[1,2]

In this context, the plasmon modes of such tips that most efficiently couple with molecules are those featuring charge localization at the tip apex. Previous works have shown that the spatial electric field distribution over the molecular plane is much affected by the apex geometrical features, thus corroborating that tip geometrical features can drastically affect plasmon-mediated molecular properties.[1–3]

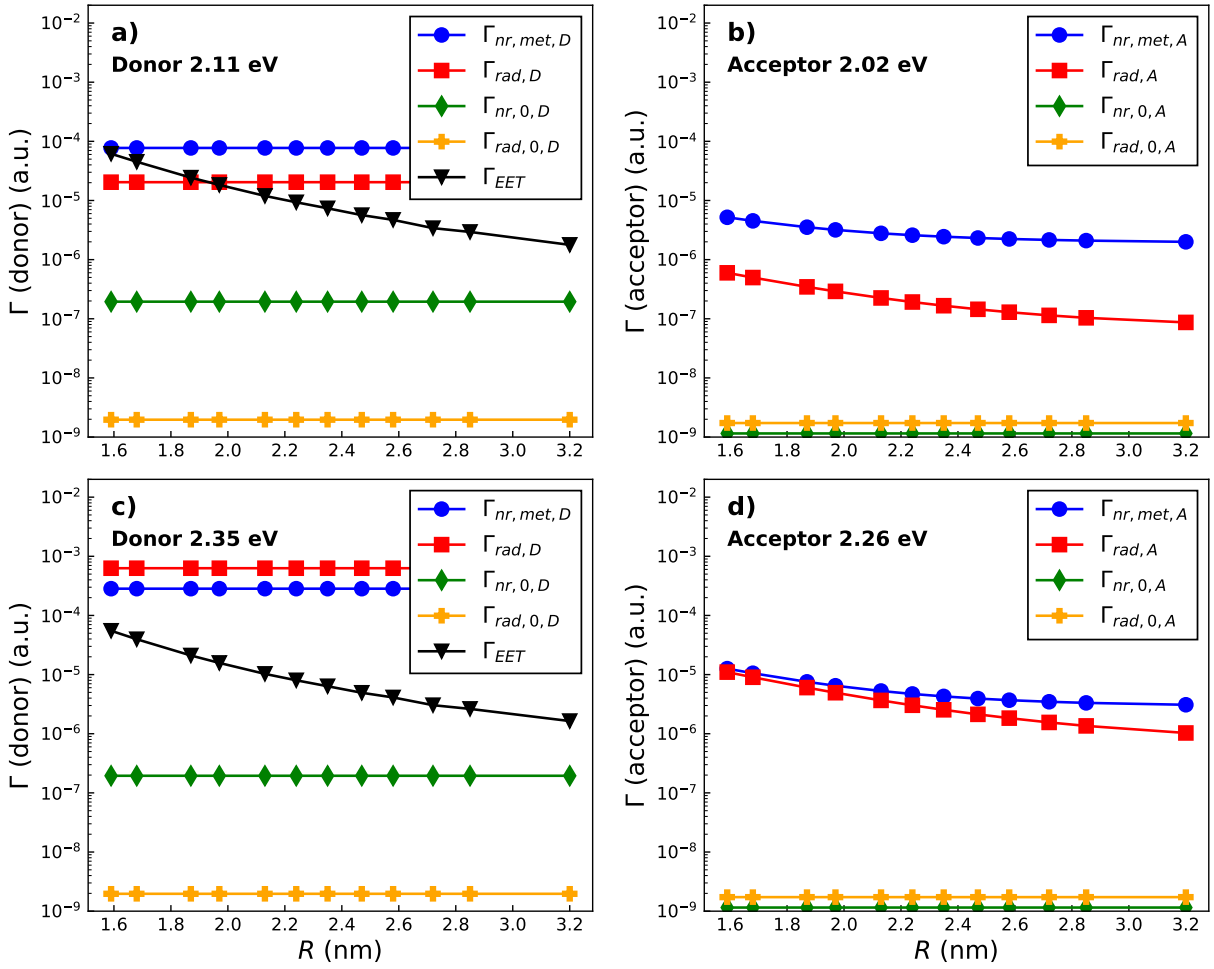

Supplementary Figure 2: Comparison of donor and acceptor S_1 states decay rates that contribute to the EET efficiency, computed as in Eq. 7, as a function of donor-acceptor distance in a logarithmic scale in the presence of the tip structure of Figure 3b (main text).The metallic response affecting the different rates has been evaluated at the respective donor and acceptor excitation frequencies ($\omega_{\mathrm{D}} \approx 2.11$ eV and $\omega_{\mathrm{A}} \approx 2.02$ eV, panels a and b, respectively) and with the donor frequency shifted to the tip's resonance peak energy ($\omega_{\mathrm{D}} = 2.35$ eV) while keeping the same difference between donor and acceptor $\omega_{\mathrm{DA}} \approx 0.09$ eV (panels c and d, respectively). Panels a and c show the nonradiative decay rate of the donor induced by the metal ($\Gamma_{\mathrm{nr,met,D}}$, blue line), the radiative decay rate of the donor in the presence of the metal ($\Gamma_{\mathrm{rad,D}}$, red line), the intrinsic nonradiative decay rate of the donor ($\Gamma_{\mathrm{nr,0,D}}$), the intrinsic (vacuum) radiative decay rate of the donor ($\Gamma_{\mathrm{rad,0,D}}$) and the metal-mediated electronic energy transfer rate (Γ_{EET},black line). Panels b and d show the corresponding quantities for the acceptor molecule (excluding the EET rate), evaluated at the acceptor frequency.

Supplementary Note 4. Dependence of EET results on tip-molecule distance

All results reported in main text are obtained with a fixed tip-molecule distance for a given tip setup. Increasing the tip-molecule distance leads to an overall increase of $\mathrm{RET}_{\mathrm{eff}}$ as illustrated in Supplementary Figure 3. This result is in agreement with what is observed in Figure 6 (main text) moving out of resonance. Indeed, in that case the absolute value of $\mathrm{RET}_{\mathrm{eff}}$ increases because of smaller plasmon-mediated radiative and non-radiative decay rates that enter into the denominator of Eq. 7 (main text). Enlarging the molecule-metal separation also leads to a similar trend as plasmon effects on molecular decay rates progressively attenuate because the mutual interaction gets weaker.

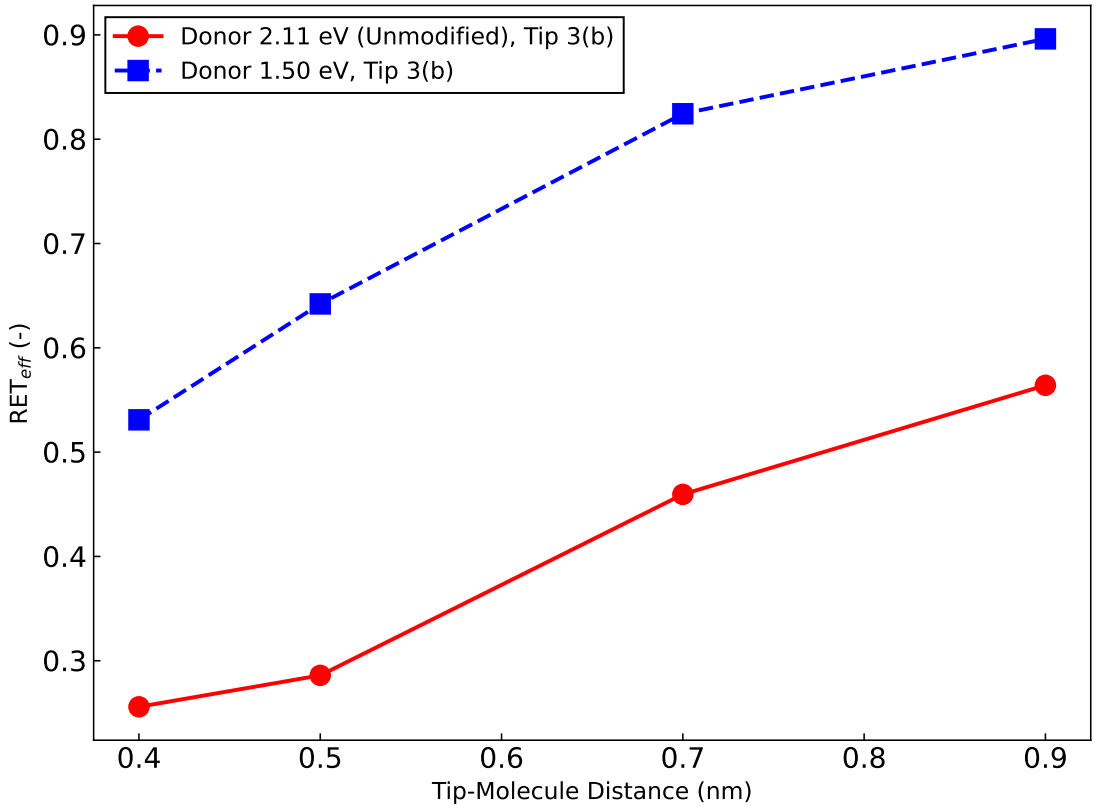

Supplementary Figure 3: Comparison of $\mathrm{RET}_{\mathrm{eff}}$ as a function of tip-donor distance obtained using the tip structure of Figure 3b, and evaluated at the donor absorption frequency of 2.11 eV (unmodified donor frequency, red line), and with absorption frequency shifted to 1.50 eV (blue line). The donor-acceptor separation is kept fixed at ≈ 2 nm.

Supplementary Note 5. Dependence of EET results on spectral overlap between PdPc and H_2Pc S_2 state

The spectral overlap value entering into Eq. 9 is set to the experimental[4] value of 1.4 eV^{-1} when the S_1 state (Q_x band) of H_2Pc is involved, whereas the corresponding experimental value for the S_2 state (Q_y band) is missing, since its contribution to the spectral overlap in ref.[4] has been neglected. All results reported in the main text consider the same J value for both states, as sizable changes of the spectral overlap values for the S_2 state contribution do not lead to qualitative differences in the RET_{eff} decay trend, as shown in Supplementary Figure 4.

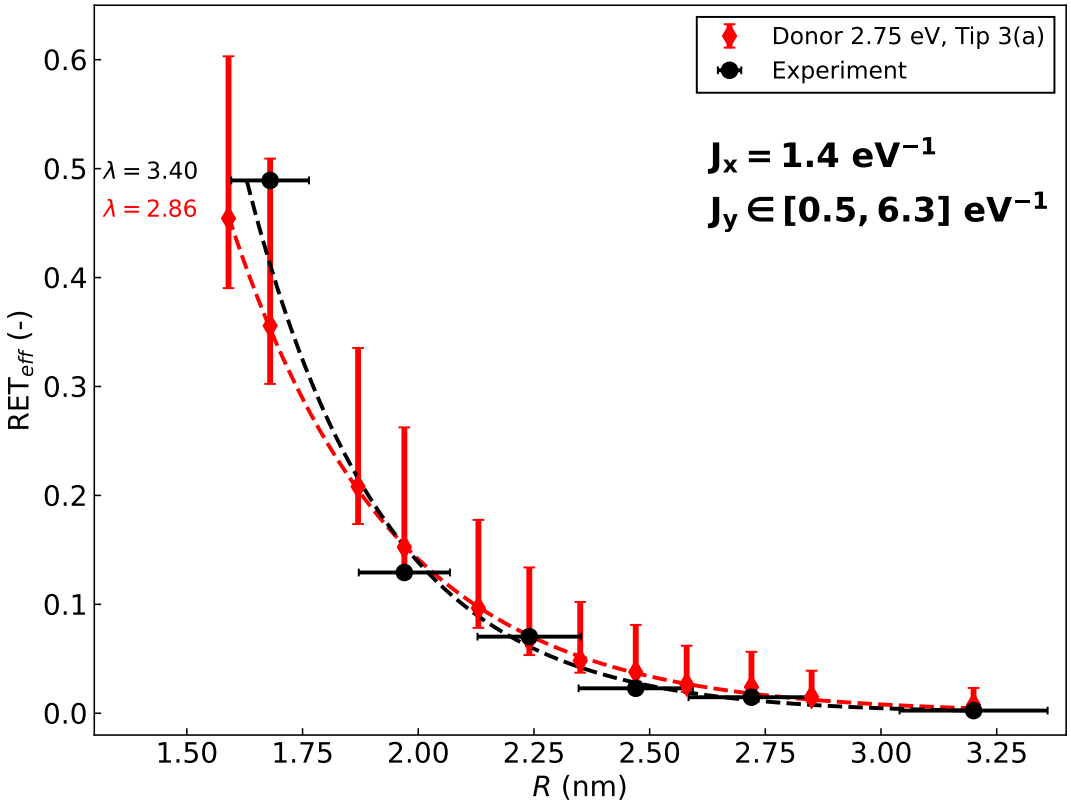

Supplementary Figure 4: RET_{eff} as a function of donor-acceptor distance obtained using the tip structure of Figure 3a, and evaluated with the donor absorption frequency set to 2.75 eV. The spectral overlap value is set to the experimental value of 1.4 eV^{-1} for the S_1 state of H_2Pc (J_x), while the error bars of the J value for the S_2 state (J_y) span the range $0.5 - 6.3\,eV^{-1}$. The lower (upper) extreme of each red bar represents the corresponding RET_{eff} value computed using $J_y = 0.5\,eV^{-1}$ ($J_y = 6.3\,eV^{-1}$).

Supplementary References

(1) Yang, B.; Chen, G.; Ghafoor, A.; Zhang, Y.; Zhang, Y.; Zhang, Y.; Luo, Y.; Yang, J.; Sandoghdar, V.; Aizpurua, J.; others Sub-nanometre resolution in single-molecule photoluminescence imaging. *Nature Photonics* **2020**, *14*, 693–699.

(2) Romanelli, M.; Dall'Osto, G.; Corni, S. Role of metal-nanostructure features on tip-enhanced photoluminescence of single molecules. *The Journal of Chemical Physics* **2021**, *155*, 214304.

(3) Doppagne, B.; Neuman, T.; Soria-Martinez, R.; López, L. E. P.; Bulou, H.; Romeo, M.; Berciaud, S.; Scheurer, F.; Aizpurua, J.; Schull, G. Single-molecule tautomerization tracking through space-and time-resolved fluorescence spectroscopy. *Nature nanotechnology* **2020**, *15*, 207–211.

(4) Cao, S.; Rosławska, A.; Doppagne, B.; Romeo, M.; Féron, M.; Chérioux, F.; Bulou, H.; Scheurer, F.; Schull, G. Energy funnelling within multichromophore architectures monitored with subnanometre resolution. *Nature Chemistry* **2021**, *13*, 766–770.

Chapter 3.

Effective Single-Mode Methodology for Strongly Coupled Multimode Molecular-Plasmon Nanosystems

Both previous chapters share the same classical description of the plasmonic system, and moving from chapter 1 to chapter 2 only the molecular complexity of the system being modelled has been increased, going from single molecule phenomena to excited state processes that simultaneously involve different molecules. Nevertheless, as mentioned in the *Introduction*, there are cases where such classical descriptions of the plasmonic body are not enough to properly describe systems properties. This occurs when plasmon-molecule strong-coupling is investigated, which leads to the formation of plexcitonic states where a strong mixing between molecular and plasmonic wavefunctions take place and so a profound change of the system eigenstates arise. In such cases, the plasmonic system needs also to be quantized, and to properly describe those scenarios *ab initio* QED quantum chemistry methods that account for plasmonic or field degrees of freedom at the level of the full system Hamiltonian have been recently developed[1–3]. Despite their accuracy in describing strongly-coupled systems involving molecules and quantized fields or quantized plasmons, their computational cost gets quickly prohibitive even for small molecules composed of few tens of atoms because of the additional complexity coming from the field degrees of freedom. In this regard, developing methods able to tackle strongly-coupled systems while retaining a computationally feasible approach is desirable.

In this chapter, which is reproduced as a published article in *Nano Letters* with permission (Copyright 2023 American Chemical Society), an effective mode approach to treat strongly-coupled molecular-plasmon nanosystems featuring multiple relevant quantized plasmon modes is presented. The developed theory is general, and it is here applied to the *ab initio* QED-CC method, the latter being an extension of standard Coupled Cluster to describe molecules strongly interacting with quantized fields or quantized plasmon modes. The original QED-CC theory has been explicitly formulated as a single-mode theory[1], and its direct extension to multimode systems would make simulations extremely costly, considering that already standard CC is well-known to be accurate but rather expensive. The idea behind the effective mode theory is to develop an effective approach able to capture the main effects arising from an ensemble of modes coupled to a given molecule, while retaining a computationally-feasible methodology.The

developed effective mode theory has been tested on a system composed of a single molecule (either H_2 or para-nitroaniline) surrounded by three ellipsoidal silver nanoparticles, showing that albeit approximate it significantly improves over single mode QED-CC when multimode effects cannot be neglected, approaching exact benchmark QED-FCI results while retaining the same computational cost of single mode QED-CC.
Such methodology could prove to be useful in investigating chirality in hybrid molecular-plasmonic systems. Indeed, plasmon-mediated circular dichroism is a rapidly expanding field of research nowadays, which focuses on combining chiral molecules with plasmonic structures to obtain hybrid systems that feature strong circular dichorism signals, thus potentially resulting in promising applications in the field of biosensing and enantioselctive catalysis[4, 5]. There are two possible mechanisms that are thought to be responsible for such CD signals. The first is called "induced chirality" and it entails electromagnetic coupling between a chiral molecule and a plasmonic NP. In this case, CD signals nearby the plasmonic resonance region are often observed and they are ascribed to local field effects which amplify the intrinsic molecular chirality signal[6]. In this scenario strong-coupling between chiral molecules and achiral/chiral plasmonic particles is attracting lots of interest at the moment which even culminated in the emergence of an entirely new field of research called "Chiral Polaritonics (or Plexcitonics)"[7–10]. The second mechanism is instead named "structural" or "intrinsic" chirality. In this case, the plasmonic nanoparticles present intrinsically chiral geometrical features as a result of the synthesis procedure which often involves chiral molecules. The origin of the detected CD signals in such systems is still debated, but it has been recently shown that the geometrical chirality of such particles can lead to CD signals that match the experimental evidence and such spectral features fall in the frequency region where high-order modes contribute to the optical signal, thus pointing attention to plasmon modes going beyond simple dipolar resonances[11–14]. This whole field is still in its infancy and further theoretical and experimental investigations are surely needed to unravel how molecular chirality could be affected by plasmonic interactions. For instance, it could be interesting to understand which kind of plasmonic shapes and so plasmon modes, could be used to maximize the CD response of such systems. For these reasons, especially when analyzing strong plasmon-molecule coupling in chiral systems, limiting oneself to single-mode theories could be too simplistic, thus making the effective mode scheme an handy tool in this view.

In this work, which has been carried out during my research stay in the group of Prof. Henrik Koch (NTNU, Trondheim, Norway), Rosario Roberto Riso (NTNU) and I developed the theory under the supervision of Prof. Henrik Koch. I implemented the effective mode theory and interfaced it with the eT[15] program that has been used to perform QED-CC calculations. I performed all calculations related to QED-CC, and QED-CC effective mode, whereas Enrico Ronca and Rosario Roberto Riso performed QED-FCI benchmark calculations. Writing of the initial draft, figures preparation and replies to referee's comments were equally shared among me and Rosario.

References

(1) Haugland, T. S.; Ronca, E.; Kjønstad, E. F.; Rubio, A.; Koch, H. *Physical Review X* **2020**, *10*, 041043.

(2) Ruggenthaler, M.; Flick, J.; Pellegrini, C.; Appel, H.; Tokatly, I. V.; Rubio, A. *Physical Review A* **2014**, *90*, 012508.

(3) DePrince, A. E. *The Journal of chemical physics* **2021**, *154*, 094112.

(4) Hentschel, M.; Schäferling, M.; Duan, X.; Giessen, H.; Liu, N. *Science advances* **2017**, *3*, e1602735.

(5) Kumar, J.; Liz-Marzán, L. M. *Colloidal Synthesis of Plasmonic Nanometals* **2020**, 845–865.

(6) Slocik, J. M.; Govorov, A. O.; Naik, R. R. *Nano letters* **2011**, *11*, 701–705.

(7) Schäfer, C.; Baranov, D. G. *The Journal of Physical Chemistry Letters* **2023**, *14*, 3777–3784.

(8) Baranov, D. G.; Schäfer, C.; Gorkunov, M. V. *ACS Photonics* **2023**, *10*, 2440–2455.

(9) Riso, R. R.; Grazioli, L.; Ronca, E.; Giovannini, T.; Koch, H. *Phys. Rev. X* **2023**, *13*, 031002.

(10) Yang, J.; Hu, H.; Zhang, Q.; Zu, S.; Chen, W.; Xu, H. *Nanophotonics* **2024**, *13*, 357–368.

(11) Carone, A.; Mariani, P.; Desert, A.; Romanelli, M.; Marcheselli, J.; Garavelli, M.; Corni, S.; Rivalta, I.; Parola, S. *ACS nano* **2022**, *16*, 1089–1101.

(12) Mun, J.; Rho, J. *Optics Letters* **2018**, *43*, 2856–2859.

(13) Mun, J.; Rho, J. *Nanophotonics* **2019**, *8*, 941–948.

(14) Wu, T.; Zhang, W.; Wang, R.; Zhang, X. *Nanoscale* **2017**, *9*, 5110–5118.

(15) Folkestad, S. D.; Kjønstad, E. F.; Myhre, R. H.; Andersen, J. H.; Balbi, A.; Coriani, S.; Giovannini, T.; Goletto, L.; Haugland, T. S.; Hutcheson, A., et al. *The Journal of Chemical Physics* **2020**, *152*.

NANO LETTERS

pubs.acs.org/NanoLett Letter

Effective Single-Mode Methodology for Strongly Coupled Multimode Molecular-Plasmon Nanosystems

Marco Romanelli,[¶] Rosario Roberto Riso,[¶] Tor S. Haugland, Enrico Ronca, Stefano Corni,* and Henrik Koch*

Cite This: *Nano Lett.* 2023, 23, 4938−4946 Read Online

ACCESS | Metrics & More | Article Recommendations | Supporting Information

ABSTRACT: Strong coupling between molecules and quantized fields has emerged as an effective methodology to engineer molecular properties. New hybrid states are formed when molecules interact with quantized fields. Since the properties of these states can be modulated by fine-tuning the field features, an exciting and new side of chemistry can be explored. In particular, significant modifications of the molecular properties can be achieved in plasmonic nanocavities, where the field quantization volume is reduced to subnanometric volumes, thus leading to intriguing applications such as single-molecule imaging and high-resolution spectroscopy. In this work, we focus on phenomena where the simultaneous effects of multiple plasmonic modes are critical. We propose a theoretical methodology to account for many plasmonic modes simultaneously while retaining computational feasibility. Our approach is conceptually simple and allows us to accurately account for the multimode effects and rationalize the nature of the interaction between multiple plasmonic excitations and molecules.

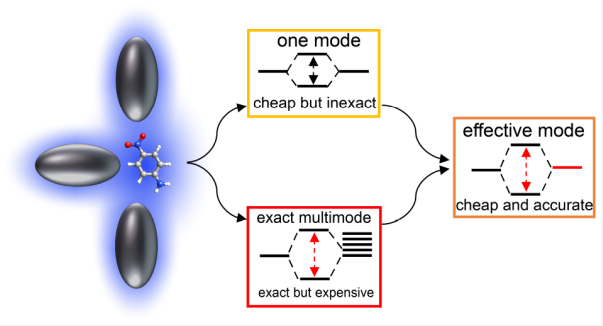

KEYWORDS: *plasmonics, strong coupling, coupled cluster theory*

Strong light−matter coupling between molecules and electromagnetic fields leads to the formation of new hybrid states, known as polaritons, where the quantum nature of the electromagnetic field entangles with purely molecular states.[1−8] The resulting polaritons can display different key features compared to the original states, potentially leading to new chemical/photochemical reactivity,[1,9−15] energy transfer processes,[16−21] or relaxation channels,[15,22−24] among others. While photonic cavities are an obvious choice, other fields, like the ones produced by electronic excitations in plasmonic nanostructure, can also be used to achieve the strong coupling regime. Despite their highly lossy nature, plasmonic nanocavities can confine the electromagnetic fields even down to subnanometric volumes.[25] The resulting interaction could be instrumental for a wide range of applications, such as sensing,[26−29] high-resolution spectroscopy,[30−32] single-molecule imaging,[32−34] and photocatalysis.[35−39]

Recent works point out that the simultaneous contribution of multiple plasmonic modes, going beyond the simplest dipolar resonances, might be critical for a number of phenomena,[40−43] e.g., the chiro-optical response of light−matter systems.[44−51] In such cases, theoretical models that capture multiple plasmon modes simultaneously are of the utmost importance.

Several *ab initio* quantum electrodynamics (QED) methods for strongly coupled systems have been proposed, e.g., quantum electrodynamics density functional theory (QEDFT),[3,52,53] QED coupled cluster (QED-CC),[54−58] and quantum electrodynamics full configuration interaction (QED-FCI).[55,59] Despite its computational affordability, QEDFT inherits the intrinsic problems of exchange and correlation functionals,[60,61] whereas QED-CC, albeit more accurate, is computationally demanding. The latter method has recently been extended to model quantized plasmonic modes obtained through a polarizable continuum model (PCM)[62] description of the nanoparticle response (Q-PCM-NP).[63] In its current implementation, however, QED-CC cannot take into account more than one plasmon mode at a time. Generalization of the original theory to the multimode case will quickly become computationally unfeasible.

In this paper, we couple the existing plasmon QED-CC method to a scheme that captures the main effects of multiple plasmons into a single effective mode. This allows us to retain the same computational cost of a single-mode QED-CC calculation while accounting for the multimode effects.

Received: February 24, 2023
Revised: May 16, 2023
Published: May 23, 2023

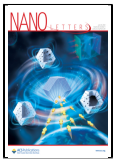

We first present a formal definition of the effective mode, followed by a numerical example on a test case system. Specifically, the effective mode approach is tested on a system composed of three nanoparticles (NPs) surrounding either a hydrogen or a *para*-nitroaniline (PNA) molecule. For hydrogen, we benchmark the effective mode approach against multimode QED-FCI. At the end, our final considerations and perspectives on the proposed method are given.

In our framework, the nanoparticle (NP) is described using the Drude−Lorentz dielectric function model,[64] that is

$$\epsilon(\omega) = 1 + \frac{\Omega_P^2}{\omega_0^2 - \omega^2 - i\gamma\omega} \tag{1}$$

where Ω_P is the bulk plasma frequency; ω_0 is the natural frequency of the bound oscillator; and γ is the damping rate. Together, these quantities define the nanoparticle material. The technique to quantize the NP linear response through a PCM-based theory has already been reported in a previous work.[63] In summary, the nanoparticle surface is described as a discretized collection of tesserae, labeled by j, each of which can host a variable surface charge representing the NP response to a given external perturbation.[65−67] The key quantity obtained from the PCM-based quantization scheme is q_{pj} which can be identified as the transition charge sitting on the jth tessera of the NP for a given excited state p. The collection of all the charges for a given p-mode represents one possible normal mode of the NP (a plasmon), with frequency ω_p. The detailed theory formulation can be found in the original work[63] where the above-mentioned quantities are explicitly derived.

On this basis, the Hamiltonian used to describe the interaction between the nanoparticle and the molecule equals

$$H = H_e + \sum_p \omega_p b_p^\dagger b_p + \sum_{pj} q_{pj} V_j (b_p^\dagger + b_p) \tag{2}$$

where H_e is the standard electronic Hamiltonian;[68] ω_p is the frequency of the pth nanoparticle mode; and the operators $b_p^\dagger$ and b_p create and annihilate plasmonic excitations of frequency ω_p, respectively. The interaction between the molecule and the plasmon is mediated through the bilinear term

$$V = \sum_{pj} q_{pj} V_j (b_p^\dagger + b_p) \tag{3}$$

In eq 3, V_j is the molecular electrostatic potential operator evaluated at the jth tessera of the NP, while q_{pj} is the quantized charge of mode p that lies on the jth tessera. From eq 3, the plasmon−molecule coupling for a transition going from the molecular state S_0 to S_n and exciting the plasmon mode p reads

$$g_{pn} = \langle S_n, 1_p | \sum_j q_{pj} V_j (b_p^\dagger + b_p) | S_0, 0 \rangle = \sum_j q_{pj} V_j^{S_0 \to S_n} \tag{4}$$

where $V_j^{S_0 \to S_n}$ is the potential coming from the $S_0 \to S_n$ transition density at the jth tessera of the NP surface. The coupling terms in eq 4 are the key quantities for simpler approaches to the strong-coupling regime, such as the Jaynes−Cummings (JC) model.[69] This is also the starting point of the effective mode derivation presented in this work. Using the full Hamiltonian in eq 2 is indeed computationally expensive because of the elevated number of plasmon modes that need to be considered. For this reason, it is customary to only include one mode in the Hamiltonian. While the single-mode approximation has been used with great success in the past, there are instances where a multimode approach is necessary. One example, for instance, is when multiple plasmonic excitations are almost resonant with the same molecular excitation or, as already discussed previously, when circular dichroism phenomena are studied. To reduce the computational cost while retaining a reasonable accuracy, it would be desirable to define a single effective boson that accounts, on average, for the effect of many modes. In our framework the effective mode will be obtained starting from a multimode JC Hamiltonian.

The generalization of the single-mode JC Hamiltonian to a multimode plasmonic system is

$$H_{JC}^{multi} = \omega_n \sigma^\dagger \sigma + \sum_p \omega_p b_p^\dagger b_p + \sum_p g_{pn} (b_p^\dagger \sigma + b_p \sigma^\dagger) \tag{5}$$

where ω_n is the frequency of the $S_0 \to S_n$ excitation and $\sigma^\dagger$, σ is the molecular raising and lowering operators.

$$\sigma = |S_0\rangle\langle S_n| \quad \sigma^\dagger = |S_n\rangle\langle S_0| \tag{6}$$

In our case, ω_n and g_{pn} are the excitation energies and the plasmon-mediated transition coupling elements computed using coupled cluster singles and doubles (CCSD) (more details can be found in the SI). Diagonalization of the Hamiltonian in eq 5 yields the mixed plasmonic−molecular wave functions with corresponding energies. We will simply use the term "polaritonic" to generally refer to those hybrid states from now on even though a mixed plasmon−electronic excitation state is properly called plexciton.[63] In the single mode case, the two eigenstates, typically called lower and upper polaritons (LP, UP), are given by

$$\begin{aligned} |\psi^{LP}\rangle &= |S_n, 0\rangle C_{mol}^{LP} + b_1^\dagger |S_0, 0\rangle C_1^{LP} \\ |\psi^{UP}\rangle &= |S_n, 0\rangle C_1^{LP} - b_1^\dagger |S_0, 0\rangle C_{mol}^{LP} \end{aligned} \tag{7}$$

with C_{mol}^{LP} and C_1^{LP} being the coefficients of the molecular excited state with no plasmons and the molecular ground state with one plasmonic excitation, respectively. These coefficients also appear in the UP wave function because of the orthogonality constraints.

On the other hand, the eigenfunctions of the Hamiltonian in eq 5 for the multimode case read

$$\begin{aligned} |\psi_{multi}^{LP}\rangle &= |S_n, 0\rangle C_{mol}^{LP} + \sum_p b_p^\dagger |S_0, 0\rangle C_p^{LP} \\ |\psi_{multi}^{UP}\rangle &= |S_n, 0\rangle C_{mol}^{UP} + \sum_p b_p^\dagger |S_0, 0\rangle C_p^{UP} \end{aligned} \tag{8}$$

where the coefficients defining the two polaritonic wave functions do not have to satisfy the strict relation in eq 7. Moreover, they can be rewritten as

https://doi.org/10.1021/acs.nanolett.3c00735
Nano Lett. 2023, 23, 4938−4946

$$
\begin{aligned}
|\psi_{\text{multi}}^{\text{LP}}\rangle &= |S_n, 0\rangle C_{\text{mol}}^{\text{LP}} + \sum_p C_p^{\text{LP}} b_p^\dagger |S_0, 0\rangle \\
&= |S_n, 0\rangle C_{\text{mol}}^{\text{LP}} + \sum_p \frac{C_p^{\text{LP}}}{N^{\text{LP}}} b_p^\dagger |S_0, 0\rangle N^{\text{LP}} \\
&= |S_n, 0\rangle C_{\text{mol}}^{\text{LP}} + \tilde{b}_{\text{LP}}^\dagger |S_0, 0\rangle N^{LP} \\
|\psi_{\text{multi}}^{\text{UP}}\rangle &= |S_n, 0\rangle C_{\text{mol}}^{\text{UP}} + \sum_p C_p^{\text{UP}} b_p^\dagger |S_0, 0\rangle \\
&= |S_n, 0\rangle C_{\text{mol}}^{\text{UP}} + \sum_p \frac{C_p^{\text{UP}}}{N^{\text{UP}}} b_p^\dagger |S_0, 0\rangle N^{UP} \\
&= |S_n, 0\rangle C_{\text{mol}}^{\text{UP}} + \tilde{b}_{\text{UP}}^\dagger |S_0, 0\rangle N^{\text{UP}}
\end{aligned} \tag{9}
$$

where index p labels the plasmon modes and the normalization factors N^{LP} and N^{UP} are defined as

$$
N^{\text{LP}} = \left(\sum_p |C_p^{\text{LP}}|^2\right)^{1/2} \quad N^{\text{UP}} = \left(\sum_p |C_p^{\text{UP}}|^2\right)^{1/2} \tag{10}
$$

The effective lower and upper polariton bosons are given by

$$
\begin{aligned}
\tilde{b}_{\text{LP}}^\dagger &= \sum_p \frac{C_p^{\text{LP}} b_p^\dagger}{N^{\text{LP}}} \\
\tilde{b}_{\text{UP}}^\dagger &= \sum_p \frac{C_p^{\text{UP}} b_p^\dagger}{N^{\text{UP}}}
\end{aligned} \tag{11}
$$

and they have been introduced to describe the plasmon part of the lower and upper polaritons. The normalization term $N^{\text{LP/UP}}$ is needed to ensure that the bosons still respect the commutation relations:

$$
[\tilde{b}_{\text{LP}}, \tilde{b}_{\text{LP}}^\dagger] = 1 \text{ and } [\tilde{b}_{\text{UP}}, \tilde{b}_{\text{UP}}^\dagger] = 1 \tag{12}
$$

We point out that, unlike the single-mode case in eq 7, the effective lower and upper polariton boson operators are different from each other. Moreover, the two bosons have a nonzero overlap such that

$$
[\tilde{b}_{\text{LP}}, \tilde{b}_{\text{UP}}^\dagger] \neq 0 \tag{13}
$$

The effective mode approximation comes into play when we seek a single effective mode $\tilde{b}$ that replaces both $\tilde{b}_{\text{LP}}$ and $\tilde{b}_{\text{UP}}$ such that the energies obtained using the effective upper and lower polaritonic states

$$
\begin{aligned}
|\tilde{\psi}^{\text{LP}}\rangle &= |S_n, 0\rangle C_{\text{mol}} + \tilde{b}^\dagger |S_0, 0\rangle N \\
|\tilde{\psi}^{\text{UP}}\rangle &= |S_n, 0\rangle N - \tilde{b}^\dagger |S_0, 0\rangle C_{\text{mol}} \\
N^2 &= \sum_p |C_p|^2
\end{aligned} \tag{14}
$$

are as close as possible to the ones obtained using the multimode JC model. We notice that in eq 14 the C_p coefficients are now common to both the lower and upper polariton wave functions. Specifically, they are optimized by minimizing the functional

$$
\begin{aligned}
F(\mathbf{C}) &= \sqrt{(\Delta E^{\text{LP}})^2 + (\Delta E^{\text{UP}})^2} \\
\Delta E^{\text{LP/UP}} &= \frac{\langle \tilde{\psi}^{\text{LP/UP}} | H_{\text{JC}}^{\text{multi}} | \tilde{\psi}^{\text{LP/UP}} \rangle}{\langle \tilde{\psi}^{\text{LP/UP}} | \tilde{\psi}^{\text{LP/UP}} \rangle} - E_{\text{multi}}^{\text{LP/UP}}
\end{aligned} \tag{15}
$$

where $E_{\text{multi}}^{\text{LP}}$ and $E_{\text{multi}}^{\text{UP}}$ are the LP and UP energies obtained by diagonalizing the Hamiltonian in eq 5. The optimal coefficients defining the effective mode are the actual output of that functional minimization and are system specific; that is, the effective mode composition will vary if the molecule and/or the plasmonic system change. Besides this, we note that the two solutions shown in eq 14 resemble the structure of the exact single-mode case in eq 7. Nonetheless, the plasmonic part of the wave function captures the effect of multiple modes at the same time. The procedure described here can easily be generalized to the case of an optical cavity.

Once the effective mode has been defined, the Hamiltonian in eq 2 can be rewritten as

$$
H = H_{\text{e}} + \sum_{pqr} U_{rp}^\dagger \omega_p U_{pq} \tilde{b}_r^\dagger \tilde{b}_q + \sum_{pqj} q_{jp} V_j U_{pq} (\tilde{b}_q + \tilde{b}_q^\dagger) \tag{16}
$$

where $\tilde{b}_1 = \tilde{b}$ is the effective mode defined in the previous section and the other bosonic operators fulfill

$$
[\tilde{b}_p, \tilde{b}_q^\dagger] = \delta_{pq} \tag{17}
$$

The two bosonic bases are related by a unitary transformation U

$$
\tilde{b}_p = \sum_q b_q U_{qp} \qquad U_{q1} = \frac{C_q}{N} \tag{18}
$$

Truncating the plasmon modes in eq 16 to only include the effective mode $\tilde{b}$, the Hamiltonian reads

$$
H = H_{\text{e}} + \tilde{\omega} \tilde{b}^\dagger \tilde{b} + \sum_j \tilde{q}_j V_j (\tilde{b} + \tilde{b}^\dagger) \tag{19}
$$

where the following quantities have been introduced

$$
\tilde{\omega} = \sum_p U_{1p}^\dagger \omega_p U_{p1} \quad \tilde{q}_j = \sum_p q_{jp} U_{p1} \tag{20}
$$

The quantized charge $\tilde{q}_j$, of the effective plasmon mode $\tilde{b}$, allows for a direct visualization of the effective mode properties (see Figure 2c).

Starting from the Hamiltonian in eq 19, we can use any single-mode QED method to study the effects of multiple plasmonic modes on molecular properties. In this work, we focus on the QED-CC approach. The QED-CC approach is the natural extension of standard coupled cluster theory to the strong coupling regime. The wave function is parametrized as

$$
|\psi\rangle = \exp(T)|\text{HF}\rangle \otimes |0\rangle \tag{21}
$$

where $|\text{HF}\rangle$ is the reference Slater determinant (usually obtained through a Hartree−Fock like procedure), while $|0\rangle$ denotes the plasmonic vacuum. The cluster operator T is defined as

https://doi.org/10.1021/acs.nanolett.3c00735
Nano Lett. 2023, 23, 4938−4946

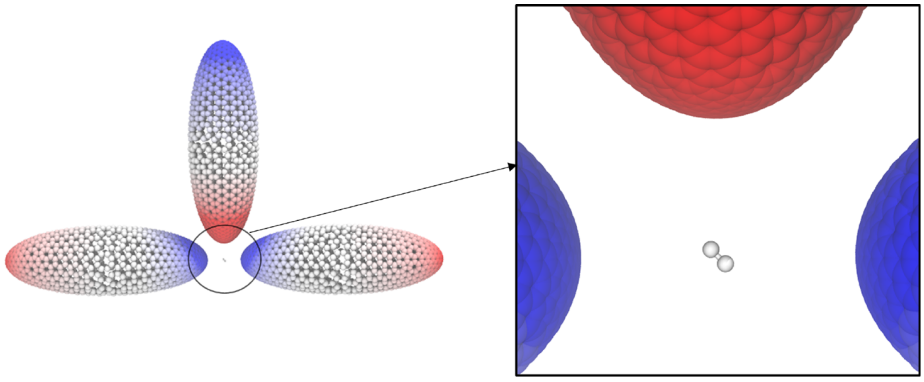

Figure 1. Setup employed to test the effective mode scheme. The plasmonic system consists of 3 ellipsoidal NPs surrounding an H_2 molecule in the yz plane. The beads composing the NPs represent the centroids of each tessera upon surface discretization and host a given quantized charge q_{pj}. The lowest (in energy) plasmon mode is shown. Red beads refer to positive charges, whereas blue ones refer to negative charges. Each NP is ≈0.6 nm far from H_2.

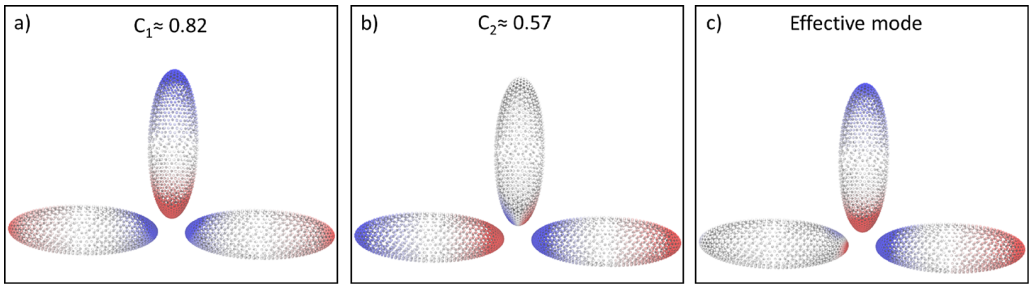

Figure 2. First (a) and second (b) quasi-degenerate plasmon modes of the setup shown in Figure 1. The energy splitting between these two modes is ≈16 meV, and they both significantly couple to the $S_0 \rightarrow S_1$ transition of H_2. Their contribution to the effective mode is shown at the top of the panel. (c) Visualization of the optimized effective mode. Only the two most important modes are reported in panels (a) and (b), but the first 12 modes coupling to the molecular transition contribute to the effective mode optimization.

$$T = \sum_{ai} t_i^a E_{ai} + \frac{1}{2}\sum_{aibj} t_{ij}^{ab} E_{ai}E_{bj} + \Gamma b^\dagger + \sum_{ai} s_i^a E_{ai} b^\dagger + \frac{1}{2}\sum_{aibj} s_{ij}^{ab} E_{ai}E_{bj} b^\dagger, \tag{22}$$

with each term corresponding to an electron, electron−plasmon, or plasmon excitation. In eq 22, the electronic second quantization formalism has been adopted such that[68]

$$E_{pq} = \sum_{\sigma} a_{p\sigma}^\dagger a_{q\sigma} \tag{23}$$

where $a_{p\sigma}^\dagger$ and $a_{q\sigma}$ create and annihilate an electron with spin σ in orbitals p and q, respectively. Following the commonly used notation, we denote the unoccupied HF orbitals with the letters a, b, c..., while for the occupied orbitals we use i, j, k.[68] Inclusion of the full set of excitations in eq 22 leads to the same results as QED-FCI. In this work we truncate T to include up to one plasmon excitation as well as single and double electronic excitations in line with what has been presented in ref 54. The parameters t_i^a, t_{ij}^{ab}, s_i^a, s_{ij}^{ab}, and Γ are called amplitudes. They are determined solving the projection equations

$$\Omega_{\mu,n} = \langle \mu, n | e^{-T} \bar{H} e^{T} | \mathrm{HF}, 0 \rangle = 0 \tag{24}$$

where μ is an electronic excitation, while n is a plasmonic excitation. We adopted the notation

$$|\mu, n\rangle = |\mu\rangle \otimes |n\rangle \tag{25}$$

The $\bar{H}$ operator is the molecule-plasmon Hamiltonian in eq 19 transformed with a coherent state. This accounts for the polarization of the plasmonic system induced by the molecular charge density in the HF state.

$$\bar{H} = e^{-z(\tilde{b}-\tilde{b}^\dagger)} H e^{z(\tilde{b}-\tilde{b}^\dagger)} \qquad z = -\frac{1}{\tilde{\omega}}\langle \mathrm{HF}| \sum_j \tilde{q}_j V_j |\mathrm{HF}\rangle \tag{26}$$

The setup we employed to test the effective mode approach consists of three identical ellipsoidal NPs, each one featuring a long-axis length of 6.0 nm and a short-axis length of 2.0 nm. In between the nanoellipses we placed first an H_2 and later a PNA molecule that are approximately 0.6 nm away from the three structures, as shown in Figure 1. This setup was chosen because it has degenerate (or almost degenerate) plasmon modes with significant coupling to the molecule. Moreover, the plasmon frequencies can easily be modulated, for instance by changing the aspect ratio of the ellipsoidal NPs (see Figure S2 in the SI as an example). Additional details about the computational methodologies can be found in the last section of the SI.[34,70,71]

The NP setup shown in Figure 2 has two almost degenerate low excitations (Figure 2 a and b) at 12.661 and 12.677 eV, whose coupling parameters with the first H_2 transition are 8.6 and 15.2 meV, respectively. Both excitations will significantly contribute to the effective mode. Specifically, their coefficients

https://doi.org/10.1021/acs.nanolett.3c00735
Nano Lett. 2023, 23, 4938−4946

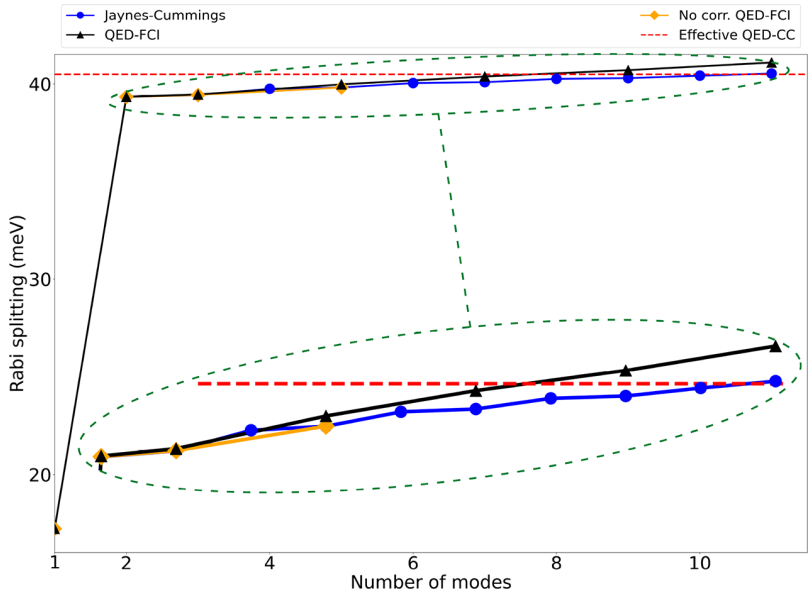

Figure 3. Computed Rabi splitting for the setup shown in Figure 1 as a function of the number of plasmonic modes included in the Hamiltonian. The calculations have been perfomed with the following methods: multimode Jaynes−Cummings, QED-FCI, and QED-FCI without relaxation of the electronic wave function (no corr. QED-FCI). We highlight that the latter curve is basically overlapped with the blue one. The effective mode QED-CC (dashed red line) recovers most of the multiphoton contribution. We note that the effective mode optimization has been computed using the first 12 plasmon modes of the nanoparticle setup with nonzero coupling with the molecular transition, starting from the low-energy modes. In order to contribute significantly to the splitting, the modes need to both couple with the electronic transition and be close in energy to the molecular excitation. Only some of the relevant modes are bright (such as those shown in Figure 2a,b); that is, they have a nonzero transition dipole moment. Others are dark, even though their coupling with the molecule is sizable.

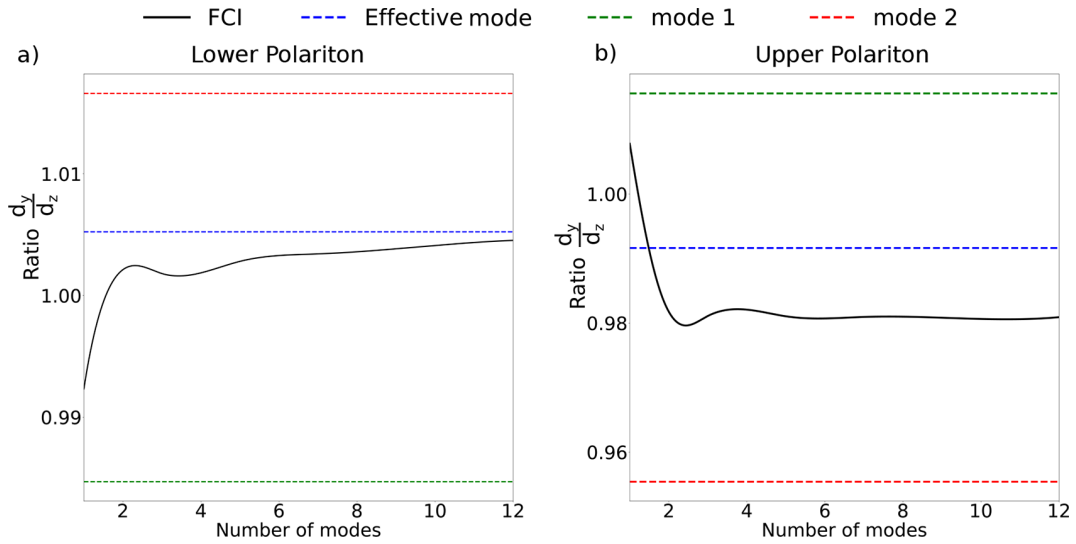

Figure 4. Ratio of the *y* and *z* components of the LP (a)/UP (b) transition dipole for the setup of Figure 1 in 4 different cases: QED-CC using mode 1 (dashed green line) or mode 2 only (dashed red line), effective mode QED-CC (dashed blue line), and QED-FCI (solid black curve). The QED-FCI data are reported as a function of the number of plasmonic modes included in the Hamiltonian, up to 12, which corresponds to the maximum number of modes employed in the effective mode optimization.

in the expansion of the effective mode (see eq 18) are reported in the top part of Figure 2.

In Figure 3 we show how the inclusion of multiple plasmon modes affects the H_2 Rabi splitting. Results are shown for the multimode JC Hamiltonian, QED-FCI, and the effective mode approach for QED-CC. We notice that, as expected, the single-mode approximation underestimates the Rabi splitting by almost a factor of two. All the multimode methods therefore show a large improvement once the second mode has been added. Inclusion of additional modes still enlarges the splitting, although we note that the change is quite small when compared to the improvement observed adding the second plasmon in the picture. Despite using a single bosonic operator, the effective mode QED-CC allows us to almost exactly capture the multimode effect with a predicted Rabi splitting of 40.49 meV compared to 41.09 meV (QED-FCI value). We notice that the QED-FCI and JC results are not exactly equal and that the error increases when more modes

https://doi.org/10.1021/acs.nanolett.3c00735
Nano Lett. 2023, 23, 4938−4946

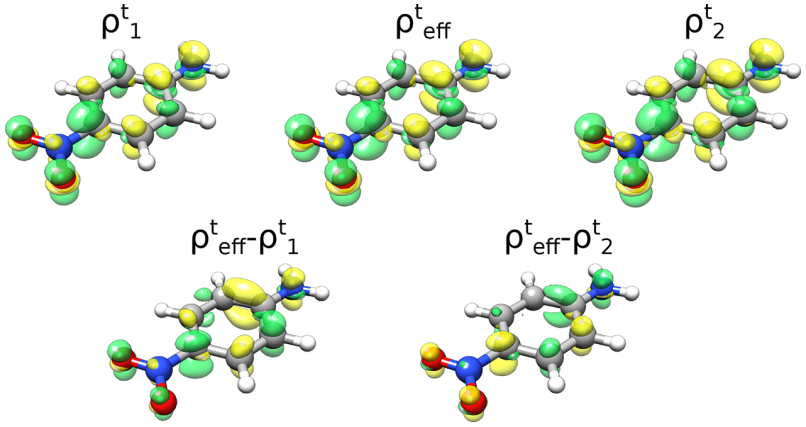

Figure 5. PNA transition density plots for the GS → LP transition (see setup of Figure S6 in the SI), computed using QED-CC with modes 1 and 2 or the effective mode. Positive density contributions are reported in yellow, whereas negative ones are reported in green. The difference between the transition density obtained with the effective mode and either mode 1 or mode 2 is also shown, thus allowing an easier visualization of the major changes in the PNA transition density upon changing the plasmonic part of the QED-CC Hamiltonian.

are considered. This difference is due to the relaxation of the electronic ground and excited states induced by the presence of the nanoparticle. This effect is not captured unless an *ab initio* approach is used. If the electronic wave function is not optimized in the QED-FCI calculations, thus not accounting for the mutual polarization with the NP (the no corr. QED-FCI in Figure 3), the difference between QED-FCI and JC is dramatically reduced. Nonetheless, the differences between the *ab initio* method and the two-level approximation are small when compared to the improvement from 1 to 2 modes.

We also investigated other excited-state properties, like the molecular contribution to the transition dipole moment in the GS → LP/UP transition. As shown in Figure 4a,b, the ratio between the molecular *y* and *z* components (the H_2 molecule lies in the *yz* plane) of the polaritonic transition dipole approaches the exact QED-FCI limit when the effective mode is used. On the other hand, the agreement is significantly worse using either mode 1 or mode 2 separately. This shows that the effective mode not only improves the Rabi splitting description compared to the single-mode approximation but also provides a better description of the most important excited state properties, e.g., transition dipoles/densities.

The qualitative picture does not change if a more complicated molecule like paranitroaniline (PNA) is placed between the three nanoellipsoidal structures (see Figure S6 of the SI). Comparing the multimode JC results with the effective mode approach for PNA, we notice that, similarly to the H_2 case, the effective mode QED-CC recovers most of the multimode contribution. Specifically, the Rabi splitting predicted by QED-CC is almost the same as using 5 field modes in the JC approach (78.3 meV). In Figure 5, we compare the GS → LP transition densities of PNA when either the effective mode or a single-mode approach is used. Notably, an enhancement of the LP charge transfer character can be observed moving from the single-mode QED-CC with the lowest plasmon mode (ρ_1^t of Figure 2a) to the effective mode QED-CC, ρ_{eff}^t. The difference between the two transition densities, $\rho_{\text{eff}}^t - \rho_1^t$, indeed shows an increased negative density contribution on the NO_2 group (acceptor) and an increased positive density contribution on the NH_2 group (donor). The opposite trend is observed in the case of mode 2 (Figure 2b), meaning that in the mode 2 case more charge is transferred compared to the effective mode case. These findings can easily be rationalized using the theory described above. Indeed, since mode 2 favors the charge separation more than mode 1, the effective plasmon, that is, a linear combinations of mode 1 and mode 2, predicts an intermediate transfer between the two. Since an increasing number of modes are coupled with the main molecular transition, nanoplasmonic systems with multiple almost degenerate excitations represent a promising option to increase the field effects without reducing the field quantization volume.

To conclude, building on the previously developed Q-PCM-NP/QED-CC model,[63] we propose here a framework to account for multimode environments using a single effective mode. Our approach captures the main features arising from the simultaneous coupling to multiple plasmons while retaining the same computational cost of single-mode methods.[54,63] Physical quantities, such as Rabi splittings and transition dipoles, are correctly reproduced, as verified by benchmarking against exact multimode QED-FCI for the hydrogen molecule surrounded by 3 ellipsoidal nanoparticles. The same theoretical approach is applied to a larger organic molecule, *para*-nitroaniline (PNA), where QED-FCI or multimode calculations are out of reach. Our results demonstrate that the inclusion of multiple modes is critical to correctly evaluate the plasmon−matter interaction in the case of quasi-degenerate plasmonic modes. In these cases, indeed, the single-mode approximation naturally breaks down. We notice that the effective mode scheme can be applied to any kind of wave function approximation and is not specific for plasmonic systems. We also point out that the effective mode is optimized to correctly reproduce the upper and lower polaritons only. Therefore, no improvement in the description of the ground state should be expected with this methodology. A generalization of the method should, however, be able to model the effect of multiple plasmonic modes on the molecular ground state. This topic will be the subject of a future publication. As a number of *ab initio* QED methods have started to appear recently,[3,52−57,59,72] the here-developed effective mode approach will be of great use in all those cases where multimode effects need to be taken into account, while retaining a computationally feasible methodology.[44−48]

https://doi.org/10.1021/acs.nanolett.3c00735
Nano Lett. 2023, 23, 4938−4946

■ ASSOCIATED CONTENT

Supporting Information

The Supporting Information is available free of charge at https://pubs.acs.org/doi/10.1021/acs.nanolett.3c00735.

Computational details and additional numerical tests regarding Rabi splitting convergence; effect of NP shape and molecule location on the effective mode scheme; transition dipole asymptotic behavior of Figure 4; weak-coupling regime; analysis of the PNA rabi splitting similar to Figure 3 (PDF)

■ AUTHOR INFORMATION

Corresponding Authors

Stefano Corni − *Department of Chemical Sciences, University of Padova, 35131 Padova, Italy; CNR Institute of Nanoscience, 41125 Modena, Italy; Padua Quantum Technologies Research Center, University of Padova, 35131 Padova, Italy;* orcid.org/0000-0001-6707-108X; Email: stefano.corni@unipd.it

Henrik Koch − *Department of Chemistry, Norwegian University of Science and Technology, 7491 Trondheim, Norway; Scuola Normale Superiore, 56126 Pisa, Italy;* orcid.org/0000-0002-8367-8727; Email: henrik.koch@sns.it

Authors

Marco Romanelli − *Department of Chemical Sciences, University of Padova, 35131 Padova, Italy;* orcid.org/0000-0002-4330-9740

Rosario Roberto Riso − *Department of Chemistry, Norwegian University of Science and Technology, 7491 Trondheim, Norway;* orcid.org/0000-0002-6870-4237

Tor S. Haugland − *Department of Chemistry, Norwegian University of Science and Technology, 7491 Trondheim, Norway;* orcid.org/0000-0002-9153-9866

Enrico Ronca − *Department of Chemistry, Biology and Biotechnology, University of Perugia, 06123 Perugia, Italy;* orcid.org/0000-0003-0494-5506

Complete contact information is available at: https://pubs.acs.org/10.1021/acs.nanolett.3c00735

Author Contributions

¶These authors equally contributed to the work.

Notes

The authors declare no competing financial interest.

■ ACKNOWLEDGMENTS

R.R.R, T.S.H., and H.K. acknowledge funding from the Research Council of Norway through FRINATEK Project No. 275506. This work has received funding from the European Research Council (ERC) under the European Union's Horizon 2020 Research and Innovation Programme (grant agreement No.101020016). M.R. acknowledges MIUR "Dipartimenti di Eccellenza" under the project Nanochemistry for energy and Health (NExuS) for funding the Ph.D. grant.

■ REFERENCES

(1) Fregoni, J.; Garcia-Vidal, F. J.; Feist, J. Theoretical Challenges in Polaritonic Chemistry. *ACS Photonics* **2022**, *9*, 1096−1107.

(2) Bloch, J.; Cavalleri, A.; Galitski, V.; Hafezi, M.; Rubio, A. Strongly correlated electron−photon systems. *Nature* **2022**, *606*, 41−48.

(3) Flick, J.; Ruggenthaler, M.; Appel, H.; Rubio, A. Atoms and molecules in cavities, from weak to strong coupling in quantum-electrodynamics (QED) chemistry. *P. Natl. Acad. Sci.* **2017**, *114*, 3026−3034.

(4) Galego, J.; Garcia-Vidal, F. J.; Feist, J. Cavity-induced modifications of molecular structure in the strong-coupling regime. *Phys. Rev. X* **2015**, *5*, 041022.

(5) Scholes, G. D. Polaritons and excitons: Hamiltonian design for enhanced coherence. *P. R. Soc. A* **2020**, *476*, 20200278.

(6) Ramezani, M.; Halpin, A.; Fernandez-Dominguez, A. I.; Feist, J.; Rodriguez, S. R.-K.; Garcia-Vidal, F. J.; Gomez Rivas, J. Plasmon-exciton-polariton lasing. *Optica* **2017**, *4*, 31−37.

(7) Sáez-Blázquez, R.; Cuartero-González, Á.; Feist, J.; García-Vidal, F. J.; Fernández-Domínguez, A. I. Plexcitonic quantum light emission from nanoparticle-on-mirror cavities. *Nano Lett.* **2022**, *22*, 2365−2373.

(8) Sánchez-Barquilla, M.; Fernández-Domínguez, A. I.; Feist, J.; García-Vidal, F. J. A theoretical perspective on molecular polaritonics. *ACS photonics* **2022**, *9*, 1830−1841.

(9) Feist, J.; Galego, J.; Garcia-Vidal, F. J. Polaritonic Chemistry with Organic Molecules. *ACS Photonics* **2018**, *5*, 205−216.

(10) Fregoni, J.; Granucci, G.; Coccia, E.; Persico, M.; Corni, S. Manipulating azobenzene photoisomerization through strong light−molecule coupling. *Nat. comm.* **2018**, *9*, 1−9.

(11) Hutchison, J. A.; Schwartz, T.; Genet, C.; Devaux, E.; Ebbesen, T. W. Modifying chemical landscapes by coupling to vacuum fields. *Angew. Chem., Int. Ed.* **2012**, *51*, 1592−1596.

(12) Lather, J.; Bhatt, P.; Thomas, A.; Ebbesen, T. W.; George, J. Cavity catalysis by cooperative vibrational strong coupling of reactant and solvent molecules. *Angew. Chem.* **2019**, *131*, 10745−10748.

(13) Fregoni, J.; Granucci, G.; Persico, M.; Corni, S. Strong coupling with light enhances the photoisomerization quantum yield of azobenzene. *Chem.* **2020**, *6*, 250−265.

(14) Kowalewski, M.; Bennett, K.; Mukamel, S. Cavity femtochemistry: Manipulating nonadiabatic dynamics at avoided crossings. *J. Phys. Chem. Lett.* **2016**, *7*, 2050−2054.

(15) Antoniou, P.; Suchanek, F.; Varner, J. F.; Foley IV, J. J. Role of cavity losses on nonadiabatic couplings and dynamics in polaritonic chemistry. *J. Phys. Chem. Lett.* **2020**, *11*, 9063−9069.

(16) Coles, D. M.; Somaschi, N.; Michetti, P.; Clark, C.; Lagoudakis, P. G.; Savvidis, P. G.; Lidzey, D. G. Polariton-mediated energy transfer between organic dyes in a strongly coupled optical microcavity. *Nat. Mater.* **2014**, *13*, 712−719.

(17) Du, M.; Martínez-Martínez, L. A.; Ribeiro, R. F.; Hu, Z.; Menon, V. M.; Yuen-Zhou, J. Theory for polariton-assisted remote energy transfer. *Chem. Sci.* **2018**, *9*, 6659−6669.

(18) Georgiou, K.; Michetti, P.; Gai, L.; Cavazzini, M.; Shen, Z.; Lidzey, D. G. Control over energy transfer between fluorescent BODIPY dyes in a strongly coupled microcavity. *ACS Photonics* **2018**, *5*, 258−266.

(19) Zhong, X.; Chervy, T.; Zhang, L.; Thomas, A.; George, J.; Genet, C.; Hutchison, J. A.; Ebbesen, T. W. Energy transfer between spatially separated entangled molecules. *Angew. Chem., Int. Ed.* **2017**, *56*, 9034−9038.

(20) Sáez-Blázquez, R.; Feist, J.; Fernández-Domínguez, A.; García-Vidal, F. Organic polaritons enable local vibrations to drive long-range energy transfer. *Phys. Rev. B* **2018**, *97*, 241407.

(21) Sáez-Blázquez, R.; Feist, J.; Romero, E.; Fernández-Domínguez, A. I.; García-Vidal, F. J. Cavity-modified exciton dynamics in photosynthetic units. *J. Phys. Chem. Lett.* **2019**, *10*, 4252−4258.

(22) Munkhbat, B.; Wersäll, M.; Baranov, D. G.; Antosiewicz, T. J.; Shegai, T. Suppression of photo-oxidation of organic chromophores by strong coupling to plasmonic nanoantennas. *Science adv* **2018**, *4*, No. eaas9552.

(23) Felicetti, S.; Fregoni, J.; Schnappinger, T.; Reiter, S.; de Vivie-Riedle, R.; Feist, J. Photoprotecting uracil by coupling with lossy nanocavities. *J. Phys. Chem. Lett.* **2020**, *11*, 8810−8818.

(24) Gu, B.; Mukamel, S. Manipulating nonadiabatic conical intersection dynamics by optical cavities. *Chem. Sci.* **2020**, *11*, 1290−1298.
(25) Chikkaraddy, R.; De Nijs, B.; Benz, F.; Barrow, S. J.; Scherman, O. A.; Rosta, E.; Demetriadou, A.; Fox, P.; Hess, O.; Baumberg, J. J. Single-molecule strong coupling at room temperature in plasmonic nanocavities. *Nature* **2016**, *535*, 127−130.
(26) Petryayeva, E.; Krull, U. J. Localized surface plasmon resonance: Nanostructures, bioassays and biosensing—A review. *Anal. Chim. Acta* **2011**, *706*, 8−24.
(27) Cathcart, N.; Chen, J. I. L. Sensing Biomarkers with Plasmonics. *Anal. Chem.* **2020**, *92*, 7373−7381.
(28) Etchegoin, P. G.; Le Ru, E. C. A perspective on single molecule SERS: current status and future challenges. *Phys. Chem. Chem. Phys.* **2008**, *10*, 6079−6089.
(29) Vo-Dinh, T. SERS chemical sensors and biosensors: new tools for environmental and biological analysis. *Sensor Actuat B-Chem.* **1995**, *29*, 183−189.
(30) Maccaferri, N.; Barbillon, G.; Koya, A. N.; Lu, G.; Acuna, G. P.; Garoli, D. Recent advances in plasmonic nanocavities for single-molecule spectroscopy. *Nanoscale Adv.* **2021**, *3*, 633−642.
(31) Haran, G. Single-molecule Raman spectroscopy: a probe of surface dynamics and plasmonic fields. *Acc. Chem. Res.* **2010**, *43*, 1135−1143.
(32) Zhang, R.; Zhang, Y.; Dong, Z.; Jiang, S.; Zhang, C.; Chen, L.; Zhang, L.; Liao, Y.; Aizpurua, J.; Luo, Y. E.; et al. Chemical mapping of a single molecule by plasmon-enhanced Raman scattering. *Nature* **2013**, *498*, 82−86.
(33) Yang, B.; Chen, G.; Ghafoor, A.; Zhang, Y.; Zhang, Y.; Zhang, Y.; Luo, Y.; Yang, J.; Sandoghdar, V.; Aizpurua, J.; et al. Sub-nanometre resolution in single-molecule photoluminescence imaging. *Nat. Photonics* **2020**, *14*, 693−699.
(34) Romanelli, M.; Dall'Osto, G.; Corni, S. Role of metal-nanostructure features on tip-enhanced photoluminescence of single molecules. *J. Chem. Phys.* **2021**, *155*, 214304.
(35) Cortés, E.; Besteiro, L. V.; Alabastri, A.; Baldi, A.; Tagliabue, G.; Demetriadou, A.; Narang, P. Challenges in plasmonic catalysis. *ACS Nano* **2020**, *14*, 16202−16219.
(36) Zhang, X.; Chen, Y. L.; Liu, R.-S.; Tsai, D. P. Plasmonic photocatalysis. *Rep. Prog. Phys.* **2013**, *76*, 046401.
(37) Kale, M. J.; Avanesian, T.; Christopher, P. Direct photocatalysis by plasmonic nanostructures. *ACS Catal.* **2014**, *4*, 116−128.
(38) Zhou, L.; Swearer, D. F.; Zhang, C.; Robatjazi, H.; Zhao, H.; Henderson, L.; Dong, L.; Christopher, P.; Carter, E. A.; Nordlander, P.; et al. Quantifying hot carrier and thermal contributions in plasmonic photocatalysis. *Science* **2018**, *362*, 69−72.
(39) Lou, Z.; Wang, Z.; Huang, B.; Dai, Y. Synthesis and activity of plasmonic photocatalysts. *ChemCatChem.* **2014**, *6*, 2456−2476.
(40) Delga, A.; Feist, J.; Bravo-Abad, J.; Garcia-Vidal, F. Theory of strong coupling between quantum emitters and localized surface plasmons. *J. Opt.* **2014**, *16*, 114018.
(41) Feist, J.; Fernández-Domínguez, A. I.; García-Vidal, F. J. Macroscopic QED for quantum nanophotonics: emitter-centered modes as a minimal basis for multiemitter problems. *Nanophotonics* **2020**, *10*, 477−489.
(42) Medina, I.; García-Vidal, F. J.; Fernández-Domínguez, A. I.; Feist, J. Few-mode field quantization of arbitrary electromagnetic spectral densities. *Phys. Rev. Lett.* **2021**, *126*, 093601.
(43) Sánchez-Barquilla, M.; García-Vidal, F. J.; Fernández-Domínguez, A. I.; Feist, J. Few-mode field quantization for multiple emitters. *Nanophotonics* **2022**, *11*, 4363−4374.
(44) Carone, A.; Mariani, P.; Désert, A.; Romanelli, M.; Marcheselli, J.; Garavelli, M.; Corni, S.; Rivalta, I.; Parola, S. Insight on Chirality Encoding from Small Thiolated Molecule to Plasmonic Au@Ag and Au@Au Nanoparticles. *ACS Nano* **2022**, *16*, 1089−1101.
(45) Mun, J.; Rho, J. Importance of higher-order multipole transitions on chiral nearfield interactions. *Nanophotonics* **2019**, *8*, 941−948.
(46) Mun, J.; Rho, J. Surface-enhanced circular dichroism by multipolar radiative coupling. *Opt. Lett.* **2018**, *43*, 2856−2859.
(47) Wu, T.; Zhang, W.; Wang, R.; Zhang, X. A giant chiroptical effect caused by the electric quadrupole. *Nanoscale* **2017**, *9*, 5110−5118.
(48) Govorov, A. O.; Fan, Z. Theory of Chiral Plasmonic Nanostructures Comprising Metal Nanocrystals and Chiral Molecular Media. *ChemPhysChem* **2012**, *13*, 2551−2560.
(49) Stevenson, P. R.; Du, M.; Cherqui, C.; Bourgeois, M. R.; Rodriguez, K.; Neff, J. R.; Abreu, E.; Meiler, I. M.; Tamma, V. A.; Apkarian, V. A.; et al. Active Plasmonics and Active Chiral Plasmonics through Orientation-Dependent Multipolar Interactions. *ACS Nano* **2020**, *14*, 11518−11532.
(50) Lininger, A.; Palermo, G.; Guglielmelli, A.; Nicoletta, G.; Goel, M.; Hinczewski, M.; Strangi, G.; et al. Chirality in light−matter interaction. *Adv. Mater.* **2022**, 2107325.
(51) Khaliq, H. S.; Kim, I.; Zahid, A.; Kim, J.; Lee, T.; Badloe, T.; Kim, Y.; Zubair, M.; Riaz, K.; Mehmood, M. Q.; et al. Giant chiro-optical responses in multipolar-resonances-based single-layer dielectric metasurfaces. *Photonics Res.* **2021**, *9*, 1667−1674.
(52) Ruggenthaler, M.; Flick, J.; Pellegrini, C.; Appel, H.; Tokatly, I. V.; Rubio, A. Quantum-electrodynamical density-functional theory: Bridging quantum optics and electronic-structure theory. *Phys. Rev. A* **2014**, *90*, 012508.
(53) Tokatly, I. V. Time-Dependent Density Functional Theory for Many-Electron Systems Interacting with Cavity Photons. *Phys. Rev. Lett.* **2013**, *110*, 233001.
(54) Haugland, T. S.; Ronca, E.; Kjønstad, E. F.; Rubio, A.; Koch, H. Coupled Cluster Theory for Molecular Polaritons: Changing Ground and Excited States. *Phys. Rev. X* **2020**, *10*, 041043.
(55) Haugland, T. S.; Schäfer, C.; Ronca, E.; Rubio, A.; Koch, H. Intermolecular interactions in optical cavities: An ab initio QED study. *J. Chem. Phys.* **2021**, *154*, 094113.
(56) DePrince, A. E., III Cavity-modulated ionization potentials and electron affinities from quantum electrodynamics coupled-cluster theory. *J. Chem. Phys.* **2021**, *154*, 094112.
(57) Pavosevic, F.; Flick, J. Polaritonic unitary coupled cluster for quantum computations. *J. Phys. Chem. Lett.* **2021**, *12*, 9100−9107.
(58) Riso, R. R.; Haugland, T. S.; Ronca, E.; Koch, H. On the characteristic features of ionization in QED environments. *J. Chem. Phys.* **2022**, *156*, 234103.
(59) Riso, R. R.; Haugland, T. S.; Ronca, E.; Koch, H. Molecular orbital theory in cavity QED environments. *Nat. comm.* **2022**, *13*, 1−8.
(60) Flick, J.; Schäfer, C.; Ruggenthaler, M.; Appel, H.; Rubio, A. Ab Initio Optimized Effective Potentials for Real Molecules in Optical Cavities: Photon Contributions to the Molecular Ground State. *ACS Photonics* **2018**, *5*, 992−1005.
(61) Pellegrini, C.; Flick, J.; Tokatly, I. V.; Appel, H.; Rubio, A. Optimized Effective Potential for Quantum Electrodynamical Time-Dependent Density Functional Theory. *Phys. Rev. Lett.* **2015**, *115*, 093001.
(62) Mennucci, B. Polarizable continuum model. *Wires. Comput. Mol. Sci.* **2012**, *2*, 386−404.
(63) Fregoni, J.; Haugland, T. S.; Pipolo, S.; Giovannini, T.; Koch, H.; Corni, S. Strong Coupling between Localized Surface Plasmons and Molecules by Coupled Cluster Theory. *Nano Lett.* **2021**, *21*, 6664−6670.
(64) Jackson, J. D. *Classical electrodynamics*; John Wiley & Sons: New York, 1999.
(65) Cances, E.; Mennucci, B.; Tomasi, J. A new integral equation formalism for the polarizable continuum model: Theoretical background and applications to isotropic and anisotropic dielectrics. *J. Chem. Phys.* **1997**, *107*, 3032−3041.
(66) Corni, S.; Pipolo, S.; Cammi, R. Equation of Motion for the Solvent Polarization Apparent Charges in the Polarizable Continuum Model: Application to Real-Time TDDFT. *J. Phys. Chem. A* **2015**, *119*, 5405−5416.

https://doi.org/10.1021/acs.nanolett.3c00735
Nano Lett. 2023, 23, 4938−4946

(67) Mennucci, B.; Corni, S. Multiscale modelling of photoinduced processes in composite systems. *Nat. Rev. Chem.* **2019**, *3*, 315−330.
(68) Helgaker, T.; Jorgensen, P.; Olsen, J. *Molecular electronic-structure theory*; John Wiley & Sons, 2014.
(69) Jaynes, E.; Cummings, F. Comparison of quantum and semiclassical radiation theories with application to the beam maser. *Proc. IEEE* **1963**, *51*, 89−109.
(70) Folkestad, S. D.; Kjønstad, E. F.; Myhre, R. H.; Andersen, J. H.; Balbi, A.; Coriani, S.; Giovannini, T.; Goletto, L.; Haugland, T. S.; Hutcheson, A.; et al. e T 1.0: An open source electronic structure program with emphasis on coupled cluster and multilevel methods. *J. Chem. Phys.* **2020**, *152*, 184103.
(71) Geuzaine, C.; Remacle, J.-F. Gmsh: A 3-D finite element mesh generator with built-in pre- and post-processing facilities. *Int. J. Numer. Meth. Eng.* **2009**, *79*, 1309−1331.
(72) Mandal, A.; Montillo Vega, S.; Huo, P. Polarized Fock states and the dynamical Casimir effect in molecular cavity quantum electrodynamics. *J. Phys. Chem. Lett.* **2020**, *11*, 9215−9223.

https://doi.org/10.1021/acs.nanolett.3c00735
Nano Lett. 2023, 23, 4938−4946

Supporting information: Effective single-mode methodology for strongly coupled multimode molecular-plasmon nanosystems

Marco Romanelli,[†,#] Rosario Roberto Riso,[‡,#] Tor S. Haugland,[‡] Enrico Ronca,[¶] Stefano Corni,[*,†,§,‖] and Henrik Koch[*,‡,⊥]

†*Department of Chemical Sciences, University of Padova, via Marzolo 1, 35131 Padova, Italy*

‡*Department of Chemistry, Norwegian University of Science and Technology, 7491 Trondheim, Norway*

¶*Department of Chemistry, Biology and Biotechnology, University of Perugia, Via Elce di Sotto, 8, 06123, Perugia, Italy*

§*CNR Institute of Nanoscience, via Campi 213/A, 41125 Modena, Italy*

‖*Padua Quantum Technologies Research Center, University of Padova, 35131 Padova, Italy*

⊥*Scuola Normale Superiore, Piazza dei Cavalieri 7, 56126 Pisa, Italy*

#*These authors equally contributed to the work*

E-mail: stefano.corni@unipd.it; henrik.koch@sns.it

1 Additional numerical tests on the H_2 case

1.1 Numerical convergence of Rabi splitting

We checked whether results reported in Fig.3 (main text) are converged with respect to the number of modes included in the Hamiltonian. Notably, the molecule-mode coupling value decreases as the mode order increases (see Fig.S1a). This is due to the fact that higher-order modes feature charge distributions that vary so rapidly over space that the molecule does not feel any net electric field. Consequently, the corresponding Rabi splitting including more and more modes rapidly converge (see Fig.S1b).

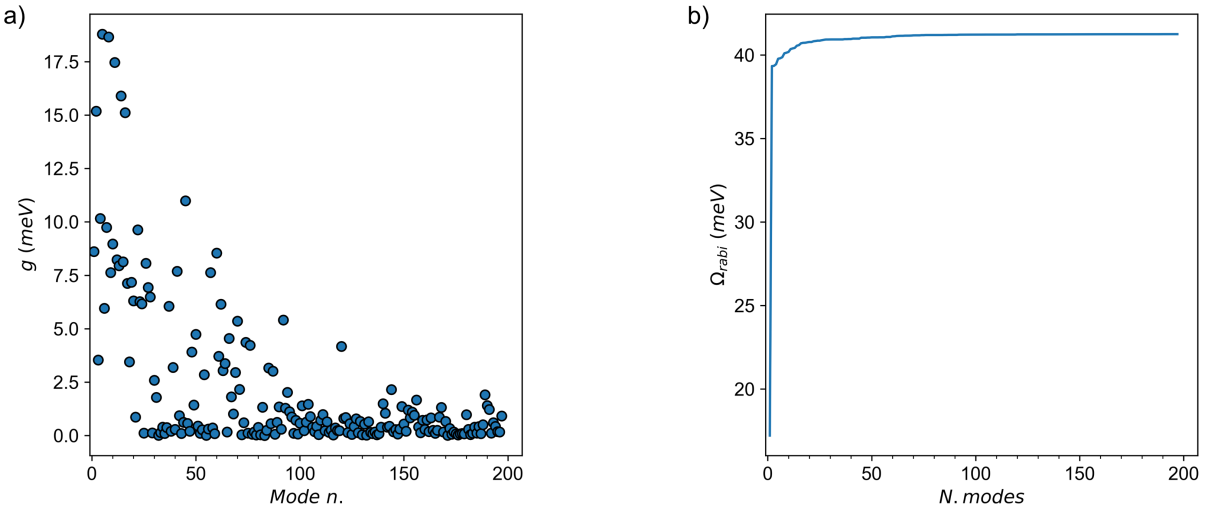

Figure S1: a) Computed coupling between the H_2 molecular transition and a given mode n. The progression goes from low-order mode, such as dipolar ones, up to high-order multipolar modes. b) Computed Jaynes-Cummings Rabi splitting as a function of the number of plasmonic modes included in the Hamiltonian, whose correspoding coupling with the molecule is reported in panel a).

1.2 Effect of NPs shape on Rabi splitting and effective mode

In this section we tested the performance of the effective mode approach on a setup similar to the one used in Fig.1 (main text) except for the aspect ratios (AR) of the ellipsoidal nanoparticles. In particular, an AR decrease (Fig.S2) leads to the well-know blue-shift of

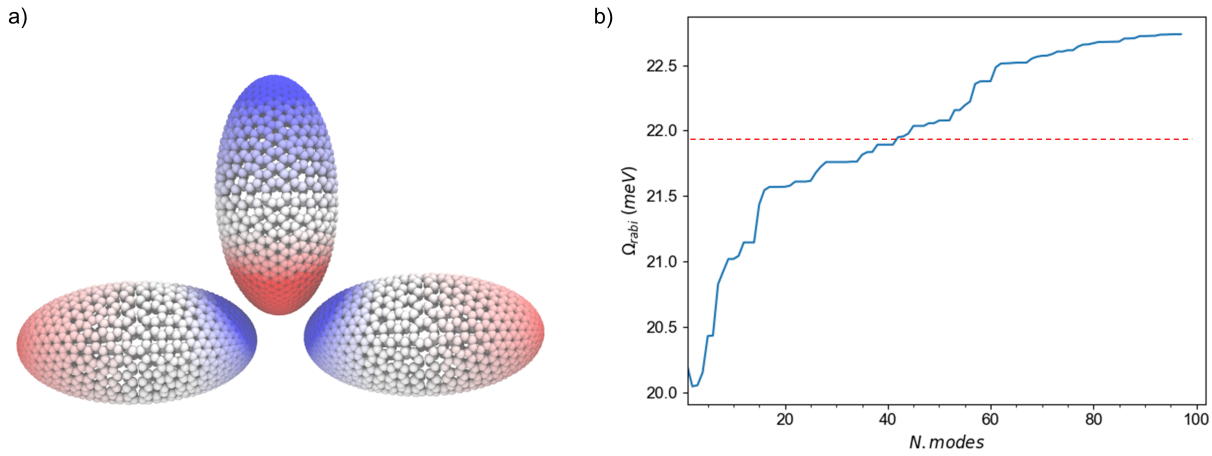

Figure S2: a) Lowest plasmon mode obtained with three ellipsoidal NPs arranged as in Fig.1 (main text), but having a smaller aspect ratio ($AR = 2$). Each NP of Fig.1 (main text) features an aspect ratio of $AR = 3$. The decrease of AR leads to a blue-shift of all modes frequencies, in particular the lowest mode shown now lies ≈ 200 meV above the H_2 molecular transition. b) Jaynes-Cummings rabi splitting as a function of n. of modes included in the Hamiltonian (blue line) obtained after shifting all modes frequencies of system a) such that the lowest mode gets in resonance with the H_2 transition. The horizontal steps in the rabi splitting trend comes from modes that do not couple to the molecule, thus not contributing to the polaritonic splitting. The red-dashed line is the corresponding QED-CC effective mode result.

the corresponding dipolar plasmon modes, leading to a situation where the H_2 molecular transition is non-resonant with the plasmonic modes.

If all modes frequencies obtained with the setup of Fig.S2a are shifted such that the lowest mode gets in resonance with the H_2 molecular transition, we end up with a situation where a proper Rabi splitting can be measured (Fig.S2b). However, in this case higher-energy modes do not add a significant contribution to the Rabi splitting (indeed in going from $1 \rightarrow 100$ modes the corresponding rabi splitting changes by just ≈ 3 meV). The reason for this is that the AR decrease not only induces a blue-shift of modes frequencies, but also increase the mode-mode energy separation. Only the lowest plasmonic mode, therefore, is in resonance with the molecular transition and significantly contributes to the splitting. The others modes are too high in energy to provide sizeable mixing.

1.3 Transition dipole asymptotic behaviour

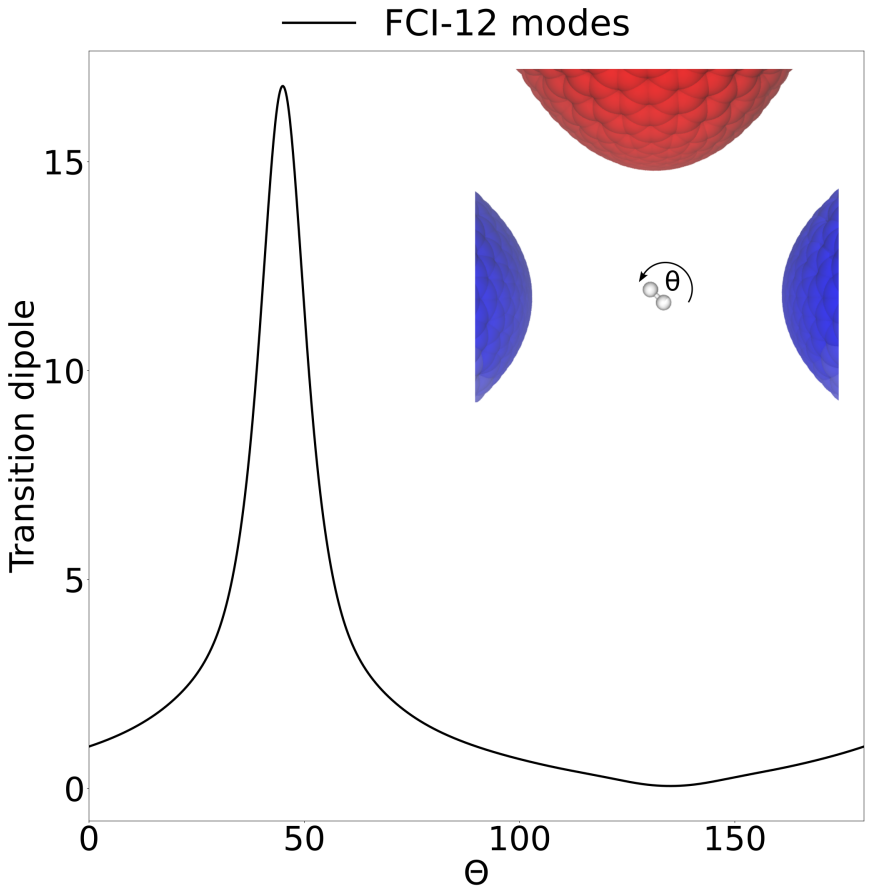

Figure S3: Dispersion with respect to the hydrogen orientation of the $\frac{d_y}{d_z}$ ratio for the lower polariton in the setup of Figs. 1-3 main text. $\Theta = 0$ corresponds to the initial geometry of Fig.1 where the H_2 molecule is inclined at 45°.

In Fig.4 of the main text, we display how the ratio between the y and z components of the transition dipole is affected by the multimode description. In particular, we observe that when the H_2 molecule is inclined at 45°, the $\frac{d_y}{d_z}$ ratio at the QED-FCI level is a bit above one for the LP and a bit lower than one for the UP. Every mode changes the value of the $\frac{d_y}{d_z}$ ratio (some significantly, some to a lesser extent). This is because, while in vacuum $\frac{d_y}{d_z}$ for the H_2 molecule is exactly equal to one, every new mode adds some spacial anisotropy differentiating between the y and z directions. Since in the strong coupling regime the

plasmons influence the molecular structure, the setup anisotropy is reflected in the behaviour of the electronic property. The aforementioned nanoparticle anisotropy is easily visualized from the two main modes reported in Fig.2 of the main text, whose transition dipoles lie on y and on z respectively. The dispersion of $\frac{d_y}{d_z}$ with respect to the hydrogen orientation is shown in Fig.S3. All significant modes have been included in the QED-FCI calculations and only the lower polariton dispersion has been plotted, as the upper polariton shows the same qualitative behaviour. We observe that by and large the geometrical features remain prevalent, with a maximum when the molecule is oriented on y (45°) and a minimum when the H-H bond is oriented along z (135°).

1.4 Different molecule spatial location

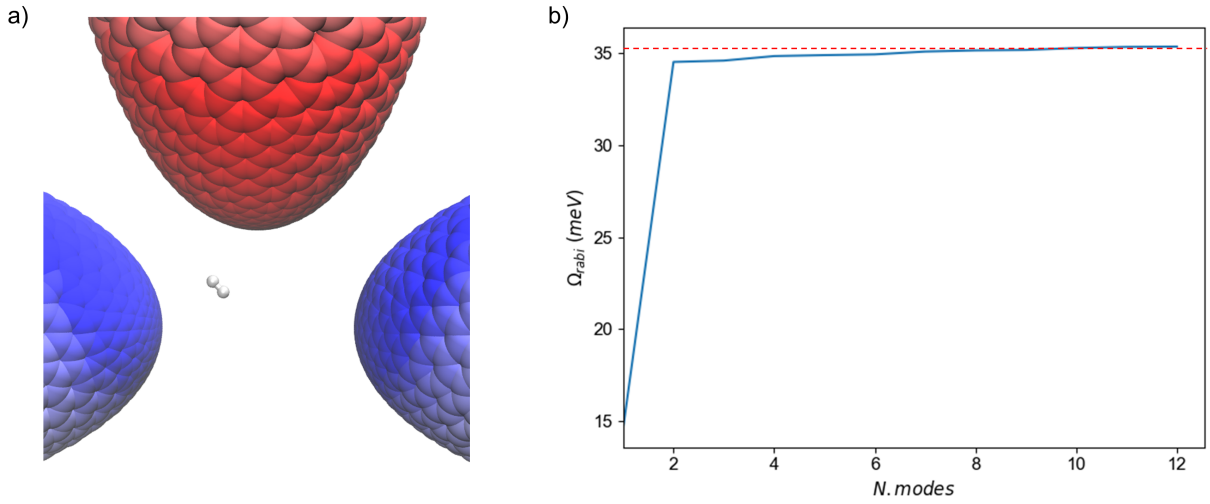

Figure S4: a)Same NPs setup shown in Fig.1 main text, but with the H_2 molecule shifted closer to two NPs edges, away from the center. b) Multimode JC Rabi splitting as a function of the number of modes included in the Hamiltonian (blue curve) obtained with setup shown in panel a) and corresponding QED-CC effective mode results (red dashed line). Only modes significantly coupled to the molecular transition have been considered, as in Fig.3 main text.

Analogous calculations to those shown in main text Figs.1-3 have been repeated with same NPs setup but different molecule location, i.e. by displacing the H_2 molecule closer to two NPs edges, see Fig.S4a. Both the multimode Jaynes-Cummings and QED-effective

mode results (Fig.S4) do not change qualitatively compared to what is shown in Fig.3 (main text). We just note that the Rabi splitting observed with such a molecular displacement is smaller compared to the case where the H_2 is placed exactly at center of the three NPs (main text, Figs. 1-3).

1.5 Weak coupling regime

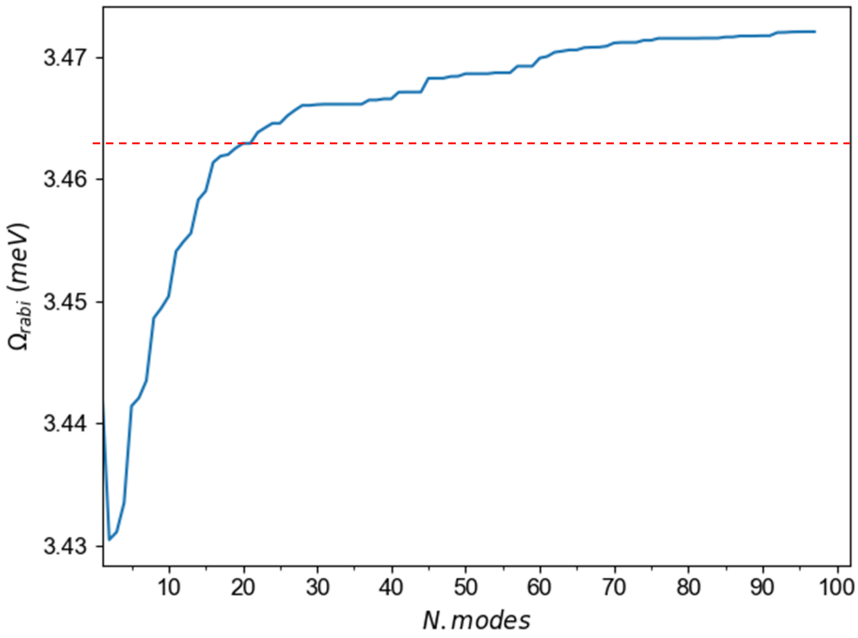

Figure S5: JC Rabi splitting as a function of the number of modes included in the Hamiltonian obtained using the same setup of Fig.1 (main text), but scaling the corresponding modes-molecule coupling values to be in the weak coupling regime. The red-dashed line is the effective mode result.

Based on the setup shown in Fig.1 (main text), we additionally test our effective mode scheme in the weak coupling limit, that has been artificially obtained by scaling the corresponding mode-molecule coupling values by 1/5 (physically speaking this screening effect could be induced by enlarging the NPs-molecule distance, for instance). The results are shown in Fig.S5, which clearly represent a typical weak coupling situation since the maximum Rabi splitting achieved is in the order of $\approx 3.5\ meV$, thus making it practically

negligible. Besides, we note that in this case the effective mode correction, although improving over the one mode case, is not essential. Indeed, going from $1 \rightarrow 100$ modes, the predicted Rabi splitting only changes by $\approx 0.04\ meV$. In this situation, a semiclassical description would be enough to properly describe purely molecular properties (such as excitation energies and excited state decay rates) influenced by the presence of the plasmons.[1] Moreover, a semiclassical approach would also allow for the explicit inclusion of all mode effects, since they are intrinsically embodied in the classical response function.[1,2]

2 PNA Rabi splitting: multimode effects

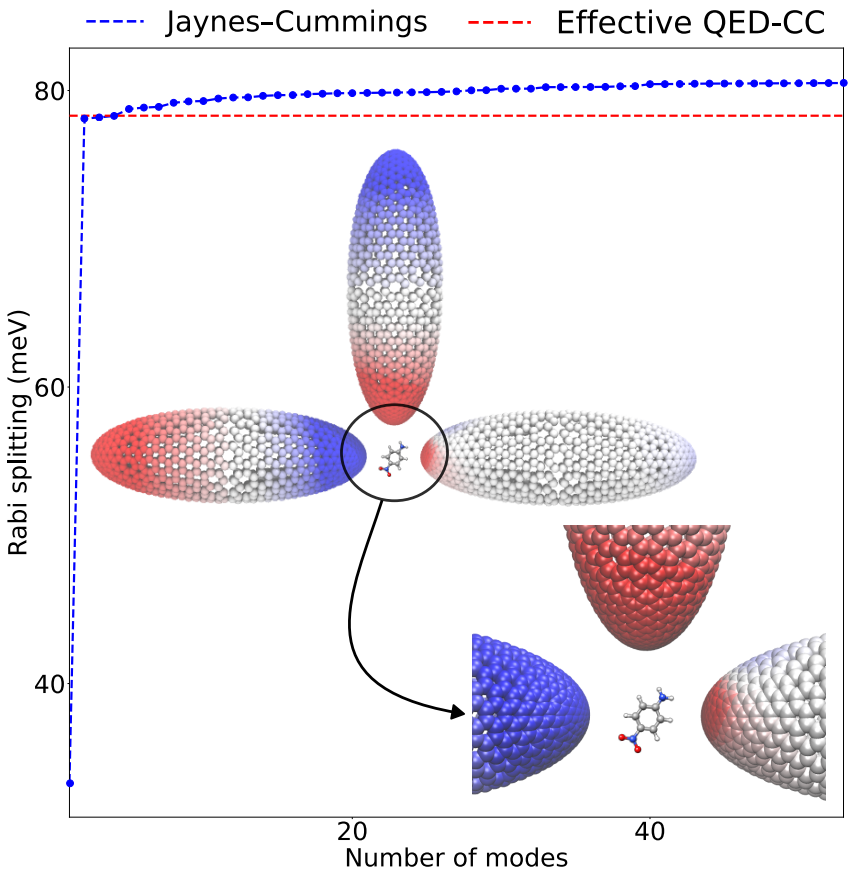

Figure S6: Computed Rabi splitting for a setup of 3 ellipsoidal NPs surrounding a PNA molecule. The average distance from the metallic surfaces is ≈ 0.6 nm (setup shown as inset). The dashed blue line are the results obtained through the multimode Jaynes-Cummings Hamiltonian (see Eq.5, main text), whereas the red one is the outcome of the QED-CC effective mode approach. Visualization of the optimized effective mode is shown in the inset.

3 Computational details

We first tested the effective mode methodology for H_2 in order to make direct comparisons with QED-FCI benchmark calculations (larger systems would not have been computationally feasible). The surface meshes were created using the Gmsh code[3] and consist of $\approx$ 4500

tesserae. The Drude-Lorentz parameters used to define the metal dielectric function are $\Omega_P = 8.605$ eV, $\gamma = 0.217$ eV and $\omega_0 = 12.517$ eV, which is very close to the value adopted for silver in previous literature works.[4] The damping rate and the natural frequency of the oscillator were chosen such that the NPs lowest plasmon mode is resonant with the H_2 $S_0 \rightarrow S_1$ molecular transition, around 12.7 eV according to CCSD/aug-cc-pVDZ calculations in vacuum.[5–7] In order to avoid fictitious charge transfer effects between the nanoparticles, an *a posteriori* charge normalization scheme, described in Ref.,[8] has been applied to each NP.

A similar setup was used for testing the effective mode performance with the PNA molecule since it features a richer molecular structure and is relevant for practical applications.[9,10] This time ω_0 was set to 4.354 eV such that the first plasmonic modes match the first transition of PNA at approximately 4.8 eV, according to CCSD/cc-pVDZ.[5–7] The electronic calculations were performed using a development version of the eT program.[11]

References

(1) Fregoni, J.; Haugland, T. S.; Pipolo, S.; Giovannini, T.; Koch, H.; Corni, S. Strong Coupling between Localized Surface Plasmons and Molecules by Coupled Cluster Theory. *Nano Lett.* **2021**, *21*, 6664–6670.

(2) Corni, S.; Pipolo, S.; Cammi, R. Equation of Motion for the Solvent Polarization Apparent Charges in the Polarizable Continuum Model: Application to Real-Time TDDFT. *J. Phys. Chem. A* **2015**, *119*, 5405–5416.

(3) Geuzaine, C.; Remacle, J.-F. Gmsh: A 3-D finite element mesh generator with built-in pre- and post-processing facilities. *Int. J. Numer. Meth. Eng.* **2009**, *79*, 1309–1331.

(4) Zeman, E. J.; Schatz, G. C. An accurate electromagnetic theory study of surface enhancement factors for silver, gold, copper, lithium, sodium, aluminum, gallium, indium, zinc, and cadmium. *J. Phys. Chem.* **1987**, *91*, 634–643.

(5) Pritchard, B. P.; Altarawy, D.; Didier, B.; Gibsom, T. D.; Windus, T. L. A New Basis Set Exchange: An Open, Up-to-date Resource for the Molecular Sciences Community. *J. Chem. Inf. Model.* **2019**, *59*, 4814–4820.

(6) Dunning, T. H. Gaussian basis sets for use in correlated molecular calculations. I. The atoms boron through neon and hydrogen. *J. Chem. Phys.* **1989**, *90*, 1007–1023.

(7) Kendall, R. A.; Dunning, T. H.; Harrison, R. J. Electron affinities of the first-row atoms revisited. Systematic basis sets and wave functions. *J. Chem. Phys.* **1992**, *96*, 6796–6806.

(8) Romanelli, M.; Dall'Osto, G.; Corni, S. Role of metal-nanostructure features on tip-enhanced photoluminescence of single molecules. *J. Chem. Phys.* **2021**, *155*, 214304.

(9) Alturki, A. A.; Alharbi, A. F.; Zoromba, M. S.; Abdel-Aziz, M.; Al-Hossainy, A. Poly-

meric solar cell with 18.06poly(para-nitroaniline)/TiO2 composites. *Opt.* **2023**, *136*, 113502.

(10) Ito, S.; Chen, P.; Comte, P.; Nazeeruddin, M. K.; Liska, P.; Péchy, P.; Grätzel, M. Fabrication of screen-printing pastes from TiO2 powders for dye-sensitised solar cells. *Prog. Photovolt.* **2007**, *15*, 603–612.

(11) Folkestad, S. D.; Kjønstad, E. F.; Myhre, R. H.; Andersen, J. H.; Balbi, A.; Coriani, S.; Giovannini, T.; Goletto, L.; Haugland, T. S.; Hutcheson, A., et al. e T 1.0: An open source electronic structure program with emphasis on coupled cluster and multilevel methods. *J. Chem. Phys.* **2020**, *152*, 184103.

Chapter 4.

Sub-picosecond collapse of molecular polaritons to pure molecular transition in plasmonic photoswitch-nanoantennas

As shown in the previous chapters, single-molecule manipulation is nowadays possible thanks to extremely-sophisticated experimental apparatus. Nevertheless, that accurate control over single molecules is only possible under extreme conditions, such as cryogenic temperatures and ultra-high vacuum, thus making it far from possible real life applications, where often large numbers of molecules in less-controlled conditions are involved. In this view, investigating collective effects arising from the interaction between an ensemble of molecules and plasmonic systems under mild conditions is of utmost importance.

In this chapter, which is reported as a published article in *Nature Communications*, a collective plexcitonic state originating from a collection of merocyanine molecules strongly coupled to plasmonic alluminum nanoellipses at room temperature is investigated by combining theory and experiments. The purpose of this work is to directly probe such system at ultrafast timescales (sub-picosend regime), where plasmon dynamics take place. It is indeed well-known[1] that upon excitation of LSPR transitions plasmon dephasing quickly occurs, approximately in ≈ 10 fs from the initial excitation, later leading to a series of dissipative processes that eventually result in dissipation of the LSPR initial energy. Therefore, the possibility of using plasmonic systems to ultimately tailor molecular photochemistry thanks to strong plasmon-molecule coupling is still elusive, given that most photochemical reactions proceed on longer timescales[2]. The core idea of this work, which has been done in collaboration with the experimental groups of Prof. Nicolò Maccaferri (Umeå University, Sweden) and Prof. Alexandre Dmitriev (University of Gothenburg, Sweden), is to directly probe the ultrafast dynamics of collective plexciton states after initial optical pumping, in order to understand how the resulting molecular electron dynamics is affected by ultrafast plasmon dephasing. Noteworthily, by combining theoretical simulations and pump-probe experiments, it is disclosed that the collective plexciton state that is populated upon optical pumping collapses to a singly-excited molecular state due to plasmon dephasing. The resulting temporal dynamics that is actually probed is ascribed to an intramolecular excited state dynamics which is accelerated with respect to isolated molecules due to the interaction with the plasmonic local field.

In this work I took care of developing and implementing the theoretical model that has been used to simulate the experimental data. All simulations and code developments were done by me under the supervision of Dr. Jacopo Fregoni and Prof. Stefano Corni. I wrote a first draft of the theory part of the manuscript and I created the corresponding figures as well. Further text refinements as well as replies to referee's comments related to theoretical modelling were addressed by me under the supervision of Dr. Jacopo Fregoni and Prof. Stefano Corni.

References

(1) Koya[†], A. N.; Romanelli[†], M.; Kuttruff[†], J.; Henriksson[†], N.; Stefancu[†], A.; Grinblat[†], G.; De Andres[†], A.; Schnur[†], F.; Vanzan[†], M.; Marsili[†], M.; Rahaman[†], M., et al. *Applied Physics Reviews* **2023**, *10*, 021318.

(2) Turro, N. J., *Modern molecular photochemistry*; University science books: 1991.

nature communications

Article

https://doi.org/10.1038/s41467-023-39413-5

Sub-picosecond collapse of molecular polaritons to pure molecular transition in plasmonic photoswitch-nanoantennas

Received: 7 February 2023

Accepted: 9 June 2023

Published online: 06 July 2023

Check for updates

Joel Kuttruff[1,11], Marco Romanelli[2,11], Esteban Pedrueza-Villalmanzo[3,4,11], Jonas Allerbeck[1,5], Jacopo Fregoni[6], Valeria Saavedra-Becerril[4], Joakim Andréasson[4], Daniele Brida[7], Alexandre Dmitriev[3] ✉, Stefano Corni[2,8] ✉ & Nicolò Maccaferri[7,9,10] ✉

Molecular polaritons are hybrid light-matter states that emerge when a molecular transition strongly interacts with photons in a resonator. At optical frequencies, this interaction unlocks a way to explore and control new chemical phenomena at the nanoscale. Achieving such control at ultrafast timescales, however, is an outstanding challenge, as it requires a deep understanding of the dynamics of the collectively coupled molecular excitation and the light modes. Here, we investigate the dynamics of collective polariton states, realized by coupling molecular photoswitches to optically anisotropic plasmonic nanoantennas. Pump-probe experiments reveal an ultrafast collapse of polaritons to pure molecular transition triggered by femtosecond-pulse excitation at room temperature. Through a synergistic combination of experiments and quantum mechanical modelling, we show that the response of the system is governed by intramolecular dynamics, occurring one order of magnitude faster with respect to the uncoupled excited molecule relaxation to the ground state.

Hybrid light-matter polaritonic states arise as a consequence of a coherent energy exchange between the confined electromagnetic field in resonators and the radiating transitions in molecules or, more in general, quantum emitters. The associated strong modification of the energy levels offers tantalizing opportunities of tuning various fundamental properties of matter, such as molecular chemical reactivity or electrical conductivity. As such, the so-called strong coupling regime holds a key potential in a broad range of fields, such as all-optical logic[1,2], lasing[3], superfluidity[4], chemistry[5], and quantum computing[6,7]. The fundamental requirement for strong coupling lies in boosting the light-emitter interaction to such an extent that the coherent energy exchange between light and emitters becomes greater than the individual decay rates. Such boost can be achieved by either resorting to a large number of emitters or by confining the electromagnetic field to sub-wavelength volumes. For the former, the most common resonators are photonic cavities, where the

[1]Department of Physics, University of Konstanz, Universitätsstraße 10, 78464 Konstanz, Germany. [2]Department of Chemical Sciences, University of Padova, via Marzolo 1, 35131 Padova, Italy. [3]Department of Physics, University of Gothenburg, Origovägen 6B, 412 96 Gothenburg, Sweden. [4]Department of Chemistry and Chemical Engineering, Chalmers University of Technology, Kemigården 4, 412 96 Göteborg, Sweden. [5]nanotech@surfaces Laboratory, Empa, Swiss Federal Laboratories for Materials Science and Technology, Überlandstrasse 129, 8600 Dübendorf, Switzerland. [6]Department of Physics, Universidad Autónoma de Madrid, Ciudad Universitaria de Cantoblanco, 28049 Madrid, Spain. [7]Department of Physics and Materials Science, University of Luxembourg, 162a avenue de la Faïencerie, L-1511 Luxembourg, Luxembourg. [8]CNR Institute of Nanoscience, via Campi 213/A, 41125 Modena, Italy. [9]Department of Physics, Umeå University, Linnaeus väg 24, 901 87 Umeå, Sweden. [10]Umeå Centre for Microbial Research, Umeå University, 901 87 Umeå, Sweden. [11]These authors contributed equally: Joel Kuttruff, Marco Romanelli, Esteban Pedrueza-Villalmanzo. ✉e-mail: alexd@physics.gu.se; stefano.corni@unipd.it; nicolo.maccaferri@umu.se

electromagnetic field is confined by metallic mirrors (e.g, Fabry-Pérot cavities[8] or multilayer heterostructures[9]), and polaritons emerge as collective excitations between the light modes and the ensemble of emitters (~10^6–10^{10} molecules). For the latter, sub-wavelength confinement of light has been historically achieved by exploiting plasmonic architectures[10], and more recently also all-dielectric nanostructures[11–14]. In the context of plasmonics, near-field enhancement of the electromagnetic field is possible via localized surface plasmon resonances (LSPRs) with an effective mode volume of 1–100 nm^3 [15,16], thus allowing the formation of polaritons even with a relatively limited number of emitters (from a single emitter to 10^3). Due to the broad range of potential applications, the nature of polaritonic states formation and dynamics have been extensively researched over the last decade[17]. Coherent time-domain control of the reversible energy exchange between photons and matter, referred to as Rabi oscillations, has been demonstrated in J-aggregates and metal nanostructures[18], and for semiconductor quantum wells in a microresonator[19]. As well, various incoherent pathways to modify the polaritonic states on ultrafast timescales have been investigated, including charge transfer[20,21], saturation of semiconductor transitions[22], and ground-state bleaching in molecular systems[23–25].

The emerging branch of chemistry using strong coupling to modify chemical reactions is referred to as polaritonic chemistry[26]. There, polaritonic states have been applied to selectively suppress or enhance chemical reactions both in the ground and the excited states[27–30], opening up new chemical reaction pathways, including, among others, remote chemistry[31], singlet fissions[32], and selective isomerization[33–35]. Such manipulation of photochemistry makes use of the strong coupling with light to rearrange the electronic energy levels of molecules[36,37]. Achieving such control on ultrafast timescales promises many emerging applications combining ultrafast optics and light-driven chemistry[38]. This is exceptionally motivating in the context of molecular photoswitches that have already shown potential for inkless paper[39], stimuli-responsive materials[40], self-healing polymers[41], and all-optical switching[42], due to the ability to externally alter their molecular structure by light. One of the most famous photoswitches is spiropyran, which exist in a spiro (SP) and a merocyanine (MC) isomer. UV light triggers the SP→MC isomerization, whereas the reverse reaction is induced by visible light. These compounds display intriguing properties as ultrafast molecular photoswitches, due to the sub-ps kinetics associated with their molecular interconversion[43], and might be key elements to implement future all-optical molecular transistor technologies. The signature feature of the MC form is the emergence of a strong $\pi - \pi^*$ absorption resonance in the visible spectrum[44]. While the evidence that strong coupling with the $\pi - \pi^*$ transition modifies the SP-MC photoconversion rate is a milestone for polaritonic chemistry[36], the opportunities for this system at ultrafast timescales are still unexplored.

Here, we devise an archetypical platform capable of selectively accessing the weak and strong coupling regimes and follow the polariton dynamics after impulsive femtosecond-laser excitation. The platform consists in an array of two-mode anisotropic plasmon antennas and spiropyran photoswitches converting to MC form via continuous UV irradiation. To track the role of the coherent plasmon-molecules interaction on ultrafast timescales, we follow the time-evolution of polaritonic states with pump-probe experiments, where the dynamics of the strong coupling is referenced to the weak coupling in the exact same system. Quantum simulations, comprising a theoretical framework based on extending the original Tavis-Cummings Hamiltonian[45] allow us to interpret the experimental findings assuming changes in the fundamental properties of the coupled system. Our experimental and theoretical analysis reveals an ultrafast modification of the polaritonic state composition, identifying the main relaxation channel as the localization of the initial polaritonic coherent excitation on a molecular excitation. Intramolecular dynamics leads to sub-ps changes of the polaritonic state manifold, one order of magnitude faster than expected from the pure transition time of excited molecules back to the ground state. Revealed sub-ps timescale control of the chemical energy landscape is crucial to advance polaritonic chemistry to the ultrafast regime.

Results

We employ anisotropic aluminum nanoellipse antennas (see Methods and Supplementary Note 1 for fabrication details), displaying two orthogonal and spectrally separated LSPRs. A polystyrene nanofilm containing the spiropyran molecules (initially in the SP isomeric form) is spin-coated on top of the nanoantennas and subsequently irradiated with UV light to photo-isomerize the molecules to the MC configuration. The nanoantennas are designed such that the MC molecular absorption is resonant with the long-axis LSPR, whereas it is detuned from the short-axis LSPR, giving rise to strong and weak coupling regimes, respectively. The steady-state optical response of the hybrid system is shown in Fig. 1 for excitation along the long axis (sketched in Fig. 1a) and short axis (sketched in Fig. 1b) of the nanoantennas, respectively. While only the plasmon contribution is visible for the long axis case before UV irradiation (no MC isomers present, orange curve in Fig. 1c), lower (LP) and upper (UP) polaritonic states immediately emerge (black curve in Fig. 1c) upon UV-induced photoconversion of SP to MC, with the corresponding activation of the $\pi - \pi^*$ MC molecular transition. This is a characteristic signature of the system entering the strong coupling regime, or at least being at its onset[46–48]. Conversely, when excited along the short axis (Fig. 1d), the spectrum of the coupled plasmon-MC system (black curve) is governed by the superposition of LSPR (pink curve) and the molecular absorption. In this case, the plasmon with low extinction efficiency is out-of-resonance with the molecular transition, leading to two spectral peaks simply superimposing on each other. The absence of notable shifts of the absorption peaks with respect to the bare states in this case signals the weak-coupling regime. To distinguish between the two regimes, we analyze with a full quantum model the modification of the energies of molecular electronic states due to the interaction with the nanoantenna plasmon modes. First, in order to simulate the SP and MC linear absorption spectra (experimental spectra are shown in the inset in Fig. 1d, simulations can be found in Supplementary Note 2.1), the respective molecular ground state geometries are optimized (see Supplementary Fig. 5), and the vertical excitation energies to the first eight excited states of each isomer are calculated. The S_1 excited state of MC is then optimized at the same level of theory (in a solvent mimicking the polymer matrix), yielding the relaxed configuration of MC in the S_1 state minimum (see Supplementary Fig. 6). The electronic energy associated to this point is ~0.4 eV lower than the vertical excitation energy at the ground state geometry, meaning that the molecule is not in its equilibrium configuration upon vertical excitation from S_0 to S_1. Interactions between different MC molecules and the nanoantennas is evaluated by means of an ad-hoc quantum model, which extends the original Tavis-Cummings (TC) Hamiltonian[49] by explicitly quantizing the modes of arbitrarily shaped nanoparticles[50]. The choice of this modeling strategy comes from the fact that the nanoantennas do not display any sophisticated geometrical features that may lead to "picocavity" formation[51] and the associated single-molecule strong coupling effects. Hence, investigating collective molecular phenomena while retaining the geometrical shape of the nanoantennas is required in this case. The calculations (Fig. 1e, f) corroborate the interpretation of the experimental spectra (more details on the theoretical model can be found in the Methods section and in the SI. In the latter, a quantitative discussion on the two coupling regimes is reported, see Supplementary Note 2.2).

After assessing that the system can enter the strong coupling regime by driving the long-axis LSPR, pump-probe measurements are performed on the hybrid system in both weak and strong coupling

https://doi.org/10.1038/s41467-023-39413-5

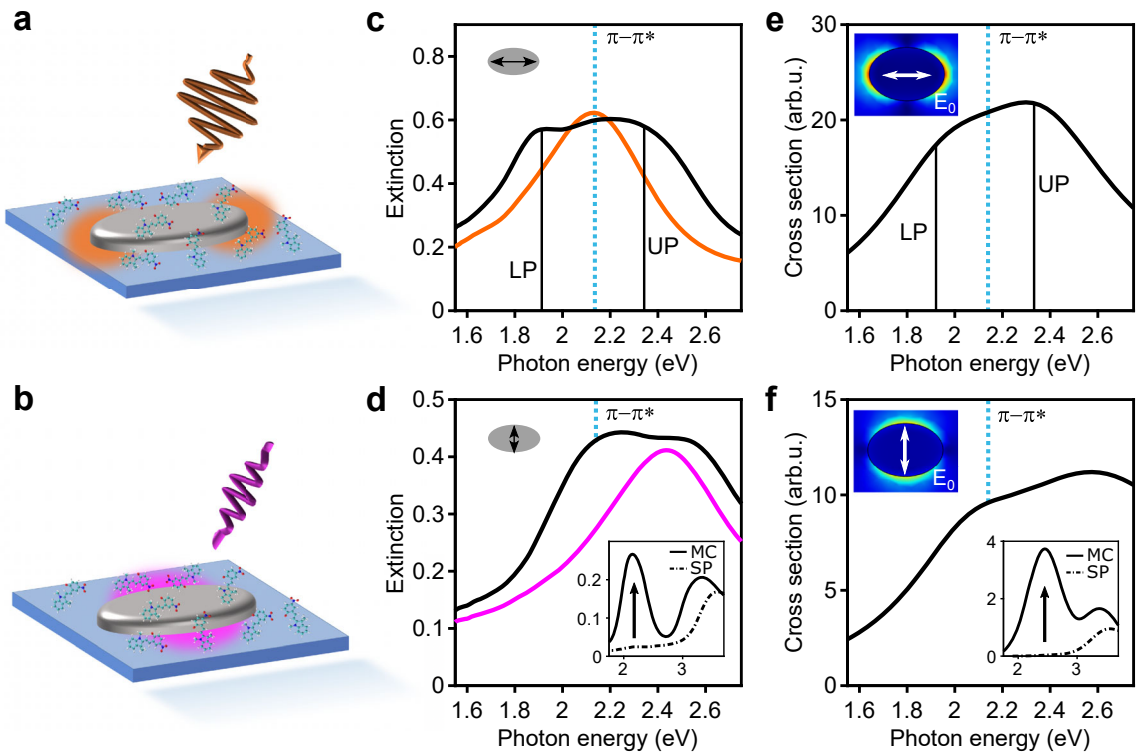

Fig. 1 | Hybrid system consisting of photo-switchable molecules and aluminum nanoellipse. a, **b** Sketch of the localized plasmon dipolar excitation along the long (**a**) and short (**b**) axes of the nanoantenna. The plasmon near fields are schematically indicated by hot spots (orange and pink) in the sketch. **c**, **d** Experimental extinction spectra for the long axis (**c**) and the short axis (**d**) before (colored) and after (black) UV-induced photoswitching of the spiro isomer (SP) to the merocyanine isomer (MC). The inset in **d** shows the absorption of a molecular film before (dash-dotted) and after (solid) UV irradiation, where the π–π^* molecular absorption emerges at 2.15 eV (also indicated by the blue dotted lines). **e**, **f** Absorption cross sections obtained from our model Hamiltonian for long (**e**) and short (**f**) axis excitation of the hybrid system. Bottom inset in **f** shows the simulated molecular absorption cross section obtained after ground state optimizations of the molecular structure in the SP (dash-dotted) and MC (solid) configurations. Top insets show confined electric near fields at both plasmonic resonances calculated using the finite elements method.

regimes and referenced to a UV-exposed film (to trigger the SP→MC isomerization) of pristine spiropyran molecules, i.e., without the presence of the nanoantennas, as well as to the antenna array without UV switching the molecular film to the MC form.

The ultrafast response in all four cases (pristine molecules, antennas immersed in SP, molecules weakly coupled, and molecules strongly coupled to the nanoantennas LSPRs) is studied using a two-color pump-probe scheme based on a broadly tunable fs-laser spectroscopy platform operating at multi-kHz repetition rate[52]. Pump pulses with a temporal duration of 50 fs are tuned to photon energy of 2.3 eV, that is above the $\pi - \pi^*$ transition of the MC molecular form. Time delayed broadband probe pulses span a spectral range from 1.75 eV to 2.5 eV and are compressed to below 20 fs duration. The pump-induced change of probe transmission $\Delta T/T$ is monitored for various time delays Δt between pump and probe pulses (see "Methods" section for more details). We first studied the transient transmission of the bare MC film (see Fig. 2). Figure 2a shows $\Delta T/T$ as a function of Δt and the probe photon energy. For positive Δt, a broadband positive signal can be observed, indicating a transient bleaching of the molecular absorption, as previously observed for instance in ref. 53.

Such bleaching provides a direct measurement of the S_1 excited state population at each time, since less photons can be absorbed by the remaining molecules in the MC ground state. In Fig. 2b, we plot spectral cuts of the 2D map shown in Fig. 2a. A clear red-shifting of $\Delta T/T$ with increasing Δt can be observed (see Supplementary Note 3.2. for more details). This can be explained by probe-stimulated photoemission taking place during vibrational relaxation from the Franck-Condon point (where the molecule is vertically excited) toward the S_1 minimum, as sketched in Fig. 2c. The left panel in Fig. 2c shows the excitation of MC into the Franck-Condon configuration of the S_1 state. The molecular structure then relaxes to a lower energy configuration, subsequently leading to the observed redshift due to the stimulated emission back into the ground state (right panel). From the experiment, we find a maximum spectral shift of +0.25 eV, consistent with the value obtained theoretically (+0.4 eV; see also Supplementary Fig. 6).

In the pump-probe experiments on the antennas without UV-induced switching of the molecular film to the MC form, we see that the contribution of the antennas to the transient signal is at least one order of magnitude reduced compared to the response of the hybrid system (see discussion in Supplementary Note 3.3). This experiment is crucial to support that the effects observed in our experiments and reported hereafter really stem from the interaction of the plasmonic and molecular systems.

In Fig. 3, we show the ultrafast dynamics of the hybrid system upon light irradiation polarized either along the long or short axes of the nanoantennas, and using the same pump fluence as in the isolated molecules experiments discussed above. In general, sample geometry can lead to enhancement of certain spectral features in the ultrafast response of the specimen due to multiple interference, as observed for example in optical cavity strong coupling (see ref. 54.). In such cases, absolute absorption should be obtained via measuring both, transient reflection as well as transient transmission. In our simple geometry, however, interference is negligible in determining the ultrafast response and we can reliably use the transient change in transmission $\Delta T/T$ as a measure to follow the time-evolution of the polaritonic states. In particular, temporal and spectral dynamics are not affected by this choice.

https://doi.org/10.1038/s41467-023-39413-5

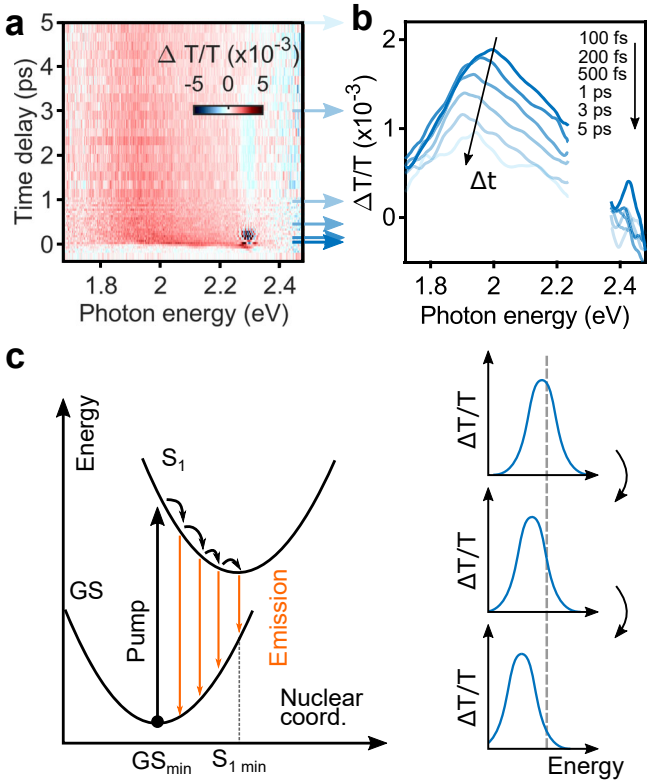

Fig. 2 | Ultrafast dynamics of the MC isomer. a Transient transmission signal as function of time delay between pump and probe pulses and probe photon energy. **b** Pump-probe spectra at increasing pump-probe delay (top to bottom) indicating a redshift of $\Delta T/T$. **c** Scheme of the wave packet relaxation dynamics on the S_1 excited state after the pump pulse. The red-shifting positive $\Delta T/T$ signal experimentally observed in panel **b** can be interpreted as stimulated emission from the S_1 surface while the system is relaxing towards the closest excited state minimum, S_1 min (left panel). Resulting $\Delta T/T$ spectra are schematically shown in the right panel.

The transient transmission for the long-axis pumping is shown in Fig. 3a as a function of Δt and the probe photon energy. For positive time delays, we observe a characteristic positive-negative-positive (red-blue-red) spectral shape. Furthermore, our time and energy resolutions allow to track the spectral evolution of $\Delta T/T$, as shown in Fig. 3b, where spectral cuts of the pump-probe 2D map (Fig. 3a) are plotted for increasing values of Δt. As indicated by the blue dashed arrow in Fig. 3b, we observe a blueshift of around 20 meV of the negative $\Delta T/T$ peak within 1 ps after the optical excitation. The observed positive-negative-positive transient spectral lineshape was previously reported, for example, in molecules vibrationally coupled to a cavity[23], so called plexcitonic systems[55], or in an excitonic transition coupled to a plasmonic lattice[20]. It can be interpreted as a shift of the absorption peaks towards each other, and thus a reduction of the spectral separation of the UP and LP bands, seen as negative differential transmission around 2.1 eV. While this may be intuitively understood as a pump-induced decrease of the number of molecules effectively coupled to the mode[36,56,57] – thus resulting in a reduction of the Rabi splitting – explaining the spectral time evolution of $\Delta T/T$ as shown in Fig. 3b requires a more advanced analysis. After impulsive optical excitation, the upper polariton states of the hybrid system are populated and quickly dephase within few tens of femtoseconds, well below the time resolution of our experiment (≈ 50 fs).

We then assume that the molecule contributing most to the polariton (some molecules are more coupled to the modes than others, depending on their distance and orientation with respect to the nanoantennas) starts to relax on its S_1 excited state, eventually resulting in a system composed by N-1 molecules in their ground state and one molecule vibrationally relaxing on its S_1 excited state. We remark that N here should be interpreted as the number of molecules in strong coupling with the given plasmon mode, rather than all irradiated molecules (see also Supplementary Note 2.2). Being in their ground state, the $S_0 \rightarrow S_1$ electronic transition for the N-1 remaining molecules is still resonant with the long-axis plasmon; instead, the relaxation of the individual molecule on its excited state entails a redshift of the stimulated emission (we note that this is the typical composition that can be obtained for a dark state).

The polaritonic energy landscape is thus transiently modified by the intramolecular dynamics of the individual molecule, observable as a spectral time evolution of $\Delta T/T$ probed by the delayed optical pulse. To interpret the experimental results, we simulated the transient signal by taking the difference between the absorption spectrum of the 1-excitation-space polaritons (shown in Fig. 1), which is the transient spectral signature of ground state bleaching (GSB), and the signal coming from the localized red-shifting excited molecular state. The latter term requires computing both the stimulated emission (SE) to the ground state and the absorption toward the 2-excitation-space polaritonic manifold (excited state absorption, ESA)[58]. These quantities are then combined according to Eq.1 (see Numerical calculations section), yielding the transient data of Fig. 3c, f. (note that ESA and SE contributions do have opposite signs). Here, we perform the 2-excitation-space calculations (see Methods section for additional details) for increasing energy shift of the molecular transition, thus resembling the vibrational relaxation of the molecular structure. The energy shift values are based on the TDDFT results and consistent with experimental energy shifts of Fig. 2. The 2-excitation calculations have been repeated for different frequency shifts of the target molecule, and can reproduce the blueshift of the transient signal observed experimentally. By tracking the spectral position of the negative dip in the $\Delta T/T$ spectra (Fig. 3b, c), we obtain blueshifts of ~20 meV in the experiment and 25 meV in the simulation. The time dynamics of the relaxation process is not directly simulated, but is modeled by fitting the experimental data, as described in Fig. 3 and related discussion in the Methods section.

Moreover, we emphasize that the spectral blueshift of $\Delta T/T$ within the first picosecond is not an optically induced shift, but rather originates from a molecular excited state energy shift due to vibrational relaxation. Notably, simulating the transient signal via calculation of both the 1- and 2-excitation-space polaritonic manifold can reproduce well both the positive-negative-positive motive of the experimental transient spectra and the slight blueshift of the negative peak at increasing Δt, as we show in Fig. 3c. The observed spectral evolution of $\Delta T/T$ can therefore be reasonably assigned to a molecular vibrational relaxation that affects the composition of the polaritonic states manifold.

A simplified sketch describing the resulting rearrangement of electronic energy levels upon optical pumping is depicted in Fig. 4. The origin of the positive-negative-positive motive follows from what was already anticipated above: the arrival wavefunction following the probe absorption in our modeling approach is dominated by the product state of an excited molecule state times the 1-excitation polariton of the remaining N-1 molecules ($^2UP/LP_{N-1}$ in Fig. 4c). The corresponding UP-LP splitting is therefore reduced compared to the ground state absorption, thus leading to the characteristic differential positive-negative-positive $\Delta T/T$ transient spectral signature. This is schematically represented in Fig. 4d where the peak-to-peak separation of the blue curves is smaller than the corresponding one of Fig. 4b, the latter showing the linear absorption spectral shape. Besides, note that SE is providing a minor contribution to the signal (see Supplementary Fig. 13 for explicit comparison of GSB, ESA, and SE contributions).

Upon vibrational relaxation, the state before probe absorption (red energy level of Fig. 4c) is decreasing its energy faster than what the

https://doi.org/10.1038/s41467-023-39413-5

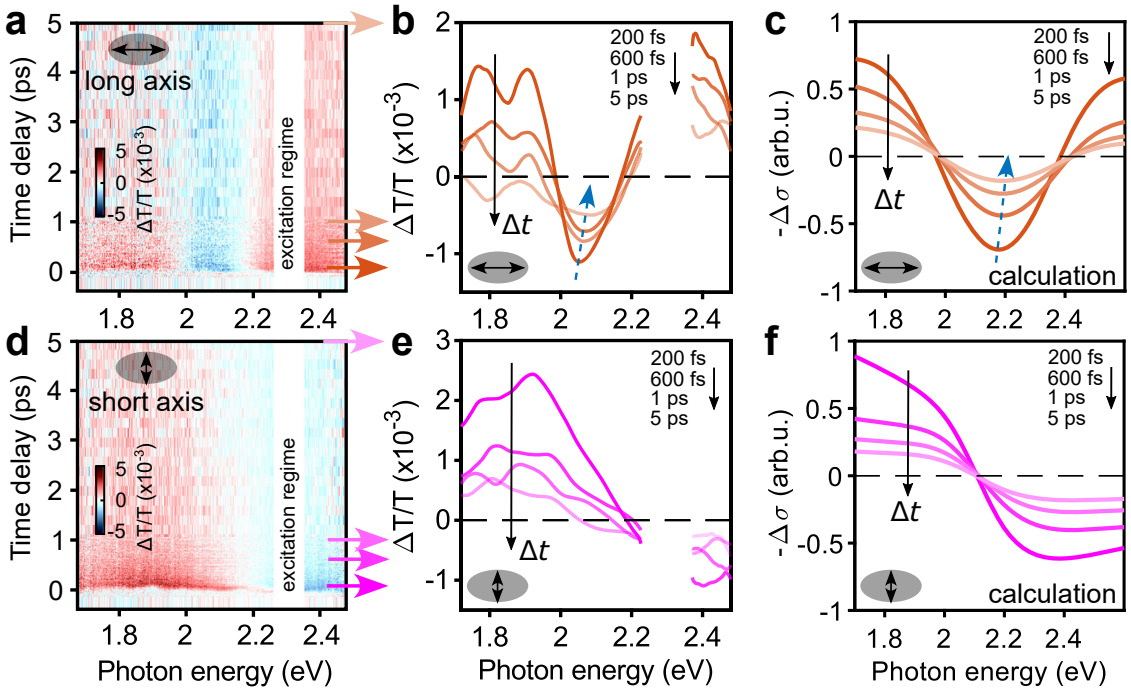

Fig. 3 | Ultrafast dynamics of the hybrid system in the strong and weak coupling regimes. a Transient transmission as function of time delay between pump and probe pulses and probe photon energy when excited along the long axis of the nanoantennas, where the longitudinal plasmon frequency is perfectly tuned to the excitation energy of the MC isomer. **b** Spectral cuts of the pump-probe map in **a** at 200 fs, 600 fs, 1 ps, and 5 ps. **c** Simulated transient response for the long-axis pumping case. We highlight that the plotted quantity -Δσ, which is the change in absorption cross section (with a minus sign) upon pumping, corresponds to transient transmissivity up to a constant multiplicative factor. Spectral dynamics are well reproduced by red-shifting the molecular transition of one MC (see sketch in Fig. 4c) according to vibrational relaxation of the molecule. The energy shift values employed correspond to those obtained at 200 fs, 600 fs, 1 ps, and 5 ps after excitation (see numerical calculations section for more details on this energy shift-to-time delay connection). **d**–**f** Transient transmission, spectral cuts and simulated transient response for the excitation along the short axis of the nanoantennas, where the MC isomer are off to the plasmon resonance and one of them is gradually red-shifted by the same values as in **c**. Dashed line is the zero-crossing of the transient signal. In this case, the excited state relaxation does not influence the dynamics of the weakly coupled system, due to the large initial frequency mismatch with the plasmon resonance. The corresponding simulated 2D maps can be found in Supplementary Fig. 12.

arrival 2-excitation states do ($^2UP_{N-1}$ and $^2LP_{N-1}$ of Fig. 4c) leading to a slight blueshift of the transient signal (see the blue-shifting ESA contribution of Fig. 4d whose time evolution is schematically indicated by the blue arrow and corresponding dashed curve). This is reasonable, since the starting state is essentially a localized excited state of the molecule, while in the arrival state the excitation is partly delocalized on vibrational unrelaxed molecules, with higher energy. On a side note, we observe that the magnitude of the simulated $\Delta T/T$ signal increases over time, in contrast to what is being observed experimentally. Such discrepancy is expected and is explained by the lack of population decay in the simulations, which physically may be caused by either stimulated emission or non-radiative decay to the ground state. To phenomenologically account for this signal decay, we added an exponential decay on top of the simulated signal (details can be found in the Numerical calculations section), thus resulting in the simulated spectral cuts of Fig. 3c, f that indeed feature a decreasing magnitude over time.

In Fig. 3d, the transient transmission in the weak coupling regime (i.e., for the short-axis pumping system) is shown. In contrast to the strong coupling case, we now observe a differential (positive-negative) transient spectral lineshape, indicative of a shift in linear absorption of the system. Spectral cuts are shown in Fig. 3e. There are spectral changes of the differential signal over time, however, no clear spectral shift can be identified.

The same differential signal is again well captured by the theoretical simulations shown in Fig. 3f. In this case, due to the initial frequency mismatch between the short-axis nanoantenna resonance and the MC transition, the pump quickly drives the system towards a regime where only N–1 remaining MCs are actually able to couple with the short-axis plasmon mode, already at early times, thus reducing the redshift of the molecular absorption caused by the weak coupling with the plasmon compared to ground state absorption, leading then to the positive-negative spectral feature observed. We remark that even in the weak coupling regime the signal that is being observed is not coming from mere isolated molecules, but it is rather originated by the modified molecular and plasmon responses because of the locally enhanced plasmonic field.

We now discuss the timescales of the observed ultrafast dynamics in more detail (see Fig. 5). The transient transmission of the bare MC film is shown in Fig. 5a, where the signal at the probe photon energy of the $\pi - \pi^*$ transition (2.1 eV) is shown by the red circles. The bi-exponential behavior follows from an ultrafast (on femtosecond timescale) spectral shift of $\Delta T/T$ and a subsequent picosecond decay. More in detail, the induced stimulated emission from the S_1 state quickly redshifts due to vibrational relaxation of the molecules from the Franck–Condon configuration towards the S_1 minimum, leading to a sub-ps (200 fs) change of $\Delta T/T$ at fixed probe photon energy. At lower probe photon energy of 1.85 eV (blue circles), corresponding to the excited state S_1 minimum, only a slower (on picosecond timescale) decay of $\Delta T/T$ is observable, related to the transition of the molecules back to the ground state, with a time constant of 12 ps. Interestingly, in the weak coupling case (Fig. 5b), a sub-ps decay appears at the relaxed transition energy of 1.85 eV. This can be inferred to an initial plasmonic component of the decay, which is due to the weak interaction of the molecular transition with the plasmon. After the localization of the wavepacket on the

https://doi.org/10.1038/s41467-023-39413-5

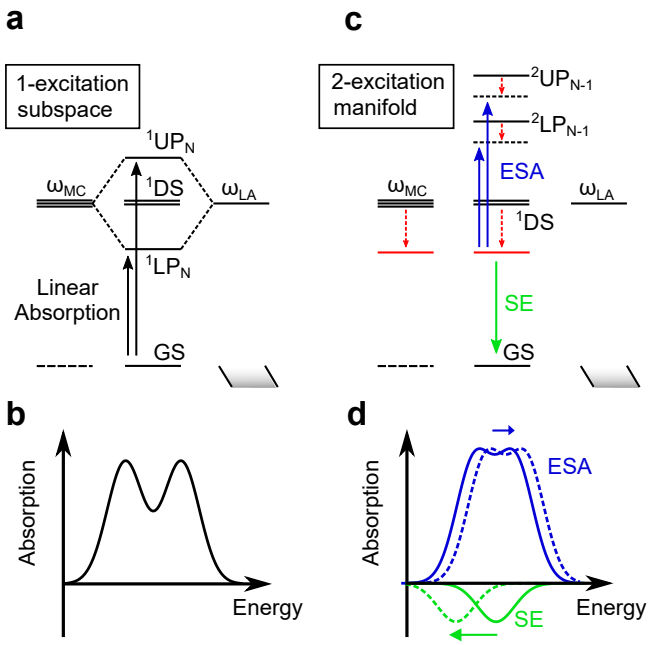

Fig. 4 | Visual representation of electronic state reconfiguration after optical pumping in the strong coupling regime. a Sketch of the electronic energy levels according to the theoretical model before optical pumping of a merocyanince (MC) sample strongly coupled to the long-axis plasmon. The 1 superscript in the state labels refers to polaritonic states belonging to the 1-excitation subspace obtained through diagonalization of the Hamiltonian in the 1-excitation basis. ^{1}DS represent molecular dark states. **b** Schematic representation of the linear absorption corresponding to the energy levels shown in panel **a**. **c** Sketch of the electronic energy levels after optical pumping. The pump mostly populates ^{1}UP at early times, which quickly dephases (≈ tens of fs), collapsing to a single localized MC excited state, which was originally contributing most to ^{1}UP state (red energy level). Subsequently, that state undergoes vibrational relaxation (red dashed arrows), during which the probe can promote both stimulated emission (SE) to the ground state and excited state absorption (ESA) to the 2-excitation manifold. The two bright states of that manifold accessible from the localized state, here labeled as $^2UP_{N-1}$ and $^2LP_{N-1}$ and referred to in the text as arrival wavefunctions following probe absorption, can be mostly seen as product states composed of the localized excited state and the 1-excitation UP and LP states due to the other N–1 remaining molecules. Indeed, the energy of those states is less affected by the vibrational relaxation (the magnitude of the dashed arrows represents the relative energy evolution over time). **d** Schematic representation of the ESA and SE contributions (here shown separately for the sake of clarity) originating from the localized state, and their changes over time indicated as dashed curves. In order to obtain the transient signal $\Delta T/T$ (Fig. 3c), the sum of the ESA and SE spectra is subtracted from the computed linear absorption.

molecular states, the system decays in the same way as the bare molecules. By subtracting the response of the unperturbed molecules (see Supplementary Note 3.4. for more details), we can extract this ultrafast component induced by the weak coupling of the molecular transition to the plasmonic excitation (blue diamonds in Fig. 5b), yielding an exponential relaxation with time constant of 400 fs (dashed line in Fig. 5b). In the strong coupling case (Fig. 5c), the same analysis reveals the ultrafast response at the UP (upper panel in Fig. 5c) and LP (lower panel in Fig. 5c) hybrid states, yielding time constants of 350 fs and 360 fs, respectively. The acceleration of excited state decay both in the weak and strong coupling case compared to the bare molecules most likely occurs by plasmonic interaction via enhancement of non-radiative decay channels, as well as Purcell-like enhancement of radiative decay (see Supplementary Note 2.3 for a theoretical analysis). It should be noted however, that at this point we cannot quantitatively distinguish between non-radiative and radiative decay contributions in our experiments.

In their seminal work on spiropyran molecules coupled to optical cavities, Hutchison et al.[36] observed a quick decay of the upper polariton state to the lower polariton state and a longer-lived population of the lower polariton of several picoseconds. In contrast, we observe the same decay constants at the LP and UP spectral position. In agreement with the theoretical model (Fig. 4), this suggests that we merely observe the decay of the molecule excited state (thus affecting the overall ultrafast response), that is accelerated due to interaction with the metal nanoantennas. This apparent discrepancy between the two experiments can be explained by the poor quality factor (and thus higher damping) of plasmon modes as compared to cavity modes, resulting in shorter lifetimes of the coherent hybrid excitations, as for example shown in[22]. Thus, our combined analysis finds a dominant role of the accelerated intramolecular dynamics on the ultrafast response of the hybrid photoswitch-nanoantennas that is at least one order of magnitude faster than is expected from the transition of uncoupled excited MC molecules back to the ground state. Therefore, this is the right timescale to be probed to reveal strong-coupling effects on molecular photochemistry and photophysics.

Discussion

We presented an in-depth study combining advanced quantum modeling and pump-probe spectroscopy of light-matter coupling in a prototypical photoswitchable molecular-plasmon system stably working at room temperature. The optical anisotropy of the plasmonic resonator allows simultaneous access to weak and strong coupling regimes, depending on the incoming light polarization with respect to the nanoantennas two main axes. In both weak and strong coupling regimes, experiments show the potential to affect the chemical energy landscape of the hybrid system on sub-picosecond timescales, observing a significantly faster dynamics of the excitation with respect to the purely molecular relaxation time. We demonstrate that this effect cannot be explained by a simple plasmon non-radiative decay, which occurs in the first few tens of femtoseconds, but rather originates from the complex intramolecular dynamics within the coupled plasmon-molecules system. A quantum model based on the extension of the Tavis-Cumming Hamiltonian, which can capture the ultrafast dynamics in both the weak and the strong coupling regimes, was developed. This theoretical framework allows also to closely map the ultrafast dynamics to changes of the electronic states in the hybrid system. Our synergistic approach combining ultrafast spectroscopy and advanced quantum modeling paves the way for deep understanding of the ultrafast dynamics in coupled plasmon-molecules systems in general. We believe that our results provide exciting foundation for the further exploration of the synthesis and characterization of strongly coupled photoswitch systems, towards a full control of ultrafast chemical processes at the nanoscale.

Methods

Fabrication and steady-state optical characterization

Aluminun nanoellipses are fabricated via hole-colloidal lithography[59]. Briefly, a sacrificial layer of PMMA is spin-coated on a quartz substrate, with a thickness around 250 nm. After depositing polystyrene (PS) beads of 100 nm diameter, a Cr mask is evaporated on top while the sample is tilted 45° with respect to the surface, allowing to cast a shadow on the PMMA surface with an elliptic shape. After tape-stripping the beads from the surface, O_2 plasma etching generates holes that allow the deposition of Al by e-beam evaporation. The final metasurface sample is obtained by lifting off the PMMA with acetone in an ultrasonic bath.

SP molecules were mixed with PS polymer in toluene and spin-coated on top of the Al metasurface and leave to evaporate at room temperature, forming a thin film covering the Al ellipses. More details regarding the fabrication are reported in the Supplementary Information.

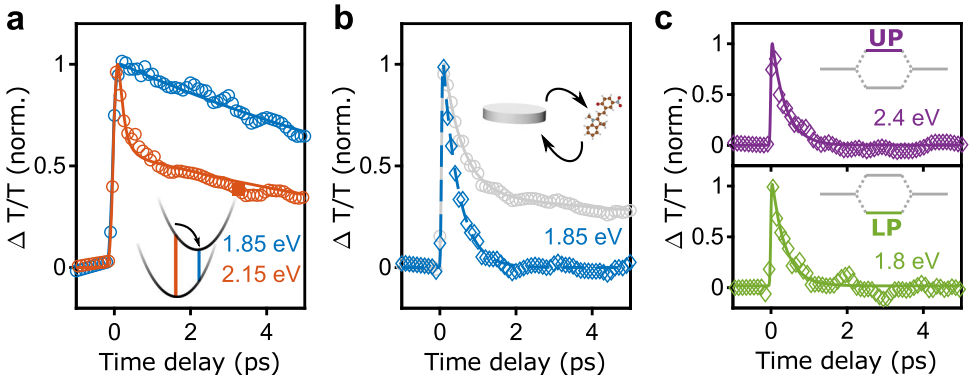

Fig. 5 | Ultrafast dynamics of molecular and polaritonic states. a Time-resolved cut of the 2D pump-probe data of the bare merocyanine reference film at the energy of the steady-state molecular transition, 2.15 eV (orange), and at the S_1 excited state minimum, 1.85 eV (blue). Ultrafast component corresponds to the vibrational relaxation of the molecule, while the slower picosecond component is related to the transition back to the ground state. **b** Cut for the hybrid system in the weak coupling case at the S_1 minimum. The gray curve is the raw data and blue curve is the remaining femtosecond decay, obtained by subtracting the slower component shown in **a**. **c** Ultrafast decay in the strong coupling case at the energy of the upper (2.4 eV) and lower (1.8 eV) polariton states, respectively. The slow component has been subtracted as in **b**.

Steady-state optical characterization shown in Fig. 1c, d was performed with white light polarized along the LA and SA of the Al nanoellipses, respectively. To convert the SP to its MC configuration, the sample was continuously illuminated with UV light (365 nm). The photoconversion was monitored by measuring the absorption at the $\pi - \pi^*$ transition (2.1 eV).

Pump-probe spectroscopy

The experimental platform used in this study is based on a commercial Yb:KGW regenerative amplifier system working at a laser repetition rate of 50 kHz. Pump pulses are generated by a noncollinear optical parametric amplifier (NOPA) working in the visible spectral range, where a bandpass filter is used before the parametric amplification to restrict the spectrum to a central photon energy of 2.3 eV and spectral bandwidth of 50 meV. The pump-induced change of transmission is probed by a white-light supercontinuum generated from sapphire between 1.75 eV and 2.5 eV, which is temporally compressed using dielectric chirped mirrors. The pump pulse energy is set to 20 μJ/cm^2 and the probe pulse energy is adjusted to ensure at least a 1:10 energy ratio compared to the pump. Using a spherical mirror with 300 mm focal length, spot sizes of 120 μm and 150 μm are set for probe and pump pulses, respectively. Pump and probe pulses have parallel polarization and interact with the sample at a small noncollinearity angle, allowing to spatially block the pump pulse after sample interaction. Remaining scattering from the pump is then removed from the data in post-processing. A fast spectrometer camera spectrally resolves the probe pulse after sample interaction. For all measurements, the dye molecules are prepared in their MC configuration, as described above. Photoisomerization of some MC molecules during the pump-probe measurements is taken into account (see Supplementary Note 3.1 for more details).

Numerical calculations

Quantum mechanical calculations of isolated bare SP and MC molecules were performed by means of Gaussian 16[60], the solvent was considered as an implicit medium through the default Gaussian implementation of the IEF-PCM formalism[61]. The choice of using ethylbenzene as implicit solvent to reproduce the polystyrene environment was done because of its close structural resemblance to the styrene molecule (they also present almost identical dielectric constants) and its prompt availability in the Gaussian package. The aluminum nanoellipse was created through the Gmsh code[62], (see Supplementary Fig. 7) and the coupling numerical values were computed through our homemade code TDPlas[50]. More precisely, one single nanoparticle (considering the elliptical shape, see Supplementary Fig. 7) is surrounded by many MC molecules following an elliptical grid pattern (shown in Supplementary Fig. 8), where each molecule is described as a point dipole oriented perpendicularly to the metal surface. Unlike the standard TC Hamiltonian, here we do not assume a constant coupling. Instead, we evaluate the coupling of each molecule with each plasmon mode, depending on its position and orientation w.r.t. the electromagnetic field associated to the plasmonic modes. In addition, we consider simultaneously the two (LA and SA) plasmon modes to include the two individual field distributions (electric near-field calculated via finite elements method shown inset of Fig. 1e, f). The coupling values for each molecule are numerically evaluated considering a Drude-Lorentz quantized description of the metallic response[50] and are then used to set up a Hamiltonian (see Eqs. 7–8, Supplementary Note 2.2) through which the steady-state absorption spectrum can be simulated. The eigenvalues and eigenvectors of the resulting Hamiltonian, that is, the energies and state composition of the polaritonic states, are then used to obtain the steady-state (linear) spectra by making use of a linear response expression of the polarizability, evaluated as a sum over the polaritonic energy levels. The same Hamiltonian written in the 2-excitation space (see Supplementary Note 2.2) is then diagonalized to obtain information about the 2-excitation-space polaritons and simulate the transient signal observed in the pump-probe experiments shown in Fig. 3, according to:

$$-\Delta\sigma = \mathrm{GSB} - (\mathrm{ESA} + \mathrm{SE}), \tag{1}$$

where the explicit theoretical expression for computing each term of Eq. 1 is described in the SI (Supplementary Note 2.2).

The simulated raw data for the LA-SA case of Fig. 3c, f featured constant deviations from the zero baseline, so a-posteriori constant shifts have been applied to each transient spectrum to obtain the data reported in Fig. 3c, f. More precisely, each simulated curve has been overall positively shifted to make its inflection point aligned with the zero baseline. Moreover, to quantitatively estimate the time scale of the vibrational relaxation dynamics, and thus allowing us to have a 1-to-1 mapping between molecular energy shifts (which are the actual input in the calculations) and time delays reported in Fig. 3c, f, we fit the experimental energy shift of bare relaxing MC molecules (see Fig. 2 and Supplementary Note 3.2) to obtain the time constant of the vibrational relaxation. We then express the energy shift as $\Delta\omega(t) = \Delta\omega_{max}\left(1 - e^{-t/\tau_2}\right)$ with $\Delta\omega_{max} = 200$ meV and $\tau_2 = 200$ fs, as shown in Supplementary Fig. 19. We note that this procedure does not take into consideration that pump and probe pulses have a finite

temporal width and that even polaritons, which are formed at early times, also feature a small-yet-finite lifetime. Both these contributions, that we are neglecting in the fitting procedure, may slightly affect the connection between molecular energy shifts and time delays that we are making use of in Fig. 3c, f. We remark that this 1-to-1 mapping is used to facilitate the comparison with the experimental data, creating a bridge between the molecular energy shift and time delay.

In addition to that, as described in the main next, the lack of population decay in the simulations leads to an ever-increasing magnitude of the $\Delta T/T$ simulated signal, so to phenomenologically account for such missing feature we added an exponential decay on top of the simulated data like e^{-t/τ_1} for $t < 1$ ps with $\tau_1 = 400$ fs (based on the experimental signal). Moreover, since the experimental data of Fig. 3a, d presents a constant magnitude after ≈1 ps that is roughly 1/5 of the intensity at early times, the same constant feature has been applied to the simulated data to recover a similar spectral trend at longer times (>1 ps).

Similar approaches that use fitted rates and phenomenological decays in theoretical models to better comprehend experimental signals have been widely used before[63–67].

As a final note, the linewidths (decay rates) associated with each polaritonic transition that are required for the simulated spectra are obtained by resorting to a non-Hermitian formulation of the Hamiltonian where energies of the uncoupled states bring an imaginary component which corresponds to either a molecular or plasmonic decay rate, corresponding to vibrational broadening and plasmon damping, respectively (see SI for the values considered)[68,69]. The diagonalization of such Hamiltonian directly returns the decay rates of the polaritons as imaginary component of their associated eigenvalues[70]. We highlight that the decay rates employed in the Hamiltonian are used to account for the broadening of the transitions (corresponding to a lifetime of ≈ few fs for the plasmon linewidth and ≈100 fs for the molecular transition, see SI), whereas the phenomenological decay previously mentioned ($\tau_1 = 400$ fs) was used to account for population decay (i.e. signal intensity decrease) over time because of non-radiative decay. Explicit theory formulation can be found in the SI.

Data availability

The authors declare that the data supporting the findings of this study are available within the paper, its supplementary information files, and from the corresponding authors upon request.

Code availability

The code used for the simulations is available upon reasonable request from M.R. and S.C.

References

1. Ballarini, D. et al. All-optical polariton transistor. *Nat. Commun.* **4**, 1778 (2013).
2. Zasedatelev, A. V. et al. A room-temperature organic polariton transistor. *Nat. Photon.* **13**, 378–383 (2019).
3. Arnardottir, K., Moilanen, A., Strashko, A., Törmä, P. & Keeling, J. Multimode organic polariton lasing. *Phys. Rev. Lett.* **125**, 233603 (2020).
4. Amo, A. et al. Superfluidity of polaritons in semiconductor microcavities. *Nat. Phys.* **5**, 805–810 (2009).
5. Nagarajan, K., Thomas, A. & Ebbesen, T. Chemistry under vibrational strong coupling. *J. Am. Chem. Soc.* **143**, 16877–16889 (2021).
6. Boulier, T. et al. Microcavity polaritons for quantum simulation. *Adv. Quant. Technol.* **3**, 2000052 (2020).
7. Zasedatelev, A. V. et al. Single-photon nonlinearity at room temperature. *Nature* **597**, 493–497 (2021).
8. Schwartz, T., Hutchison, J., Genet, C. & Ebbesen, T. Reversible switching of ultrastrong light-molecule coupling. *Phys. Rev. Lett.* **106**, 196405 (2011).
9. Kuttruff, J. et al. Ultrafast all-optical switching enabled by epsilon-near-zero-tailored absorption in metal-insulator nanocavities. *Commun. Phys.* **3**, 114 (2020).
10. Chikkaraddy, R. et al. Single-molecule strong coupling at room temperature in plasmonic nanocavities. *Nature* **535**, 127–130 (2016).
11. Cambiasso, J. et al. Bridging the gap between dielectric nanophotonics and the visible regime with effectively lossless gallium phosphide antennas. *Nano Lett.* **17**, 1219–1225 (2017).
12. Regmi, R. et al. All-dielectric silicon nanogap antennas to enhance the fluorescence of single molecules. *Nano Lett.* **16**, 5143–5151 (2016).
13. Zywietz, U. et al. Electromagnetic resonances of silicon nanoparticle dimers in the visible. *ACS Photon.* **2**, 913–920 (2015).
14. Caldarola, M. et al. Non-plasmonic nanoantennas for surface enhanced spectroscopies with ultra-low heat conversion. *Nat. Commun.* **6**, 7915 (2015).
15. Maier, S. Plasmonic field enhancement and SERS in the effective mode volume picture. *Opt. Express* **14**, 1957 (2006).
16. Hugall, J., Singh, A. & van Hulst, N. Plasmonic cavity coupling. *ACS Photonics* **5**, 43–53 (2018).
17. Fregoni, J., Garcia-Vidal, F. J. & Feist, J. Theoretical challenges in polaritonic chemistry. *ACS Photonics* **9**, 1096–1107 (2022).
18. Vasa, P. et al. Real-time observation of ultrafast Rabi oscillations between excitons and plasmons in metal nanostructures with J-aggregates. *Nat. Photonics* **7**, 128–132 (2013).
19. Dominici, L. et al. Ultrafast control and Rabi oscillations of polaritons. *Phys. Rev. Lett.* **113**, 226401 (2014).
20. Du, W. et al. Ultrafast modulation of exciton–plasmon coupling in a monolayer WS_2–AG nanodisk hybrid system. *ACS Photonics* **6**, 2832–2840 (2019).
21. Shan, H. et al. Direct observation of ultrafast plasmonic hot electron transfer in the strong coupling regime. *Light Sci. Appl.* **8**, 9 (2019).
22. Vasa, P. et al. Ultrafast manipulation of strong coupling in metal –molecular aggregate hybrid nanostructures. *ACS Nano* **4**, 7559–7565 (2010).
23. Dunkelberger, A., Davidson, R., Ahn, W., Simpkins, B. & Owrutsky, J. Ultrafast transmission modulation and recovery via vibrational strong coupling. *J. Phys. Chem. A* **122**, 965–971 (2018).
24. Dunkelberger, A., Spann, B., Fears, K., Simpkins, B. & Owrutsky, J. Modified relaxation dynamics and coherent energy exchange in coupled vibration-cavity polaritons. *Nat. Commun.* **7**, 13504 (2016).
25. Sample, A. et al. Strong coupling between plasmons and molecular excitons in metal–organic frameworks. *Nano Lett.* **21**, 7775–7780 (2021).
26. Feist, J., Galego, J. & Garcia-Vidal, F. Polaritonic chemistry with organic molecules. *ACS Photonics* **5**, 205–216 (2017).
27. Zeng, P. et al. Photoinduced electron transfer in the strong coupling regime: waveguide–plasmon polaritons. *Nano Lett.* **16**, 2651–2656 (2016).
28. Galego, J., Garcia-Vidal, F. & Feist, J. Cavity-induced modifications of molecular structure in the strong-coupling regime. *Phys. Rev. X* **5**, 041022 (2015).
29. Kowalewski, M., Bennett, K. & Mukamel, S. Cavity femtochemistry: manipulating nonadiabatic dynamics at avoided crossings. *J. Phys. Chem. Lett.* **7**, 2050–2054 (2016).
30. Munkhbat, B., Wersäll, M., Baranov, D., Antosiewicz, T. & Shegai, T. Suppression of photo-oxidation of organic chromophores by strong coupling to plasmonic nanoantennas. *Sci. Adv.* **4**, eaas9552 (2018).
31. Du, M. Theory reveals novel chemistry of photonic molecules. *Chem* **5**, 1009–1011 (2019).
32. Martínez-Martínez, L., Du, M., Ribeiro, R., Kéna-Cohen, S. & Yuen-Zhou, J. Polariton-assisted singlet fission in acene aggregates. *J. Phys. Chem. Lett.* **9**, 1951–1957 (2018).
33. Galego, J., Garcia-Vidal, F. & Feist, J. Suppressing photochemical reactions with quantized light fields. *Nat. Commun.* **7**, 1–6 (2016).

temporal width and that even polaritons, which are formed at early times, also feature a small-yet-finite lifetime. Both these contributions, that we are neglecting in the fitting procedure, may slightly affect the connection between molecular energy shifts and time delays that we are making use of in Fig. 3c, f. We remark that this 1-to-1 mapping is used to facilitate the comparison with the experimental data, creating a bridge between the molecular energy shift and time delay.

In addition to that, as described in the main next, the lack of population decay in the simulations leads to an ever-increasing magnitude of the $\Delta T/T$ simulated signal, so to phenomenologically account for such missing feature we added an exponential decay on top of the simulated data like e^{-t/τ_1} for $t < 1$ ps with $\tau_1 = 400$ fs (based on the experimental signal). Moreover, since the experimental data of Fig. 3a, d presents a constant magnitude after ≈1 ps that is roughly 1/5 of the intensity at early times, the same constant feature has been applied to the simulated data to recover a similar spectral trend at longer times (>1 ps).

Similar approaches that use fitted rates and phenomenological decays in theoretical models to better comprehend experimental signals have been widely used before[63–67].

As a final note, the linewidths (decay rates) associated with each polaritonic transition that are required for the simulated spectra are obtained by resorting to a non-Hermitian formulation of the Hamiltonian where energies of the uncoupled states bring an imaginary component which corresponds to either a molecular or plasmonic decay rate, corresponding to vibrational broadening and plasmon damping, respectively (see SI for the values considered)[68,69]. The diagonalization of such Hamiltonian directly returns the decay rates of the polaritons as imaginary component of their associated eigenvalues[70]. We highlight that the decay rates employed in the Hamiltonian are used to account for the broadening of the transitions (corresponding to a lifetime of ≈ few fs for the plasmon linewidth and ≈100 fs for the molecular transition, see SI), whereas the phenomenological decay previously mentioned ($\tau_1 = 400$ fs) was used to account for population decay (i.e. signal intensity decrease) over time because of non-radiative decay. Explicit theory formulation can be found in the SI.

Data availability

The authors declare that the data supporting the findings of this study are available within the paper, its supplementary information files, and from the corresponding authors upon request.

Code availability

The code used for the simulations is available upon reasonable request from M.R. and S.C.

References

1. Ballarini, D. et al. All-optical polariton transistor. *Nat. Commun.* **4**, 1778 (2013).
2. Zasedatelev, A. V. et al. A room-temperature organic polariton transistor. *Nat. Photon.* **13**, 378–383 (2019).
3. Arnardottir, K., Moilanen, A., Strashko, A., Törmä, P. & Keeling, J. Multimode organic polariton lasing. *Phys. Rev. Lett.* **125**, 233603 (2020).
4. Amo, A. et al. Superfluidity of polaritons in semiconductor microcavities. *Nat. Phys.* **5**, 805–810 (2009).
5. Nagarajan, K., Thomas, A. & Ebbesen, T. Chemistry under vibrational strong coupling. *J. Am. Chem. Soc.* **143**, 16877–16889 (2021).
6. Boulier, T. et al. Microcavity polaritons for quantum simulation. *Adv. Quant. Technol.* **3**, 2000052 (2020).
7. Zasedatelev, A. V. et al. Single-photon nonlinearity at room temperature. *Nature* **597**, 493–497 (2021).
8. Schwartz, T., Hutchison, J., Genet, C. & Ebbesen, T. Reversible switching of ultrastrong light-molecule coupling. *Phys. Rev. Lett.* **106**, 196405 (2011).
9. Kuttruff, J. et al. Ultrafast all-optical switching enabled by epsilon-near-zero-tailored absorption in metal-insulator nanocavities. *Commun. Phys.* **3**, 114 (2020).
10. Chikkaraddy, R. et al. Single-molecule strong coupling at room temperature in plasmonic nanocavities. *Nature* **535**, 127–130 (2016).
11. Cambiasso, J. et al. Bridging the gap between dielectric nanophotonics and the visible regime with effectively lossless gallium phosphide antennas. *Nano Lett.* **17**, 1219–1225 (2017).
12. Regmi, R. et al. All-dielectric silicon nanogap antennas to enhance the fluorescence of single molecules. *Nano Lett.* **16**, 5143–5151 (2016).
13. Zywietz, U. et al. Electromagnetic resonances of silicon nanoparticle dimers in the visible. *ACS Photon.* **2**, 913–920 (2015).
14. Caldarola, M. et al. Non-plasmonic nanoantennas for surface enhanced spectroscopies with ultra-low heat conversion. *Nat. Commun.* **6**, 7915 (2015).
15. Maier, S. Plasmonic field enhancement and SERS in the effective mode volume picture. *Opt. Express* **14**, 1957 (2006).
16. Hugall, J., Singh, A. & van Hulst, N. Plasmonic cavity coupling. *ACS Photonics* **5**, 43–53 (2018).
17. Fregoni, J., Garcia-Vidal, F. J. & Feist, J. Theoretical challenges in polaritonic chemistry. *ACS Photonics* **9**, 1096–1107 (2022).
18. Vasa, P. et al. Real-time observation of ultrafast Rabi oscillations between excitons and plasmons in metal nanostructures with J-aggregates. *Nat. Photonics* **7**, 128–132 (2013).
19. Dominici, L. et al. Ultrafast control and Rabi oscillations of polaritons. *Phys. Rev. Lett.* **113**, 226401 (2014).
20. Du, W. et al. Ultrafast modulation of exciton–plasmon coupling in a monolayer WS_2–AG nanodisk hybrid system. *ACS Photonics* **6**, 2832–2840 (2019).
21. Shan, H. et al. Direct observation of ultrafast plasmonic hot electron transfer in the strong coupling regime. *Light Sci. Appl.* **8**, 9 (2019).
22. Vasa, P. et al. Ultrafast manipulation of strong coupling in metal –molecular aggregate hybrid nanostructures. *ACS Nano* **4**, 7559–7565 (2010).
23. Dunkelberger, A., Davidson, R., Ahn, W., Simpkins, B. & Owrutsky, J. Ultrafast transmission modulation and recovery via vibrational strong coupling. *J. Phys. Chem. A* **122**, 965–971 (2018).
24. Dunkelberger, A., Spann, B., Fears, K., Simpkins, B. & Owrutsky, J. Modified relaxation dynamics and coherent energy exchange in coupled vibration-cavity polaritons. *Nat. Commun.* **7**, 13504 (2016).
25. Sample, A. et al. Strong coupling between plasmons and molecular excitons in metal–organic frameworks. *Nano Lett.* **21**, 7775–7780 (2021).
26. Feist, J., Galego, J. & Garcia-Vidal, F. Polaritonic chemistry with organic molecules. *ACS Photonics* **5**, 205–216 (2017).
27. Zeng, P. et al. Photoinduced electron transfer in the strong coupling regime: waveguide–plasmon polaritons. *Nano Lett.* **16**, 2651–2656 (2016).
28. Galego, J., Garcia-Vidal, F. & Feist, J. Cavity-induced modifications of molecular structure in the strong-coupling regime. *Phys. Rev. X* **5**, 041022 (2015).
29. Kowalewski, M., Bennett, K. & Mukamel, S. Cavity femtochemistry: manipulating nonadiabatic dynamics at avoided crossings. *J. Phys. Chem. Lett.* **7**, 2050–2054 (2016).
30. Munkhbat, B., Wersäll, M., Baranov, D., Antosiewicz, T. & Shegai, T. Suppression of photo-oxidation of organic chromophores by strong coupling to plasmonic nanoantennas. *Sci. Adv.* **4**, eaas9552 (2018).
31. Du, M. Theory reveals novel chemistry of photonic molecules. *Chem* **5**, 1009–1011 (2019).
32. Martínez-Martínez, L., Du, M., Ribeiro, R., Kéna-Cohen, S. & Yuen-Zhou, J. Polariton-assisted singlet fission in acene aggregates. *J. Phys. Chem. Lett.* **9**, 1951–1957 (2018).
33. Galego, J., Garcia-Vidal, F. & Feist, J. Suppressing photochemical reactions with quantized light fields. *Nat. Commun.* **7**, 1–6 (2016).

34. Fregoni, J., Granucci, G., Persico, M. & Corni, S. Strong coupling with light enhances the photoisomerization quantum yield of azobenzene. *Chem* **6**, 250–265 (2020).
35. Satapathy, S. et al. Selective isomer emission via funneling of exciton polaritons. *Sci. Adv.* **7**, eabj0997 (2021).
36. Hutchison, J., Schwartz, T., Genet, C., Devaux, E. & Ebbesen, T. Modifying chemical landscapes by coupling to vacuum fields. *Angew. Chem. Int. Ed.* **51**, 1592–1596 (2012).
37. Hirai, K., Takeda, R., Hutchison, J. & Uji-i, H. Modulation of prins cyclization by vibrational strong coupling. *Angew. Chem.* **132**, 5370–5373 (2020).
38. Fassioli, F., Park, K., Bard, S. & Scholes, G. Femtosecond photophysics of molecular polaritons. *J. Phys. Chem. Lett.* **12**, 11444–11459 (2021).
39. Samanta, D. et al. Reversible chromism of spiropyran in the cavity of a flexible coordination cage. *Nat. Commun.* **9**, 641 (2018).
40. Zhang, Q., Qu, D. & Tian, H. Photo-regulated supramolecular polymers: shining beyond disassembly and reassembly. *Adv. Opt. Mater.* **7**, 1900033 (2019).
41. Li, M., Zhang, Q., Zhou, Y. & Zhu, S. Let spiropyran help polymers feel force! *Prog. Polym. Sci.* **79**, 26–39 (2018).
42. Großmann, M. et al. Light-triggered control of plasmonic refraction and group delay by photochromic molecular switches. *ACS Photonics* **2**, 1327–1332 (2015).
43. Buback, J. et al. Ultrafast Bidirectional Photoswitching of a Spiropyran. *J. Am. Chem. Soc.* **132**, 16510–16519 (2010).
44. Klajn, R. Spiropyran-based dynamic materials. *Chem. Soc. Rev.* **43**, 148–184 (2014).
45. Tavis, M. & Cummings, F. W. Exact solution for an N-molecule—radiation-field hamiltonian. *Phys. Rev.* **170**, 379–384 (1968).
46. Baudrion, A. et al. Reversible strong coupling in silver nanoparticle arrays using photochromic molecules. *Nano Lett.* **13**, 282–286 (2012).
47. Eizner, E., Avayu, O., Ditcovski, R. & Ellenbogen, T. Aluminum nanoantenna complexes for strong coupling between excitons and localized surface plasmons. *Nano Lett.* **15**, 6215–6221 (2015).
48. Gupta, N. S. et al. Complex plasmon-exciton dynamics revealed through quantum dot light emission in a nanocavity. *Nat. Commun.* **12**, 1310 (2021).
49. Garraway, B. The Dicke model in quantum optics: Dicke model revisited. *Philos. Trans. R. Soc. A: Math. Phys. Eng. Sci.* **369**, 1137–1155 (2011).
50. Fregoni, J. et al. Strong coupling between localized surface plasmons and molecules by coupled cluster theory. *Nano Lett.* **21**, 6664–6670 (2021).
51. Benz, F. et al. Single-molecule optomechanics in "picocavities". *Science* **354**, 726–729 (2016).
52. Grupp, A. et al. Broadly tunable ultrafast pump-probe system operating at multi-kHz repetition rate. *J. Opt.* **20**, 014005 (2017).
53. Ruetzel, S. et al. Photoisomerization among ring-open merocyanines. I. Reaction dynamics and wave-packet oscillations induced by tunable femtosecond pulses. *J. Chem. Phys.* **140**, 224310 (2014).
54. Schwartz, T. et al. Polariton dynamics under strong light–molecule coupling. *ChemPhysChem* **14**, 125–131 (2013).
55. Peruffo, N., Mancin, F. & Collini, E. Ultrafast dynamics of multiple plexcitons in colloidal nanomaterials: the mediating action of plasmon resonances and dark states. *J. Phys. Chem. Lett.* **13**, 6412–6419 (2022).
56. Xiang, B. et al. Two-dimensional infrared spectroscopy of vibrational polaritons. *Proc. Natl Acad. Sci. USA* **115**, 4845–4850 (2018).
57. Ribeiro, F. R. et al. Theory for nonlinear spectroscopy of vibrational polaritons. *J. Phys. Chem. Lett.* **9**, 3766–3771 (2018).
58. DelPo, C. et al. Polariton transitions in femtosecond transient absorption studies of ultrastrong light–molecule coupling. *J. Phys. Chem. Lett.* **11**, 2667–2674 (2020).
59. Fredriksson, H. et al. Hole–Mask colloidal lithography. *Adv. Mater.* **19**, 4297–4302 (2007).
60. Gaussian 16, Revision B.01, Frisch, M. J. et al. Gaussian, Inc., (Wallingford CT, 2016) https://gaussian.com/citation/.
61. Tomasi, J., Mennucci, B. & Cammi, R. Quantum mechanical continuum solvation models. *Chem. Rev.* **105**, 2999–3094 (2005).
62. Geuzaine, C. & Remacle, J. Gmsh: a 3-D finite element mesh generator with built-in pre- and post-processing facilities. *Int. J. Numer. Methods Eng.* **79**, 1309–1331 (2009).
63. Nan, F. et al. Unusual and tunable one-photon nonlinearity in gold-dye plexcitonic fano systems. *Nano Lett.* **15**, 2705–2710 (2015).
64. Bergfield, J. & Hendrickson, J. Signatures of plexcitonic states in molecular electroluminescence. *Sci. Rep.* **8**, 2314 (2018).
65. Baranov, D. et al. Novel nanostructures and materials for strong light–matter interactions. *ACS Photonics* **5**, 24–42 (2018).
66. Neuman, T. & Aizpurua, J. Origin of the asymmetric light emission from molecular exciton–polaritons. *Optica* **5**, 1247–1255 (2018).
67. Zheng, P., Kang, J., Paria, D., Kang, J. U. & Barman, I. Molecular radiative energy shifts under strong oscillating fields. *Small* **17**, 2007244 (2021).
68. Felicetti, S. et al. Photoprotecting uracil by coupling with lossy nanocavities. *J. Phys. Chem. Lett.* **11**, 8810–8818 (2020).
69. Antoniou, P., Suchanek, F., Varner, J. & Foley, J. Role of cavity losses on nonadiabatic couplings and dynamics in polaritonic chemistry. *J. Phys. Chem. Lett.* **11**, 9063–9069 (2020).
70. Finkelstein-Shapiro, D. et al. Understanding radiative transitions and relaxation pathways in plexcitons. *Chem* **7**, 1092–1107 (2021).

Acknowledgements

N.M. and D.B. acknowledge support from the Luxembourg National Research Fund (Grant No. C19/MS/13624497 'ULTRON'). N.M., D.B., and S.C. acknowledge support from the European Union under the FETOPEN-01-2018-2019-2020 call (Grant No. 964363 'ProID'). D.B. acknowledges support from the European Research Council through grant no. 819871 (UpTEMPO) and from ERDF Program (Grant No. 2017-03-022--19 'Lux-Ultra-Fast'). J.K. acknowledges the German Research Foundation via SFB 1432. A.D. acknowledges the Swedish Research Council (Grant No. 2017-04828) and Swedish Research Council for Sustainable Development (Formas) (Project No. 2021-01390). N.M. acknowledges support from the Swedish Research Council (grant no. 2021-05784), Kempestiftelserna (grant no. JCK-3122) and the Wenner-Gren Foundation (grant no. UPD2022-0074). N.M. and S.C. acknowledge from the European Innovation Council (grant n. 101046920 'iSenseDNA').

Author contributions

J.K. designed and performed the pump-probe experiments with the support of J.A. (Jonas Allerbeck). M.R., J.F., and S.C. developed the theory and performed the quantum simulations. E.P.-V. and A.D. designed and fabricated the plasmonic photoswitch-nanoantennas and performed steady-state optical, chemical, and photochemical characterization with the support of V.S.-B. and J.A. (Joakim Andréasson). D.B. contributed to the data analysis and discussion. N.M. conceived the idea and supervised the work. J.K., M.R., E.P.-V., A.D., S.C., and N.M. analyzed and discussed the results, and wrote the manuscript with input from all the authors.

Funding

Open access funding provided by Umea University.

Competing interests

The authors declare no competing interests.

Additional information

Supplementary information The online version contains supplementary material available at https://doi.org/10.1038/s41467-023-39413-5.

Correspondence and requests for materials should be addressed to Alexandre Dmitriev, Stefano Corni or Nicolò Maccaferri.

Peer review information *Nature Communications* thanks the anonymous reviewer(s) for their contribution to the peer review of this work. A peer review file is available.

Inventory of Supplementary Information

SUPPLEMENTARY INFORMATION

Sub-picosecond collapse of molecular polaritons to pure molecular transition in plasmonic photoswitch-nanoantennas

Joel Kuttruff[1¶], Marco Romanelli[2¶], Esteban Pedrueza-Villalmanzo[3,4¶], Jonas Allerbeck[1,5], Jacopo Fregoni[6], Valeria Saavedra-Becerril[4], Joakim Andréasson[4], Daniele Brida[7], Alexandre Dmitriev[3]*, Stefano Corni[2,8]*, and Nicolò Maccaferri[7,9,10]*

[1] Department of Physics, University of Konstanz, 78457, Konstanz, Germany

[2] Department of Chemical Sciences, University of Padova, via Marzolo 1, 35131 Padova, Italy

[3]Department of Physics, University of Gothenburg, Origovägen 6B, 412 96, Gothenburg, Sweden

[4] Department of Chemistry and Chemical Engineering, Chalmers University of Technology, Kemigården 4, 412 96 Göteborg, Sweden

[5] nanotech@surfaces Laboratory, Empa, Swiss Federal Laboratories for Materials Science and Technology, Überlandstrasse 129, 8600 Dübendorf, Switzerland

[6] Department of Physics, Universidad Autónoma de Madrid, Ciudad Universitaria de Cantoblanco, 28049 Madrid, Spain

[7] Department of Physics and Materials Science, University of Luxembourg, 162a avenue de la Faïencerie, L-1511 Luxembourg, Luxembourg

[8] CNR Institute of Nanoscience, via Campi 213/A, 41125 Modena, Italy

[9] Department of Physics, Umeå University, Linnaeus väg 24, 90187 Umeå, Sweden

[10] Umeå Centre for Microbial Research, Umeå University, 901 87 Umeå, Sweden

¶These authors contributed equally

*alexd@physics.gu.se; *stefano.corni@unipd.it; *nicolo.maccaferri@umu.se

Supplementary Note 1. Sample fabrication.

Supplementary Note 1.1 – Fabrication procedures

Quartz substrates (2 x 2 cm^2) were cleaned by immersing them consecutively in acetone and isopropanol in an ultrasonic bath, to be finally rinsed in DI water and dried with nitrogen. Hole-mask colloidal lithography (HCL) **[1]** nanofabrication technique was employed to deposit Al nano-ellipses. Briefly, a PMMA layer (950 PMMA A4) was spin-coated for 60 seconds at 3000 rpm. After a brief O2 plasma treatment (5 s, 250 mTorr at 50 W), an aqueous polyelectrolyte layer of PDDA solution at 0.2% was pipetted into the surface and rinsed with DI water after 1 minute. Then, an aqueous solution of polystyrene (PS) beads of 100 nm-diameter (0.2 % in volume) were pipetted and rinsed with DI water after 2 minutes. A 10 nm Cr layer is then evaporated on top of the tilted substrate, so the shadow of the PS beads generates an elliptical-hole mask. After tape-stripping of the PS beads, O2 plasma etching (5 min, 250 mTorr at 50 W) generates the holes in the PMMA, and 60 nm e-beam evaporated Al is deposited. Finally, hot acetone in an ultrasonic bath is used in the final lift-off step. The final nanoellipses have a long axis of around 140 nm and short axis of 100 nm. The spiropyran (1,3,3-Trimethylindolino-6´-nitrobenzopyrylospiran, from Tokyo Chemical Industry) is mixed with poly(styrene) standard (MW= 45730, Aldrich Chem. Co.) (PS) in a ratio spiropyran:PS of 2:0.5 wt% and dissolved in toluene (Merck). The as-prepared solution is spinned onto the Al nanoellipse sample at 3000 rpm for 60 seconds. This generates a transparent thin film with a thickness of around 50 nm, determined by profilometry (Surface profiler Tencor AS700). The samples were characterized using scanning electron microscopy (SEM) (Zeiss Supra 55VP at 30 kV, see Supplementary Figure 1) and in tapping mode AFM (Bruker Dimension 3100 SPM, see Supplementary Figure 2).

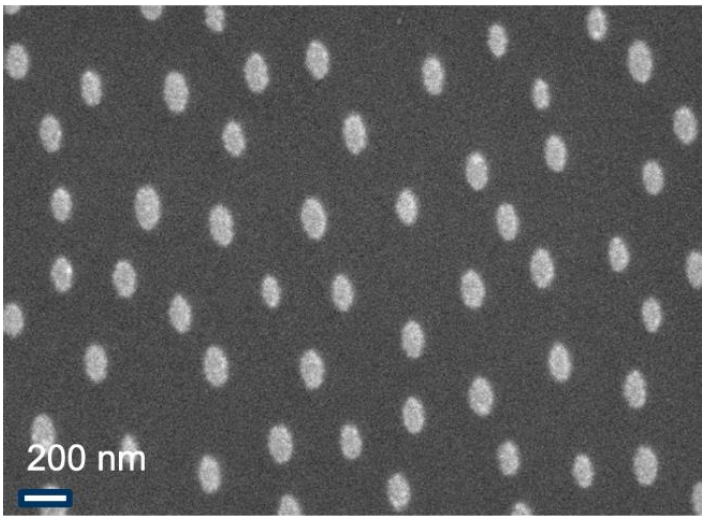

Supplementary Figure 1: *SEM image of the aluminum nanoellipses prepared by hole-mask colloidal lithography.*

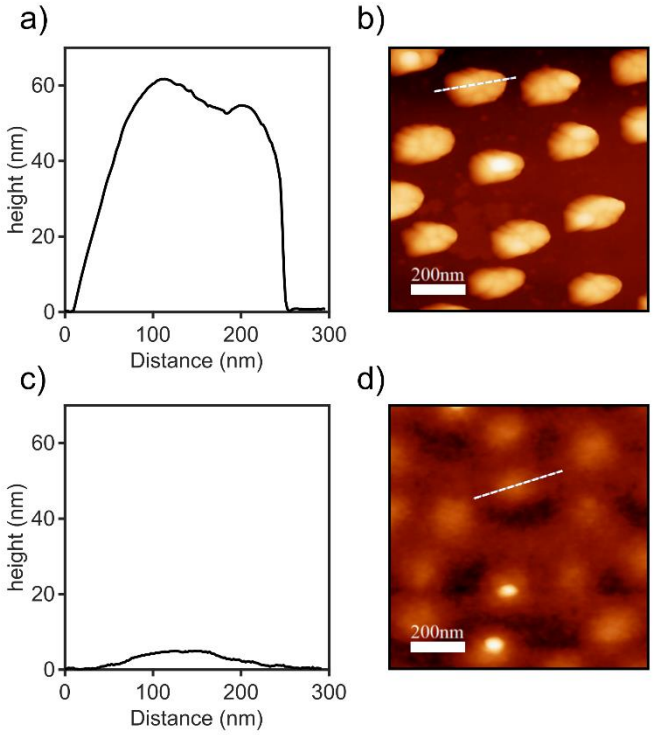

Supplementary Figure 2: *AFM characterization of the samples.* ***a*** *height profile of the nanoellipse without SP layer along the dashed line indicated in (b).* ***b*** *AFM amplitude (b) measured on the sample without SP layer.* ***c,d*** *Same as (a),(b) for sample with the SP layer. Scale bar is 200 nm.*

Supplementary Note 1.2 – Determination of the molecular density and photoconversion yield

In order to determine the molecular density in a SP thin film, we dissolve a substrate of 1.5 x 1.5 cm^2 containing a film of polystyrene and SP molecules as described in Supplementary Note 1.1 (Supplementary Figure 3, black line) in 1.5 ml of acetonitrile (molar absorption coefficient for SP **[2]**: ε=7500 M^{-1} cm^{-1} at 341 nm, Absorption maximum = 0.206) in a 4 mm optical path cuvette (Supplementary Figure 3, red line). The concentration is around 68 μM, and with a film thickness of 50 nm we obtain a molecular density of around 5,5 SP molecules/nm^3.

Finally, we determined the photo-conversion yield of the SP isomer to the MC isomer in the thin film. Comparing the efficiency of the UV-induced SP →MC isomerization in the molecular film (without ellipses) to the corresponding process in acetonitrile fluid solution using identical light flux and sample geometry, we found that the rate of ring opening in acetonitrile was a factor around 6 faster (k_{sol} = 0.39 min^{-1} in acetonitrile, k_{film}= 0.067 min^{-1} in the film, 365 nm UV light at 0.9 mW/cm^2 at the samples). The isomerization quantum yield for this spiropyran in acetonitrile is reported to be 0.12 **[3]** implying that the corresponding number in the film is expected to be around 0.02.

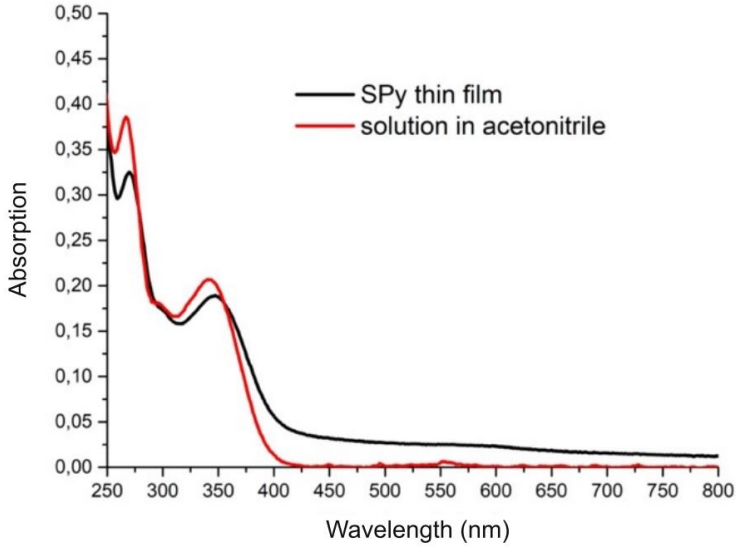

Supplementary Figure 3: *Spectra associated with the determination of the molecular density in the SP thin film. Black line spectrum represents the original SP thin film and the red line the spectrum of the same film when it is dissolved in acetonitrile.*

Supplementary Note 2. Computational part.

Supplementary Note 2.1 – Quantum mechanical calculations of the isolated spiropyran and merocyanine molecules

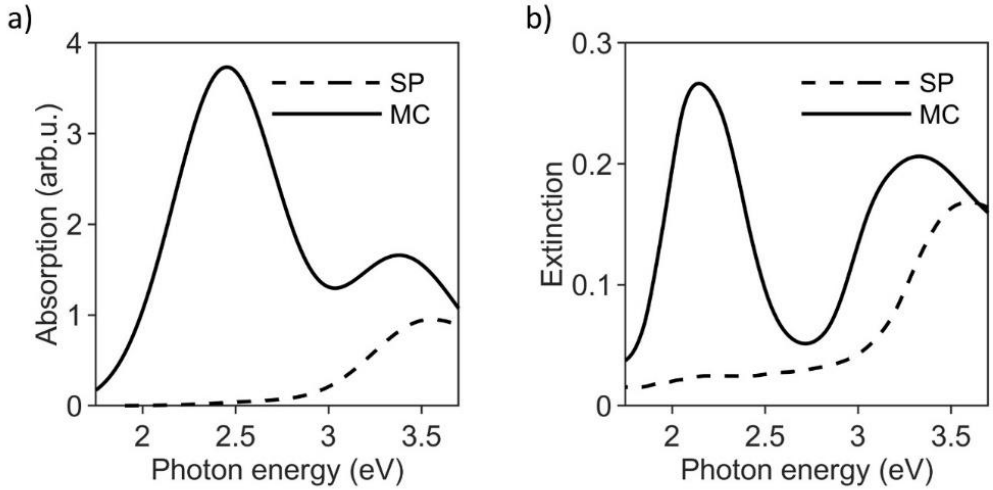

Supplementary Figure 4: *a) Simulated linear absorption in Ethylbenzene at TD-DFT/B3LYP 6-31g(d,p). b) Experimental extinction spectra of the polystyrene film containing the molecules.*

The ground state structures of the two molecules were optimized at B3LYP/6-31g(d,p) level of theory using the Gaussian 16 package **[4]** in vacuum:

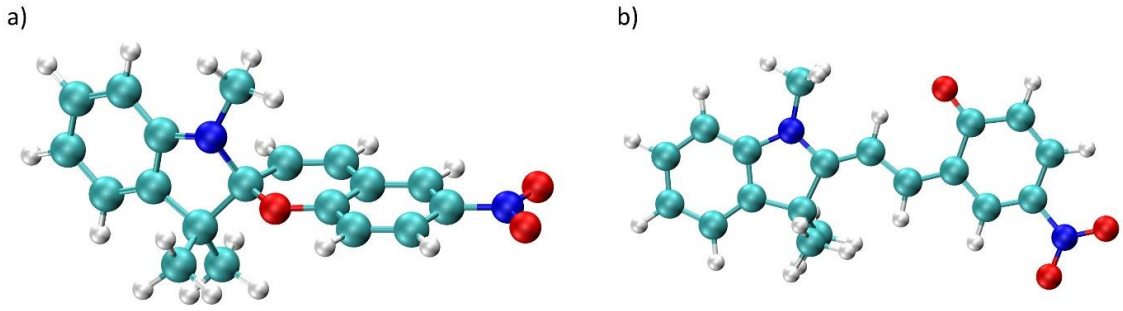

Supplementary Figure 5*: a) Ground state optimized structure of the SP isomer. b) Ground state optimized structure of the MC isomer.*

From the two structures reported in Supplementary Figure 5, vertical excitation energies at TD-DFT/B3LYP 6-31g(d,p) for the first 8 excited states were computed, including ethylbenzene as an implicit solvent using the standard IEF-PCM **[5]** implementation of the Gaussian 16 package. The resulting simulated linear absorption (obtained with a Half-Width-Half-Height broadening of 0.333 eV for each transition) is reported above in Supplementary Figure 4, displaying a very good agreement with the experimental counterpart. In addition to the ground-state optimized structures, the S_1 state of the merocyanine isomer was optimized in solvent to find the closest excited-state minimum towards which the system can relax upon excitation. According to TDDFT/B3LYP 6-31g(d,p) vertical excitation energies computed at the two different nuclear geometries corresponding to ground and excited state minima (the relaxed S_1 structure is shown in Supplementary Figure 6 panel b), the predicted Stokes-shift is ≈ 0.4 eV thus suggesting that the red-shift of the ΔT/T pump-probe signal reported in the main text Figure 2 (≈ 0.3 eV), can indeed be assigned to stimulated emission of excited MCs relaxing towards the S_1 minimum.

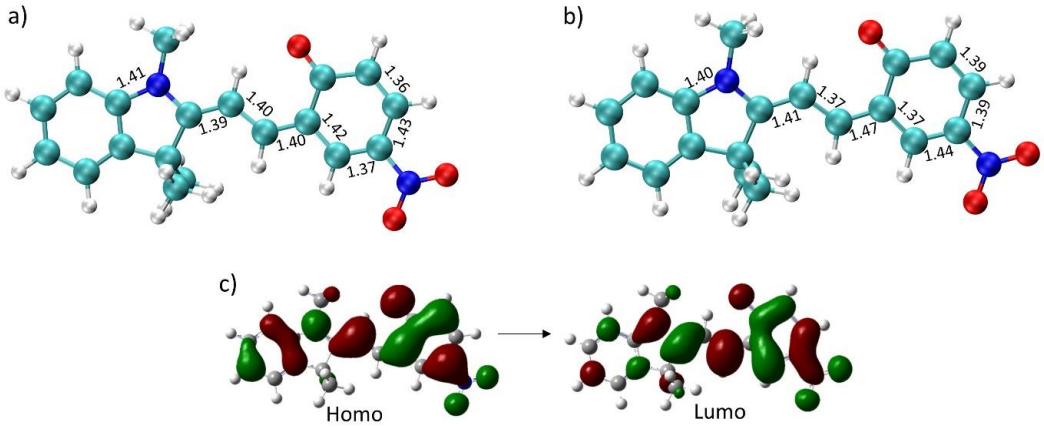

Supplementary Figure 6: *a) Ground state optimized structure of MC b) Excited state optimized structure of MC. The bond lengths are in Å in both figures. c) $S_0 \rightarrow S_1$ bright transition of the MC (peaking at 2.45 eV in our simulations, see Supplementary Figure 4) mostly involves the HOMO → LUMO orbitals here reported.*

Supplementary Note 2.2 – Theoretical model to simulate the optical response of the coupled system

The nanoellipse employed in the simulations throughout this work was created using the Gmsh code **[6]** (Supplementary Figure 7).Its associated extinction spectra obtained with different polarizations of the incoming electric field are reported in Supplementary Figure 10 panel a).

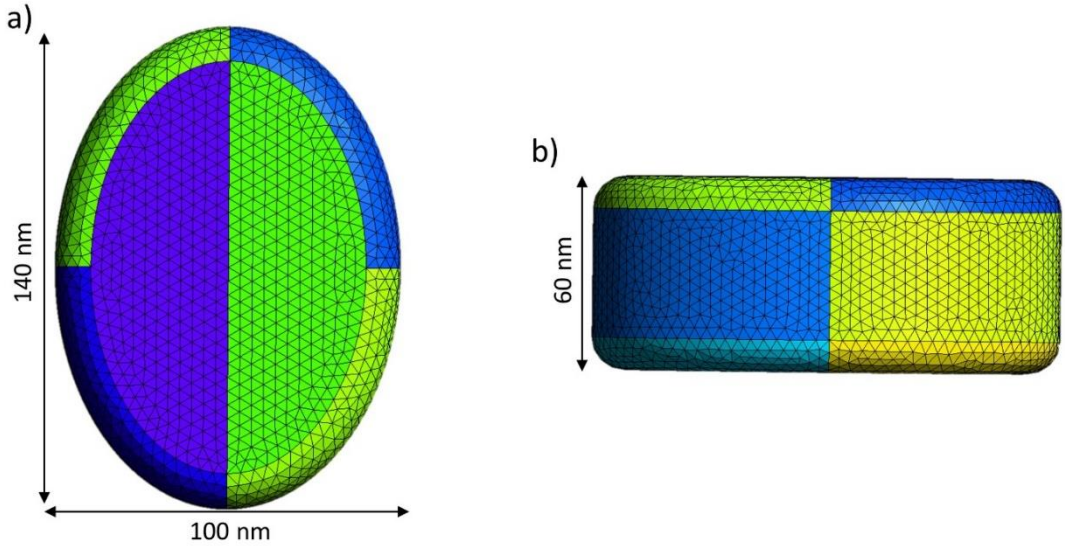

Supplementary Figure 7: *Nanoellipse created with the gmsh code and employed in the simulations: front view a), side view b). The surface elements, called tessera, that are here observable result from the surface mesh discretization operated by the gmsh code and it is necessary to numerically evaluate the coupling parameters with the MC molecules, see details below.*

In order to analyze the optical properties of the hybrid light-matter states (i.e. Polaritons) mentioned in the main text, we employed the quantization scheme of the metallic response based on a single Drude-Lorentz oscillator model of the dielectric function as developed previously **[7]**. In short, starting from a classical description of the nanoparticle within the PCM-NP framework **[8]** subject to an external frequency-dependent perturbation (in the quasi-static limit), one can obtain the following expression:

$$\mathrm{q}(\omega) = \mathrm{Q}^{\mathrm{IEF}}(\omega)\mathrm{V}(\omega) \tag{1}$$

Where $\mathrm{q}(\omega)$ is a collection of polarization surface charges that account for the nanoparticle linear response under the external electrostatic potential $\mathrm{V}(\omega)$ and $\mathrm{Q}^{\mathrm{IEF}}(\omega)$ is the frequency-dependent response function, that can be recast into a diagonal form as **[9]**:

$$\mathrm{Q^{IEF}}(\omega) = -\mathrm{S}^{-\frac{1}{2}}\mathrm{TK}(\omega)\mathrm{T}^{\dagger}\mathrm{S}^{-\frac{1}{2}} \tag{2}$$

with

$$\mathrm{K_p}(\omega) = \frac{2\pi + \Lambda_p}{2\pi\dfrac{\varepsilon(\omega)+1}{\varepsilon(\omega)-1} + \Lambda_\mathrm{p}} \tag{3}$$

where $\mathrm{K}(\omega)$ is the diagonal response matrix derived from eigenvalues Λ_p of the appropriate IEF matrix **[9]**, $\varepsilon(\omega)$ is the frequency dependent dielectric function and S is the matrix storing the electrostatic potentials between discrete points of the dielectric.
Based on this classical description and assuming a single Drude-Lorentz oscillator model for the metal dielectric function one can retrieve the following quantum response function**[7]**

$$\mathrm{Q_{kj}^{quant}}(\omega) = -\sum_\mathrm{p} \frac{\langle 0|\hat{\mathrm{q}}_\mathrm{k}|\mathrm{p}\rangle\langle \mathrm{p}|\hat{\mathrm{q}}_\mathrm{j}|0\rangle}{\omega_\mathrm{p} + \omega + i\Gamma/2} + \frac{\langle \mathrm{p}|\hat{\mathrm{q}}_\mathrm{k}|0\rangle\langle 0|\hat{\mathrm{q}}_\mathrm{j}|\mathrm{p}\rangle}{\omega_\mathrm{p} - \omega - i\Gamma/2} \tag{4}$$

where each matrix element k, j of the matrix response function $Q^{quant}(\omega)$ is evaluated on the representative points of the tesserae k and j, and ω_p is the frequency of a given plasmon mode computed as:

$$\omega_\mathrm{p}^2 = \omega_0^2 + \left(1 + \frac{\Lambda_\mathrm{p}}{2\pi}\right)\frac{\Omega_\mathrm{p}^2}{2} \tag{5}$$

with Ω_p being the plasma frequency of the bulk metal, and Γ is the damping rate of the DL oscillator. It is important to notice that elements as $\langle 0|\hat{q}_k|p\rangle$ represent the quantized transition charges sitting on the k-th tessera related to the mode p, so for a given plasmon mode p a collection of quantized charges (one for each tessera) is given. These quantities, that are analogous to molecular transition densities, can be used to numerically evaluate the coupling strength between a selected plasmon mode and a given molecule, that reads:

$$\hat{\mathrm{g}}_\mathrm{p} = \sum_\mathrm{j} q_{p,j}\hat{\mathrm{V}}_\mathrm{j} \tag{6}$$

Where $\hat{\mathrm{V}}_\mathrm{j}$ is the molecular electrostatic potential operator evaluated at the position of the j-th tessera where the $q_{p,j}$ charge related to the p mode lies on.

Considering the previously mentioned theoretical background, in order to shed light on the optical response of the coupled system the aluminum nanoellipse of Supplementary Figure 7 was surrounded by many merocyanine molecules (MCs), each one described as a point-dipole and an ad-hoc Tavis-Cummings-like Hamiltonian (in atomic units, au) was set up:

$$\hat{\mathrm{H}} = \sum_{\mathrm{i}=1}^{\mathrm{N}} \overline{\omega}_{\mathrm{MC}} \hat{\sigma}_{\mathrm{i}}^{\dagger} \hat{\sigma}_{\mathrm{i}} + \overline{\omega}_{\mathrm{LA}} \hat{\mathrm{a}}_{\mathrm{LA}}^{\dagger} \hat{\mathrm{a}}_{\mathrm{LA}} + \overline{\omega}_{\mathrm{SA}} \hat{\mathrm{a}}_{\mathrm{SA}}^{\dagger} \hat{\mathrm{a}}_{\mathrm{SA}} + \sum_{\mathrm{i}=1}^{\mathrm{N}} g_{\mathrm{i,LA}} \left(\hat{\mathrm{a}}_{\mathrm{LA}}^{\dagger} \hat{\sigma}_{\mathrm{i}} + \hat{\mathrm{a}}_{\mathrm{LA}} \hat{\sigma}_{\mathrm{i}}^{\dagger} \right) + \sum_{\mathrm{i}=1}^{\mathrm{N}} g_{\mathrm{i,SA}} \left(\hat{\mathrm{a}}_{\mathrm{SA}}^{\dagger} \hat{\sigma}_{\mathrm{i}} + \hat{\mathrm{a}}_{\mathrm{SA}} \hat{\sigma}_{\mathrm{i}}^{\dagger} \right)$$

(7)

Where the $\hat{\sigma}_{\mathrm{i}}$ and $\hat{\sigma}_{\mathrm{i}}^{\dagger}$ are the typical molecular transfer operators and $\hat{\mathrm{a}}_{\mathrm{LA}}^{\dagger}$ ($\hat{\mathrm{a}}_{\mathrm{LA}}$) is the creation (annihilation) operator related to the long-axis mode of the nanoellipse, whereas $\hat{\mathrm{a}}_{\mathrm{SA}}^{\dagger}$ ($\hat{\mathrm{a}}_{\mathrm{SA}}$) is the corresponding operator for the short axis mode. We also note that $\overline{\omega}_{\mathrm{MC}} = \omega_{\mathrm{MC}} - i\Gamma_{\mathrm{MC}}$, $\overline{\omega}_{\mathrm{LA}} = \omega_{\mathrm{LA}} - i\Gamma_{\mathrm{LA}}$ and $\overline{\omega}_{\mathrm{SA}} = \omega_{\mathrm{SA}} - i\Gamma_{\mathrm{SA}}$ where each imaginary component contains the corresponding decay rate of the uncoupled state. The inclusion of the decay rate as an imaginary part results in a non-Hermitian Hamiltonian, previously applied to the case of individual molecules **[10-11]** and more recently to plexcitonic systems **[12]**. The molecular decay rate is set to $\Gamma_{\mathrm{MC}} = 1.5 \times 10^{-4}\mathrm{au}$ based on the linewidth of the experimental data shown in Supplementary Figure 4, whereas $\Gamma_{\mathrm{LA}} = 0.038\mathrm{au}$ and $\Gamma_{\mathrm{SA}} = 0.053\mathrm{au}$ were chosen on the basis of the fitted DL parameters as described in Supplementary Figure 10.

In the 1-excitation-space the Hamiltonian shown above (7) reads:

$$\hat{H} = \sum_{i=1}^{N} \overline{\omega}_{MC} |G_1..E_i..G_N;0,0\rangle\langle 0,0;G_1..E_i..G_N| + \overline{\omega}_{LA} |G_1..G_N;1,0\rangle\langle 1,0;G_1..G_N| + \overline{\omega}_{SA} |G_1..G_N;0,1\rangle\langle 0,1;G_1..G_N| + \sum_{i=1}^{N} g_{i,LA} |G_1..G_N;1,0\rangle\langle 0,0;G_1..E_i..G_N| + adj. + \sum_{i=1}^{N} g_{i,SA} |G_1..G_N;0,1\rangle\langle 0,0;G_1..E_i..G_N| + adj.$$

(8)

Where $\mathrm{G_i}$ stands for the ground state of the i-th molecule, $\mathrm{E_i}$ means the excited state of the i-th molecule and $g_{\mathrm{i,LA}}$ ($g_{\mathrm{i,SA}}$) is the coupling strength between the i-th molecule $\mathrm{G_i}$->$\mathrm{E_i}$ transition and the long-axis (short-axis) plasmon mode. Note that unlike the original TC Hamiltonian, here each molecule features its own coupling strength and orientation with respect to the given plasmon modes (two simultaneously considered in this work). The values of $g_{\mathrm{i,LA}}$ ($g_{\mathrm{i,SA}}$) were calculated for each molecule by the interaction of the $\mathrm{G_i}$->$\mathrm{E_i}$ transition dipole with the relevant plasmonic mode charges **[7]**. Since each molecule interacts differently with the given plasmon modes, not all of them equally contribute to the polaritonic states. The Inverse Partecipation Ration (IPR) defined as $\mathrm{IPR} = \frac{1}{\sum_{\mathrm{i}=1}^{\mathrm{N}} |\mathrm{C_i}|^4}$ is a well-known quantifier for measuring exciton delocalization over many different molecules, and it can also be used in our case to have a quantitative estimate of the degree of molecular delocalization of the polaritonic states**[13]**. In the ideal limit of N identical molecules equally coupled to a given mode, the analytical solution**[17]** of the TC Hamiltonian would give a coefficient on each molecular state participating to the polaritonic wavefunction of $\frac{1}{\sqrt{2N}}$, and since in our simulation setup N is equal to 590, the corresponding IPR coefficient in the case of N molecules all equally contributing to the polaritonic states should be $\mathrm{IPR} = \frac{1}{\frac{\mathrm{N}}{4\mathrm{N}^2}} = 4\mathrm{N} = 2360$. In the LA case, the computed IPR is $\mathrm{IPR_{LA}} = 1037$, while in the SA case it is $\mathrm{IPR_{SA}} = 370$, thus clearly showing that in both cases the excitation of the collective polaritonic state is not equally shared among all molecules, since some of them are more

coupled to the modes than others. Therefore, changing the properties of a single molecule among those that are strongly contributing to the polaritonic state can provide appreciable effects in collective response.

Diagonalization of such Hamiltonian (8) gives access to the 1-excitation-space polaritonic energies (eigenvalues) and corresponding polaritonic wavefunctions (eigenvectors). Transition dipoles from the GS to each 1-excitation-space polariton (1PL), that is $\langle \mathrm{GS}|\hat{\mu}|1\mathrm{PL}\rangle = \boldsymbol{\mu_{1PL}}$, were calculated by linear combination of molecular terms obtained by the TDDFT calculations of the previous section, such as $\langle \mathrm{GS}|\hat{\mu}|\mathrm{E}_1..\mathrm{G_N};0,0\rangle = \boldsymbol{\mu_1}$, and plasmonic terms, like $\langle \mathrm{GS}|\hat{\mu}|\mathrm{G}_1..\mathrm{G_N};1,0\rangle = \boldsymbol{\mu_{LA}}$ and $\langle \mathrm{GS}|\hat{\mu}|\mathrm{G}_1..\mathrm{G_N};0,1\rangle = \boldsymbol{\mu_{SA}}$. Such plasmonic transition dipoles are evaluated as $\sum_{\mathrm{j}} q_{p,j}\mathbf{r_j}$,where $\mathbf{r_j}$ is the position of the center of each tessera where the quantized surface charge $q_{p,j}$ lies on , for a given mode p.

The decay rates (linewidths) $\Gamma_{1\mathrm{PL}}$ associated to each polaritonic state are directly obtained from the imaginary component of the eigenvalues of the Hamiltonian (8).

Once these quantities are computed, the linear response expression of the polarizability of the entire system (molecule+nanostructure) as a sum over the polaritonic states reads:

$$\alpha_{\mathrm{ij}}(\omega) = \sum_{1\mathrm{PL}} \frac{\langle \mathrm{GS}|\hat{\mu}_{\mathrm{i}}|1\mathrm{PL}\rangle\langle 1\mathrm{PL}|\hat{\mu}_{\mathrm{j}}|\mathrm{GS}\rangle}{\omega_{1\mathrm{PL}} + \omega + i\Gamma_{1\mathrm{PL}}/2} + \frac{\langle \mathrm{GS}|\hat{\mu}_{\mathrm{i}}|1\mathrm{PL}\rangle\langle 1\mathrm{PL}|\hat{\mu}_{\mathrm{j}}|\mathrm{GS}\rangle}{\omega_{1\mathrm{PL}} - \omega - i\Gamma_{1\mathrm{PL}}/2} \tag{9}$$

with $\langle \mathrm{GS}|\hat{\mu}_{\mathrm{i}}|1\mathrm{PL}\rangle = \boldsymbol{\mu_{1PL,i}}$ being the i-th component of the transition dipole to a given polaritonic state 1PL with energy $\omega_{1\mathrm{PL}}$ and damping rate $\Gamma_{1\mathrm{PL}}$. Such quantity (9) is used to evaluate the absorption cross section (reported in panels e-f, Figure 1 main text) through **[14]**:

$$\sigma_{\mathrm{ii}}(\omega) = \frac{4\pi\omega}{c}\mathrm{Im}\{\alpha_{\mathrm{ii}}(\omega)\} \tag{10}$$

where ii is either xx or yy in our simulations for the LA or SA case, respectively. This is because the experiments are done with polarized light pulses, so only some components of the polarizability tensor become relevant.

On a side note, we observe that the simulated spectra in the LA case (Figure 1e, main text) features a Rabi splitting that well reproduce the experimental one (Figure 1c) even though the simulated peaks appear to be broader. Indeed, by fitting the bare plasmonic experimental extinction spectrum with a Lorentzian function (see Supplementary Figure 11) we obtain a linewidth Γ of ≈ 0.022 au. (τ ≈ 1.1 fs) that is slightly smaller than the corresponding simulated value (Supplementary Figure 10). On these grounds, to quantitatively assess which coupling regime we are dealing with in the LA case (which is the case corresponding to zero detuning between plasmon energy and molecules energies), we resort to the well-known ratio**[15]** $\frac{2\Omega_{\mathrm{rabi}}}{\Gamma_1+\Gamma_2}$, with Ω_{rabi} being the energy separation of the polaritonic states and Γ_1, Γ_2 being the decay rates of the uncoupled system.

Considering that $\Gamma_1 = \Gamma_{\mathrm{LA}} = 0.022$ au , $\Gamma_2 = \Gamma_{\mathrm{MC}} = 1.5 \times 10^{-4}$au ($\tau_2$ ≈ 150 fs) and that the computed rabi splitting value is ≈ 410 meV (≈ 0.015 au) , we obtain $\frac{2\Omega_{\mathrm{rabi}}}{\Gamma_{\mathrm{LA}}+\Gamma_{\mathrm{MC}}}$ ≈ 1.4, thus corroborating that we are

at least undoubtedly at the onset**[16]** of a strong coupling regime, and proper polaritonic states are formed in the LA case.

In order to simulate the pump-probe transient response shown in Figure 3 main text, ground state bleaching (GSB), stimulated emission (SE) and excited state absorption (ESA) terms of eq.1 (Numerical calculations section of main text) have to be computed. The GSB signal comes from eqs. 9-10, whereas the ESA term can be computed through the 2-excitation-space states (2PL), thus the following Hamiltonian has to be diagonalized:

$$\begin{aligned}\widehat{\mathrm{H}} = &\sum_{\mathrm{i}=1}^{\mathrm{N}}\sum_{\mathrm{j}>\mathrm{i}} 2\bar{\omega}_{\mathrm{MC}}\left|\mathrm{E_iE_j}..\mathrm{G_N};0,0\right\rangle\left\langle 0,0;\mathrm{E_iE_j}..\mathrm{G_N}\right| + \sum_{\mathrm{i}=1}^{\mathrm{N}}(\bar{\omega}_{\mathrm{LA}}+\bar{\omega}_{\mathrm{MC}})|\mathrm{E_i}..\mathrm{G_N};1,0\rangle\langle 1,0;\mathrm{E_i}..\mathrm{G_N}| \\ &+ 2\bar{\omega}_{\mathrm{LA}}|\mathrm{G_1}..\mathrm{G_N};2,0\rangle\langle 2,0;\mathrm{G_1}..\mathrm{G_N}| + \sum_{\mathrm{i}=1}^{\mathrm{N}}\sum_{\mathrm{j}>\mathrm{i}} g_{\mathrm{j,LA}}\left|\mathrm{E_iE_j}..\mathrm{G_N};0,0\right\rangle\left\langle 1,0;\mathrm{E_iG_j}..\mathrm{G_N}\right| \\ &+ \mathrm{adj.} + \sum_{\mathrm{i}=1}^{\mathrm{N}}\sqrt{2}g_{\mathrm{i,LA}}|\mathrm{E_i}..\mathrm{G_N};1,0\rangle\langle 2,0;\mathrm{G_i}..\mathrm{G_N}| \\ &+ \mathrm{adj.} + \text{corresponding terms of SA mode}\end{aligned} \tag{11}$$

We note that considering the 2-excitation-space polaritons, in addition to the more canonical 1-excitation-space states, was recently suggested to be a theoretically robust way for interpreting transient pump-probe data of molecules in QED cavities by A. DelPo et al. **[17]**. We also remark that eigenenergies and eigenstates of our Hamiltonian (11) exactly match the analytical results reported in their work in the limit of identical molecules and couplings with all transition dipoles oriented along the direction of the cavity mode.

As mentioned in the main text, we assume that the pump-induced excitation of the polaritonic state (see Figures 3-4, main text) leads to the population of one localized molecular state $|\mathrm{MC}^*\rangle$ upon plasmon dephasing, from which SE to the GS and ESA to the 2-excitation-space polaritons transiently take place. The SE spectrum is simulated using (9) and (10), based on the wavefunction of the emitting state $|\mathrm{MC}^*\rangle$ obtained through diagonalization of the 1-excitation Hamiltonian (8) with one red-shifted MC. Indeed, the formation of this localized state $|\mathrm{MC}^*\rangle$ comes from diagonalization of the Hamiltonian (8) once one of the diagonal elements $\bar{\omega}_{\mathrm{MC}}$ corresponding to one MC molecule that was originally contributing most to the collective state gets red-shifted as $\bar{\omega}_{\mathrm{MC}^*} = \bar{\omega}_{\mathrm{MC}} - \delta$ (with δ being the frequency shift because of vibrational relaxation, see Numerical calculations section, main text) and it can be easily understood in the framework of perturbation theory. In the LA case ,where $\omega_{\mathrm{MC}} = \omega_{\mathrm{LA}}$, the largest computed single-molecule coupling with the LA mode is ≈ 18 meV (after scaling the actual value by a factor of 15, see Supplementary Figures 8-9 below and related discussion), so as δ increases (for instance it is already ≈ 50 meV at 50 fs after the pump excitation, see 1-to-1 mapping in Numerical calculation section of main text) we approach a perturbative regime where $\frac{g}{\delta} \ll 1$, therefore by diagonalizing the Hamiltonian (8) with such δ values we basically get one state corresponding to the red-shifted molecule, and collective polaritonic states of the N-1 remaining molecules, along with their associated dark states. In the SA case this regime is reached even more quickly as before applying any frequency shift there is already a zero-order frequency detuning between ω_{MC} and ω_{SA} of ≈ 300 meV.

On the other hand, the ESA term can be obtained through equation (10), having:

$$\alpha_{ij}(\omega) = \sum_{2PL} \frac{\langle MC^*|\hat{\mu}_i|2PL\rangle\langle 2PL|\hat{\mu}_j|MC^*\rangle}{(\omega_{2PL} - \omega_{MC^*}) + \omega + i|\Gamma_{2PL} - \Gamma_{MC^*}|/2} + \frac{\langle MC^*|\hat{\mu}_i|2PL\rangle\langle 2PL|\hat{\mu}_j|MC^*\rangle}{(\omega_{2PL} - \omega_{MC^*}) - \omega - i|\Gamma_{2PL} - \Gamma_{MC^*}|/2}$$

(12)

Where the 2-excitation-space polaritons are in this case obtained through diagonalization of (11) with all the diagonal elements corresponding to the red-shifted MC molecule modified accordingly to account for the frequency shift (similarly to the frequency shift shown above for the 1-excitation Hamiltonian, but this time applied to all diagonal elements of (11) where that molecule appears). Since Figure 3 (main text) presents data at different time delays, which corresponds in our picture to different frequency shifts because of vibrational relaxation, the diagonalization of (8) and (11) with some red-shifted diagonal elements have been performed multiple times, each time for a different frequency shift value corresponding to a given time delay, following the 1-to-1 mapping mentioned in the Numerical calculations section of main text.

We remark that the N-1 simplified picture that we also make use of in the main text for explaining the results follows directly from this complete model once the shift is such that $\frac{g}{\bar{\omega}_{LA/SA} - \bar{\omega}_{MC^*}} \ll 1$. Under this regime, diagonalization of (8) leads to the localized molecular state $|MC^*\rangle$ on which the initial collective excitation is collapsed, and from this state the bright states that can be populated upon probe absorption (ESA contribution) which are obtained by diagonalizing (11) with corresponding shifted diagonal elements can be mostly seen as polaritonic states of the N-1 remaining molecules.

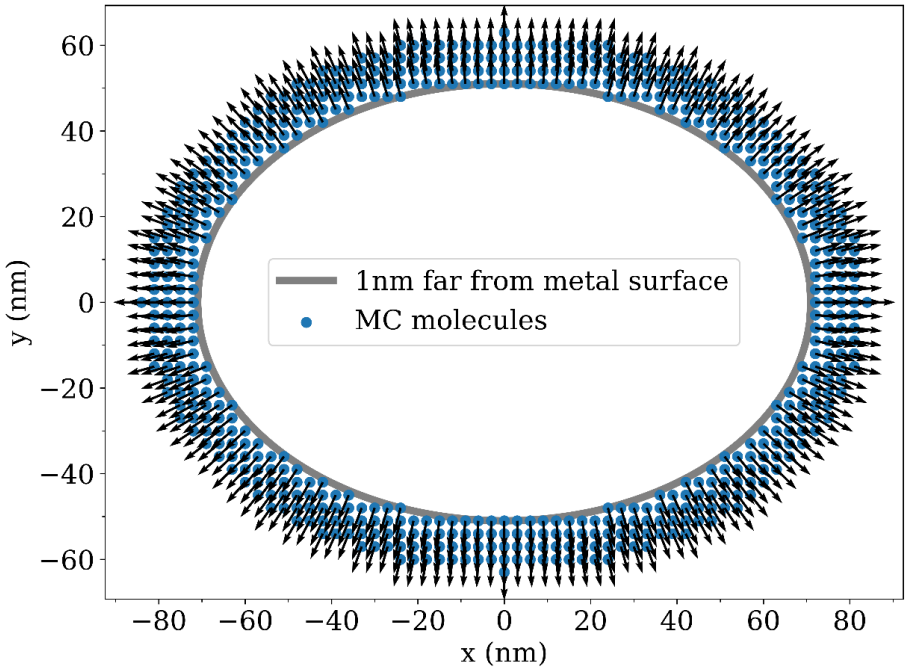

Supplementary Figure 8: *2D slice of the elliptical grid employed in the simulations. Each blue dot represents a MC molecule described as a point-dipole oriented perpendicular to the metal surface. The nearest neighbor distance was set to 3 nm, which corresponds to the sample concentration of 2% wt (≈ 1 molecule per 26 nm^3). Data provided in the main text was obtained with such setup on a 2D layer of molecules only, scaling the coupling values accordingly to match with the experimental linear absorption of the coupled system. More detailed information regarding the computed coupling strength with the full 3D grid are reported in Supplementary Figure 9.*

As described in Supplementary Figure 8, the data reported in the main text was obtained considering a single 2D grid layer of molecules located at half height of the nanoellipse to save computational time, and the corresponding calculated coupling values have been increased until a good matching with the experimental linear absorption was found (see Figure 1 main text). (We recall the relation between the Rabi splitting energy Ω_{R} and the number of molecules N_{res} resonantly coupled to the mode in the simplified case of equal coupling for all the molecules, i.e., $\Omega_{\mathrm{R}} \propto \sqrt{N_{\mathrm{res}}}$).
Despite this computationally convenient choice, calculations with full 3D grid of MCs surrounding the nanoellipse were also performed in order to assess whether the computed couplings of the real 3D system were large enough to correctly reproduce the experimental data (without any ad hoc increase). As shown in Supplementary Figure 9 panel a), two distinct grid steps have been tested, 3.0nm (corresponding to 1 molecule per 27 nm^3) and 2.0 nm (corresponding to 1 molecule per 8 nm^3) respectively, and it turned out that in the tightest 3D grid case (2 nm step size, green curve), by employing a multiplying factor of 2 for the computed couplings, the corresponding Rabi splitting is slightly larger than the experimental one, which perfectly matches with that predicted assuming 1 single 2D layer with step size of 3nm and couplings scaled by a factor of 15 (blue curve). These numerical tests point out that in the realistic limit of a full 3D grid having an intermediate step size between 2 and 3 nm the calculated couplings would reproduce the experimental data, thus corroborating the theoretical model.

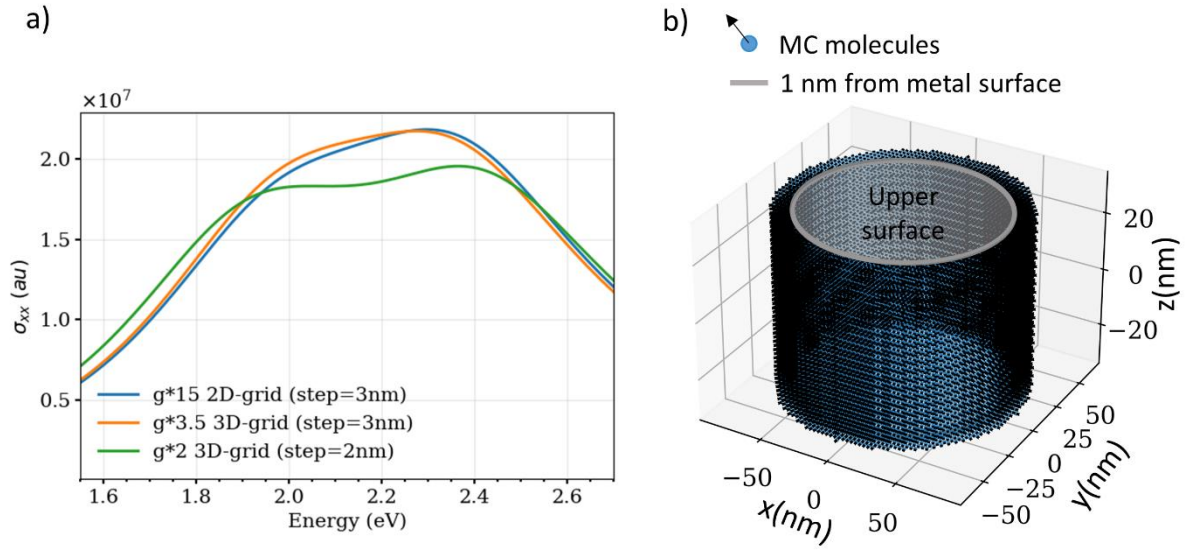

Supplementary Figure 9: *a) Simulated linear absorption of the polaritonic system (LA case) considering different grids and scaling factors for the computed couplings: 2D grid only (step size 3 nm between nearest neighbors and couplings scaled by a factor of 15) (blue line), 3D grid (step size 3nm and couplings scaled by a factor of 3.5) (orange line) and 3D grid (step size 2nm and couplings scaled by a factor of 2). b) Scheme of the 3D grid employed to obtain the orange line panel a.*

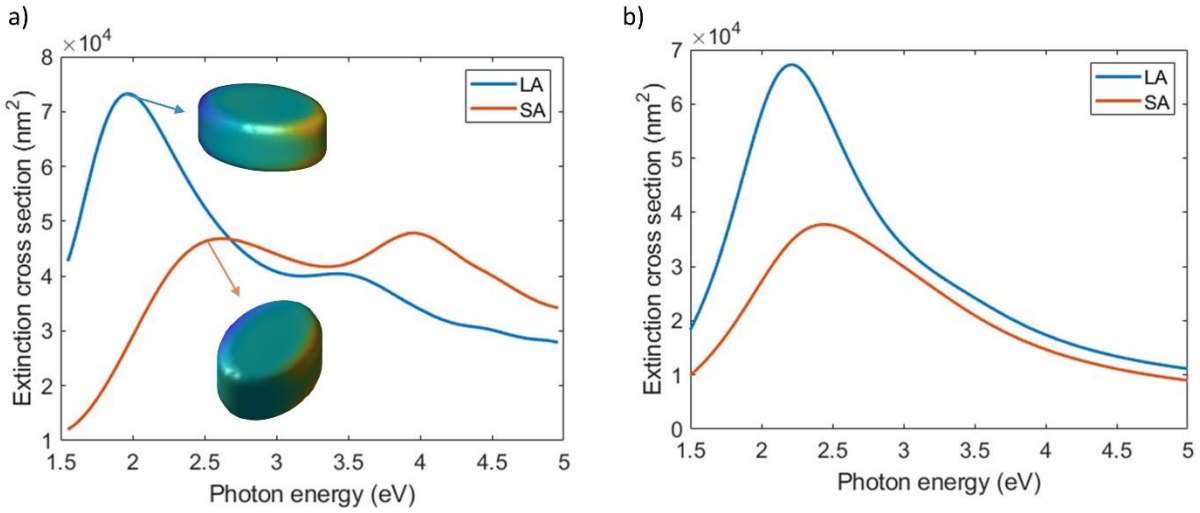

Supplementary Figure 10: *a) Simulated extinction spectra of the model nanoellipse computed by solving the full Maxwell equations through the MNPBEM code* ***[18]*** *for two distinct electric field polarizations of the incoming wave: long-axis direction (blue line) and short-axis direction (orange line). The aluminum dielectric function employed in the simulations is that of McPeak et al.* ***[19]*** *and the environment refractive index was set to 1.5. The two small insets display the surface charge distribution associated with the corresponding main peaks (dipolar plasmon resonances of interest); the yellow color represents positive charges, whereas blue represents negative ones. The two peak energies are very close to the experimental ones (2.15 and 2.45 eV after Spy deposition, Figure 1 panels c-d main text). b) Simulated quasistatic extinction spectra of the same nanoellipse by adopting a single Drude-Lorentz oscillator model for the dielectric function and tuning the corresponding parameters to reproduce the principal features of the two main dipolar resonances shown in panel a). The plasma frequency was set to 0.025 au (eq. 5) and the following decay rates* Γ_{LA}*=0.038 au and* Γ_{SA}*=0.053 au for the long-axis (LA) and short-axis (SA) plasmons were employed.*

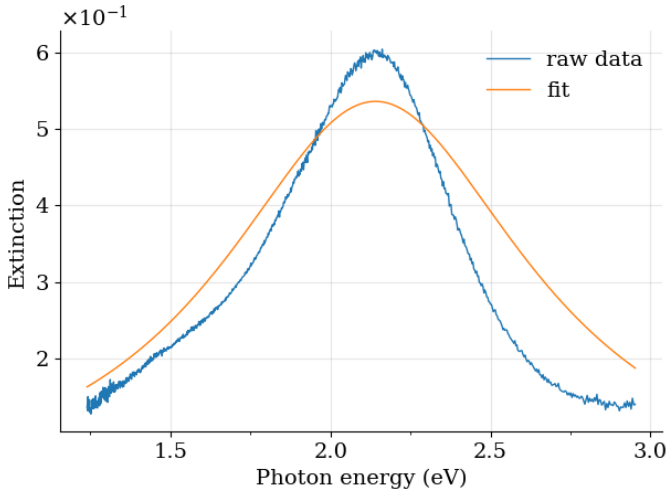

Supplementary Figure 11: *Experimental plasmonic extinction spectrum in the LA case (blue curve) and corresponding fitted curve (orange) obtained with a Lorentzian function:* $\frac{\Gamma}{\pi*((\omega-\omega_0)^2+\Gamma^2)}$***.*** *The fitting procedure yielded Γ≈0.022 au (≈600 meV) that is somewhat smaller than the value obtained from simulations (Supplementary Figure 10).*

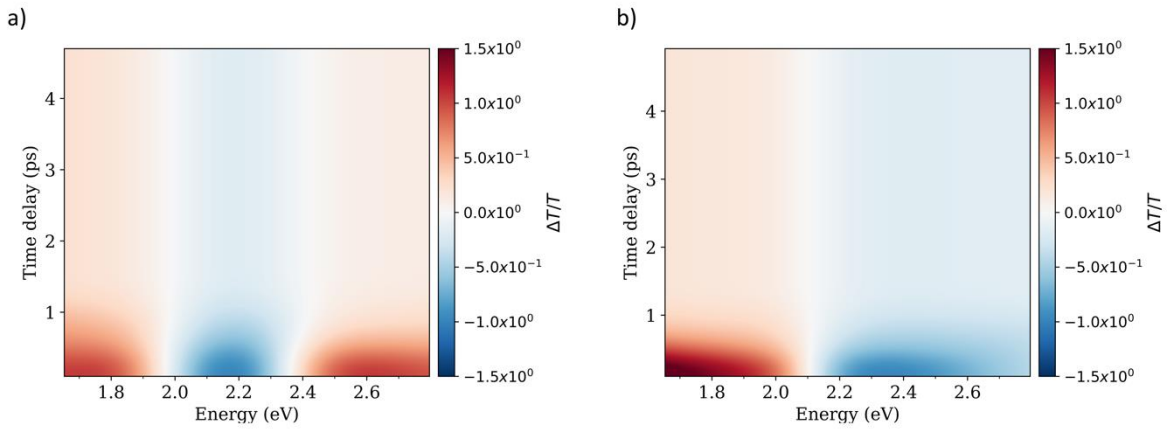

Supplementary Figure 12: *Pump-probe simulated 2D maps in the LA (a) and SA (b) case according to the procedure described in the Numerical calculations part of the Methods section, main text. Since the experimental signal shown in Figure 3 a-d (main text) presents a constant magnitude after ≈1 ps that is roughly 1/5 of the intensity at early times, the same constant feature has been applied here to recover a similar spectral trend at longer times (> 1ps).*

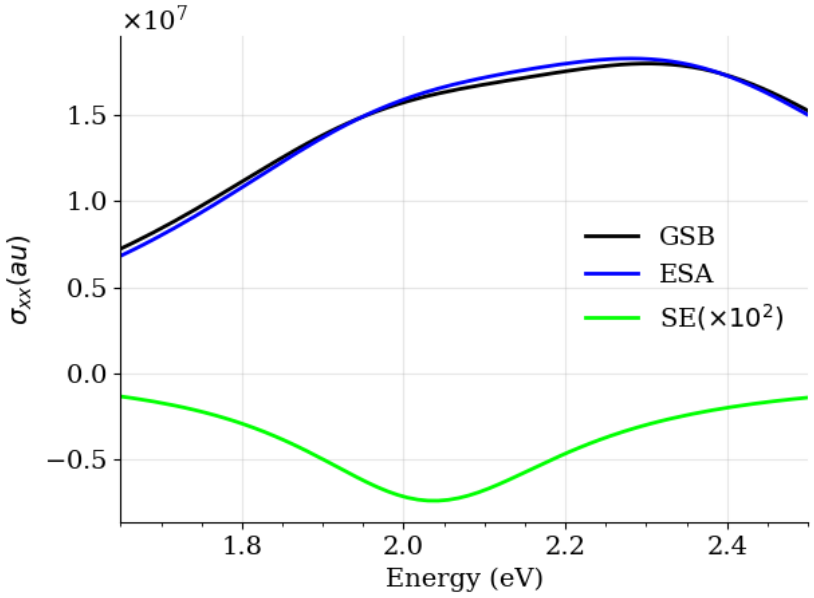

Supplementary Figure 13: *Explicit GSB, ESA and SE contributions obtained through the theoretical model at 200 fs from the pump excitation. The time delay corresponds to a merocyanine frequency shift of 125 meV (see 1-to-1 mapping between molecular energy shifts and time-delay in the Numerical calculations section of main text). The three contributions are combined according to eq.1 (main text) to get the transient data reported in Figure 3c (main text). Note that GSB and ESA appear with opposite signs in that equation. The SE contribution is originating from a single molecule state (see Figure 4, main text), indeed it is considerably smaller than GSB or ESA contributions which are the predominant terms (the SE signal has been scaled by 10^2 in the plot to ease visual inspection).*

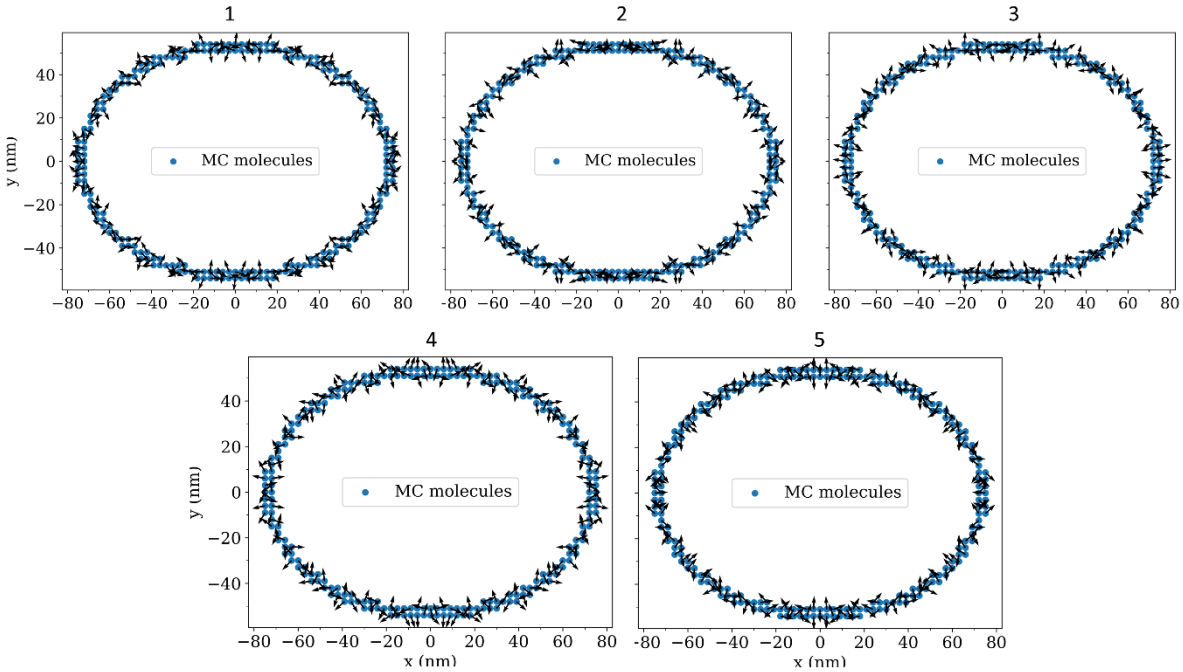

Supplementary Figure 14: *Different (1-5) randomly oriented merocyanines (here represented as point-dipoles) used to obtain the results reported in Supplementary Figure 12 to test the robustness of the theoretical simulations against different alignments of the dipoles with respect to the nanoantenna.*

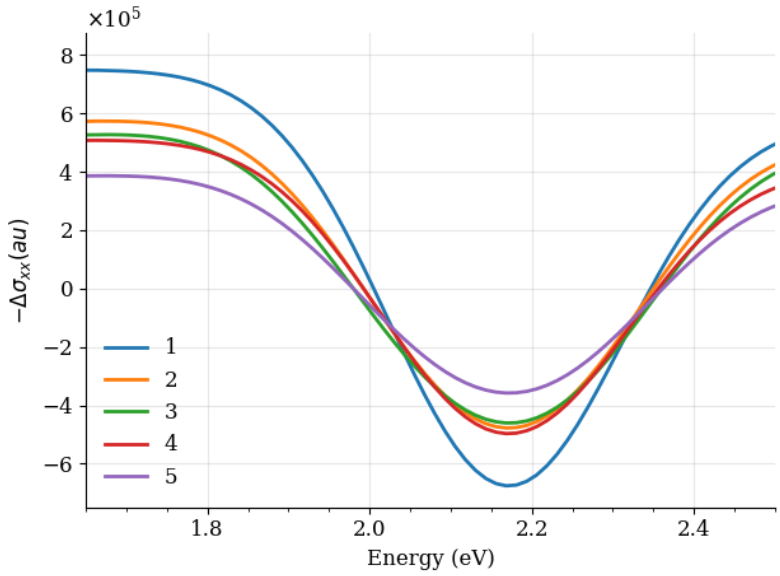

Supplementary Figure 15: *Simulated transient response in the LA case for each (1-5) set of randomly distributed dipoles of Supplementary Figure 14 considering a frequency shift of 100 meV for one MC molecule. Although some differences are visible, the overall qualitative signal trend always match with the experimental one (Figure 3 a-c, main text). In particular, we note that no spectral shift is observed for the different configurations, thus proving that dipoles' orientation does not affect the interpretation of the ultrafast dynamics observed.*

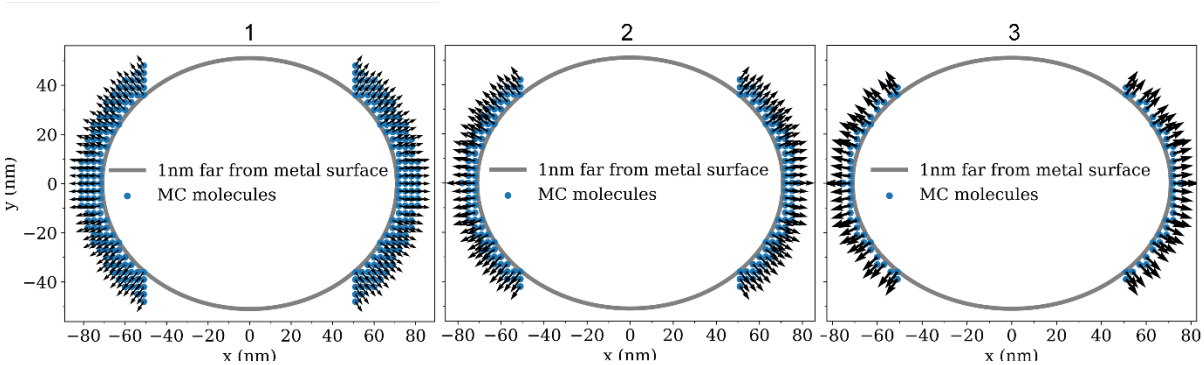

Supplementary Figure 16: *Different thicknesses of the molecular layer around the nanoantenna (1-3). From 1 to 3 the thickness decreases and so does the number of emitters (merocyanines, here represented as point dipoles) coupled to the LA mode.*
The corresponding simulated linear and transient optical signals are reported in Supplementary Figure 17.

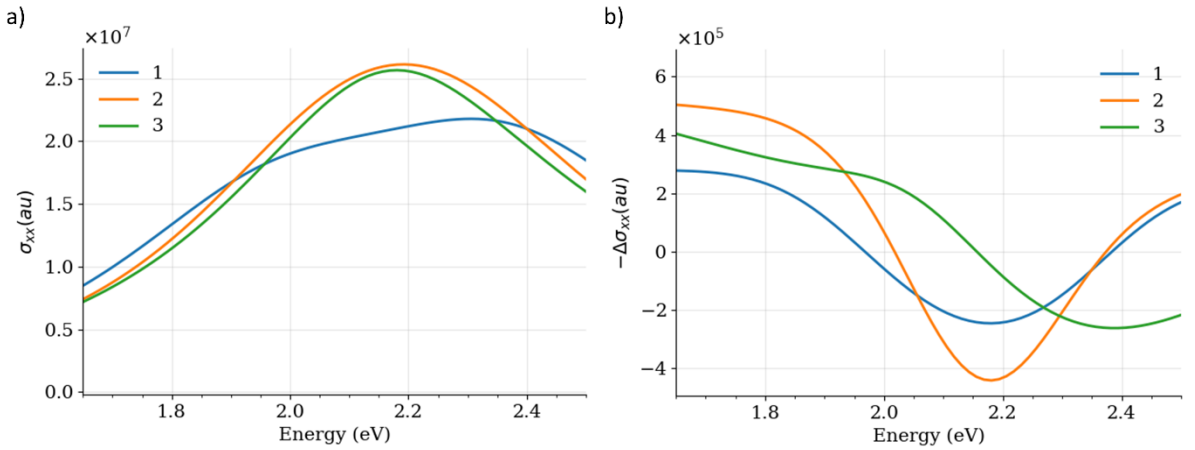

Supplementary Figure 17: *Simulated linear(a) and transient(b) spectra of the corresponding setups of Supplementary Figure 16. The transient data of panel b is obtained considering a frequency shift of 125 meV for a single MC molecule, which would correspond to the signal probed at 200 fs (see Numerical calculations section of main text for the energy-to-time delay mapping). All simulations have been performed by scaling the molecule-nanoantenna couplings so that setup n.1 yields a linear absorption matching the one of Figure 1c (main text) that was obtained considering a thicker layer of molecules (Supplementary Figure 8). Notably, as the molecular layer thickness (and so the number of emitters) decreases, the simulated transient signal (panel b) seems to approach a spectral line shape (green curve) that resembles what we get for the SA case (Figure 3f main text), which is the weakly-coupled system.*

Supplementary Note 2.3 – Theoretical discussion on the experimental results of Figure 5 (main text)

The data shown in Figure 5 (main text) illustrate the presence of an accelerated molecular decay both in the weakly (Figure 5b) and strongly coupled case (Figure 5c) compared to isolated molecules (Figure 5a). Interestingly, by following the wavefunction composition of the localized molecular state in the LA case during the vibrational dynamics we noticed that a residual coupling with the plasmon is still present. Notably, this coupling slightly increases when the localized molecular state approaches the energy of the lower polariton state of the remaining N-1 molecules. On this ground, we can reasonably relate the observed accelerated decay of the localized excitation to a plasmonic

effect, leading to the sub-ps decay that is shown in Figure 5b-c. Indeed, this residual plasmonic component leads to a fast decay that can be estimated to be $\Gamma_{\mathrm{MC}^*} \approx \left|C_{\mathrm{MC}^*-\mathrm{p}}\right|^2 * \Gamma_{\mathrm{LA}}$ (where $C_{\mathrm{MC}^*-\mathrm{p}}$ is the coefficient of the localized state wavefunction on the LA plasmonic state, whose squared modulus is ≈ 3.5*10^{-3}, and $\Gamma_{\mathrm{LA}} = 0.038\ \mathrm{au.}\ (\tau \approx 0.6\ \mathrm{fs})$ is the LA plasmon decay rate, Supplementary Figure 10) which corresponds to a lifetime of ≈ 0.2 ps.

A similar reasoning for the short axis case (SA) leads to a comparable value.

Additionally, we can (although just theoretically) decompose such enhanced decay in a radiative and a non-radiative contribution. The radiative contribution can be estimated as**[20]**:

$$\Gamma_{\mathrm{rad}}^{\mathrm{LA}} = \frac{4}{3}\frac{\omega^3}{c^3}|\boldsymbol{\mu}_{\mathbf{tot}}|^2 \tag{13}$$

With$\boldsymbol{\mu}_{\mathbf{tot}}$ being the total dipole of the localized state calculated as described in section 2.2, which then presents a plasmonic contribution as mentioned above, and hence intrinsically accounts for the Purcell-enhanced radiative emission. In both the LA and SA cases we obtain that $\Gamma_{\mathrm{rad}}^{\mathrm{LA/SA}}$ is almost an order of magnitude smaller than the corresponding value of Γ_{MC^*} , pointing to the enhanced non-radiative decay as prevailing.

Supplementary Note 3. Time-resolved experiments.

Supplementary Note 3.1 – Nonlinear optical response of Spiropyran and influence of photoisomerisation in pump-probe experiments

To study the transient transmission of merocyanine molecules, as shown in the main manuscript, the molecular film is illuminated with UV light that photoswitches SP molecules to their MC isomer. The pump-probe measurements are then performed on the switched sample. Via continuous spectrum acquisition, we can track both the nonlinear optical response $\Delta T/T$ and the linear transmission T simultaneously during the pump-probe measurement. The linear Transmission T at 2.15 eV during one such measurement on the merocyanine thin film is shown in Supplementary Figure 18 a). After switching on the UV light source at time $t = 0$, T decreases rapidly due to activation of the MC $\pi - \pi^*$ transition. Subsequently, T increases again due to back-photoswitching of MC to the SP form induced by irradiation with the optical pump and probe pulses. Hence, this should lead to less MC molecules contributing to the pump-probe signal over time. We can track the magnitude of the pump-probe signal by repetitively performing the same pump-probe scan while monitoring the transient transmission $\Delta T/T$. More in detail, the 2D map shown in Figure 2 a) of the main manuscript is averaged in energy from 1.75 eV to 2.25 and then averaged in time from 0.5 ps to 5 ps, providing a measure of the signal magnitude of the individual pump-probe scan. The data for repetitive measurements is shown in Supplementary Figure 18 b). The source of the observed decrease is a decrease in the number of MC molecules due to visible-light-induced back-photoswitching to the SP form. Hence, we observe the same time constant of the decay as shown in a). Indeed, the SP molecules do not contribute to the pump-probe signal, as shown in Supplementary Figure 18 c), where a pump-probe measurement is performed on the SP molecular film without prior UV illumination. Note that a small change of Δ T⁄T can be observed at the temporal overlap of pump and probe pulses. Such artefact can be caused by coherent interaction of pump and probe pulses mediated by higher-order susceptibilities of the molecular film**[21]**. However, such coherent artefacts are localized at t=0 and

thus do not contribute to the pump-probe signal at t>0. This allows a mapping of the pump-probe signal strength to the number of molecules that are still in their MC form. Thus, in order to correct for the decreasing number of molecules, the pump-probe data can be renormalized by the curve shown in a).

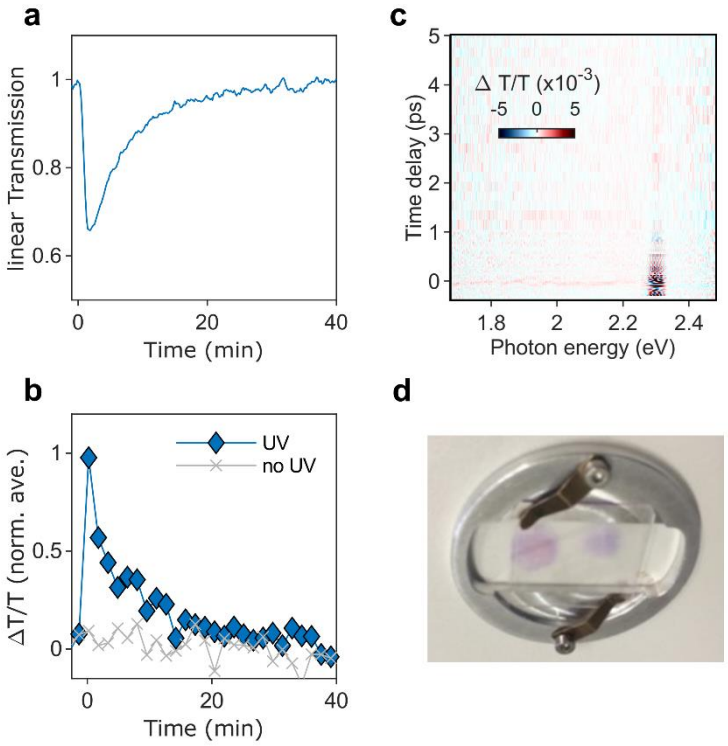

Supplementary Figure 18: *a) Linear transmission of the molecular film during pump-probe measurements. The UV light source is switched on at t=0 min. Illumination with visible light pulses causes MC molecules to switch back to the SP form. b) Energy(1.75-2-25 eV)- and time(0.5-1 ps)-averaged $\Delta T/T$ for repetitive pump-probe scans (blue diamonds) on the UV illuminated sample. Grey stars is data recorded on the film without UV illumination. c) 2D pump-probe spectrum acquired on the SP molecules without UV illumination. d) Photograph of the sample 2 days after performing ~100 pump-probe scans. Irradiated spots appear with a purplish color, indicative of permanent damage of the sample.*

Finally, after performing many measurements on the same spot on the sample, a permanent change of color can be observed (Supplementary Figure 18 d), related to photodegradation of the molecular film. Such photodecomposition, i.e. irreversible side reactions that lead to unwanted byproducts, was also found in previous works **[22]**. Usually, up to $\sim 10^8$pump pulses (~1h of measurements) can be applied to one spot before permanent damage. To obtain measurements of the pristine sample, the sample can then be moved, such that a new spot is irradiated.

Supplementary Note 3.2 – Determination of vibrational relaxation time scale

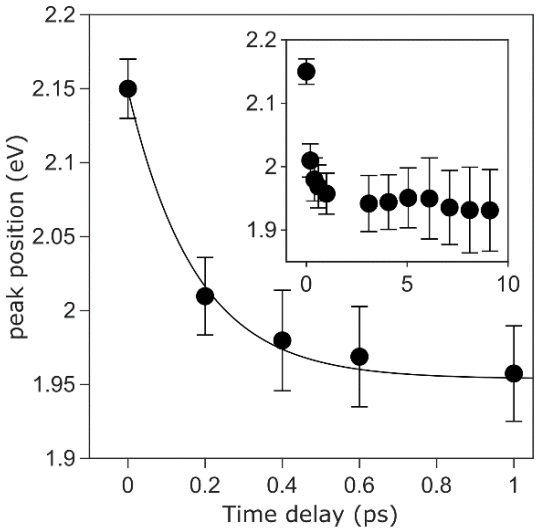

Supplementary Figure 19: *Peak positions of $\Delta T/T$ obtained via fitting of energy-resolved cuts of the 2D pump-probe data shown in Figure 2 a) of the main manuscript with a Gaussian spectral profile. Error bars represent 95% confidence bounds and are obtained from the Gaussian fit. Inset is a zoom-out of the data. A red-shift due to vibrational relaxation on the MC excited state is clearly reflected by the data. Solid line shows an exponential fit to the data.*

In order to determine the time scale of the molecular vibration on the MC excited state, energy-resolved cuts shown in Figure 2 of the main manuscript are fitted with a Gaussian profile, allowing to obtain the peak position of $\Delta T/T$ for each time delay (see Supplementary Figure 19). Clearly, the red-shift that is observed in the 2D map shown in Figure 2 a) of the main manuscript is reflected by the fitted peak positions. Solid line shows an exponential fit yielding a time constant of (200 ± 100) fs.

Supplementary Note 3.3 – Ultrafast response of aluminum ellipse antennas

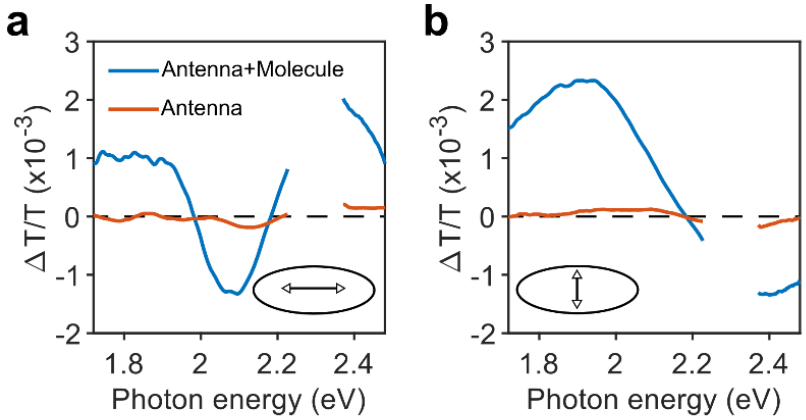

Supplementary Figure 20: *Spectrally resolved $\Delta T/T$ at pump-probe time delay of 150 fs for excitation along the long (a) and short (b) axis of the antenna. Blue curves are recorded after UV switching of SP to MC and orange curves are recorded without UV switching.*

In order to characterize individual elements composing the polaritonic system, we further studied the dynamic response of the aluminum ellipse antennas to the optical pump. Before coating the antenna array with the molecular film, the plasmonic resonances lie outside of the spectral region that is probed in our experiments, due to static change in the environmental refractive index. Hence, to mitigate this issue, we performed pump-probe experiments on the antenna array without UV switching the molecular film to the MC form. Since there is no observable dynamics of the molecules in their SP form (compare Supplementary Figure 18 panel b and c), this allows to retrieve the antennae's response in their realistic environment. Results before (orange) and after UV switching (blue) are shown in Supplementary Figure 20 for long and short axis excitation. A small differential signal can be observed for the antenna response (orange), most likely due to local heating of the metal leading to a spectral shift of the plasmonic resonances. However, this contribution of the antenna to the transient signal is at least one order of magnitude reduced compared to the response of the hybrid system, confirming that the effect observed in our experiments really stems from the interaction of the plasmonic and molecular systems.

Supplementary Note 3.4 – Fitting procedure of pump-probe time traces

To obtain fitted curves presented in Figure 5 of the main manuscript, single-,

$$M(t) = \frac{1}{2}\left[erf\left(\frac{t-t_0}{\sigma}\right)+1\right]\cdot\left[Aexp\left(\frac{-t-t_0}{\tau_1}\right)+C_0\right],$$

and bi-exponential,

$$M(t) = \frac{1}{2}\left[erf\left(\frac{t-t_0}{\sigma}\right)+1\right]\cdot\left[Aexp\left(\frac{-t-t_0}{\tau_1}\right)+Bexp\left(\frac{-t-t_0}{\tau_2}\right)+C_0\right],$$

fitting functions are used. More in detail, for the cut at the MC $\pi-\pi^*$ transition (2.15 eV, orange curve in Figure 5 a), a bi-exponential fit is performed, thus reflecting the fast shift induced by vibrational relaxation of MC molecules (captured by τ_2), followed by the slow transition of excited MC molecules to their ground state (captured by τ_1). For the cut at the Franck-Condon minimum of the MC excited state (1.85 eV, blue curve), a single-exponential fit is performed, reflecting only the transition of excited MC molecules to their ground state. We note that a slightly slower rise of the curve compared to the previous case can be observed (increase in σ) which is due to the vibrational relaxation of the excited MC molecules and subsequent shift of the stimulated emission towards the Franck-Condon minimum. In the following, the obtained time constant τ_1 serves as a reference for the transition time of excited MC molecules to their ground state. In order to separate this relaxation of uncoupled MC molecules from dynamics induced by coupling with the Al antennas, we subtract a single-exponential decay with time constant τ_1 from the time-traces of the coupled system. Raw data (grey) and data with the curve subtracted (blue) are shown in Figure 5 b in the main manuscript. Indeed, the subtraction leaves only a single-exponential decay that follows from interaction with the plasmons and can be fitted using a single-exponential function, now reflecting the time constant of the plasmonic-induced decay. The same subtraction is performed in Figure 5 c in the main manuscript, again leaving only the component induced by coupling with the plasmons. Raw data of Figure 5 c is shown in Supplementary Figure 21.

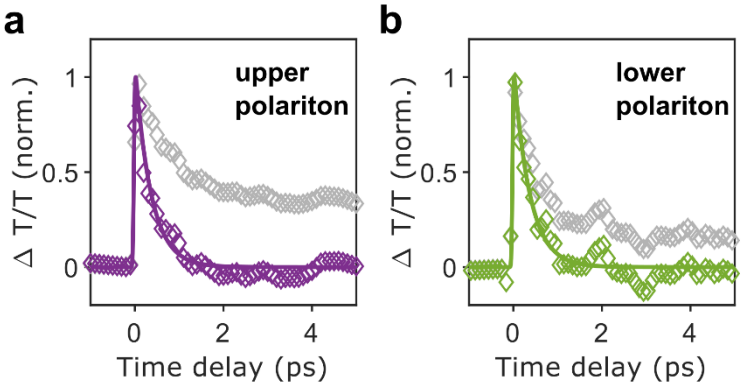

Supplementary Figure 21: *$\Delta T/T$ at spectral position of upper (a) and lower (b) polariton states, respectively. Grey is raw data and colored is the data after subtraction of the slow decay component, as shown in main manuscript Figure 5c.*

Supplementary References

[1] Fredriksson, H. et al. Hole–Mask Colloidal Lithography. *Advanced Materials* 19, 4297-4302 (2007).
[2] Remon, P. et al. Molecular Implementation of Sequential and Reversible Logic Through Photochromic Energy Transfer Switching. *Chem. Eur. J.* 17, 6492 – 6500 (2011).
[3] Görner, H. Photochromism of nitrospiropyrans: effects of structure, solvent and temperature. *Physical Chemistry Chemical Physics*, *3*(3), 416-423 (2001).
[4] Gaussian 16, Revision B.01, Frisch, M. J et al. J. Gaussian, Inc., Wallingford CT, 2016.
[5] Tomasi, J., Mennucci, B. & Cammi, R. Quantum Mechanical Continuum Solvation Models. *Chemical Reviews* 105, 2999-3094 (2005).
[6] Geuzaine, C. & Remacle, J. Gmsh: A 3-D finite element mesh generator with built-in pre- and post-processing facilities. *International Journal for Numerical Methods in Engineering* 79, 1309-1331 (2009).
[7] Fregoni, J. et al. Strong Coupling between Localized Surface Plasmons and Molecules by Coupled Cluster Theory. *Nano Letters* 21, 6664-6670 (2021).
[8] Mennucci, B. & Corni, S. Multiscale modelling of photoinduced processes in composite systems. *Nature Reviews Chemistry* 3, 315-330 (2019).
[9] Corni, S., Pipolo, S. & Cammi, R. Equation of Motion for the Solvent Polarization Apparent Charges in the Polarizable Continuum Model: Application to Real-Time TDDFT. *The Journal of Physical Chemistry A* 119, 5405-5416 (2014).
[10] Felicetti, S. et al. Photoprotecting Uracil by Coupling with Lossy Nanocavities. *The Journal of Physical Chemistry Letters* 11, 8810-8818 (2020).
[11] Antoniou, P., Suchanek, F., Varner, J. & Foley, J. Role of Cavity Losses on Nonadiabatic Couplings and Dynamics in Polaritonic Chemistry. *The Journal of Physical Chemistry Letters* 11, 9063-9069 (2020).
[12] Finkelstein-Shapiro, D. et al. Understanding radiative transitions and relaxation pathways in plexcitons. *Chem* 7, 1092-1107 (2021).
[13] Scholes, G. Limits of exciton delocalization in molecular aggregates. *Faraday Discussions.* 221, 265-280 (2019)
[14] S. Mukamel, Principles of nonlinear optical spectroscopy (Oxford University Press, 1995).
[15] Dovzhenko D. S. et al. Light–matter interaction in the strong coupling regime: configurations, conditions, and applications. *Nanoscale,* 10, 3589-3605 (2018).
[16] Gupta, N. S. et al. Complex plasmon-exciton dynamics revealed through quantum dot light emission in a nanocavity. Nature Communications 12, 1310 (2021)
[17] DelPo, C. et al. Polariton Transitions in Femtosecond Transient Absorption Studies of Ultrastrong Light–Molecule Coupling. *The Journal of Physical Chemistry Letters* 11, 2667-2674 (2020).
[18] Hohenester, U. & Trügler, A. MNPBEM – A Matlab toolbox for the simulation of plasmonic nanoparticles. *Computer Physics Communications* 183, 370-381 (2012).
[19] McPeak, K. et al. Plasmonic Films Can Easily Be Better: Rules and Recipes. *ACS Photonics* 2, 326-333 (2015).
[20] Hohenester, U. et al. Interaction of Single Molecules With Metallic Nanoparticles. IEEE J Sel Top Quantum Electron, 14,1430-1440 (2008).
[21] Palfrey, S.L. et al. Coherent interactions in pump–probe absorption measurements: the effect of phase gratings. *J. Opt. Soc. Am. B* 2, 674-679 (1985)
[22] Rafal Klajn. Spiropyran-based dynamic materials. *Chemical Society Reviews*, 43(1):148–184 (2014).

Additional notes after thesis review

In the long axis case, the differential transmission signal ($\frac{\Delta T}{T}$), which is proportional to the simulated quantity $-\Delta\sigma$ that is the minus change in absorption cross-section upon pumping, features a negative peak around 2.1 eV. This spectral feature can be understood in light of the rabi splitting contraction that is experienced by the collective system upon pump excitation. Indeed, the initial pump pulse promotes the formation of a collective plexciton system that is formed by N molecules strongly-coupled to the plasmon mode, whose linear absorption is schematically represented below in Fig. 4a (solid black). After plasmon dephasing and consequent polaritonic collapse, the remaining system wavefunction before probe absorption can be described as the product state of an excited molecular state times N-1 molecules in the ground state. At this stage the probe pulse arrives and promotes another collective polaritonic excitation that results in a contracted rabi splitting as the LP-UP splitting in collective strong-coupling is proportional to the square root of the number of molecules coupled to the mode. As a result of this the corresponding system absorption lineshape features a reduced rabi splitting, as depicted in Fig. 4a (solid red). Since the transient signal is computed as $-\Delta\sigma$, subtraction of the red spectrum from the black one of Fig. 4a results in the positive-negative-positive transient spectral lineshape that is observed (sketch in Fig. 4b).

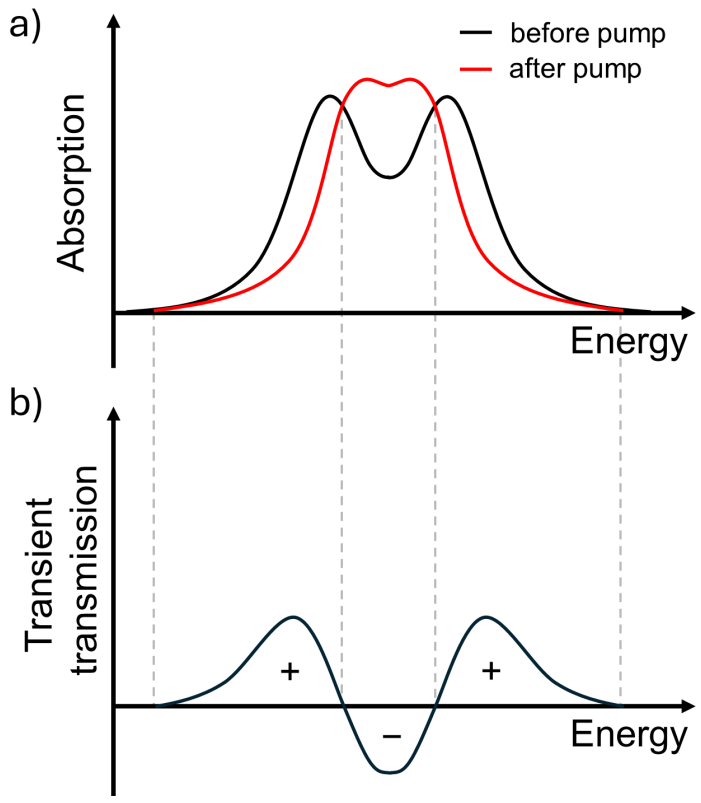

Figure 4: a) Pictorial sketch of the absorption spectrum of the collective polaritonic system before (solid black) and after (solid red) optical pumping. The corresponding differential transmission signal is shown in panel b).

Chapter 5.

Identifying differences between semi-classical and full-quantum descriptions of plexcitons

The principal finding that can be drawn from chapter 4 is that plasmon losses, which are inherently present in plasmonic metals, can drastically affect the plexciton lifetime and related molecular electron dynamics. Therefore, a proper theoretical modelling of plexcitonic phenomena cannot disregard an explicit inclusion of plasmonic relaxation dynamics. This concept directly brings us to this chapter, which is reported as a manuscript draft currently in preparation and also constitutes the final chapter of this PhD thesis.

In this chapter, a real-time molecular electron dynamics propagation of molecules interacting with classical or quantized plasmonic nanostructures is reported. Plasmon dissipative losses are explicitly taken into account by resorting to a Stochastic Schrödinger Equation (SSE) formalism, which is a convenient way to include environment-induced effects within an open quantum system extension of the standard Schrödinger equation. By building on previous PCM-NP works[1, 2], a full-quantum model, which involves both quantum chemistry molecular description and quantized plasmon modes, is presented and directly compared to the semi-classical analogue, the latter featuring a classical modelling of the plasmonic system. Given that both models share the same theoretical ingredients, it is possible to theoretically and numerically compare them on an equal footing, thus pinpointing fundamental differences between the two in describing interactions between molecules and plasmonic structures under different interaction regimes and driving conditions.

By inspecting the molecular excited state population upon excitation it is observed that under high-intensity driving fields, the semi-classical model fails to properly describe the NP-induced molecular excited state decay, thereby agreeing with previous studies[3, 4]. Furthermore, it is surprisingly shown that even under the weak-coupling and low-intensity driving limits, where the two descriptions are expected to yield identical results, a small-yet-observable discrepancy is observed when plasmonic and molecular transitions are not resonant. Notably, this small difference is traced back to the different way resonant and anti-resonant plasmonic response properties enter into the two models.

In this work, the code implementation of the full-quantum model and all simulations shown in the manuscript have been performed by me. The derivation of the analytical models reported in the Supporting Information that have been used to rationalize the results shown in the main

text has been done by me under the supervision of Prof. Corni. The current manuscript version has been drafted by me.

References

(1) Coccia, E.; Corni, S. *The Journal of Chemical Physics* **2019**, *151*, 044703.

(2) Fregoni, J.; Haugland, T. S.; Pipolo, S.; Giovannini, T.; Koch, H.; Corni, S. *Nano Letters* **2021**, *21*, 6664–6670.

(3) Waks, E.; Vuckovic, J. *Physical review letters* **2006**, *96*, 153601.

(4) Waks, E.; Sridharan, D. *Physical Review A* **2010**, *82*, 043845.

Identifying differences between semi-classical and full-quantum descriptions of plexcitons

Marco Romanelli[†] and Stefano Corni[*,†,‡,¶]

†*Department of Chemical Sciences, University of Padova, via Marzolo 1, 35131 Padova, Italy*

‡*CNR Institute of Nanoscience, via Campi 213/A, 41125 Modena, Italy*

¶*Padua Quantum Technologies Research Center, University of Padova, 35131 Padova, Italy*

E-mail: stefano.corni@unipd.it

Abstract

Strong light-matter coupling between molecules and plasmonic nanoparticles give rise to new hybrid eigenstates of the coupled system, commonly referred to as polaritons, or more precisely, plexcitons. Over the last decade it has been amply shown that molecular electron dynamics and photophysics can be drastically affected by such interactions, thus paving the way for light-induced control of molecular excited-state properties and reactivity. Here, by combining *ab initio* molecular description and classical or quantum modelling of arbitrarily-shaped plasmonic nanostructures within Stochastic Schrödinger Equation, we present two approaches, one semi-classical and one full-quantum, to follow in real-time the electronic dynamics of plexcitons while realistically taking plasmonic dissipative losses into account. The full-quantum theory is compared with the semi-classical analogue under different interaction regimes, showing (numerically and theoretically) that even in the weak-field and weak-coupling limit a small-yet-observable difference arises.

1 Introduction

Plexcitonic systems, namely nanohybrid architectures composed of plasmonic nanostructures interacting with molecular species, have been drawing ever-increasing attention over the past few years since they proved to be a non-invasive way of changing molecular properties as a result of light-matter coupling.[1–6] Indeed, many recent works have illustrated the possibility of using plasmonic platforms to affect not only absorption and emission properties of photoactive molecules,[7–15] but also energy transfer rates,[16–20] photorelaxation channels[21–26] and photochemical reactions,[5,27–33] just to mention a few.

The degree of coupling between molecular emitters and plasmonic resonators in such cases can span different regimes, being defined "weak" when it is small with respect to the dissipative losses of the coupled system, or "strong" in the opposite scenario.[34,35] Usually, in the former case perturbative semiclassical approaches are believed to suffice to capture the modified molecular response due to the weak plasmon-molecule interaction and they have been widely used to account for enhancement (Purcell effect) or suppression of radiative molecular emission, quenching of molecular excited states lifetimes and also molecular excitation energies shifts because of the nearby plasmonic nanoparticles (NPs)[36–44] (known as "medium-induced Lamb shift").

On the other hand, when the light-matter coupling is large enough to exceed the dissipative losses of the coupled system, and the molecular and plasmonic excitations are resonant, new hybrid molecular-plasmonic eigenstates, commonly named plexcitons, are actually formed, resulting in a coherent energy exchange between the molecular excited state and the plasmonic system, thus defining the onset of the "strong coupling" regime.[28,34,45,46]

Since the seminal work of Hutchison et al.,[47] controlling photochemical reaction rates and photocatalytic processes thanks to confined light modes has given rise to a vibrant and active area of research. If, on the one hand, plasmonic nanocavities enable the confinement of light in sub-nanometric volumes, thus boosting the light-matter interaction to such an extent that even single-molecule strong coupling becomes feasible,[48] on the other they are

typically associated to large (fast) dissipative losses because of the well-known ultrafast plasmon dephasing process, happening on a femtosecond (fs) time scale, which quickly leads to a non-radiative dissipation of the initial plasmonic excitation.[49–51] Since these processes are commonly faster than usual electronic processes taking place in photo-excited molecules, tailoring them for chemical applications calls for theoretical models able to describe those dynamical interactions, whether they are "weak" or "strong", while realistically taking account of such dissipative losses, as they can drastically affect the resulting molecular electron dynamics and thus being impactful for possible applications.

In the following, building on the previously-developed modelling strategy aimed at describing in real-time the electron dynamics of molecules close to classically-described plasmonic nanostructures,[52–54] hereafter labelled as semi-classical (SC) approach, we push that theory one step further to plexcitonic wavefunctions, based on the quantized description of the plasmonic response.[55] We refer to such picture as full-quantum model (FQ), but we remark that it does not entail a full quantum field theory description of the ongoing interactions among particles and fields. Indeed, the adopted plasmonic quantization scheme[55] is derived to obtain the very same classical macroscopic linear response polarization of the metal structure (in that sense full-quantum refers to full-quantization of classical field), in agreement with previous macroscopic quantum electrodynamics (macroscopic QED) approaches.[56,57]

Limiting ourselves to time-dependent modelling, different approaches based on semiclassical Maxwell-Bloch equations, coupled harmonic oscillator models, density-matrix propagation through master equations and Heisenberg-Langevin equations have been used before,[58–73] but in the majority of those cases the molecules are simply described as two-state quantum emitters and the metallic NPs that are considered are typically characterized by simple shapes for which analytical solutions of the scattering Green's function are easily available. In this context, full-quantum models rooted in macroscopic QED have also been used to investigate the population dynamics of multiple two-state emitters coupled to complex bath spectral densities representing realistic metal environments.[57,74–76] Other macroscopic

QED-based approaches investigated molecular emission features in the presence of planar metallic mirrors,[77–80] but in all these cases a simplified description of the emitters is considered. On the other hand, real-time *ab initio* investigations based on using Real-Time Time-Dependent Density Functional Theory (RT-TDDFT) for the full system have recently started to emerge, but due to the high computational cost of such simulations only small metal clusters consisting of at most tens of atoms have been described, thus limiting a direct comparison with realistic experimental setups.[81–92]In particular, none of these models couple an atomistic quantum description of real molecular structures with NPs of arbitrary shape and dimension, thus tackling systems of real complexity and practical usage. This is the core feature of the methods that we hereby present, which combine state of the art quantum chemistry description of molecules with classical (SC) or quantum modelling (FQ) of arbitrarily-shaped plasmonic NPs, laying the groundwork for a direct comparison of the two regimes on an equal footing.

Dissipative losses of the system are treated using a Stochastic Schrödinger Equation (SSE) formalism, which is an alternative approach to density-matrix based propagation that focuses on following directly in time the system wave-function evolution under the influence of the surroundings.[93,94]

Previous works[59,95,96] have shown that the predicted total absorbed power by dipolar emitters coupled to spherical plasmonic NPs differ between semi-classical and full-quantum descriptions under high intensity driving fields. More precisely, results derived from semi-classical Maxwell-Bloch equations leads to an overestimation of the system absorbed power compared to the exact full-quantum results obtained by full master equation propagation. The origin of this divergence has been related to non-linear effects that arise upon exciting the system with high-intensity fields because of emitters saturation and optical bistability.[97–100] On the other hand, when the weak-coupling and weak-field limits[59,101,102] do apply, the two approaches are expected to give the same results, even in the presence of environment-induced dissipation.[59,101]

In the following, by providing a direct comparison between the two descriptions in a system composed of a plasmonic NP and a molecule, we do numerically confirm the expected divergence under strong-field excitation, but we also observe a slight difference in the molecular excited state population upon external driving when the molecular and plasmon systems are not resonant, even under linear excitation regimes. We find out that the origin of this discrepancy is intimately connected to the anti-resonant term of the NP linear response polarizability, which enters in different ways in the SC and FQ models.

It is worth pointing out that these two approaches are theoretically and numerically comparable since they share the same theoretical ingredients (the numerical response to an external oscillating and spatially varying electric field is identical for both by construction), thus allowing to pinpoint fundamental differences in the way plasmon-molecules interactions are described in the two cases.

2 Results and discussion

In the SC picture, the molecule is described at quantum mechanical level, but the plasmonic NP is treated as a classical polarizable continuum object with the PCM-NP model, which has been previously developed in our group.[39,54] It essentially relies on solving the electromagnetic problem of coupling a quantum chemistry molecular description with the nearby homogeneous plasmonic system by numerically solving the corresponding Poisson's equation through a Boundary-Element-Method (BEM)[103] approach. The NP response to external perturbations (e.g. molecular electron densities or external fields) is expressed in terms of surface charges liying on the NP discretized surface whose discretization is needed to numerically solve the BEM problem (more details can be found in SI 1.1). In this picture, the system Hamiltonian $\hat{H}_S(t)$, here renamed $\hat{H}_{SC}(t)$ for the actual SC case, reads:

$$\hat{H}_{SC}(t) = \hat{H}_{mol} - \vec{\hat{\mu}} \cdot \vec{E}_{ext}(t) + (\mathbf{q}_{ref}(t) + \mathbf{q}_{pol}(t)) \cdot \hat{\mathbf{V}} \tag{1}$$

where $\hat{H}_{mol}$ is the time-independent molecular Hamiltonian, $\vec{E}_{ext}(t)$ is the time-dependent external electric field that is used to drive the system, $\vec{\hat{\mu}}$ is the molecular dipole operator, $\mathbf{q}_{ref}(t)$ and $\mathbf{q}_{pol}(t)$ are vectors collecting the NP response charges on the NP's discretized surface induced by direct polarization of the incoming exciting field ($\mathbf{q}_{ref}(t)$) and by the time-dependent nearby molecular electron density ($\mathbf{q}_{pol}(t)$), and $\hat{\mathbf{V}}$ is the molecular electrostatic potential operator evaluated at the nanoparticle surface where response charges lie on.[39,54] We point out that the $\mathbf{q}_{pol}(t)$ term leads to a non-linear self-interaction effect because those response charges are induced on the NP by the presence of the nearby molecular density and can in turn generate an electric field that can act back on the molecule itself. In the SC limit, under the quasi-static approximation, the imaginary component of this self-interaction contribution leads to an additional non-radiative decay rate for molecular excited states, representing energy transfer to the NP, where the excitation is then quickly dissipated.[38,40] This decay process is typically faster than any other intrinsic molecular decay rate[15,104] when molecules are very close to metallic NPs ($< 1\,\text{nm}$) and so its effect cannot be neglected. Herein, since the main goal of the present work is to compare the SC and FQ models on a perfectly consistent ground, we solely focus on this NP-induced decay channel. Therefore, in the SC picture the wavefunction time-propagation is directly performed with the Hamiltonian $\hat{H}_{SC}(t)$ of eq.1 and no additional decay operators have to be included (see SI 1.1).

On the other hand, in the FQ picture the plasmonic NP is also quantized, so the system Hamiltonian becomes

$$\hat{H}_{FQ}(t) = \hat{H}_{0,FQ} - \vec{\hat{\mu}} \cdot \vec{E}_{ext}(t) \tag{2}$$

where $\hat{H}_{0,FQ}$ is the full plasmon-molecule Hamiltonian,[55]

$$\hat{H}_{0,FQ} = \hat{H}_{mol} + \sum_{p} \omega_p \hat{b}_p^\dagger \hat{b}_p + \sum_{pj} q_{pj} \hat{V}_j (b_p^\dagger + b_p) \tag{3}$$

where ω_p is the frequency of the p^{th} quantized plasmon mode of the NP and $\hat{b}_p^\dagger$, $\hat{b}_p$ are the corresponding plasmonic creation and annihilation operators, respectively. In eq.3, the j in-

dex labels the j^{th} surface element of the NP (called "tessera") after numerical discretization that is needed to solve the BEM equations, leading then to the corresponding quantized surface charge q_{pj} for a given p^{th} plasmon mode. $\hat{V}_j$ is instead the molecular electrostatic potential operator evaluated at the j^{th} tessera.

The full derivation of the Q-PCM-NP quantization scheme has been detailed elsewhere.[55] Here it is important to remark that the quantum model is derived to provide the very same linear response polarization in the nanoparticle as the classical one. Further details on the FQ model can be found in SI 1.2.

The wavefunction propagation is then performed in a SSE framework to consistently include plasmon-induced losses as in the SC picture. This is achieved by using the following Hamiltonian,

$$\hat{H}_{SSE,FQ}(t) = \hat{H}_{FQ}(t) + \sum_p l_{p,FQ}(t)\hat{S}_{p,FQ} - \frac{i}{2}\sum_p \hat{S}^{\dagger}_{p,FQ}\hat{S}_{p,FQ} \tag{4}$$

with

$$\hat{S}_{p,FQ} = \sqrt{\Gamma_p}\mathbb{1}_{\mathbb{mol}} \otimes (|0\rangle \langle 1_p|) \tag{5}$$

where $\mathbb{1}_{\mathbb{mol}}$ is the identity operator on the molecular states, and Γ_p is the decay rate of the p^{th} quantized mode. The second term of the r.h.s of eq.4 is a fluctuation term modelled by a Wiener process $l_{p,FQ}(t)$, i.e. white noise associated with the Markov approximation, whereas the last term of eq.4 represents environment-induced dissipation.[52,94] Propagation with the Hamiltonian of eq.4 is performed by means of a quantum jump algorithm[94] (further details in SI 1.3).

The SC and FQ models have been compared on a system composed of a plasmonic ellipsoidal NP and N-methyl-6-quinolone molecule (for simplicity we will refer to the latter simply as quinolone), as shown in Fig.1. The choice of such molecular species has been made due to its interesting and previously-investigated excited state properties,[105] but for the purpose of the present work other molecules may have been chosen. The quinolone molecule

is described at the level of Configuration Interaction Singles (CIS) and only its lowest excited state ($|e\rangle$) is considered in the following for simplicity. The coupled system is driven by a pulse of gaussian shape resonant with the lowest NP plasmon mode frequency $\omega_p = 2.95\,\text{eV}$ (further computational details can be found in SI 2).

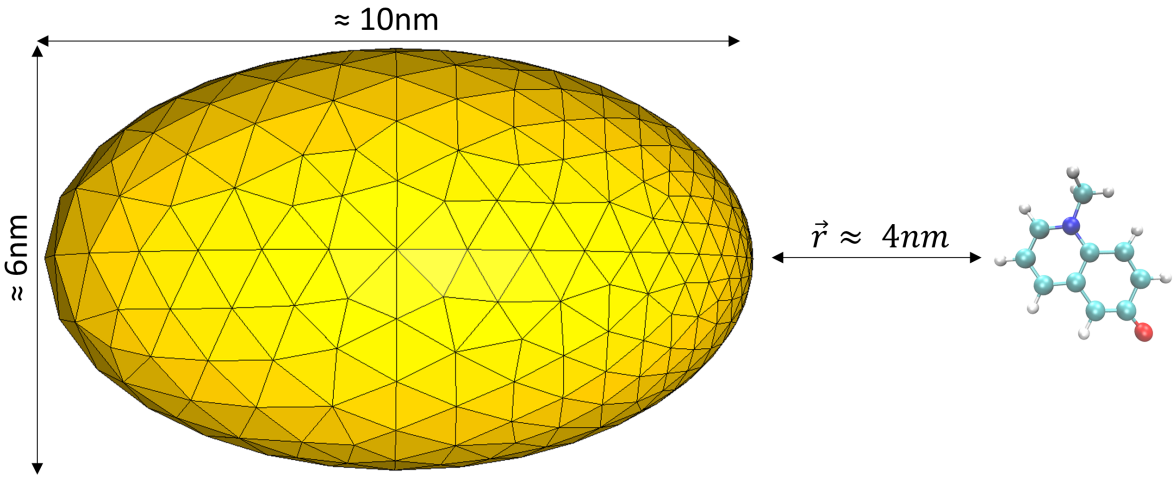

Figure 1: System under investigation composed of a plasmonic gold NP of ellipsoidal shape and N-methyl-6-quinolone molecule. The molecule -NP dimensions are not to scale.

Under high intensity driving fields the two approaches are expected to diverge.[98–101] An intuitive qualitative explanation of the origin of this divergence can be grasped by considering an oscillating two-state dipolar emitter close to a classically described plasmonic body.[106] In that case, the time-dependent emitter's wavefunction can be expressed as $|\psi(t)\rangle = C_g(t)\,|g\rangle + C_e(t)\,|e\rangle\,e^{-i\omega_{eg}t}$ and so the corresponding oscillating dipole moment becomes $\langle\psi(t)|\,\hat{\mu}\,|\psi(t)\rangle = \langle g|\,\hat{\mu}\,|g\rangle\,|C_g|^2 + \langle g|\,\hat{\mu}\,|e\rangle\,2\Re(C_g^* C_e)cos(\omega_{eg}t)$ up to first-order. The oscillating contribution polarizes the nearby plasmonic body whose reaction field can act back on the dipole itself, thus leading to a self-interaction contribution mediated by the metal that is $\propto |C_g|^2|C_e|^2 f = (1-|C_e|^2)|C_e|^2 f$ with f being a complex function that accounts for the plasmon response. In the quasistatic limit the imaginary component of this self-interaction accounts for the emitter decay to the plasmonic system[106] and only when $|C_e|^2 << 1$ the expression just derived reduces to the excited state population times the decay rate. In the opposite limit

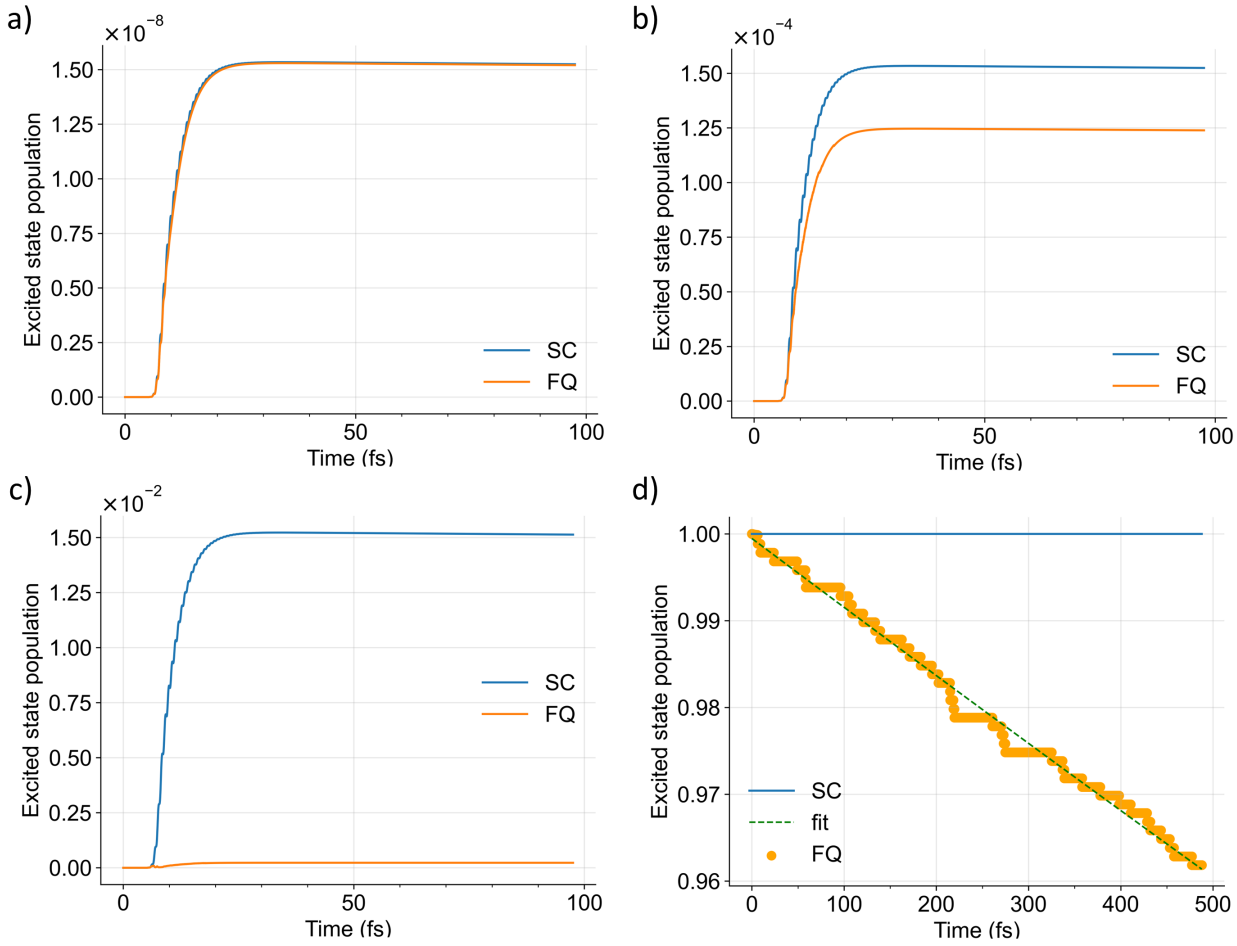

Figure 2: Molecular excited state population over time obtained via SC (blue) and FQ (orange) models under resonance condition ($\delta = \omega_e - \omega_p = 0$) for different driving field intensities a)-c). The same setup of Fig. 1 is excited with a Gaussian pulse (SI 2) resonant with the lowest NP plasmon mode $\omega_p = 2.95\,\text{eV}$ featuring an intensity of a) $3.5 \times 10^4\,\text{W/cm}^2$, b) $3.5 \times 10^8\,\text{W/cm}^2$ and c) $3.5 \times 10^{10}\,\text{W/cm}^2$. The extreme limit where the entire molecular population would be in the excited state is reported in d), where the system is initiated in the molecular excited state already at time zero. In this case time-propagation begins from this extreme condition and no driving field is applied. The green dashed line is the result of fitting the corresponding data points with an exponential decay function $f(t) = ke^{-t/\tau}$.

where the excited state population approaches 1 because of sufficiently-intense driving fields, the decay probability becomes zero due to the $(1 - |C_e|^2)$ factor. In fact, in that limit and from a semi-classical perspective, the emitter excited state would be fully populated, and since it is a stationary solution it has no way to exchange energy with the plasmonic system as its electron density do not oscillate over time and so cannot perturb the NP. Conversely,

in the full-quantum description the purely molecular state is no longer an eigenstate of the coupled Hamiltonian and so its time-varying electron density can oscillate, leading to decay through the NP. This qualitative explanation is numerically verified in Fig. 2, where the molecular excited state population upon excitation (SI 1.2, eq.19) under different driving conditions is shown. As the driving field intensity increases (panels a-c of Fig. 2), the FQ and SC approaches start to show discrepancies in the molecular excited state population over time, and that difference is even more pronounced in the extreme limit of having the entire molecular population on the molecular excited state (panel d). In that case the SC model does not predict any form of decay, since a stationary solution of the SC system is fully populated and hence its electron density does not change over time, which prevents it from interacting with the NP and so leading to plasmon-induced decay, as discussed above. On the other hand, the FQ picture correctly captures the NP-induced molecular decay. Indeed, by fitting the FQ results with an exponential decay function a lifetime of $\approx 10\,\mathrm{ps}$ is observed, thereby confirming the presence of an excited state decay process. In this non linear regime many quantum jumps take place (SI 1.3), resulting in the jagged profile of Fig. 2d, which is obtained averaging over 1000 trajectories. A more formal description of this phenomenon based on fluctuation-dissipation theorem can be found in refs.[107,108]

On the other hand, in the weak field and weak coupling limit one could expect that both models provide the same results.[59,101] Surprisingly, when there is a frequency detuning between the molecular and plasmon frequencies ($\delta = \omega_e - \omega_p \neq 0$), we observe a small-yet-appreciable difference in the results (Fig. 3a). Interestingly, when the system is taken into resonance the discrepancy disappears(Fig. 3b).

In order to shed light on this observed mismatch, a slightly-simplified system is considered so that an analytical model can be made to infer the origin of that discrepancy. Basically, the same setup of Fig.1 is investigated but the n. of plasmonic modes of $\hat{H}_{0,FQ}$ is restricted to one, namely only the lowest dipolar mode is considered. This approximation, which is reasonable since the molecule-NP coupling at $\approx 4\,\mathrm{nm}$ distance is mostly dominated by dipolar

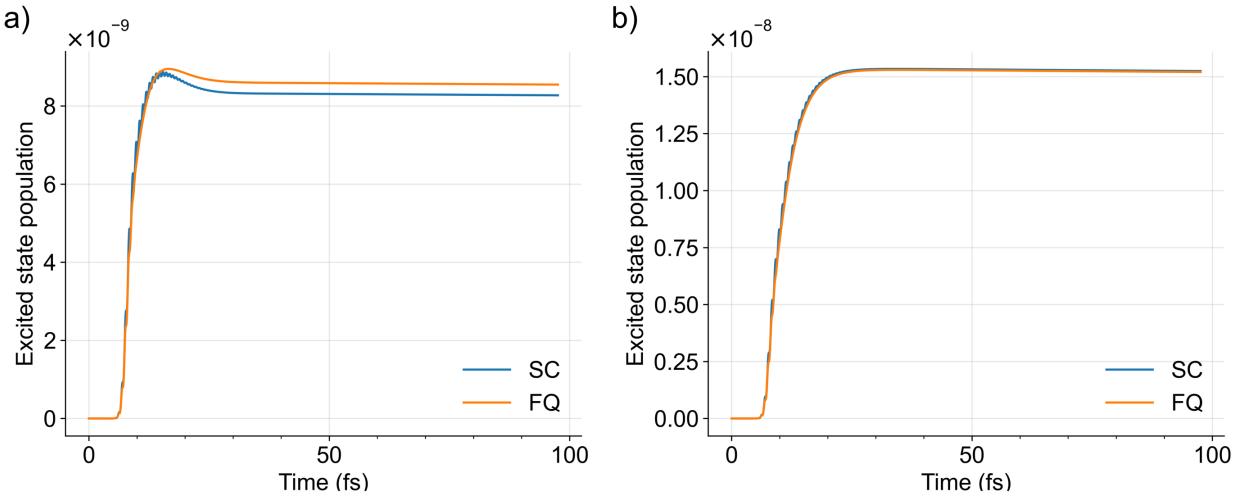

Figure 3: Molecular excited state population over time obtained via SC (blue) and FQ (orange) approaches under different frequency detuning cases, (a) $\delta = \omega_e - \omega_p \approx 100\,\text{meV}$ and (b) $\delta = 0$. The system (Fig. 1) is excited with a Gaussian pulse resonant with the lowest NP plasmon mode $\omega_p = 2.95\,\text{eV}$ and whose intensity is $3.5 \times 10^4\,\text{W/cm}^2$ (see SI 2).

interactions, is also coherently applied to the corresponding SC simulations by setting to zero the contribution to the overall classical response charges (eq. 1) originating from non-dipolar modes embedded in the NP response function.[54,55]

Clearly, the results displayed in Fig. 4 show that when $\delta \neq 0$ there is a small-yet-observable mismatch between the two approaches which vanish under resonance condition, $\delta = 0$.

This unforeseen result can be rationalized by resorting to an analytical model for the the molecular excited state population $\left|C_{e,SC/FQ}(t)\right|^2$ in the single mode case under the weak-coupling and weak-field approximations. Indeed, using first-order perturbation theory it can be shown that (derivation is detailed in SI 3)

$$
\begin{aligned}
|C_{e,SC}(t)|^2 &\approx \frac{E_0^2|\vec{\mu}_e|^2}{4}\left(1 + \frac{4|\vec{\mu}_p|^4}{\Gamma_p^2|\vec{r}|^6} - \frac{4|\vec{\mu}_p|^4}{(4\omega_p^2+\Gamma_p^2)|\vec{r}|^6} + \frac{8|\vec{\mu}_p|^2\omega_p}{(4\omega_p^2+\Gamma_p^2)|\vec{r}|^3}\right)\frac{1}{\delta^2} \\
|C_{e,FQ}(t)|^2 &\approx \frac{E_0^2|\vec{\mu}_e|^2}{4}\left(1 + \frac{4|\vec{\mu}_p|^4}{\Gamma_p^2|\vec{r}|^6}\right)\frac{1}{\delta^2}
\end{aligned}
\tag{6}
$$

where $|\vec{\mu}_e|$ and $|\vec{\mu}_p|$ are the molecular and plasmonic transition dipoles, respectively. The latter can be easily computed as $\sum_j q_{pj}\vec{r}_j$ with $\vec{r}_j$ being the position vector pointing to the

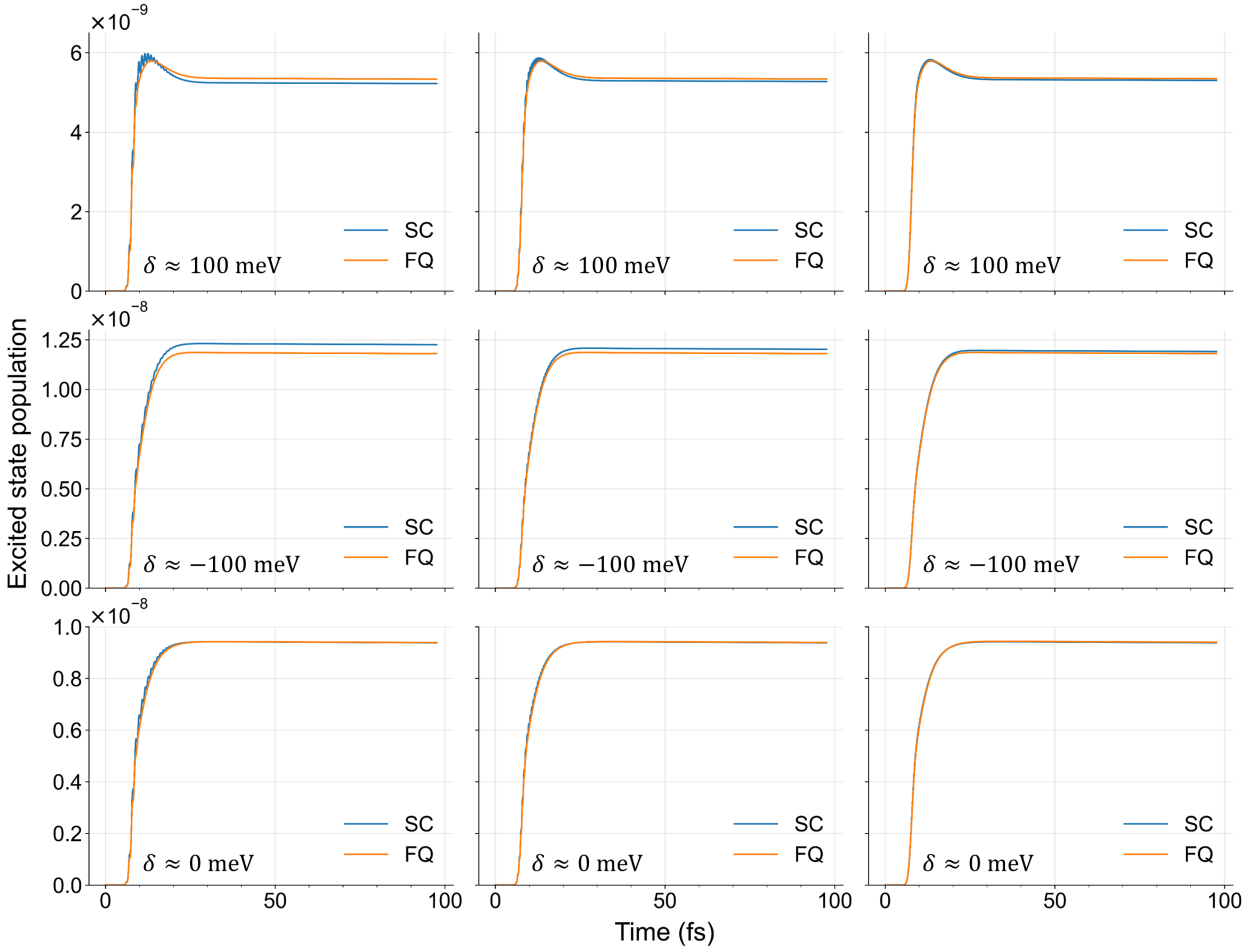

Figure 4: Molecular excited state population over time obtained via SC (blue) and FQ (orange) approaches including only the lowest plasmon dipolar mode in the models. Results under different detuning conditions are shown. Within each rank, from left to right the absolute value of the plasmon mode frequency ω_p is doubled each time and so the molecular frequency ω_e is coherently modified to preserve the same δ value among calculations displayed in the same row. Each simulation is performed by driving the system with a Gaussian pulse of same shape but resonant with the corresponding ω_p value and whose intensity is $3.5 \times 10^4\,\mathrm{W/cm^2}$.

j^{th} quantized surface charge.

Notably, the origin of the two additional terms appearing solely in the SC expression can be traced back to the anti-resonant term of the NP linear response polarizability (SI 3.1) which defines the classical response charges of eq.1 and enters in different ways in the FQ and SC models. Indeed, if simulations are repeated scaling the Drude-Lorentz dielectric function parameters (SI 1.1, eq.2) such that the absolute value of ω_p increases while keeping the values

of plasmonic charges q_{pj} and detuning δ fixed (SI 4), the observed discrepancy progressively vanish, also in the case of $\delta \neq 0$. This can be understood in light of eq. 6 where the additional terms only present in the SC expression roughly depend on $\approx (\omega_p)^{-2}$ or $\approx (\omega_p)^{-1}$, and so their contribution becomes progressively more and more negligible as the absolute value of ω_p increases, while keeping all other quantities appearing in that expression constant. This is indeed what is reported in Fig.4 for each value of δ moving from left to right. Remarkably, in agreement with eq. 6 FQ curves reported in Fig. 4 do not exhibit any appreciable change as ω_p increases, whereas SC curves do vary, approaching the FQ results for large ω_p values. The same behaviour is still observed when different absolute values of δ are considered.
On the other hand, when $\delta = 0$ the two curves are already almost-perfectly superimposed and nothing more can be inferred from eq. 6 as both expressions diverge for $\delta \to 0$. Nevertheless, it can be qualitatively shown (SI 3.3) that when the molecule and plasmon excitations are resonant, the dominating contribution to the molecular excited state population is equally described numerically by both models when the driving field is resonant with the plasmon mode frequency, as in the investigated case, thus justifying, albeit not quantitatively, why under resonance condition both models yield the same result.

3 Conclusions

In this work, by combining Stochastic Schrödinger Equation, *ab initio* description of target molecules and BEM-based modelling of arbitrarily-shaped plasmonic nanoparticles within the PCM-NP framework,[38,39,52,54,55,94] we directly compare full-quantum and semi-classical modelling of plexcitons, while realistically accounting for ultrafast plasmonic dissipative processes. The presented full-quantum theory is compared with the semi-classical analogue under different excitation regimes. Upon high-intensity driving, sizeable differences between the two approaches are observed, thereby confirming previous findings on similar systems.[98–101] Furthermore, it is surprisingly disclosed that even within the weak-field and weak-coupling

limits an unexpected small-yet-appreciable difference arises in the molecular excited state population upon low-intensity driving. By resorting to a simplified analytical model the origin of such discrepancy has been traced back to the anti-resonant term of the classical NP polarizability, which enters into the full-quantum and semi-classical models in different ways and turned out to be responsible for the observed discrepancy. The illustrated theory paves the way for real-time investigation of plexcitons beyond the linear regime while retaining *ab initio* description of molecules and accurate modelling of arbitrarily-shaped plasmonic nanostructures.

As the field of plexcitonic chemistry is drawing ever-increasing attention, we believe the theory presented here will be instrumental in narrowing the gap towards accurate control of molecular excited-state processes by means of plasmon-molecule coupling.

Acknowledgement

The authors acknowledge Giulia Dall'Osto for insightful preliminary discussions and numerical tests. M.R. acknowledges MIUR "Dipartimenti di Eccellenza" under the project Nanochemistry for energy and Health (NExuS) for funding the Ph.D. grant. Computational work has been carried out on the C3P (Computational Chemistry Community in Padua) HPC facility of the Department of Chemical Sciences of the University of Padua.

Supporting Information Available

Additional material can be found in the supporting information:

Details about FQ and SC theoretical models; Computational details; Analytical models to derive eq. 6; Scaling plasmonic quantities to perform simulations reported in Fig. 4.

References

(1) Zhao, Q.; Zhou, W.-J.; Deng, Y.-H.; Zheng, Y.-Q.; Shi, Z.-H.; Ang, L. K.; Zhou, Z.-K.; Wu, L. Plexcitonic strong coupling: unique features, applications, and challenges. *Journal of Physics D: Applied Physics* **2022**, *55*, 203002.

(2) Ma, J.; Cheng, Y.; Sun, M. Plexcitons, electric field gradient and electron–phonon coupling in tip-enhanced Raman spectroscopy (TERS). *Nanoscale* **2021**, *13*, 10712–10725.

(3) Manuel, A. P.; Kirkey, A.; Mahdi, N.; Shankar, K. Plexcitonics–fundamental principles and optoelectronic applications. *Journal of Materials Chemistry C* **2019**, *7*, 1821–1853.

(4) Thomas, R.; Thomas, A.; Pullanchery, S.; Joseph, L.; Somasundaran, S. M.; Swathi, R. S.; Gray, S. K.; Thomas, K. G. Plexcitons: the role of oscillator strengths and spectral widths in determining strong coupling. *ACS nano* **2018**, *12*, 402–415.

(5) Fregoni, J.; Garcia-Vidal, F. J.; Feist, J. Theoretical challenges in polaritonic chemistry. *ACS photonics* **2022**, *9*, 1096–1107.

(6) Feist, J.; Galego, J.; Garcia-Vidal, F. J. Polaritonic chemistry with organic molecules. *ACS Photonics* **2018**, *5*, 205–216.

(7) Lee, J.; Crampton, K. T.; Tallarida, N.; Apkarian, V. Visualizing vibrational normal modes of a single molecule with atomically confined light. *Nature* **2019**, *568*, 78–82.

(8) Benz, F.; Schmidt, M. K.; Dreismann, A.; Chikkaraddy, R.; Zhang, Y.; Demetriadou, A.; Carnegie, C.; Ohadi, H.; De Nijs, B.; Esteban, R., et al. Single-molecule optomechanics in "picocavities". *Science* **2016**, *354*, 726–729.

(9) Imada, H.; Miwa, K.; Imai-Imada, M.; Kawahara, S.; Kimura, K.; Kim, Y. Single-

molecule investigation of energy dynamics in a coupled plasmon-exciton system. *Physical review letters* **2017**, *119*, 013901.

(10) Yang, B.; Chen, G.; Ghafoor, A.; Zhang, Y.; Zhang, Y.; Zhang, Y.; Luo, Y.; Yang, J.; Sandoghdar, V.; Aizpurua, J., et al. Sub-nanometre resolution in single-molecule photoluminescence imaging. *Nature Photonics* **2020**, *14*, 693–699.

(11) Lakowicz, J. R.; Geddes, C. D.; Gryczynski, I.; Malicka, J.; Gryczynski, Z.; Aslan, K.; Lukomska, J.; Matveeva, E.; Zhang, J.; Badugu, R., et al. Advances in surface-enhanced fluorescence. *Journal of fluorescence* **2004**, *14*, 425–441.

(12) Lakowicz, J. R. Radiative decay engineering 5: metal-enhanced fluorescence and plasmon emission. *Analytical biochemistry* **2005**, *337*, 171–194.

(13) Anger, P.; Bharadwaj, P.; Novotny, L. Enhancement and quenching of single-molecule fluorescence. *Physical review letters* **2006**, *96*, 113002.

(14) Della Sala, F.; D'Agostino, S. *Handbook of molecular plasmonics*; CRC Press, 2013.

(15) Romanelli, M.; Dall'Osto, G.; Corni, S. Role of metal-nanostructure features on tip-enhanced photoluminescence of single molecules. *The Journal of Chemical Physics* **2021**, *155*, 214304.

(16) Kong, F.-F.; Tian, X.-J.; Zhang, Y.; Zhang, Y.; Chen, G.; Yu, Y.-J.; Jing, S.-H.; Gao, H.-Y.; Luo, Y.; Yang, J.-L., et al. Wavelike electronic energy transfer in donor–acceptor molecular systems through quantum coherence. *Nature Nanotechnology* **2022**, 1–8.

(17) Cao, S.; Rosławska, A.; Doppagne, B.; Romeo, M.; Féron, M.; Chérioux, F.; Bulou, H.; Scheurer, F.; Schull, G. Energy funnelling within multichromophore architectures monitored with subnanometre resolution. *Nature Chemistry* **2021**, *13*, 766–770.

(18) Georgiou, K.; Michetti, P.; Gai, L.; Cavazzini, M.; Shen, Z.; Lidzey, D. G. Control over energy transfer between fluorescent BODIPY dyes in a strongly coupled microcavity. *ACS Photonics* **2018**, *5*, 258–266.

(19) Du, M.; Martínez-Martínez, L. A.; Ribeiro, R. F.; Hu, Z.; Menon, V. M.; Yuen-Zhou, J. Theory for polariton-assisted remote energy transfer. *Chemical science* **2018**, *9*, 6659–6669.

(20) Coles, D. M.; Somaschi, N.; Michetti, P.; Clark, C.; Lagoudakis, P. G.; Savvidis, P. G.; Lidzey, D. G. Polariton-mediated energy transfer between organic dyes in a strongly coupled optical microcavity. *Nature materials* **2014**, *13*, 712–719.

(21) Antoniou, P.; Suchanek, F.; Varner, J. F.; Foley IV, J. J. Role of cavity losses on nonadiabatic couplings and dynamics in polaritonic chemistry. *The Journal of Physical Chemistry Letters* **2020**, *11*, 9063–9069.

(22) Munkhbat, B.; Wersäll, M.; Baranov, D. G.; Antosiewicz, T. J.; Shegai, T. Suppression of photo-oxidation of organic chromophores by strong coupling to plasmonic nanoantennas. *Science advances* **2018**, *4*, eaas9552.

(23) Felicetti, S.; Fregoni, J.; Schnappinger, T.; Reiter, S.; de Vivie-Riedle, R.; Feist, J. Photoprotecting uracil by coupling with lossy nanocavities. *The Journal of Physical Chemistry Letters* **2020**, *11*, 8810–8818.

(24) Gu, B.; Mukamel, S. Manipulating nonadiabatic conical intersection dynamics by optical cavities. *Chemical science* **2020**, *11*, 1290–1298.

(25) Torres-Sánchez, J.; Feist, J. Molecular photodissociation enabled by ultrafast plasmon decay. *The Journal of Chemical Physics* **2021**, *154*, 014303.

(26) Kuttruff, J.; Romanelli, M.; Pedrueza-Villalmanzo, E.; Allerbeck, J.; Fregoni, J.; Saavedra-Becerril, V.; Andréasson, J.; Brida, D.; Dmitriev, A.; Corni, S., et al. Sub-

picosecond collapse of molecular polaritons to pure molecular transition in plasmonic photoswitch-nanoantennas. *Nature Communications* **2023**, *14*, 3875.

(27) Fregoni, J.; Granucci, G.; Persico, M.; Corni, S. Strong coupling with light enhances the photoisomerization quantum yield of azobenzene. *Chem* **2020**, *6*, 250–265.

(28) Fregoni, J.; Granucci, G.; Coccia, E.; Persico, M.; Corni, S. Manipulating azobenzene photoisomerization through strong light–molecule coupling. *Nature communications* **2018**, *9*, 1–9.

(29) Riso, R. R.; Haugland, T. S.; Ronca, E.; Koch, H. Molecular orbital theory in cavity QED environments. *Nature communications* **2022**, *13*, 1–8.

(30) Li, G.-C.; Zhang, Q.; Maier, S. A.; Lei, D. Plasmonic particle-on-film nanocavities: a versatile platform for plasmon-enhanced spectroscopy and photochemistry. *Nanophotonics* **2018**, *7*, 1865–1889.

(31) Gao, S.; Ueno, K.; Misawa, H. Plasmonic antenna effects on photochemical reactions. *Accounts of Chemical Research* **2011**, *44*, 251–260.

(32) Linic, S.; Aslam, U.; Boerigter, C.; Morabito, M. Photochemical transformations on plasmonic metal nanoparticles. *Nature materials* **2015**, *14*, 567–576.

(33) Torres-Sánchez, J.; Feist, J. Molecular photodissociation enabled by ultrafast plasmon decay. *The Journal of Chemical Physics* **2021**, *154*, 014303.

(34) Vasa, P.; Lienau, C. Strong light–matter interaction in quantum emitter/metal hybrid nanostructures. *Acs Photonics* **2018**, *5*, 2–23.

(35) Tame, M. S.; McEnery, K.; Özdemir, Ş.; Lee, J.; Maier, S. A.; Kim, M. Quantum plasmonics. *Nature Physics* **2013**, *9*, 329–340.

(36) Vukovic, S.; Corni, S.; Mennucci, B. Fluorescence enhancement of chromophores close to metal nanoparticles. Optimal setup revealed by the polarizable continuum model. *The Journal of Physical Chemistry C* **2009**, *113*, 121–133.

(37) Caricato, M.; Andreussi, O.; Corni, S. Semiempirical (ZINDO-PCM) approach to predict the radiative and nonradiative decay rates of a molecule close to metal particles. *The Journal of Physical Chemistry B* **2006**, *110*, 16652–16659.

(38) Corni, S.; Tomasi, J. Lifetimes of electronic excited states of a molecule close to a metal surface. *The Journal of chemical physics* **2003**, *118*, 6481–6494.

(39) Mennucci, B.; Corni, S. Multiscale modelling of photoinduced processes in composite systems. *Nature Reviews Chemistry* **2019**, *3*, 315–330.

(40) Hohenester, U.; Trugler, A. Interaction of single molecules with metallic nanoparticles. *IEEE Journal of Selected Topics in Quantum Electronics* **2008**, *14*, 1430–1440.

(41) Lopata, K.; Neuhauser, D. Multiscale Maxwell–Schrödinger modeling: A split field finite-difference time-domain approach to molecular nanopolaritonics. *The Journal of chemical physics* **2009**, *130*, 104707.

(42) Chen, H.; McMahon, J. M.; Ratner, M. A.; Schatz, G. C. Classical electrodynamics coupled to quantum mechanics for calculation of molecular optical properties: a RT-TDDFT/FDTD approach. *The Journal of Physical Chemistry C* **2010**, *114*, 14384–14392.

(43) Zhang, Y.; Dong, Z.-C.; Aizpurua, J. Influence of the chemical structure on molecular light emission in strongly localized plasmonic fields. *The Journal of Physical Chemistry C* **2020**, *124*, 4674–4683.

(44) Aguilar-Galindo, F.; Díaz-Tendero, S.; Borisov, A. G. Electronic structure effects in

the coupling of a single molecule with a plasmonic antenna. *The Journal of Physical Chemistry C* **2019**, *123*, 4446–4456.

(45) Thomas, R.; Thomas, A.; Pullanchery, S.; Joseph, L.; Somasundaran, S. M.; Swathi, R. S.; Gray, S. K.; Thomas, K. G. Plexcitons: The Role of Oscillator Strengths and Spectral Widths in Determining Strong Coupling. *ACS Nano* **2018**, *12*, 402–415.

(46) Peruffo, N.; Gil, G.; Corni, S.; Mancin, F.; Collini, E. Selective switching of multiple plexcitons in colloidal materials: directing the energy flow at the nanoscale. *Nanoscale* **2021**, *13*, 6005–6015.

(47) Hutchison, J. A.; Schwartz, T.; Genet, C.; Devaux, E.; Ebbesen, T. W. Modifying Chemical Landscapes by Coupling to Vacuum Fields. *Angewandte Chemie International Edition* **2012**, *51*, 1592–1596.

(48) Chikkaraddy, R.; De Nijs, B.; Benz, F.; Barrow, S. J.; Scherman, O. A.; Rosta, E.; Demetriadou, A.; Fox, P.; Hess, O.; Baumberg, J. J. Single-molecule strong coupling at room temperature in plasmonic nanocavities. *Nature* **2016**, *535*, 127–130.

(49) Stockman, M. I.; Kling, M. F.; Kleineberg, U.; Krausz, F. Attosecond nanoplasmonic-field microscope. *Nature Photonics* **2007**, *1*, 539–544.

(50) Hartland, G. V. Optical studies of dynamics in noble metal nanostructures. *Chemical reviews* **2011**, *111*, 3858–3887.

(51) Koya, A. N. et al. Advances in ultrafast plasmonics. *Applied Physics Reviews* **2023**, *10*, 021318.

(52) Coccia, E.; Corni, S. Role of coherence in the plasmonic control of molecular absorption. *The Journal of Chemical Physics* **2019**, *151*, 044703.

(53) Coccia, E.; Fregoni, J.; Guido, C.; Marsili, M.; Pipolo, S.; Corni, S. Hybrid theoretical

models for molecular nanoplasmonics. *The Journal of Chemical Physics* **2020**, *153*, 200901.

(54) Pipolo, S.; Corni, S. Real-time description of the electronic dynamics for a molecule close to a plasmonic nanoparticle. *The Journal of Physical Chemistry C* **2016**, *120*, 28774–28781.

(55) Fregoni, J.; Haugland, T. S.; Pipolo, S.; Giovannini, T.; Koch, H.; Corni, S. Strong coupling between localized surface plasmons and molecules by coupled cluster theory. *Nano Letters* **2021**, *21*, 6664–6670.

(56) Neuman, T.; Esteban, R.; Casanova, D.; García-Vidal, F. J.; Aizpurua, J. Coupling of molecular emitters and plasmonic cavities beyond the point-dipole approximation. *Nano letters* **2018**, *18*, 2358–2364.

(57) Feist, J.; Fernández-Domínguez, A. I.; García-Vidal, F. J. Macroscopic QED for quantum nanophotonics: emitter-centered modes as a minimal basis for multiemitter problems. *Nanophotonics* **2020**, *10*, 477–489.

(58) Li, T. E.; Chen, H.-T.; Subotnik, J. E. Comparison of Different Classical, Semiclassical, and Quantum Treatments of Light–Matter Interactions: Understanding Energy Conservation. *Journal of Chemical Theory and Computation* **2019**, *15*, 1957–1973.

(59) Waks, E.; Sridharan, D. Cavity QED treatment of interactions between a metal nanoparticle and a dipole emitter. *Physical Review A* **2010**, *82*, 043845.

(60) Pelton, M.; Storm, S. D.; Leng, H. Strong coupling of emitters to single plasmonic nanoparticles: exciton-induced transparency and Rabi splitting. *Nanoscale* **2019**, *11*, 14540–14552.

(61) Yang, C.-J.; An, J.-H.; Lin, H.-Q. Signatures of quantized coupling between quantum emitters and localized surface plasmons. *Physical Review Research* **2019**, *1*, 023027.

(62) Cuartero-González, A.; Fernández-Domínguez, A. Light-forbidden transitions in plasmon-emitter interactions beyond the weak coupling regime. *ACS Photonics* **2018**, *5*, 3415–3420.

(63) Cortes, C. L.; Otten, M.; Gray, S. K. Non-Hermitian approach for quantum plasmonics. *The Journal of Chemical Physics* **2020**, *152*, 084105.

(64) Nascimento, D. R.; DePrince III, A. E. Modeling molecule-plasmon interactions using quantized radiation fields within time-dependent electronic structure theory. *The Journal of Chemical Physics* **2015**, *143*, 214104.

(65) Davidsson, E.; Kowalewski, M. Simulating photodissociation reactions in bad cavities with the Lindblad equation. *The Journal of chemical physics* **2020**, *153*.

(66) Chen, X.-W.; Sandoghdar, V.; Agio, M. Coherent interaction of light with a metallic structure coupled to a single quantum emitter: from superabsorption to cloaking. *Physical review letters* **2013**, *110*, 153605.

(67) Kaminski, F.; Sandoghdar, V.; Agio, M. Finite-difference time-domain modeling of decay rates in the near field of metal nanostructures. *Journal of Computational and Theoretical nanoscience* **2007**, *4*, 635–643.

(68) Fofang, N. T.; Grady, N. K.; Fan, Z.; Govorov, A. O.; Halas, N. J. Plexciton dynamics: exciton- plasmon coupling in a J-aggregate- Au nanoshell complex provides a mechanism for nonlinearity. *Nano letters* **2011**, *11*, 1556–1560.

(69) Zhang, W.; Govorov, A. O.; Bryant, G. W. Semiconductor-metal nanoparticle molecules: Hybrid excitons and the nonlinear Fano effect. *Physical review letters* **2006**, *97*, 146804.

(70) Hoffmann, N. M.; Schäfer, C.; Säkkinen, N.; Rubio, A.; Appel, H.; Kelly, A. Bench-

marking semiclassical and perturbative methods for real-time simulations of cavity-bound emission and interference. *The Journal of Chemical Physics* **2019**, *151*.

(71) Rokaj, V.; Welakuh, D. M.; Ruggenthaler, M.; Rubio, A. Light–matter interaction in the long-wavelength limit: no ground-state without dipole self-energy. *Journal of Physics B: Atomic, Molecular and Optical Physics* **2018**, *51*, 034005.

(72) Schäfer, C.; Johansson, G. Shortcut to self-consistent light-matter interaction and realistic spectra from first principles. *Physical Review Letters* **2022**, *128*, 156402.

(73) Chen, J.; Shan, X.; Wang, X.; Huang, Y. A study of the effective Hamiltonian method for decay dynamics. *Communications in Theoretical Physics* **2023**, *75*, 035102.

(74) Medina, I.; García-Vidal, F. J.; Fernández-Domínguez, A. I.; Feist, J. Few-mode field quantization of arbitrary electromagnetic spectral densities. *Physical Review Letters* **2021**, *126*, 093601.

(75) Sánchez-Barquilla, M.; García-Vidal, F. J.; Fernández-Domínguez, A. I.; Feist, J. Few-mode field quantization for multiple emitters. *Nanophotonics* **2022**, *11*, 4363–4374.

(76) Trügler, A.; Hohenester, U. Strong coupling between a metallic nanoparticle and a single molecule. *Physical Review B* **2008**, *77*, 115403.

(77) Wang, S.; Scholes, G. D.; Hsu, L.-Y. Quantum dynamics of a molecular emitter strongly coupled with surface plasmon polaritons: A macroscopic quantum electrodynamics approach. *The Journal of Chemical Physics* **2019**, *151*, 014105.

(78) Wang, S.; Lee, M.-W.; Chuang, Y.-T.; Scholes, G. D.; Hsu, L.-Y. Theory of molecular emission power spectra. I. Macroscopic quantum electrodynamics formalism. *The Journal of chemical physics* **2020**, *153*, 184102.

(79) Wang, S.; Scholes, G. D.; Hsu, L.-Y. Coherent-to-incoherent transition of molecular

fluorescence controlled by surface plasmon polaritons. *The journal of physical chemistry letters* **2020**, *11*, 5948–5955.

(80) Chuang, Y.-T.; Wang, S.; Hsu, L.-Y. Macroscopic quantum electrodynamics approach to multichromophoric excitation energy transfer. II. Polariton-mediated population dynamics in a dimer system. *The Journal of Chemical Physics* **2022**, *157*, 234109.

(81) Sakko, A.; Rossi, T. P.; Nieminen, R. M. Dynamical coupling of plasmons and molecular excitations by hybrid quantum/classical calculations: time-domain approach. *Journal of physics: condensed matter* **2014**, *26*, 315013.

(82) Rossi, T. P.; Shegai, T.; Erhart, P.; Antosiewicz, T. J. Strong plasmon-molecule coupling at the nanoscale revealed by first-principles modeling. *Nature communications* **2019**, *10*, 3336.

(83) Kuisma, M.; Rousseaux, B.; Czajkowski, K. M.; Rossi, T. P.; Shegai, T.; Erhart, P.; Antosiewicz, T. J. Ultrastrong coupling of a single molecule to a plasmonic nanocavity: a first-principles study. *ACS photonics* **2022**, *9*, 1065–1077.

(84) Fojt, J.; Rossi, T. P.; Antosiewicz, T. J.; Kuisma, M.; Erhart, P. Dipolar coupling of nanoparticle-molecule assemblies: An efficient approach for studying strong coupling. *The Journal of Chemical Physics* **2021**, *154*.

(85) Castro, A.; Marques, M. A.; Alonso, J. A.; Rubio, A. Optical properties of nanostructures from time-dependent density functional theory. *Journal of Computational and Theoretical Nanoscience* **2004**, *1*, 231–255.

(86) Martinez, J. I.; Castro, A.; Rubio, A.; Alonso, J. Photoabsorption spectra of Ti8C12 metallocarbohedrynes: Theoretical spectroscopy within time-dependent density functional theory. *The Journal of chemical physics* **2006**, *125*.

Supporting information for: Identifying differences between semi-classical and full-quantum descriptions of plexcitons

Marco Romanelli[†] and Stefano Corni[*,†,‡,¶]

†*Department of Chemical Sciences, University of Padova, via Marzolo 1, 35131 Padova, Italy*

‡*CNR Institute of Nanoscience, via Campi 213/A, 41125 Modena, Italy*

¶*Padua Quantum Technologies Research Center, University of Padova, 35131 Padova, Italy*

E-mail: stefano.corni@unipd.it

Contents

1 Theory

1.1 semi-classical (SC) model

In the semi-classical (SC) model, the molecule is described at quantum-mechanical level using standard quantum chemistry approaches, but the plasmonic NP is treated as a classical polarizable continuum object within the PCM-NP framework.[1,2] In essence, plasmonic NPs of arbitrarily complex shape are described in the quasi-static limit, i.e. retardation effects are not included, and are coupled with a quantum chemistry description of molecules through an integral equation formalism of the Polarizable Continuum Model (IEF-PCM)[1] which basically boils down to solving the corresponding Poisson's electrostatic equation. The problem is numerically solved with a Boundary-Element-Method (BEM) approach[3] which entails a surface discretization of the NP, leading to a set of discrete surface elements, called "tesserae", that host polarization charges due to a given external perturbation (e.g. external potential, molecular densities, etc.). Such set of charges represent the NP linear response to the external perturbation and can be used to quantitatively evaluate the molecule-NP interactions and related effects.

Given these premises, the system Hamiltonian $\hat{H}_S(t)$ (see also SI 1.3), here renamed $\hat{H}_{SC}(t)$ for the actual SC case, reads

$$\hat{H}_{SC}(t) = \hat{H}_{mol} - \vec{\hat{\mu}} \cdot \vec{E}_{ext}(t) + (\mathbf{q}_{ref}(t) + \mathbf{q}_{pol}(t)) \cdot \hat{\mathbf{V}} \tag{1}$$

where $\hat{H}_{mol}$ is the time-independent molecular Hamiltonian, $\vec{E}_{ext}(t)$ is the time-dependent external electric field that is used to drive the system, $\vec{\hat{\mu}}$ is the molecular dipole operator, $\mathbf{q}_{ref}(t)$ and $\mathbf{q}_{pol}(t)$ are the vectors collecting the response charges on the nanoparticle's discretized surface induced by direct polarization of the incoming exciting field ($\mathbf{q}_{ref}(t)$) and by the time-dependent nearby molecular electron density ($\mathbf{q}_{pol}(t)$), and $\hat{\mathbf{V}}$ is the molecular electrostatic potential operator evaluated at the nanoparticle surface where response charges

lie on.[1,2]

A time-dependent version of Boundary Element Method previously developed[2,4] (TD-BEM) is used to propagate the surface charges describing the NP response that is coupled to the molecule through the molecular electrostatic potential operator.

The nanoparticle dielectric function is described using a Drude-Lorentz (DL) model,

$$\epsilon(\omega) = 1 + \frac{\Omega_{plasma}^2}{\omega_0^2 - \omega^2 - i\Gamma\omega} \tag{2}$$

where Ω_{plasma} is the metal plasma frequency, ω_0 is the natural frequency of bound oscillators and Γ is the relaxation time (damping rate) of the metal (see SI Sec. 2 for the actual values used).

In the SC case, $\hat{H}_{mol}$ of eq.1 is purely the molecular Hamiltonian, so the full system wavefunction, $|\psi_S(t)\rangle$, here renamed as $|\psi_{SC}(t)\rangle$, can be expanded on the basis of the molecular stationary eigenstates $|m\rangle$ as

$$|\psi_{SC}(t)\rangle = \sum_{m}^{N_{states}} C_m(t)\,|m\rangle \tag{3}$$

where the molecular eigenstates $|m\rangle$ can be obtained with any quantum chemistry approach. In our case we use Configuration Interaction Singles (CIS, SI 2) and the resulting Stochastic Schrödinger Equation (see SI 1.3) we aim to solve in matrix form reads:

$$i\frac{\partial \boldsymbol{C}(t)}{\partial t} = \boldsymbol{H}_{SSE,SC}(t)\boldsymbol{C}(t) \tag{4}$$

with

$$\hat{H}_{SSE,SC}(t) = \hat{H}_{SC}(t) + \sum_{q}^{M} l_{q,SC}(t)\hat{S}_{q,SC} - \frac{i}{2}\sum_{q}^{M} \hat{S}_{q,SC}^{\dagger}\hat{S}_{q,SC}\ . \tag{5}$$

$\boldsymbol{C}(t)$ is the vector of the time-dependent coefficients of eq.3 describing the wavefunction at a given time step t represented on the basis of the molecular eigenstates, whereas $\hat{H}_{SSE,SC}(t)$

is the time-dependent Hamiltonian that is used for propagating the system wavefunction according to a second-order Euler algorithm coupled with quantum jumps[5] (see also SI 1.3). The dissipative operators $\hat{S}_{q,SC}$ in eq.5 are still to be defined. Indeed, different choices may be taken, depending on the relevant decay processes that are considered for a given system. Herein, since the main goal of the present work is to compare the SC and FQ models on a perfectly consistent ground, we solely focus on the NP-induced non radiative decay, which is intrinsically included in $\hat{H}_{SC}(t)$ through $\mathbf{q}_{pol}(t)$, as mentioned in main text.
Under such assumptions eq.5 simplifies to

$$\hat{H}_{SSE,SC}(t) = \hat{H}_{SC}(t). \tag{6}$$

1.2 full-quantum (FQ) model

In the full-quantum picture (FQ), the plasmonic NP is also quantized, so the system Hamiltonian becomes

$$\hat{H}_{FQ}(t) = \hat{H}_{0,FQ} - \vec{\hat{\mu}} \cdot \vec{E}_{ext}(t) \tag{7}$$

where $\hat{H}_{0,FQ}$ is the full plasmon-molecule Hamiltonian,[6]

$$\hat{H}_{0,FQ} = \hat{H}_{mol} + \sum_{p} \omega_p \hat{b}_p^\dagger \hat{b}_p + \sum_{pj} q_{pj} \hat{V}_j (b_p^\dagger + b_p) \tag{8}$$

with ω_p being the frequency of the p^{th} quantized plasmon mode and q_{pj} being the corresponding quantized surface charge lying on the j^{th} tessera. $\hat{b}_p^\dagger$ and $\hat{b}_p$ are the corresponding plasmonic creation and annhilation operators and $\hat{V}_j$ is instead the molecular electrostatic potential operator evaluated at the j^{th} tessera. The complete derivation of the Q-PCM-NP quantization scheme that leads to eq.8 is reported in ref.[6]
Starting from eq.8 and assuming to consider two molecular states only $|g\rangle, |e\rangle$, the Hamiltonian of eq.8 can be recast into a more familiar form after inserting the molecular identity

operator $\mathbb{1}_{\mathbb{mol}} = |g\rangle\langle g| + |e\rangle\langle e|$ before and after $\hat{V}_j$, leading to

$$\begin{aligned}\hat{H}_{0,FQ} =&\omega_g |g\rangle\langle g| + \omega_e |e\rangle\langle e| + \sum_p \omega_p \hat{b}_p^\dagger \hat{b}_p + \sum_{pj} q_{pj} \Big(\hat{V}_j^{gg} |g\rangle\langle g| + \hat{V}_j^{ee} |e\rangle\langle e| + \\ & \hat{V}_j^{eg} |e\rangle\langle g| + \hat{V}_j^{ge} |g\rangle\langle e| \Big) \left(b_p^\dagger + b_p\right)\end{aligned} \tag{9}$$

where ω_g and ω_e are the energies of the corresponding molecular states and the shorthand notation $\hat{V}_j^{eg}$ stands for $\langle e| \hat{V}_j |g\rangle$.The diagonal terms of the plasmon-molecule interaction $\sum_{pj} q_{pj} \hat{V}_j^{gg}$, $\sum_{pj} q_{pj} \hat{V}_j^{ee}$ in eq.9 lead to a correction of the molecular excitation frequency $\omega_e - \omega_g$ due to the nearby NP. This contribution is numerically negligible in the present case, therefore upon setting $\omega_g = 0$ so that ω_e becomes the molecular transition frequency, we end up with the simplified expression

$$\hat{H}_{0,FQ} = \omega_e \hat{\sigma}^\dagger \hat{\sigma} + \sum_p \omega_p \hat{b}_p^\dagger \hat{b}_p + \sum_{pj} q_{pj} \hat{V}_j^{eg} \left(\hat{\sigma}^\dagger + \hat{\sigma}\right) \left(b_p^\dagger + b_p\right) \tag{10}$$

where we have introduced the molecular transfer operators $\hat{\sigma}^\dagger = |e\rangle\langle g|$, $\hat{\sigma} = |g\rangle\langle e|$ and $\hat{V}_j^{eg}$ can be taken to be real. Clearly, eq.10 leads to the well-known Jaynes-Cummings multi-mode Hamiltonian[7,8] after applying the usual rotating wave approximation to the interaction terms, namely

$$\hat{H}_{0,FQ} = \omega_e \hat{\sigma}^\dagger \hat{\sigma} + \sum_p \omega_p \hat{b}_p^\dagger \hat{b}_p + \sum_p g_p (\hat{b}_p^\dagger \hat{\sigma} + \hat{b}_p \hat{\sigma}^\dagger) \tag{11}$$

with g_p being the corresponding transition coupling element computed as,

$$g_p = \langle e, 0| \sum_j q_{pj} \hat{V}_j (b_p^\dagger + b_p) |g, 1_p\rangle \tag{12}$$

in the single-excitation subspace. In eq.12 the shorthand notation $|e, 0\rangle, |g, 1_p\rangle$ has been introduced which represents the molecular excited state with all plasmon modes in their ground state and the p^{th} plasmon mode singly excited with the molecule in its ground state, respectively. Both approximations that have been applied moving from eq.9 to eq.11 were

numerically tested in the investigated case and they proved to be valid .

The Hamiltonian of eq.11, expressed in the 1-excitation states basis,[9,10] can be fully diagonalized to obtain the 1-excitation plexcitonic states ($|\widetilde{m}\rangle$), which can be generally expressed as

$$|\widetilde{m}\rangle = \sum_{p} |e,0\rangle\, C_e^{\widetilde{m}} + |g,1_p\rangle\, C_p^{\widetilde{m}}. \tag{13}$$

In the FQ picture, the complete Hamiltonian that is used for time-propagation becomes

$$\hat{H}_{SSE,FQ}(t) = \hat{H}_{FQ}(t) + \sum_{p} l_{p,FQ}(t)\hat{S}_{p,FQ} - \frac{i}{2}\sum_{p} \hat{S}^{\dagger}_{p,FQ}\hat{S}_{p,FQ} \tag{14}$$

with

$$\hat{S}_{p,FQ} = \sqrt{\Gamma_p}\mathbb{1}_{\mathbb{mol}} \otimes (|0\rangle\,\langle 1_p|) \tag{15}$$

where Γ_p is the decay rate of the p^{th} quantized mode that is actually equal to Γ (eq.2) for every p^{th} plasmon mode originating from the Q-PCM-NP quantization scheme.[6]
Clearly, the form of the chosen decay operator of eq.15 is an assumption which implies that the only source of dissipation in the current FQ picture comes from the plasmonic part of the wavefunction. This approximation basically neglects any other intrinsic molecular relaxation channel, which often take place on a longer time scale (tens/hundreds of picoseconds). The same assumption has been consistently made in the SC model where only the NP-mediated non radiative decay has been included (see SI 1.1).

In the FQ picture the time-dependent wavefunction can be generally expressed in the plexcitonic basis (eq.13) as

$$|\psi_{FQ}(t)\rangle = \sum_{\widetilde{m}} C_{\widetilde{m}}(t)\,|\widetilde{m}\rangle\,, \tag{16}$$

thus leading to the following equation

$$i\frac{\partial \boldsymbol{C(t)}}{\partial t} = \boldsymbol{H}_{SSE,FQ}(t)\boldsymbol{C(t)} \tag{17}$$

which is the FQ analogue to eq.4, where now $\boldsymbol{C(t)}$ is the vector of time-dependent coefficients representing the wavefunction on the plexcitonic basis. Propagation is thus performed in this basis by means of a second-order Euler algorithm coupled with random quantum jumps using a Monte Carlo technique[5] (SI 1.3).

On this basis $\hat{H}_{0,FQ}$ is diagonal, but $\hat{S}^{\dagger}_{p,FQ}\hat{S}_{p,FQ}$ is not. Indeed, using eqs.13-15 it is easy to show that

$$\begin{aligned}\langle\widetilde{m}|\,\hat{S}^{\dagger}_{p,FQ}\hat{S}_{p,FQ}\,|\widetilde{m}\rangle &= \left(C_p^{\widetilde{m}}\right)^2\Gamma_p \\ \langle\widetilde{n}|\,\hat{S}^{\dagger}_{p,FQ}\hat{S}_{p,FQ}\,|\widetilde{m}\rangle &= \left(C_p^{\widetilde{n}}C_p^{\widetilde{m}}\right)\Gamma_p\end{aligned} \tag{18}$$

where the coefficients $C_p^{\widetilde{n}/\widetilde{m}}$ can be taken to be real because of the form of $\hat{H}_{0,FQ}$ (eq.11).

The physical quantity that is investigated in the present work to compare SC and FQ descriptions (see Figs. 2-4, main text) is the molecular excited state population upon driving, which according to eq.3 and eqs.13,16 respectively reads

$$\begin{aligned}|C_{e,SC}(t)|^2 &= |\langle e|\psi_{SC}(t)\rangle|^2 = |C_e(t)|^2\ , \\ |C_{e,FQ}(t)|^2 &= |\langle e,0|\psi_{FQ}(t)\rangle|^2 = \left|\sum_{\widetilde{m}} C_e^{\widetilde{m}}C_{\widetilde{m}}(t)\right|^2 .\end{aligned} \tag{19}$$

1.3 Stochastic Schrödinger Equation

In the Markovian limit, an open-quantum-system description of the system-bath interaction leads to the following Stochastic Schrödinger equation (SSE) expressed in atomic units (a.u.)

$$i\frac{d}{dt}\,|\psi_S(t)\rangle = \hat{H}_S(t)\,|\psi_S(t)\rangle + \sum_q^M l_q(t)\hat{S}_q\,|\psi_S(t)\rangle - \frac{i}{2}\sum_q^M \hat{S}_q^{\dagger}\hat{S}_q\,|\psi_S(t)\rangle\,. \tag{20}$$

$|\psi_S(t)\rangle$ and $\hat{H}_S(t)$ are the system time-dependent wavefunction and Hamiltonian, respectively, whose definitions depend on the model being used for describing the nanoparticle-molecule system (see SI 1.1 and 1.2). The operators $\hat{S}_q$ describe the effect of the surroundings

(bath) on the system through different M interaction channels, each one labelled as q and defined according to the type of dissipative process that is modelled (e.g. non-radiative decay, dephasing etc.). The non-Hermitian term of eq.20 , $-\frac{i}{2}\sum_q^M \hat{S}_q^\dagger \hat{S}_q$, represents dissipation due to the environment, while $\sum_q^M l_q(t)\hat{S}_q$ is a fluctuation term modelled as a Wiener process $l_q(t)$ i.e. white noise associated with the Markovian approximation. In our case, the SSE (eq.20) is propagated using a quantum jump algorithm which practically translates to accounting for the explicit fluctuation term of eq.20 through a Monte-Carlo like method based on random quantum jumps.[5,11–13] We remark that the explicit form of the operators appearing in eq.20 depend on the model that is used for describing the coupled system, which then differs between the SC and FQ approaches described above. Since this is a stochastic process, an independent number of trajectories N_{traj} have to be performed and by averaging the corresponding results, system properties, like populations and coherences for instance, can be obtained. In the ideal limit of an infinite number of independent realizations, the averaged results match those coming from time-propagating the system reduced density-matrix with a Lindblad-like master equation approach.[5]

2 Computational details

The quinolone molecule is described at *ab initio* level, using CIS/6-31g* in a locally-modified version of GAMESS[2,14] which accounts for the presence of the nearby NP in the determination of the molecular ground state at the classical level. The molecular excited states are determined assuming the NP classical polarization remains frozen to that proper for ground state. This means that for both the SC and FQ models, the same set of states are used. Moreover, the use of the rotating wave approximation (see eq.11) in the FQ model does not provide further change to the ground state.

According to adopted level of theory, the lowest bright excited state of quinolone features an excitation energy of $\approx 2.95\,\mathrm{eV}$. The NP optical response is modelled with a Drude-

Lorentz dielectric function (eq.2) setting $\Omega_{plasma} = 0.240\,\text{a.u.} \approx 6.5\,\text{eV}$, which is close to values previously adopted for gold,[15] $\omega_0 = 0\,\text{a.u.}$ and $\Gamma = 0.01515\,\text{a.u.}$, that corresponds to a lifetime of $\approx 2\,\text{fs}$. With such parameters, the lowest dipolar plasmon mode of the NP is basically in resonance with the molecular transition ($\omega_p \approx 2.95\,\text{eV}$).The computed transition coupling element (eq.12) between that mode, which is the most relevant since all others lie higher in energy and are scarcely coupled with the molecule, and the lowest quinolone bright excitation is $|g| \approx 2.5\,\text{meV}$ which, given the value of $\Gamma = 0.01515\,\text{a.u.} \approx 410\,\text{meV}$, results in $\frac{|g|}{\Gamma} << 1$, thus setting the present case in the weak-coupling regime.[16]

Time-dependent simulations have been performed by exciting the system with a pulse with gaussian envelope, resonant with the dipolar plasmon mode frequency $\omega_p = 2.95\,\text{eV}$,

$$\vec{E}_{ext}(t) = \hat{r} E_0 exp\left(-\frac{(t-t_0)^2}{2\sigma^2}\right) cos(\omega_p t) \tag{21}$$

where $\hat{r}$ is the unit vector pointing along the molecule-NP distance direction (Fig.1, main text), E_0 is the field amplitude set to 10^{-6}a.u. unless differently specified ($\approx 5 \times 10^5\,\text{V/m}$, corresponding to $3.5 \times 10^4\,\text{W/cm}^2$ light intensity) which ensures the weak-field limit,[17] $t_0 \approx 7\,\text{fs}$ and $\sigma \approx 1\,\text{fs}$. The coefficients $\boldsymbol{C(t)}$ of eqs.4,17 are propagated via a second-order Euler algorithm in combination with quantum jumps[4,5] using a time step of 0.1 as. Under weak-field driving 100 trajectories were run initially, but no quantum jump occurred under weak-field excitation, so results shown in Figs. 3-4 (main text) actually originate from individual wavefunction propagation. On the other hand, beyond the weak-field limit (Fig.2 main text) quantum jumps do often occur in FQ simulations, and so averaging over 1000 trajectories has been done in that case.

3 Analytical models

3.1 semi-classical picture in the weak-coupling limit

Starting from the full SC Hamiltonian of eq.1 and considering that the molecule-NP distance of the investigated setup (Fig.1 main text) is large enough to ensure that only dipolar interactions are relvant, we can apply the dipole approximation to the molecule-NP coupling terms (rightmost terms of eq.1, SI 1.1). Additionally, the $\mathbf{q}_{pol}(t)$ contribution to the classical response charges of eq.1 is typically much smaller than $\mathbf{q}_{ref}(t)$ when the plasmonic system is excited nearby plasmon resonance, the latter being directly related to the scattered field of the NP due to external driving, and so it can be neglected, thus leading to

$$\hat{H}_{SC}(t) = \hat{H}_{mol} - \vec{\hat{\mu}} \cdot \vec{E}_{ext}(t) - \vec{\hat{\mu}} \cdot \vec{E}_{scatt}(t) \tag{22}$$

where $\vec{E}_{scatt}(t)$ is the scattered field of the NP at the molecule location upon external excitation. In other words, this contribution accounts for the plasmonic local field enhancement effect.

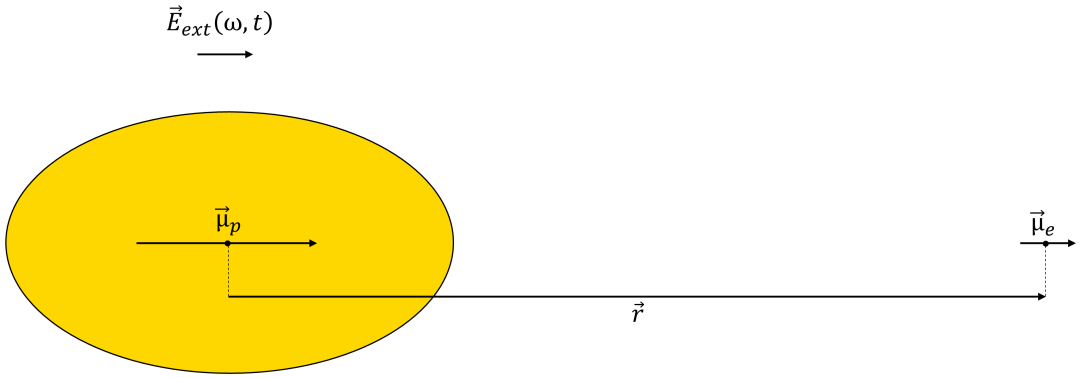

Figure S1: Schematic representation of the NP-molecule setup considered for the analytical model. $\vec{\mu}_p$ and $\vec{\mu}_e$ represent the plasmonic and molecular transition dipoles, respectively.

The setup that has been investigated (Fig.1 main text) features a large molecule-NP distance which basically ensures the validity of the weak-coupling condition. Under these

circumstances, the scattered field of the NP at the molecule position is dominated by the plasmonic dipolar response, which can then be formally expressed as

$$\vec{E}_{scatt}(\omega,\vec{r}) = \frac{3\left[\left(\vec{E}_{ext}(\omega)\alpha_{NP}(\omega)\right)\cdot\hat{r}\right]\hat{r} - \vec{E}_{ext}(\omega)\alpha_{NP}(\omega)}{|\vec{r}|^3} \tag{23}$$

with $\hat{r}$ being the unit vector pointing along the NP-molecule direction (Fig.S1) and $\alpha_{NP}(\omega)$ being the frequency-dependent NP polarizability expressed as[6]

$$\alpha_{NP}(\omega) = \sum_p \frac{\langle 0|\,\hat{\mu}\,|p\rangle\,\langle p|\,\hat{\mu}\,|0\rangle}{\omega_p - \omega - i\Gamma_p} + \frac{\langle p|\,\hat{\mu}\,|0\rangle\,\langle 0|\,\hat{\mu}\,|p\rangle}{\omega_p + \omega + i\Gamma_p} \tag{24}$$

where ω_p and Γ_p are the frequency and damping rate of the corresponding p^{th} plasmonic mode.

In principle the sum of eq.24 should run over all the plasmon modes of the NP, however, in the investigated weak-coupling limit the NP-molecule distance is large enough such that only dipolar resonances significantly contribute to the scattered field at the molecule location, thus eq.24 can be reasonably approximated to

$$\alpha_{NP}(\omega) \approx \frac{|\vec{\mu}_p|^2}{\omega_p - \omega - i\Gamma_p} + \frac{|\vec{\mu}_p|^2}{\omega_p + \omega + i\Gamma_p} \tag{25}$$

with $|\vec{\mu}_p|^2$ being the squared modulus of the transition dipole moment of the only-relevant dipolar plasmonic mode.

In our model, the NP dipolar mode is exactly aligned with the direction of the incoming external field and the molecular transition dipole (Fig.S1), thus eq.23 simplifies to

$$\vec{E}_{scatt}(\omega,\vec{r}) = \frac{2\vec{E}_{ext}(\omega)\alpha_{NP}(\omega)}{|\vec{r}|^3} \tag{26}$$

and the Hamiltonian of eq.22 becomes

$$\hat{H}_{SC}(t) = \hat{H}_{mol} - \vec{\hat{\mu}} \cdot \vec{E}_{ext}(t) \left(1 + \frac{2\alpha_{NP}(\omega)}{|\vec{r}\,|^3}\right). \tag{27}$$

Given these premises, the excited state molecular population plotted in Fig.4 main text can be inferred by means of time-dependent perturbation theory, where the second (time-dependent) term of the r.h.s of eq.27 is the actual perturbation $\hat{V}(t)$. First-order time-dependent perturbation theory leads to the usual expression for excited state coefficients,[18] namely

$$\begin{aligned} C'_{e,SC}(t) &= -i \int_{-\infty}^{t} \langle e| \hat{V}(t) |g\rangle \, e^{i\omega_e t} dt \\ &= i \int_{-\infty}^{t} \langle e| \hat{\mu} |g\rangle \cdot \vec{E}_{ext}(t) \left(1 + \frac{2|\vec{\mu}_p|^2}{(\omega_p - \omega - i\Gamma_p)|\vec{r}\,|^3} + \frac{2|\vec{\mu}_p|^2}{(\omega_p + \omega + i\Gamma_p)|\vec{r}\,|^3}\right) e^{i\omega_e t} dt \end{aligned} \tag{28}$$

where ω_e is the excitation frequency of the considered molecular transition.
Assuming then the external driving is a monochromatic oscillating perturbation in resonance with the plasmon frequency and oriented along the transition dipoles (Fig.S1), that is

$$\vec{E}_{ext}(\omega_p) = \hat{r} E_0 \frac{(e^{i\omega_p t} + e^{-i\omega_p t})}{2} \tag{29}$$

we end up with

$$C'_{e,SC}(t) = i \frac{E_0 |\vec{\mu}_e|}{2} \left(1 + \frac{2|\vec{\mu}_p|^2}{(-i\Gamma_p)|\vec{r}\,|^3} + \frac{2|\vec{\mu}_p|^2}{(2\omega_p + i\Gamma_p)|\vec{r}\,|^3}\right) \int_{-\infty}^{t} e^{i(\omega_e - \omega_p)t} + e^{i(\omega_e + \omega_p)t} dt \tag{30}$$

where $|\vec{\mu}_e|$ is the molecular transition dipole associated to the transition between the ground and the first excited state ($|g\rangle \rightarrow |e\rangle$). Solving[I] the integral of eq.30 and rearranging some

[I] To be formally correct one should consider a slowly switching perturbation as $\lim_{\epsilon \to 0} e^{\epsilon t} \hat{V}(t)$ which basically enable us to set the value of the integral at the lower limit to zero. This has been implicitly done passing from eq.30 to eq.31

terms results in

$$\begin{aligned} C'_{e,SC}(t) &= \frac{E_0|\vec{\mu}_e|}{2}\left(1+\frac{i2|\vec{\mu}_p|^2}{\Gamma_p|\vec{r}|^3}+\frac{2|\vec{\mu}_p|^2(2\omega_p-i\Gamma_p)}{(4\omega_p^2+\Gamma_p^2)|\vec{r}|^3}\right)\cdot\left(\frac{e^{i(\omega_e-\omega_p)t}}{\omega_e-\omega_p}+\frac{e^{i(\omega_e+\omega_p)t}}{\omega_e+\omega_p}\right) \\ &= \frac{E_0|\vec{\mu}_e|}{2}\left(1+\frac{i2|\vec{\mu}_p|^2}{\Gamma_p|\vec{r}|^3}+\frac{2|\vec{\mu}_p|^2(2\omega_p-i\Gamma_p)}{(4\omega_p^2+\Gamma_p^2)|\vec{r}|^3}\right)\cdot\left(\frac{e^{i\delta t}}{\delta}+\frac{e^{i(2\omega_p+\delta)t}}{2\omega_p+\delta}\right) \end{aligned} \tag{31}$$

where $\delta = \omega_e - \omega_p$, which is the frequency detuning between the molecular and plasmon frequencies, has been introduced for convenience.

Finally, taking the squared modulus of eq.31 leads to the 1^{st}-order expression of the molecular excited state population, that is

$$\begin{aligned} |C'_{e,SC}(t)|^2 = \frac{E_0^2|\vec{\mu}_e|^2}{4}\Bigg(1+\frac{16|\vec{\mu}_p|^4\omega_p^2}{(4\omega_p^2+\Gamma_p^2)^2|\vec{r}|^6}+\frac{8|\vec{\mu}_p|^2\omega_p}{(4\omega_p^2+\Gamma_p^2)|\vec{r}|^3}+\frac{4|\vec{\mu}_p|^4}{\Gamma_p^2|\vec{r}|^6}+\frac{4|\vec{\mu}_p|^4\Gamma_p^2}{(4\omega_p^2+\Gamma_p^2)^2|\vec{r}|^6} \\ -\frac{8|\vec{\mu}_p|^4}{(4\omega_p^2+\Gamma_p^2)|\vec{r}|^6}\Bigg)\cdot\left(\frac{1}{\delta^2}+\frac{1}{(2\omega_p+\delta)^2}+2\mathfrak{Re}\Big\{\frac{e^{-i2\omega_p t}}{(2\omega_p+\delta)\delta}\Big\}\right) \end{aligned} \tag{32}$$

which simplifies to

$$\begin{aligned} |C'_{e,SC}(t)|^2 = \frac{E_0^2|\vec{\mu}_e|^2}{4}\left(1+\frac{4|\vec{\mu}_p|^4}{\Gamma_p^2|\vec{r}|^6}-\frac{4|\vec{\mu}_p|^4}{(4\omega_p^2+\Gamma_p^2)|\vec{r}|^6}+\frac{8|\vec{\mu}_p|^2\omega_p}{(4\omega_p^2+\Gamma_p^2)|\vec{r}|^3}\right)\cdot \\ \left(\frac{1}{\delta^2}+\frac{1}{(2\omega_p+\delta)^2}+2\mathfrak{Re}\Big\{\frac{e^{-i2\omega_p t}}{(2\omega_p+\delta)\delta}\Big\}\right) \end{aligned} \tag{33}$$

Eq.33 is the main result of the SC derivation that is compared in the following to the analogous quantity obtained from the FQ model (SI 3.2, below).

3.2 full-quantum picture in the weak-coupling limit

In the FQ model, the Hamiltonian of interest is

$$\hat{H}_{FQ}(t) = \hat{H}_{0,FQ} - \vec{\hat{\mu}}\cdot\vec{E}_{ext}(t) \tag{34}$$

and $\hat{H}_{0,FQ}$ (SI 1.2) in the single-mode case reads

$$\hat{H}_{0,FQ} = \omega_e \sigma^\dagger \sigma + \omega_p b_p^\dagger b_p + g_p(b_p^\dagger \sigma + b_p \sigma^\dagger). \tag{35}$$

As explained in SI 1.2, the molecule-NP interaction in the FQ picture enters directly into the 0^{th} order time-independent Hamiltonian, and the remaining time-dependent perturbation is just the interaction with the external field.

Diagonalization of eq.35 in the 1-excitation states manifold leads to the usual expression of plexcitonic wavefunctions

$$\begin{aligned} |LP\rangle &= |e,0\rangle\, C_e^{LP} + |g,1\rangle\, C_p^{LP} \\ |UP\rangle &= |e,0\rangle\, C_e^{UP} + |g,1\rangle\, C_p^{UP}. \end{aligned} \tag{36}$$

The first-order wavefunction upon interaction with the external field can be expressed as[18]

$$|\psi_{FQ}^{'}(t)\rangle = C_g^{'}(t)\,|g,0\rangle\, e^{-i\omega_g t} + C_{LP}^{'}(t)\,|LP\rangle\, e^{-i\omega_{LP} t} + C_{UP}^{'}(t)\,|UP\rangle\, e^{-i\omega_{UP} t} \tag{37}$$

and since the focus of the present derivation is to obtain an analytical expression for the molecular excited state population so as to compare with the SC analogue (eq.33), we have

$$C_{e,FQ}^{'}(t) = \langle e,0|\psi_{FQ}^{'}(t)\rangle = C_{LP}^{'}(t) C_e^{LP}\,|LP\rangle\, e^{-i\omega_{LP} t} + C_{UP}^{'}(t) C_e^{UP}\,|UP\rangle\, e^{-i\omega_{UP} t}. \tag{38}$$

Time-dependent pertubation theory can be again used to obtain an expression for first-order coefficients, namely

$$\begin{aligned} C_{UP}^{'}(t) &= i\frac{E_0}{2}\int_{-\infty}^{t} \langle UP|\,\hat{\mu}\,|g,0\rangle \cdot \hat{r}\left(e^{i(\omega_{UP}-\omega_p)t} + e^{i(\omega_{UP}+\omega_p)t}\right) dt \\ C_{LP}^{'}(t) &= i\frac{E_0}{2}\int_{-\infty}^{t} \langle LP|\,\hat{\mu}\,|g,0\rangle \cdot \hat{r}\left(e^{i(\omega_{LP}-\omega_p)t} + e^{i(\omega_{LP}+\omega_p)t}\right) dt \end{aligned} \tag{39}$$

where the same monochromatic field as in the semi-classical case (eq.29) has been used.

Given the relations of eqs.36,39 and considering that the electric field direction ($\hat{r}$) is aligned with both the molecular and plasmonic transition dipoles, substitution of eq.39 into eq.38 upon solving the integrals leads to

$$\begin{aligned} C'_{e,FQ}(t) =& \frac{E_0}{2}\left(\left|C_e^{UP}\right|^2|\vec{\mu}_e| + C_e^{UP}\left(C_p^{UP}\right)^*|\vec{\mu}_p|\right)\left(\frac{e^{-i\omega_p t}}{\omega_{UP}-\omega_p}+\frac{e^{i\omega_p t}}{\omega_{UP}+\omega_p}\right)+ \\ & \frac{E_0}{2}\left(\left|C_e^{LP}\right|^2|\vec{\mu}_e| + C_e^{LP}\left(C_p^{LP}\right)^*|\vec{\mu}_p|\right)\left(\frac{e^{-i\omega_p t}}{\omega_{LP}-\omega_p}+\frac{e^{i\omega_p t}}{\omega_{LP}+\omega_p}\right). \end{aligned} \tag{40}$$

Eq.40 can be further manipulated to obtain an expression more similar to the SC analogue. Indeed, since we are in the weak-coupling limit (with $\delta = \omega_e - \omega_p > 0$) time-independent perturbation theory can be used to obtain an approximate quantitative expressions for $C_e^{UP/LP}$ and $\omega_{UP/LP}$, resulting in[18]

$$\begin{aligned} \omega_{UP} &\approx \omega_e + \frac{g^2}{\tilde{\delta}} \\ \omega_{LP} &\approx \overline{\omega_p} - \frac{g^2}{\tilde{\delta}} \\ |UP\rangle &= \left(|e,0\rangle - \frac{|g|}{\tilde{\delta}^*}|g,1\rangle\right)N \\ |LP\rangle &= \left(|g,1\rangle + \frac{|g|}{\tilde{\delta}}|e,0\rangle\right)N \\ N &= \frac{1}{\sqrt{1+\frac{g^2}{\delta^2+\Gamma_p^2}}} \end{aligned} \tag{41}$$

where we have phenomenologically introduced $\overline{\omega_p} = \omega_p - i\Gamma_p$ and so $\tilde{\delta} = \delta + i\Gamma_p$ to explicitly recover the damping rate of the plasmon mode in the FQ model, which also appears in the SC expression of eq.33. Besides, to ease the notation we set $g_p = g$ (which is also real), and given that the molecule-NP distance is large enough to ensure that only dipolar interactions are relevant, the coupling g can be explicitly expressed as

$$|g| = \frac{2|\vec{\mu}_p||\vec{\mu}_e|}{|\vec{r}|^3} \tag{42}$$

which is the dipolar coupling between two aligned dipoles. Since the two dipoles point in the same direction, $g < 0$, and so the upper state $|UP\rangle$ of eq.41 features the minus combination. Plugging the results of eq.41 into eq.40 leads to

$$\begin{aligned} C'_{e,FQ}(t) =& \frac{E_0}{2} N \left(|\vec{\mu}_e| - \frac{|g|}{\tilde{\delta}} |\vec{\mu}_p| \right) \left(\frac{e^{-i\omega_p t}}{\delta + \frac{g^2}{\delta + i\Gamma_p}} + \frac{e^{i\omega_p t}}{2\omega_p + \delta + \frac{g^2}{\delta + i\Gamma_p}} \right) + \\ & \frac{E_0}{2} N \left(\frac{g^2}{\delta^2 + \Gamma_p^2} |\vec{\mu}_e| + \frac{|g|}{\tilde{\delta}} |\vec{\mu}_p| \right) \left(\frac{e^{-i\omega_p t}}{-i\Gamma_p - \frac{g^2}{\delta + i\Gamma_p}} + \frac{e^{i\omega_p t}}{2\omega_p - i\Gamma_p - \frac{g^2}{\delta + i\Gamma_p}} \right). \end{aligned} \tag{43}$$

The expression of eq.43 can be further simplified considering that in the weak-coupling limit we are dealing with, both conditions $g << \delta$ and $g << \Gamma_p$ are satisfied, which implies that 2^{nd}-order terms like $\frac{g^2}{\delta^2 + \Gamma_p^2} \approx 0$ can be safely neglected and $N \approx 1$. It also follows that $\delta + \frac{g^2}{\delta + i\Gamma_p} \approx \delta$ and $-i\Gamma_p - \frac{g^2}{\delta + i\Gamma_p} \approx -i\Gamma_p$ apply too, thus resulting in

$$C'_{e,FQ}(t) = \frac{E_0}{2} \left[\left(|\vec{\mu}_e| - \frac{g}{\tilde{\delta}} |\vec{\mu}_p| \right) \left(\frac{e^{-i\omega_p t}}{\delta} + \frac{e^{i\omega_p t}}{2\omega_p + \delta} \right) + \frac{g}{\tilde{\delta}} |\vec{\mu}_p| \left(\frac{e^{-i\omega_p t}}{-i\Gamma_p} + \frac{e^{i\omega_p t}}{2\omega_p - i\Gamma_p} \right) \right]. \tag{44}$$

Substituting the expressions of eqs.41-42 into eq.44 and grouping the corresponding rotating ($\propto e^{-i\omega_p t}$) and counter-rotating field terms ($\propto e^{i\omega_p t}$), we end up with

$$\begin{aligned} C'_{e,FQ}(t) = \frac{E_0}{2} \Bigg[& \left(\frac{|\vec{\mu}_e|}{\delta} - \frac{2|\vec{\mu}_p|^2 |\vec{\mu}_e| (\delta - i\Gamma_p)}{|\vec{r}|^3 (\delta^2 + \Gamma_p^2) \delta} + \frac{i2|\vec{\mu}_p|^2 |\vec{\mu}_e| (\delta - i\Gamma_p)}{|\vec{r}|^3 (\delta^2 + \Gamma_p^2) \Gamma_p} \right) e^{-i\omega_p t} + \\ & \left(\frac{|\vec{\mu}_e|}{2\omega_p + \delta} - \frac{2|\vec{\mu}_p|^2 |\vec{\mu}_e|}{|\vec{r}|^3 \tilde{\delta} (2\omega_p + \delta)} + \frac{2|\vec{\mu}_p|^2 |\vec{\mu}_e|}{|\vec{r}|^3 \tilde{\delta} (2\omega_p - i\Gamma_p)} \right) e^{i\omega_p t} \Bigg] \end{aligned} \tag{45}$$

which after some simple algebraic manipulation leads to

$$C'_{e,FQ}(t) = \frac{E_0 |\vec{\mu}_e|}{2} \left[\left(1 + \frac{2i|\vec{\mu}_p|^2}{|\vec{r}|^3 \Gamma_p} \right) \frac{e^{-i\omega_p t}}{\delta} + \left(1 + \frac{2|\vec{\mu}_p|^2}{|\vec{r}|^3 (2\omega_p - i\Gamma_p)} \right) \frac{e^{i\omega_p t}}{2\omega_p + \delta} \right]. \tag{46}$$

Taking the squared modulus of eq.46 results in an expression for the molecular excited state

population in the FQ picture, that is

$$|C'_{e,FQ}(t)|^2 = \frac{E_0^2|\vec{\mu}_e|^2}{4}\left[\left(1+\frac{4|\vec{\mu}_p|^4}{|\vec{r}|^6\Gamma_p^2}\right)\frac{1}{\delta^2}+\left(1+\frac{4|\vec{\mu}_p|^4}{|\vec{r}|^6(4\omega_p^2+\Gamma_p^2)}+\frac{8|\vec{\mu}_p|^2\omega_p}{|\vec{r}|^3(4\omega_p^2+\Gamma_p^2)}\right)\cdot \frac{1}{(2\omega_p+\delta)^2}+2\mathfrak{Re}\left\{\frac{e^{-i2\omega_p t}}{(2\omega_p+\delta)\delta}\left(1+\frac{2i|\vec{\mu}_p|^2}{|\vec{r}|^3\Gamma_p}+\frac{2|\vec{\mu}_p|^2}{|\vec{r}|^3(2\omega_p+i\Gamma_p)}+ \frac{4i|\vec{\mu}_p|^4}{|\vec{r}|^6\Gamma_p(2\omega_p+i\Gamma_p)}\right)\right\}\right]. \tag{47}$$

The most dominant terms of the SC and FQ expressions (eqs. 33 and 47, respectively) are those originating from the rotating-wave terms of the incoming field, that is those terms that stem from the field component $\propto e^{-i\omega_p t}$. Therefore, retaining only those in the corresponding expressions finally brings us to

$$\begin{aligned} |C'_{e,SC}(t)|^2 &\approx \frac{E_0^2|\vec{\mu}_e|^2}{4}\left(1+\frac{4|\vec{\mu}_p|^4}{\Gamma_p^2|\vec{r}|^6}-\frac{4|\vec{\mu}_p|^4}{(4\omega_p^2+\Gamma_p^2)|\vec{r}|^6}+\frac{8|\vec{\mu}_p|^2\omega_p}{(4\omega_p^2+\Gamma_p^2)|\vec{r}|^3}\right)\frac{1}{\delta^2} \\ |C'_{e,FQ}(t)|^2 &\approx \frac{E_0^2|\vec{\mu}_e|^2}{4}\left(1+\frac{4|\vec{\mu}_p|^4}{\Gamma_p^2|\vec{r}|^6}\right)\frac{1}{\delta^2} \end{aligned} \tag{48}$$

which clearly shows that the small-yet-non-null discrepancy observed in the results of Fig.3 (main text) can be traced back to the anti-resonant term of the polarizability (eq.25) which is responsible for the additional terms of $|C'_{e,SC}(t)|^2$ that are absent in $|C'_{e,FQ}(t)|^2$ in eq.48.

3.3 Comparison of SC and FQ models under resonance condition

In Fig.4 (main text) it is shown that when the molecular and plasmonic transitions are resonant ($\delta = 0$) the FQ and SC molecular excited state population profiles are always perfectly superimposed regardless of the absolute value of ω_p, which is something that can not be easily understood by looking at the expressions of eq.48 derived above, since both diverge in this limit. This feature can be actually rationalized considering a more general model still rooted in time-dependent perturbation theory.

In the FQ picture, the full system Hamiltonian in general terms reads

$$\hat{H}_{tot} = \hat{H} + \hat{V}(t) \tag{49}$$

where $\hat{H}$ is the molecule-plasmon Hamiltonian and $\hat{V}(t) = \hat{V}e^{-i\omega t} + \hat{V}^{\dagger}e^{i\omega t}$ is a monochromatic oscillatory perturbation of frequency ω. The shape of $\hat{V}(t)$ guarantees that $\hat{H}_{tot}$ is hermitian.[19] Starting from eq.49 and considering the ground state $|g\rangle$ and two molecular and plasmon excited states $|e\rangle$, $|p\rangle$, the full system wavefunction at time t can be represented as $|\psi(t)\rangle = C_g(t)|g\rangle + C_e(t)|e\rangle + C_p(t)|p\rangle$ and usual time-dependent perturbation theory leads to the following expressions for excited state coefficients,

$$\begin{aligned} i\dot{C}_e &= \omega_e C_e + H_{ep}C_p + \left(V_{eg}e^{-i\omega t} + V_{ge}^{*}e^{i\omega t}\right) \\ i\dot{C}_p &= \omega_p C_p + H_{pe}C_e + \left(V_{pg}e^{-i\omega t} + V_{gp}^{*}e^{i\omega t}\right) \end{aligned} \tag{50}$$

where the shorthand notation $\langle e|\hat{H}|e\rangle = \omega_e$ and $\langle e|\hat{H}|p\rangle = H_{ep}$ has been introduced for convenience.

Given that the monochromatic perturbation has two separate resonant ($\propto e^{-i\omega t}$) and anti-resonant ($\propto e^{i\omega t}$) terms, the molecular and plasmon coefficients can be partitioned accordingly as

$$\begin{aligned} C_e(t) &= C_{e+}e^{-i\omega t} + C_{e-}e^{i\omega t} \\ C_p(t) &= C_{p+}e^{-i\omega t} + C_{p-}e^{i\omega t} \end{aligned} \tag{51}$$

with C_{e+} (C_{e-}) representing the resonant (anti-resonant) contribution to the molecular time-dependent excited state coefficient $C_e(t)$. The same goes for $C_p(t)$.

Upon differentiation of eqs.51 and substitution into eqs.50, the following relations arise after

collecting resonant and anti-resonant terms,

$$\begin{aligned} C_{e+} &= -\frac{H_{ep}C_{p+} + V_{eg}}{\omega_e - \omega} \\ C_{e-} &= -\frac{H_{ep}C_{p-} + V^*_{ge}}{\omega_e + \omega} \\ C_{p+} &= -\frac{H_{pe}C_{e+} + V_{pg}}{\omega_p - \omega} \\ C_{p-} &= -\frac{H_{pe}C_{e-} + V^*_{gp}}{\omega_p + \omega} \end{aligned} \tag{52}$$

which interestingly show that resonant and anti-resonant molecular and plasmonic terms do not mix in the FQ model. In other words, the resonant response of the plasmonic system solely determines the resonant response of the molecule and the same goes for the anti-resonant contribution. Eqs.52 can be made more explicit by recognizing that in the investigated case, where the molecular system is very far from the metallic surface, the coupling matrix element H_{ep} can be expressed in terms of plasmonic and molecular transition dipoles (eq.42, SI 3.2), here renamed as $\mu_p^{tr} = \langle g|\,\hat{\mu}\,|p\rangle$, $\mu_e^{tr} = \langle g|\,\hat{\mu}\,|e\rangle$, thus resulting in

$$\begin{aligned} C_{e+} &= -\frac{A_{p+} + V_{eg}}{\omega_e - \omega}\ ,\ A_{p+} = \frac{\mu_e^{tr}\mu_p^{tr}C_{p+}}{r^3} \\ C_{e-} &= -\frac{A_{p-} + V^*_{ge}}{\omega_e + \omega}\ ,\ A_{p-} = \frac{\mu_e^{tr}\mu_p^{tr}C_{p-}}{r^3} \\ C_{p+} &= -\frac{A_{e+} + V_{pg}}{\omega_p - \omega}\ ,\ A_{e+} = \frac{\mu_p^{tr}\mu_e^{tr}C_{e+}}{r^3} \\ C_{p-} &= -\frac{A_{e-} + V^*_{gp}}{\omega_p + \omega}\ ,\ A_{e-} = \frac{\mu_p^{tr}\mu_e^{tr}C_{e-}}{r^3}\ . \end{aligned} \tag{53}$$

The quantity that is analyzed in Fig.4 (main text), is the molecular excited state population upon driving the system with a field resonant with the plasmon frequency ($\omega = \omega_p$), which can be computed by taking the squared modulus of the molecular coefficient $C_e(t)$ of eq.51. Given the expressions of eq.53 and that excitation is resonant with $\omega = \omega_p$, C_{e+}, which depends on the resonant plasmonic term C_{p+}, always dominate, even when the molecular and plasmonic transitions are not resonant i.e. $\delta = \omega_e - \omega_p \neq 0$, and so the anti-resonant

terms C_{e-}, C_{p-} are always negligible.

On the other hand, in the SC picture the molecule is still described at quantum-mechanical level but the plasmonic object is classical. In this case the corresponding equations of motion for the molecular and plasmonic systems become[20]

$$\begin{aligned} i\dot{C}_e &= \omega_e C_e + \frac{\mu_p \mu_e^{tr}}{r^3} + \left(V_{eg} e^{-i\omega t} + V_{ge}^* e^{i\omega t}\right) \\ \ddot{\mu}_p + \mu_p \omega_p^2 &= K\left(\frac{\mu_e}{r^3} + \left(V e^{-i\omega t} + V^* e^{i\omega t}\right)\right) \end{aligned} \tag{54}$$

where μ_p and μ_e correspond in the FQ picture to the oscillating first-order plasmonic and molecular contributions to the expectation value of the dipole operator upon driving the coupled system, namely

$$\begin{aligned} \mu_p &= \left[\mu_p^{tr} C_{p+} + (\mu_p^{tr})^* C_{p-}^*\right] e^{-i\omega t} + \left[\mu_p^{tr} C_{p-} + (\mu_p^{tr})^* C_{p+}^*\right] e^{i\omega t} = \mu_{p+} e^{-i\omega t} + \mu_{p-} e^{i\omega t} \\ \mu_e &= \left[\mu_e^{tr} C_{e+} + (\mu_e^{tr})^* C_{e-}^*\right] e^{-i\omega t} + \left[\mu_e^{tr} C_{e-} + (\mu_e^{tr})^* C_{e+}^*\right] e^{i\omega t} = \mu_{e+} e^{-i\omega t} + \mu_{e-} e^{i\omega t}. \end{aligned} \tag{55}$$

Therefore, $\frac{\mu_p \mu_e^{tr}}{r^3}$ of eq.54 represents the interaction of the molecular quantum system $|e\rangle$ due to the classical scattered field of the plasmonic dipole μ_p whose equation of motion is that typical of an harmonic oscillator[20] driven by the external drive and by the nearby oscillating molecular dipole. The latter term is proportional to $\frac{\mu_e}{r^3}$ and is nothing but the scattered field of dipole μ_e at the nanoparticle position. K is a numerical factor representing the squared plasma frequency entering into the definition of the metal dielectric function (see ref.[20] for more details on the classical equation of motion).

Starting from eq.54 and by applying the same partitioning strategy of eq.51 to both $C_e(t)$

and μ_p the following expressions come up

$$
\begin{aligned}
C_{e+} &= -\frac{A_{p+} + V_{eg}}{\omega_e - \omega} \ , \ A_{p+} = \frac{\mu_e^{tr}\mu_{p+}}{r^3} \\
C_{e-} &= -\frac{A_{p-} + V_{ge}^*}{\omega_e + \omega} \ , \ A_{p-} = \frac{\mu_e^{tr}\mu_{p-}}{r^3} \\
\mu_{p+} &= (A_{e+} + V)\frac{K}{2\omega_p}\left(\frac{1}{\omega_p - \omega} + \frac{1}{\omega_p + \omega}\right) \ , \ A_{e+} = \frac{\mu_{e+}}{r^3} \\
\mu_{p-} &= (A_{e-} + V^*)\frac{K}{2\omega_p}\left(\frac{1}{\omega_p - \omega} + \frac{1}{\omega_p + \omega}\right) \ , \ A_{e-} = \frac{\mu_{e-}}{r^3}
\end{aligned}
\tag{56}
$$

with μ_{e+} and μ_{e-} defined according to eq.55.

Interestingly, by comparing eqs.53,56 it can be observed that in the FQ model, C_{e+}, which represents the most dominant contribution to the molecular excited state population upon driving, solely depends on C_{p+} which is $\propto (\omega_p - \omega)^{-1}$, whereas in the SC picture C_{e+} depends on μ_{p+} that is $\propto (\omega_p - \omega)^{-1} + (\omega_p + \omega)^{-1}$. Recalling that external excitation is always resonant with the plasmonic system ($\omega = \omega_p$), it can be observed that under resonance condition ($\delta = 0$ and so $\omega = \omega_e = \omega_p$) the most dominant contribution to C_{e+} (and so C_e), is numerically equally described by both models since it originates from the component $\propto (\omega_e - \omega)^{-1}(\omega_p - \omega)^{-1}$ that is present in both cases, thus justifying why FQ and SC curves of Fig.4 (main text) under resonance conditions are always superimposed. In other words, in this limit both models treat in the same way the most dominant contribution to the molecular excited state population, which comes from the resonant terms, thus leading to identical results.

On the other hand, when the plasmonic and molecular systems are not in resonance ($\delta \neq 0$) also the term $\propto (\omega_p + \omega)^{-1}$ contributing to C_{e+} in the SC model and absent in the corresponding FQ expression plays a small-yet-observable role, as shown in Fig. 4 (main text). Besides, under this condition also C_{e-} can be significant and this term enters differently in the two cases. More specifically, in the FQ model (eqs.53) this contribution only depends on the anti-resonant plasmonic response that is proportional to $\propto (\omega_p + \omega)^{-1}$, whereas in the SC picture (eqs.56) C_{e-} depends on μ_{p-} that in turn has two contributions respectively

proportional to $\propto (\omega_p - \omega)^{-1}$ and $\propto (\omega_p + \omega)^{-1}$. The first of these two terms, which is absent in the corresponding FQ expression, is numerically non-negligible because external driving is always resonant with the plasmon frequency, thus constituting an additional plausible source of discrepancy when $\delta \neq 0$.

4 Scaling NP plasmonic quantities

In the case of a plasmonic NP described by a Drude-Lorentz (DL) dielectric function model, the NP quantization scheme that has been detailed previously[6] leads to the following expressions for plasmon mode frequencies ω_p and corresponding quantize surface charges q_{pj},

$$\begin{aligned} \omega_p^2 &= \omega_0^2 + \left(1 + \frac{\lambda_p}{2\pi}\right) \frac{\Omega_{plasma}^2}{2} \\ q_{pj} &\propto \sqrt{\frac{\omega_p^2 - \omega_0^2}{2\omega_p}} \end{aligned} \tag{57}$$

where λ_p is the p^{th} eigenvalue of the NP-PCM diagonalized response function,[6] ω_0 is the frequency of DL bound oscillator and Ω_{plasma} is the metal plasma frequency, as defined in eq.2 (SI 1.1).

Starting from eq.57 it can be shown that for a given λ_p the corresponding plasmon frequency ω_p can be scaled n-times, with n being a positive integer, while keeping the value of q_{pj} constant if ω_0 and Ω_{plasma} are respectively multiplied by two real numbers a and b, such that

$$\begin{aligned} a^2 &= \left(\frac{\omega_p^2}{\omega_0^2}(n-1) + 1\right) n \\ b^2 &= n\,. \end{aligned} \tag{58}$$

Indeed, upon substituting $\omega_0 \to a\omega_0$ and $\Omega_{plasma} \to \sqrt{n}\,\Omega_{plasma}$ in eq.57 with a,b satisfying

the conditions of eq.58 it follows that

$$\begin{aligned} a^2\omega_0^2 + \left(1 + \frac{\lambda_p}{2\pi}\right)\frac{b^2\Omega_{plasma}^2}{2} &= n^2\omega_p^2 \\ q_{pj} \propto \sqrt{\frac{\omega_p^2 - \omega_0^2}{2\omega_p}} &= \sqrt{\frac{n^2\omega_p^2 - a^2\omega_0^2}{2n\omega_p}} \end{aligned} \tag{59}$$

where the last equality can be easily proved to be true using the relations of eq.58.
Eq.59 shows that with such a,b scaling parameters the plasmon mode frequency is scaled n-times while the corresponding quantized charge does not vary, thus enabling us to perform multiple simulations (Fig.4, main text) where the absolute value of ω_p is progressively increased while keeping all the other plasmonic quantities of eq.48 fixed.

References

(1) Mennucci, B.; Corni, S. Multiscale modelling of photoinduced processes in composite systems. *Nature Reviews Chemistry* **2019**, *3*, 315–330.

(2) Pipolo, S.; Corni, S. Real-time description of the electronic dynamics for a molecule close to a plasmonic nanoparticle. *The Journal of Physical Chemistry C* **2016**, *120*, 28774–28781.

(3) De Abajo, F. G.; Howie, A. Retarded field calculation of electron energy loss in inhomogeneous dielectrics. *Physical Review B* **2002**, *65*, 115418.

(4) Coccia, E.; Corni, S. Role of coherence in the plasmonic control of molecular absorption. *The Journal of Chemical Physics* **2019**, *151*, 044703.

(5) Coccia, E.; Troiani, F.; Corni, S. Probing quantum coherence in ultrafast molecular processes: An ab initio approach to open quantum systems. *The Journal of Chemical Physics* **2018**, *148*, 204112.

(6) Fregoni, J.; Haugland, T. S.; Pipolo, S.; Giovannini, T.; Koch, H.; Corni, S. Strong coupling between localized surface plasmons and molecules by coupled cluster theory. *Nano Letters* **2021**, *21*, 6664–6670.

(7) Jaynes, E. T.; Cummings, F. W. Comparison of quantum and semiclassical radiation theories with application to the beam maser. *Proceedings of the IEEE* **1963**, *51*, 89–109.

(8) Romanelli, M.; Riso, R. R.; Haugland, T. S.; Ronca, E.; Corni, S.; Koch, H. Effective Single-Mode Methodology for Strongly Coupled Multimode Molecular-Plasmon Nanosystems. *Nano Letters* **2023**, *23*, 4938–4946.

(9) DelPo, C. A.; Kudisch, B.; Park, K. H.; Khan, S.-U.-Z.; Fassioli, F.; Fausti, D.; Rand, B. P.; Scholes, G. D. Polariton transitions in femtosecond transient absorption

studies of ultrastrong light–molecule coupling. *The journal of physical chemistry letters* **2020**, *11*, 2667–2674.

(10) Kuttruff, J.; Romanelli, M.; Pedrueza-Villalmanzo, E.; Allerbeck, J.; Fregoni, J.; Saavedra-Becerril, V.; Andréasson, J.; Brida, D.; Dmitriev, A.; Corni, S., et al. Sub-picosecond collapse of molecular polaritons to pure molecular transition in plasmonic photoswitch-nanoantennas. *Nature Communications* **2023**, *14*, 3875.

(11) Dalibard, J.; Castin, Y.; Mølmer, K. Wave-function approach to dissipative processes in quantum optics. *Physical review letters* **1992**, *68*, 580.

(12) Mølmer, K.; Castin, Y.; Dalibard, J. Monte Carlo wave-function method in quantum optics. *JOSA B* **1993**, *10*, 524–538.

(13) Dum, R.; Zoller, P.; Ritsch, H. Monte Carlo simulation of the atomic master equation for spontaneous emission. *Physical Review A* **1992**, *45*, 4879.

(14) Schmidt, M. W.; Baldridge, K. K.; Boatz, J. A.; Elbert, S. T.; Gordon, M. S.; Jensen, J. H.; Koseki, S.; Matsunaga, N.; Nguyen, K. A.; Su, S., et al. General atomic and molecular electronic structure system. *Journal of computational chemistry* **1993**, *14*, 1347–1363.

(15) Zeman, E. J.; Schatz, G. C. An accurate electromagnetic theory study of surface enhancement factors for silver, gold, copper, lithium, sodium, aluminum, gallium, indium, zinc, and cadmium. *Journal of Physical Chemistry* **1987**, *91*, 634–643.

(16) Dovzhenko, D.; Ryabchuk, S.; Rakovich, Y. P.; Nabiev, I. Light–matter interaction in the strong coupling regime: configurations, conditions, and applications. *Nanoscale* **2018**, *10*, 3589–3605.

(17) Boyd, R. W. *Nonlinear optics*; Academic press, 2020.

(18) Atkins, P. W.; Friedman, R. S. *Molecular quantum mechanics*; Oxford university press, 2011.

(19) McWeeny, R. *Methods of Molecular Quantum Mechanics*, 2nd ed.; Academic Press, 1992.

(20) Dall'Osto, G.; Gil, G.; Pipolo, S.; Corni, S. Real-time dynamics of plasmonic resonances in nanoparticles described by a boundary element method with generic dielectric function. *The Journal of Chemical Physics* **2020**, *153*.

Conclusions and outlook

This PhD thesis aimed at shining light on the complex and rich physico-chemical properties arising from coupling molecules with plasmonic nanostructures, thus placing itself in the field of Molecular Plasmonics. The focus of the overall work has been on investigating the impact of plasmonic effects on molecular excited state phenomena, such as molecular light absorption and emission, energy transfer, and plexciton properties and dynamics. This has been done by employing state of the art theoretical modelling, combining quantum chemistry description of target molecular systems with classical or quantum treatment of plasmonic structures, the latter modelled as homogeneous polarizable objects of arbitrary shape.

Each reported chapter features either applications of previously developed theoretical methods to hybrid molecular-plasmonic systems of scientific relevance or new methods development that were needed to make preceding approaches more versatile and complete. There is a well-defined line connecting the various chapters which is intimately connected to the thesis aim, that is, applying and developing theoretical tools to explore light-matter interactions in molecular-plasmonic systems under different scenarios, moving from simplified single-molecule pictures to more complex interaction regimes.

The thesis begins with an investigation of one molecule interacting with a classically-described plasmonic nanostructure. In this first chapter tip-enhanced photoluminescence experiments on single-molecules are addressed by means of the PCM-NP theory. It is shown that geometrical features of usual STM tips employed for such kind of experiments drastically affect the spatial distribution and frequency dependence of the local field acting on the molecule, thus revealing the physical reasons why TEPL imaging is heavily influenced by the characteristics of plasmonic tips usually employed in experiments.

Moving from chapter 1 to chapter 2, one additional molecule comes into play, while a classically-described plasmonic STM tip is still present. By doing so, the molecular complexity of the system being investigated is pushed further and new excited state phenomena can be investigated, like molecular energy transfer. In this chapter, building on the theoretical modelling of TEPL experiments presented in chapter 1, the role of the plasmonic system in mediating molecular energy transfer is assessed. It is disclosed that common rules widely used in the energy transfer community to distinguish between Förster and Dexter mechanisms of energy transfer, i.e. exponential vs d^{-6} decay, are no longer appropriate due to the relevance of nanoscale plasmonic effects taking place in such STM junctions. Comparison with state of the art experiments on the same target system shows that the efficiency of energy transfer between a donor-acceptor pair nearby a plasmonic STM tip can exhibit an exponential decay trend even if plasmon-mediated

classical electromagnetic effects are solely considered, and so without resorting to quantum overlap of donor-acceptor wavefunctions. The latter condition is usually expected to be responsible for such steep decays in standard Dexter-like energy transfer among bare molecules.

From chapter 3 onwards, the complexity of the system being investigated is not only increased by acting on the molecular side, but also the plasmonic description changes, moving from a classical treatment of the metallic system to a fully quantum one, thus focusing on strongly-coupled molecular-plasmon nanosystems. In this regard, chapter 3 features a methodological development to include multimode effects in *ab initio* single mode QED theories by devising an effective mode approach that is applied to the QED-CC method. It is shown that effective mode QED-CC significantly improves upon the original single-mode QED-CC theory when multimode effects are relevant and non-negligible, approaching exact QED-FCI results while retaining the same computational scaling of single-mode QED-CC.

In chapter 4 collective strong-coupling is addressed by combining theory and experiments. More specifically, the focus of this chapter is on investigating the ultrafast dynamics of plexciton states arising from a collection of merocyanine molecules strongly-coupled to plasmonic aluminum nanoellipses. To this end, a quantum model of the coupled system is devised and applied to simulate the ultrafast transient response upon optical pumping. A synergistic comparison between theoretical simulations and pump-probe experiments reveals that the collective plexciton state that is formed as a result of initial optical excitation quickly collapses to a purely molecular excited state because of plasmon dephasing, happening on a fs timescale. The transient dynamics that is probed by the time-delayed optical probe pulses is indeed ascribed to an intramolecular dynamics of purely molecular excited state whose relaxation decay is accelerated due to the interaction with the plasmonic local field. The observed strong impact of plasmonic losses on plexcitons' lifetime raises serious questions about the use of plasmon-molecule strong-coupling towards controlling photochemical reactions.

Finally, in the last chapter of this thesis a direct comparison between full-quantum and semiclassical modelling of plexcitonic systems is reported, thus pinpointing fundamental differences between the two descriptions in modelling hybrid molecular-plasmonic systems under different interaction regimes. The semiclassical theory, which was employed in the first two chapters, is here directly compared with the full-quantum one, the latter scheme being closely connected to chapters 3 and 4. On the one hand, it is shown that under high-intensity driving fields, going beyond the linear regime, the semiclassical theory fails to reproduce the correct behaviour of some important system's physical quantities, such as the molecular excited state population upon driving. On the other, even within the linear regime, where the two approaches are expected to yield comparable results, it is revealed that a subtle-yet-observable difference arises, thus highlighting a fundamental discrepancy in the way plasmon-molecular interactions are described in the two cases.

The work that has been carried out during this thesis has set the stage for further investigations in the Molecular Plasmonics field, spanning different excited state phenomena and coupling regimes. As future perspectives, there are surely two direct follow-ups. On the one hand, the methods and computational schemes that have been tested and developed in this thesis could be used to probe other promising and exciting applications, such as plasmon-mediated chirality,

which is nowadays attracting so much scientific attention that is even emerging as a standalone research field, usually referred to as "Chiral Plasmonics" [1–4]. Clearly, the possibility of using plasmonic systems to boost chirality at the nanoscale could lead to a vast range of useful applications, ranging from sensing, enantiomer discrimination and enantioselective catalysis, just to name a few. On the other hand, the plasmonic quantization scheme that has been employed throughout this thesis essentially relies on a simple Drude-Lorentz model for the metal dielectric response, which is sometimes unable to capture the full features of real materials dielectric functions, especially when multiple interband transitions kick in[5]. Therefore, a more complete quantization scheme to overcome such limitation is desirable. To this end, a valuable starting point consists in modelling real metals dielectric functions, which are experimentally measured, with a fitted function built as a sum of Drude-Lorentz oscillators, defining what has been named "generic dielectric function" approach[6]. Up to now, this method has only been applied to model the classical response of plasmonic systems, therefore its extension to quantum models is desirable.

References

(1) Hentschel, M.; Schäferling, M.; Duan, X.; Giessen, H.; Liu, N. *Science advances* **2017**, *3*, e1602735.

(2) Hu, Z.; Meng, D.; Lin, F.; Zhu, X.; Fang, Z.; Wu, X. *Advanced Optical Materials* **2019**, *7*, 1801590.

(3) Cao, Z.; Gao, H.; Qiu, M.; Jin, W.; Deng, S.; Wong, K.-Y.; Lei, D. *Advanced Materials* **2020**, *32*, 1907151.

(4) Carone, A.; Mariani, P.; Desert, A.; Romanelli, M.; Marcheselli, J.; Garavelli, M.; Corni, S.; Rivalta, I.; Parola, S. *ACS nano* **2022**, *16*, 1089–1101.

(5) Kolwas, K.; Derkachova, A. *Nanomaterials* **2020**, *10*, 1411.

(6) Dall'Osto, G.; Gil, G.; Pipolo, S.; Corni, S. *The Journal of Chemical Physics* **2020**, *153*.